Impact of Structure and Defect Modification on Vanadium Oxide for Alkali-ion Battery Electrodes

Evan Uchaker

A dissertation

submitted in partial fulfillment of the

requirements for the degree of

Doctor of Philosophy

University of Washington

2015

Reading Committee:

Professor Guozhong Cao, Chair

Professor Lucien N. Brush

Professor Jihui Yang

Program Authorized to Offer Degree:

Materials Science and Engineering

University of Washington

Abstract

Impact of structure and defect modification on
vanadium oxide for alkali-ion battery electrodes

Evan Uchaker

Chair of the Supervisory Committee:
Professor Guozhong Cao
Materials Science and Engineering

The proliferation of portable electronics and electric vehicles paired with the updating of an antiquated grid system has driven the rapid progression of improved technologies related to energy distribution and storage. However, energy storage materials and devices have come to be viewed as a crux impeding advanced device development. Alkali-ion, namely lithium and sodium, batteries are a robust technology that has seen gains in performance based on materials chemistry over the past several decades. Despite years of intensive research accompanied with significant progress, the cathode remains a limiting factor towards improved battery performance because of its low capacity and exasperated degradation over long term cycling; the cathode is also one of the most expensive material components of the overall cell. Thus, research concerning new cathode material development and the improvement of already well-established cathode materials should be a top priority. Within this context, vanadium oxide is an ideally suited model material showcasing how structural or chemical alterations can have tremendous impact on device performance.

As a means towards improving electrochemical performance, the role of kinetics and thermodynamics were investigated through structural and defect chemistry manipulation in the vanadium oxide system. Structural modification, as a means towards achieving kinetic stabilization, can be utilized to develop electrodes with the chemical stability of microsized

particles that simultaneously exploit the beneficial properties associated with nanoparticles. Defect modification is a powerful means towards improving material intercalation capabilities by reducing the stress and localized electrostatic contributions which directly alter the migration energy and diffusion barriers the alkali-ion must overcome. Lithium-ion was chosen for structural (kinetic) examination as it is a mature technology that has been extensively investigated; sodium-ion was chosen for defect manipulation because the larger size and different transport characteristics of sodium ions influence the thermodynamic (and to a lesser extent the kinetic properties) of sodium-ion batteries, and can lead to unexpected electrochemical behavior. The findings gained are by no means limited to the originally investigated systems, and should be taken into consideration for an assortment of electrode materials.

Acknowledgements

Firstly, I would like to thank my advisor, Professor Guozhong Cao, for his encouragement, understanding, invaluable advice, and support throughout my graduate career. His lessons have extended well beyond science, whether by design or not, and have endowed me with a subset of guiding principles. His concern, dedication, and enthusiasm will always inspire me moving forward.

There are many people who helped me along the way during my studies, both professionally and personally. Large thanks are due to Tuesday Kuykendall with the MSE department and Scott Braswell at the NTUF for helping train me on equipment and troubleshoot experimental issues, especially when starting out. While my research group was a revolving door of visiting students and scholars during my time, there have been several members paramount to my development. I would like to express considerable thanks to Stephanie Candelaria, Nan Zhou, Yanwei Li, Jiangang Li, and Yanyi Liu for their guidance and support, particularly during the early stages of my studies. There are, what seems like, countless other former Cao Group members who helped me out at one point or another, and for that I would like to express my appreciation.

To my mother who has more strength than most, and my father who's working knowledge I envy - this would simply not be possible without your unyielding love and encouragement. Graduate school was not always an easy or smooth endeavor, but your support was steadfast and energizing. To my brother and sister for providing me some comic relief, and my extended family for always inquiring when I would actually finish school and get a real job.

Last but certainly not least, I must thank a certain someone who embarked on this journey with me four and a half years ago. While we had (roughly) no idea what we were doing, we somehow pieced things out and figured out life together. Your unconditional support has been one of my strongest motivators, and for it I will always be indebted.

To Kelsey, looking forward.

Contents

List of Tables

List of Figures

Chapter 1

Motivation and Context

1.1 Energy Demands

Energy plays an increasingly important role in modern society, and its use has historically been accommodated by considerable daily fossil fuel consumption in order to power our modern infrastructure. For the past several years, fossil fuels - including coal, petroleum, and natural gas - have meet approximately 80% of the overall US energy demands.[2] In turn, the use of and emissions from these combustion based fuel sources has led to both environmental and economic concerns regarding the depletion of natural resources, greenhouse gas emission, price volatility, and foreign resource dependence. Moreover, the Energy Information Administration (EIA) projects that world energy consumption will grow by 56% between 2010 and 2040 despite US demand maintaining at its current level thanks in large part to enhancements in efficiency and consumer awareness.[2] However, fossil fuel costs will remain a concern as resource depletion and scarcity become more of an issue.

Consequently, substantial efforts have been made to develop renewable energy harvesting technologies as energy security and environmental concerns have spurred great commercial, public, and political interests. Towards these means, the renewable energy market - including hydroelectric, geothermal, solar, wind, and biomass - has seen steady expansion in overall

Table 1.1: Range for total system levelized costs of new generation resources, (2012 USD/MWh).

Plant type	Minimum	Average	Maximum
Conventional Coal	87.0	95.6	114.4
Advanced Coal with CCS	137.3	147.4	163.3
Advanced Nuclear	92.6	96.1	102.0
Wind	71.3	80.3	90.3
Solar PV	101.4	130.0	200.9
Solar Thermal	176.8	243.1	388.0
Hydro	61.6	84.5	137.7

market share, up to 9%, while fossil fuels have merely maintained their levels of consumption over the past several years. This, of course, has unfolded as renewable technology and system costs have decreased; the comparative levelized costs (net cost to install a system divided by its expected life-time energy output) of several renewable technologies are listed in Table 1.1.[2] However, the successful implementation of these technologies is dependent on reliable and robust electrical energy storage since these energy harvesting methods are diffuse in space and intermittent in time, and because the majority of energy consumption targets cannot be directly tethered to the grid. Thus, it is imperative that we develop improved, commercially viable energy storage devices that can provide direct relief for some of the most confronting energy issues.

1.2 Energy Storage Systems

Electrical energy has been a critical industrial driver since the advent of the technological revolution (second industrial revolution). Unlike energy sources preceding this time, wood or coal, electricity must be used as it is generated or converted immediately into another form such as potential, kinetic, or chemical energy. There is a profusion of electrical energy storage devices and technologies that have been developed over the past several decades, and

a comparison of their application range in terms of energy stored and power output is shown in Fig. 1.1. [3]

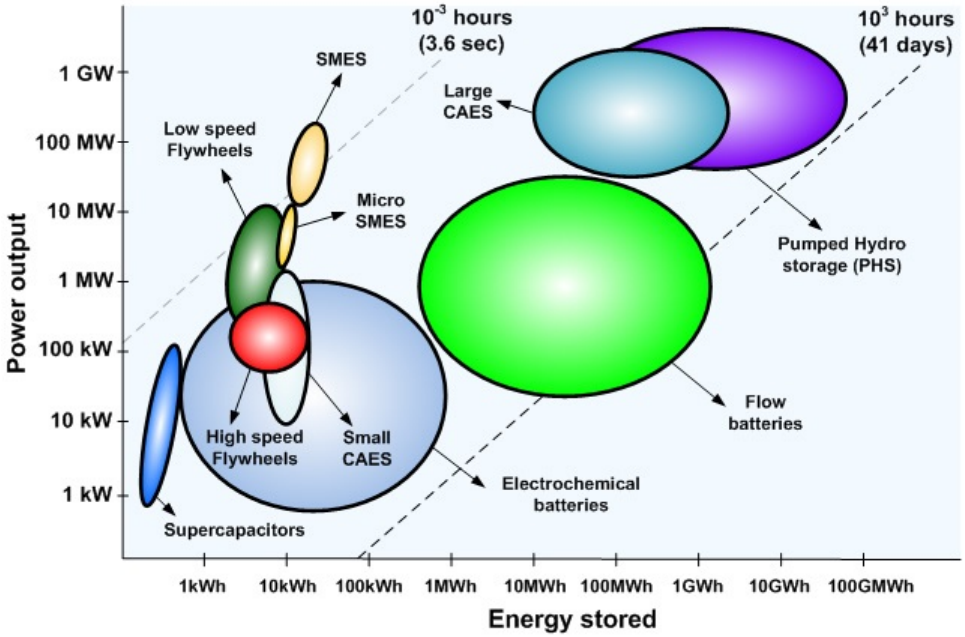

Figure 1.1: Application range of different energy storage technologies based on power output and energy stored.[3]

1.2.1 Mechanical Energy Storage

Initial developments in energy storage mainly focused on mechanical, non-chemical, storage technologies that have seen continual advancement in performance into recent years. Of these technologies, pumped-storage hydroelectricity (pumped-hydro) is by far the largest-capacity form of grid energy storage currently available, and accounts for the overwhelming majority of bulk storage capacity worldwide. The basic principle on which pumped-hydro operates is quite simple. At times of low electrical demand, excess generation capacity is used to pump water from a lower elevation source into a higher reservoir. When there is higher electrical demand, the water is released back into a lower reservoir (or body of water) after passing through a turbine that generates electricity in the process. However, it is clearly improbable for pumped-hydro to be accessible in all markets given the need for an abundance

of water and topographic variation. Compressed air energy storage (CAES) functions in a similar manner where low cost off-peak energy is stored in the form of compressed air for a latter time. Flywheels offer a mechanism of intermittent energy storage, and are used more as a means of maintaining an even power distribution.

1.2.2 Electrochemical Energy Storage

Electrochemical cells and systems play a key role in a wide range of sectors, and their continued development is crucial as society moves away from chemical/carbon based fuel systems. It should come as no surprise that there are strong similarities among the various electrochemical energy storage systems - capacitors, fuel cells, and batteries. Their most apparent mutual feature is their design which establishes that the energy storage and conversion processes take place at the phase boundary of the electrode/electrolyte interface while electron and ion transport are locally isolated.

Electrochemical Capacitors

Electrochemical capacitors (supercapacitors) consist of two electrodes separated by an ion permeable membrane (separator) saturated with electrolyte. When the electrodes are polarized *via* an applied potential, ions in the electrolyte form an electric double layer of opposite polarity in response to that of the electrode. Supercapacitors offer high specific power as well as long cyclic stability and life time, but suffer from low specific energy because they store their energy electrostatically. They are used for voltage drop compensation in weak networks, allowing for very intense peak power. Efficiencies of approximately 90% can be achieved for very long cycle lifetimes since there are no chemical reactions involved. Supercapacitors differ from traditional capacitors in that the energy is interfacially stored in the electric double layer between an electronically conducting porous electrode and the ionically conducting liquid electrolyte. Thus, the amount of charge stored per unit voltage in an electrochemical capacitor is primarily a function of the electrode size and specific

surface area. It is possible for additional charge mechanisms to occur based on surface redox reactions (pseudocapacitance).

Fuel Cells

Fuel cells, like batteries, convert the chemical energy residing in a fuel into electrical energy on demand. Fuel cells differ from batteries in that the fuel and oxidant are not contained within the same compartment but are supplied continuously from external sources, meaning that no time is lost to recharging. Fuel cells can be roughly categorized into low-temperature ($< 200°C$) and high-temperature ($> 450°C$) divisions. Low-temperature fuel cells typically use alkaline or acidic electrolytes. Hydrogen gas is the preferred fuel for low-temperature cells since the only waste products generated from its use are heat and water. In such a system, hydrogen fuel is pumped into the anode where its reduction is catalyzed by the anode itself, generating electrons and protons. The electrons power an attached load while the positively charged protons migrate to the cathode, where they are recombined with electrons and oxygen to form water and heat. Thus, the fuel cells electrodes serve to: ensure a stable interface between the reactant gas and the electrolyte, catalyze the electrode reactions, and conduct the electrons from or to the reaction sites. A significant problem is the control of the interface where the electrolyte, electrode, and gas all reside together. As the main difference among fuel cell types is the electrolyte, fuel cells are classified by the type of electrolyte they use followed by the difference in startup time.

Batteries

> *The expression 'battery' was originally used for assemblies of cannons in artillery units, but around 1750 Franklin used it, for the first time, to describe the connection of Leyden jar capacitors. Then, in 1801, David applied the term to an assembly of galvanic cells to obtain a higher power. Later, in 1808, Cruikshank used the term 'cell' to describe the compartment of a battery. Following this rea-*

soning, the word battery should be used only for an assembly of cells (in series or parallel); however, it became a technical and commercial common practice to use the word battery for even single cells.

- Karl Kordesch in a "History of Primary Batteries"

Batteries, as devices for chemically storing energy, possess the advantages of high portability, high conversion efficiency, long life, and zero exhaust release.[4] They are ideal power sources for portable devices, automobiles, and backup power supplies; accordingly, batteries power nearly all of our portable electronic devices and are used to improve the efficiency of hybrid electric vehicles. The ideal battery would offer a combination of high power and energy density, long cyclic life, stability, and potential for recyclability. Although many types of batteries have been developed with much improved energy storage performance, the fundamental structure of a battery remains the same, consisting of a negative (anode) and positive (cathode) electrode separated by an intermediate electrolyte. To date, the advancements in battery technology have mainly relied on the development and use of different types of materials for electrodes and electrolytes yielding new electrochemical reactions; the most celebrated innovation being the advent of rechargeable (secondary) batteries in addition to disposable (primary) cells. The gravimetric and volumetric energy densities of several battery chemistries are compared in Fig. 1.2.[5]

Primary batteries are non-rechargeable, and are discarded once used. The advantages of primary cells include high energy density, since there are no compromises in design to accommodate recharging, and a sloped discharge profile that can be used for accurate depth of discharge measurement. However, they are extremely wasteful both environmentally and economically; most primary cells are only capable of supplying approximately 2% of the power used in their manufacture. Some of the more common primary battery chemistries include: alkaline, silver oxide, zinc-air, and lithium.[6]

The alkaline battery derives its name from the alkaline electrolyte of potassium hydroxide it utilizes. Fundamentally, an alkaline cell involves the reaction of a metal with oxygen,

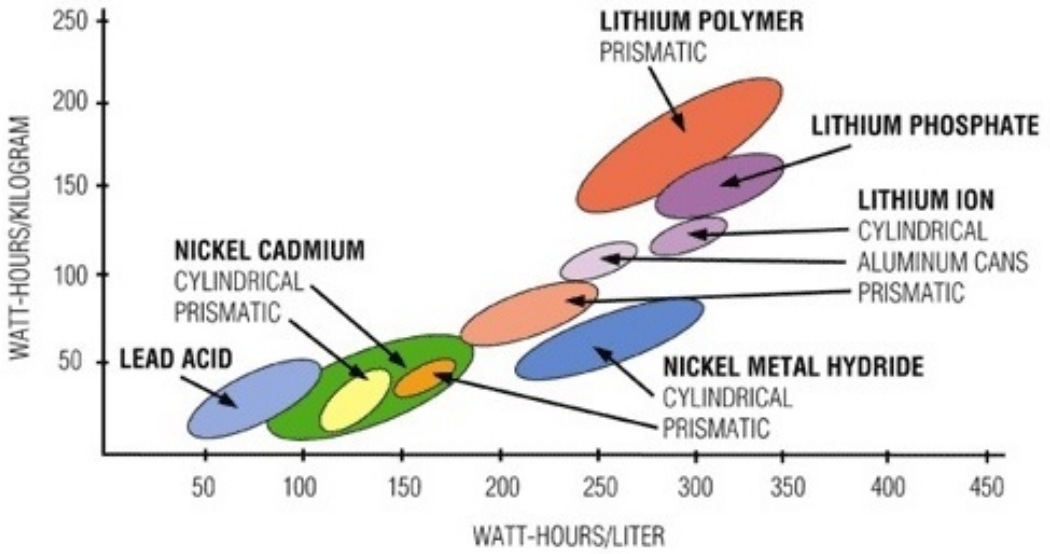

Figure 1.2: Comparison of the different battery technologies in terms of gravimetric and volumetric energy density.[5]

and the most popular version engages the reaction between zinc and manganese dioxide (Zn/MnO_2). The alkaline electrolyte of potassium hydroxide is not part of the reaction, only the zinc and manganese dioxide are consumed during discharge. Alkaline batteries account for approximately 80% of manufactured batteries in the US and over 10 billion individual units produced worldwide.[7] The capacity of an alkaline battery is strongly dependent on the load, and they are well-suited for light and intermittent load applications. The usable capacity is dependent on the application cut-off voltage as the voltage declines steadily during use, but it can deliver four times the capacity of equivalently sized nickel cadmium or nickel metal hydride cells. Because of resistance related limitations, the amount of current an alkaline battery can deliver is roughly proportional to its physical size. The batteries are relatively high in cost and are prone to leaking potassium hydroxide, a caustic agent.

A silver oxide battery uses silver oxide as cathode, zinc as anode, and an alkaline electrolyte that is typically either sodium (NaOH) or potassium hydroxide (KOH). During discharge, the silver is reduced at the cathode from Ag^+ to Ag and the zinc is oxidized from Zn to Zn^{2+}. The silver oxide system is most notably known for its high capacity per unit weight, extremely long operating life, and low self-discharge. However, its biggest downside

is the use of expensive materials (although manufacturers state the amount of silver used is minimal and is not a significant contributor to cost), but it is possible to recover the silver from spent batteries; these cells also suffer from poor low temperature performance and zinc dendrite formation can be an issue. The silver-zinc battery is a variation of the silver oxide chemistry that is rechargeable.

Zinc-air batteries are a non-rechargeable metal-air chemistry based on the oxidation of zinc with oxygen pulled from air (*via* an O_2 permeable membrane). During discharge, oxygen is reduced at the porous carbon cathode leading to the formation of hydroxyl ions (OH^-) that migrate to the anode. The anode in this case is composed of porous zinc saturated with electrolyte. The hydroxyl ions react with the zinc yielding zincate ($Zn(OH)_4^{2-}$), and the resulting electrons are released back to the cathode. Water is returned to the electrolyte as zincate decays to zinc oxide, and the anodic water and hydroxyl groups are recycled at the cathode so the water is not consumed. Cells can be easily tailored as zinc is the consumable material and the reaction rate can be controlled by the intake of oxygen. These batteries have high energy densities and are relatively inexpensive to produce, but have low power density and suffer from high self-discharge.

Lithium batteries are primary batteries that engage lithium metal as anode. Lithium cells can be grouped into three general categories: liquid cathode, solid cathode, and solid electrolyte. There are many variations of cathode material options available for this cell, and some of the most common are manganese dioxide (MnO_2), iron disulfide (FeS_2), thionyl chloride ($SOCl_2$), and sulphur dioxide (SO_2). The electrolyte is some lithium metal salt dissolved in a mixture of organic compounds, but solutes are often added to the electrolyte to increase conductivity. Lithium primary batteries were initially very attractive for their extremely high energy densities attributable to the inherent qualities of metallic lithium. However, it was quickly discovered that cycling produced unwanted anodic dendrites, that cause an electrical short after growing and penetrating the separator. Such an event is usually associated with catastrophic failure, as the cell temperature quickly rises and approaches the

melting point of lithium, causing thermal runaway. Thus, the cell design needs to include safety vents that can alleviate any over-pressure, thereby preventing uncontrollable safety issues but at the same time separating the environment from the volatile lithium. Despite initial safety concerns, primary lithium batteries are now finding steadfast application in pacemakers and defibrillators, as well as portable and lower-power consumer devices.

Secondary batteries are capable of recharge, which makes them more cost-effective over their lifetime. Generally, secondary batteries have a lower capacity and initial voltage, a flat discharge curve, higher self discharge rates, and varying recharge life ratings. Secondary batteries usually have more active (less stable) chemistries which require special handling, containment, and disposal. Some of the more common rechargeable battery chemistries include: lead-acid, zebra (NiNaCl), nickel cadmium, nickel-metal-hydride, and lithium-ion.

A lead-acid battery is composed of a lead dioxide cathode, metallic sponge lead anode, and a sulphuric acid electrolyte solution. During discharge, the lead dioxide (positive terminal) and lead sponge (negative terminal) react with the electrolyte to create lead sulfate and water. The cycle is reversed during the charging process: lead sulfate and water are electrochemically converted to lead, lead oxide, and sulfuric acid by an external potential. These batteries are extremely reliable and robust, but often large and somewhat toxic.

Molten salt (or liquid metal) batteries are a class of battery epitomized by their utilization of molten salts as electrolyte, and offer both a high energy density and a high power density as well as long cycle life. Two of the most advanced molten salt battery chemistries are the sodium-sulfur (NaS) and sodium nickel chloride (Na-$NiCl_2$) varieties, both of which are attractive from the standpoint of employing inexpensive and abundant electrode materials. In the NaS setup, molten elemental sodium at the core serves as the anode, and is separated from the molten sulfur cathode by a beta-alumina solid electrolyte (BASE). BASE is a good conductor of sodium ions, but a poor conductor of electrons, meaning that it is ideally suited for electrolyte application and thus avoids self-discharge. During discharge, Na^+ ions and their corresponding electrons are discharged from the anode towards the cathode where

sodium polysulfide (Na_2S_n) is eventually formed. Thus, the sodium anode is depleted as the cell discharges, but this can be reversed upon charge. Given the necessity for molten states, the battery typically operates in the 300 to 350°C temperature range. The sodium nickel chloride (Na-$NiCl_2$) system, also known as the sodium-metal halide or ZEBRA battery, again employs molten elemental sodium as the anode but pairs it against a porous nickel cathode. The electrolyte is molten sodium tetrachloroaluminate ($NaAlCl_4$) which is separated from the liquid anode by a sodium-conducting beta-alumina ceramic separator. When the battery is discharged, Na^+ ions migrate from the anode, through the ceramic electrolyte to reaction sites at the interior of the cathode to form NaCl. This process is reversed during discharge; thus it is clear that the positive electrode is nickel in the discharged state and nickel chloride in the charged state. The Na-$NiCl_2$ cell typically runs at an operating temperature of 245°C in order to achieve adequate battery performance by improving the ionic conductivity of the solid electrolyte and secondary liquid electrolyte. Molten salt batteries are typically used for large scale energy storage applications given their size along with required time to reheat and/or charge.

Nickel cadmium cells employ nickel oxyhydroxide, NiO(OH), as the positive electrode, porous cadmium Cd as the negative electrode, and an alkaline potassium hydroxide (KOH) electrolyte to realize an energy density approximately double that of lead acid batteries. During discharge, cadmium and nickel hydroxide, $Cd(OH)_2$ and $Ni(OH)_2$, are both formed. Upon reversal of this process, oxygen is generated at the positive (nickel) electrode and hydrogen is formed at the negative (cadmium) electrode, thus it is necessary to properly vent the device. They are capable of operating at high charge and discharge rates, can be deep cycled, and have low internal resistance. However, the major drawback of this technology is its susceptibility to memory effect that can lead to an impedance buildup.

Nickel-metal-hydride batteries utilize chemical reactions somewhat similar to those in nickel-cadmium batteries, with the main difference being the negative electrode is a hydrogen-absorbing alloy as opposed to metallic cadmium. This electrode is made from a metal

hydride, usually alloys of lanthanum and other rare earths, that serves as a solid source of reduced hydrogen that can be oxidized to form protons. The electrolyte and positive electrode are still alkaline potassium hydroxide and nickel oxyhydroxide, respectively. During discharge, the metal hydride intermetallic compound is stripped of its hydrogen, while nickel hydroxide is formed at the positive electrode. NiMH batteries have recently begun to find use in high voltage automotive applications; their energy density is more than double that of lead acid and 40% higher than that of NiCd. The significant disadvantage of NiMH batteries is the high rate of self-discharge; NiMH batteries typically lose 4% of their charge per day of storage.[6]

A Li-ion battery consists of several electrochemical cells connected in parallel and/or in series to provide a designated capacity or voltage. Li-ion batteries provide lightweight, high energy density power sources for a variety of devices. Each electrochemical cell has two electrodes separated by an electrolyte that is electrically insulating but conductive towards Li^+ ions. During discharge, when a Li-ion battery operates as a galvanic cell, Li^+ ions exit the negative electrode (typically carbon) and insert themselves into the positive electrode (typically some layered transition metal oxide compound), while electrons move externally from the negative electrode to the positive electrode. During charge, or when it operates as an electrolytic cell, Li^+ ions are driven from the positive electrode back to the negative electrode by means of a electromotive (potential based) force, while electrons move externally from the positive electrode to the negative electrode to maintain charge. During these processes, Faradaic reactions are accompanied with both mass and charge transfer through the electrodes as well as dimensional change; therefore, the surface area and the transport distance critically determine the performance of the material in question. Electrode composition, crystal structure, and microstructure will have significant impacts on the reaction rate and transfer processes as well as cyclic stability.

Research and development of new battery chemistries has been exponential over the past two decades. Unfortunately, considerable improvements in rechargeable battery technology

are still necessary in order to achieve energy sustainability. Most importantly, the energy density, power density, stability, and recharge time must be vastly enhanced in order to make smart grid and fully electric vehicle technologies an attainable reality. Therefore, developing battery technology, particularly rechargeable batteries, has become a crucial issue for science and industry over the past several decades.

1.3 Scope and Objective

This dissertation includes the experimental work and analysis of the collected results towards understanding and developing new methods and materials that allow for the exploitation of efficient alkali-ion intercalation electrodes based on vanadium oxide. In contrast to the ever-growing energy demands, the candidate pool of the intercalation electrodes is limited. The introduction of nanostructures has achieved huge (research) success in the lithium-ion battery field, as is the case with many other fields. The essential contribution of nanostructuring to the improvement of the intercalation capability lies not only in the increased specific surface area for interfacial Faradaic reactions and the reduced/favorable mass and charge diffusion paths for ions and electrons, but also in the modification of the surface thermodynamics and kinetics which facilitates phase transitions. Practical application of nanostructured materials is limited by low stability and high surface reactivity, which lead to capacity fade. Therefore, kinetically stabilized nanomaterials should be considered given their unique combination of nanoscale properties with order over the microscopic scale; such assemblies possess the structural and chemical stability of microsized electrodes while exploiting the beneficial properties associated with nanoparticles. Parallel to this, the presence of defects has been shown to modify the electrode thermodynamics and facilitate the phase transitions. The amorphous state could possibly store more ions because of its more open structure; similar results have been reported in electrodes with poor crystallinity. Materials possessing surface and bulk defects with poor crystallinity are away from equilibrium, an

effect which has previously demonstrated favorable intercalation properties. The enhanced contribution of the non-equilibrium state is due in part to three aspects: (1) enhancing the storage capacity by shifting the phase transition boundary, (2) improving the rate capability by introducing fast mass and charge transport paths, and (3) extending cyclic stability by permitting more freedom for volume change accompanying de/intercalation. The drawback of the electrodes away from equilibrium state is their chemical and structure stability.

Provided this information, it is clear that there is considerable room for an improved and a more clear understanding of nanomaterial electrode modification. The experimental work was mainly based on solution based methods such as electrochemical deposition, solvothermal precipitation, sol-gel processing, and chemical decomposition. The fabrication of structurally and defect modified nanomaterials were the two primary topics of focus. The findings garnered from these studies should, at the least, be taken into consideration for a range of electrode materials during production. The results gained are by no means limited to the originally investigated systems, but rather strive to serve as a model system showcasing how small structural or chemical alterations can have significant impact on device performance.

Chapter 2 serves as an overview of alkali-ion battery operation with special consideration for Li-ion and Na-ion chemistries. The thermodynamics, kinetics, performance considerations, and material selection of such cells are reviewed. The structure and properties of vanadium oxide pertaining to such applications are also detailed.

Chapter 3 provides a brief literature review of recently reported efforts focusing on the fabrication of nanostructures and how they can be exploited to enhance alkali-ion battery performance. This section will highlight some of the recent developments towards tailoring nanostructures and nanostructure assemblies through the synthesis of faceted (and often high energy) structures, micro/nano-structures, mesocrystals, and the manipulation of surface chemistry for Li-ion battery electrodes with superior performance characteristics. Contrarily, the disadvantages of nanostructured electrode materials are also discussed as there

are several performance issues, either lingering or deriving from nanostructuring, that are often overlooked.

Chapter 4 reports on the polyol induced solvothermal synthesis of hollow vanadyl glycolate nanostructured microspheres, their conversion to hollow nanostructured V_2O_5 microspheres, and their subsequent electrochemical properties. The work proposes a novel formation mechanism involving N_2 microbubbles that act as quasi-micelles due to the large polarization discrepancy between nitrogen and water, and provides a firm understanding of the processes leading to the observed hollow microsphere morphology. The encouraging electrochemical performance of the thermally treated material was attributed to the relatively thin walled structure that ensured fast phase penetration between the electrolyte and active material, and the inherent morphological void that can readily accommodate volume expansion and contraction upon cycling.

In Chapter 5, the solvothermal synthesis of VO_2(B) mesocrystals *via* an additive and template free process is discussed. The homoepitaxially oriented nanostructures were produced through classical as well as non-classical crystallization processes. Despite their overall micro-scale size, the mesocrystals exhibit one of the highest Li-ion intercalation performance and capacity retention values for VO_2(B) when compared to the results from other VO_2(B) structures taken from the literature, especially upon cycling at higher discharge rates. The excellent cycle stability can be attributed to the crystallographically oriented nanoparticle structure that ensures good electrochemical stability and mechanical integrity can be guaranteed for many cycles.

The positive role of the amorphous structure for V_2O_5 electrode materials used as sodium-ion battery cathode is described in Chapter 6. The crystallinity of the electrode was controlled by managing the annealing profile and environment employed. Amorphous V_2O_5 demonstrated superior sodium-ion intercalation properties as compared to its crystalline counterpart when examined as positive electrode material for Na-ion battery application. The percolation of certain diffusion channels in amorphous materials can be activated be-

cause of the disordered structure. Such effects improve charge and ionic transfer at the electrode/electrolyte interface during the sodiation process, yielding a positive electrode material for sodium-ion battery application with superior energy density and strong cycling performance. The possible relationship between the disparity in intercalation properties and structure is discussed.

Chapter 7 is a continuation of the analysis of the positive role of defects to sodium ion intercalation capability for $Na_xV_3O_8$. It was possible to control the sodium composition in the final product by adjusting the amount of sodium precursor added during synthesis. It was determined that deficient and surplus sodium contents, with respect to the ideal stoichiometry, are accommodated by the generation of oxygen vacancies and partial transition metal reduction, or cation disordering, respectively. The disparity in electrochemical performance was attributed to variations in the electronic distribution as promoted through Na-ion interactions and the direct influence of such on the oxygen framework (sub-lattice); these factors were determined to have significant impact on the migration energy and diffusion barriers.

Chapter 8 aims to draw conclusions based on the results obtained over the course of these works, and speculates on the future of related efforts.

Chapter 2

Alkali-ion Battery

2.1 Overview

Overall, batteries are a well-developed technology that have seen gains in improvement based on materials chemistry over the past century. Although many different types of batteries are produced, their fundamental design and structure remains the same - two electrodes of different potential separated by an electrolyte. Moreover, battery operation can be summarized as the conversion of chemical potential to electrical energy through Faradaic reactions that include heterogeneous charge transfer processes occurring at the surface of the electrode.

Until recently, the bulk of alkali-ion battery research focused solely on lithium-ion (Li-ion) chemistry. However, advances in energy harvesting technologies have spurred the need for an array of energy storage for both portable and stationary applications. Fig. 2.1 shows the abundance (atomic fraction) of the chemical elements in Earth's upper continental crust as a function of atomic number;[8] clearly, it is more cost-effective to use less expensive and more abundant materials when available. As the use of large format batteries becomes widespread, increasing demand for lithium commodity chemicals combined with geographically-constrained lithium mineral reserves will drive up prices. Currently, approximately 35% of the world's production of lithium-containing precursor materials is now

consumed by battery manufacturing while lithium recycling has been historically insignificant and technologies are under development.[9] Identified lithium resources total 5.5 million tons in the US and approximately 34 million tons in other countries, with approximately 50% coming from Bolivia and Chile alone.

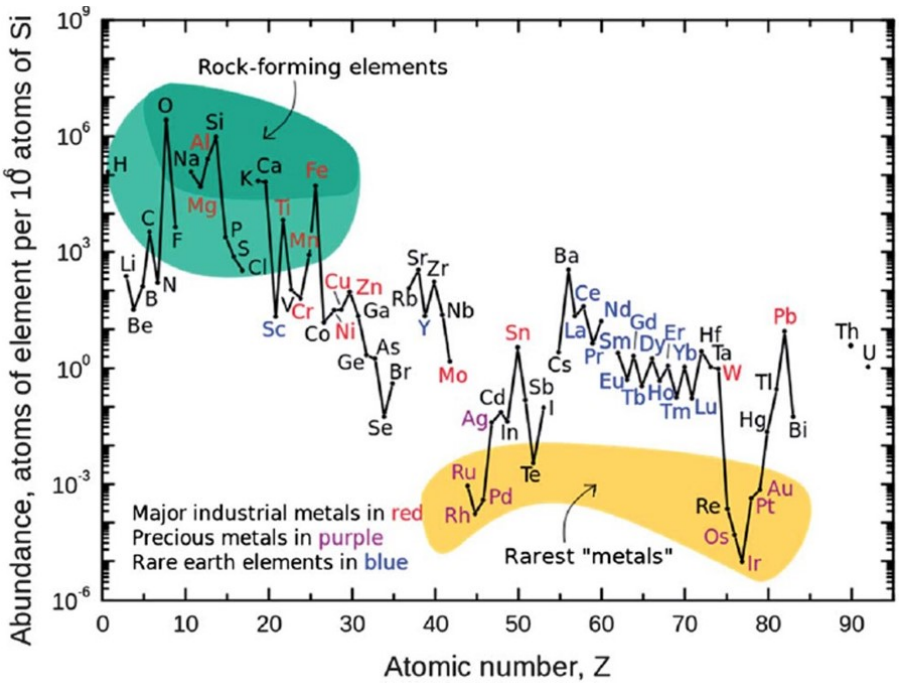

Figure 2.1: Abundance (atom fraction) of the chemical elements in Earth's upper continental crust as a function of atomic number.[9]

An alkali-ion battery consists of several electrochemical cells connected in parallel and/or in series to provide a designated capacity or voltage. Each electrochemical cell has two electrodes separated by an electrolyte that is electrically insulating but ionically conductive. During discharge, when a alkali-ion battery operates as a galvanic cell, alkali-ions exit the negative electrode (typically carbon) and insert themselves into the positive electrode (typically some layered transition metal oxide compound), while electrons move externally from the negative electrode to the positive electrode. During charge, or when it operates as an electrolytic cell, alkali-ions are driven from the positive electrode back to the negative electrode by means of a electromotive (potential based) force, while electrons move externally from the positive electrode to the negative electrode to maintain charge. A simplified schematic

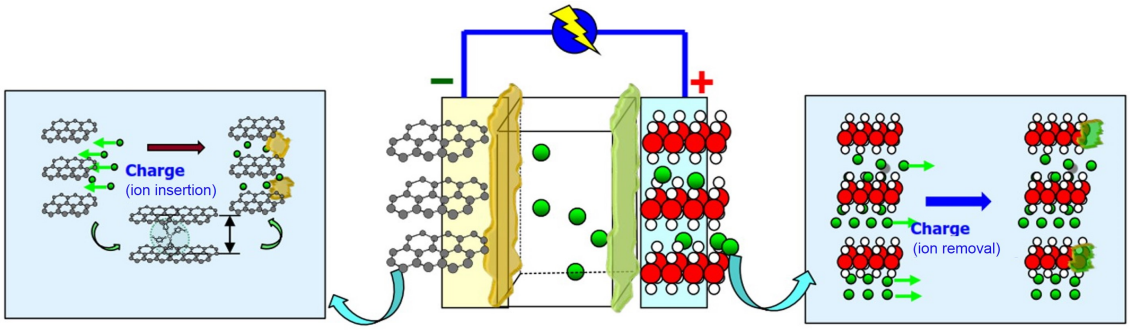

Figure 2.2: Schematic illustration of a typical alkali-ion cell and simplified charge processes (credit: Kang Xu).

of an alkali-ion battery during charge is shown in Fig. 2.2. A comparison of the three most practical alkali-ion battery chemistries is depicted in Table 2.1.

Table 2.1: Comparative qualities of lithium, sodium, and potassium for alkali-ion battery application.

Parameter	Lithium	Sodium	Potassium
Cationic radius (Å)	0.76	1.06	1.38
Atomic weight (g mol^{-1})	6.9	23.0	39.1
E° (V vs. SHE)	-3.04	-2.71	-2.92
Carbonate cost ($/ton)	5000	150	900
Metallic capacity (mA h g^{-1})	3829	1165	687
Coordination preference	octahedral and tetrahedral	octahedral and prismatic	octahedral and tetrahedral

Because of the reversibility of the cell, both oxidation and reduction reactions can occur at the same electrode meaning that the conventional designation of the electrodes (cathode and anode) switches depending on the charge state of the battery. However, further discussion will designate the electrode with a lower open circuit voltage (OCV or V_{oc}) versus alkali metal the anode, and the electrode of higher OCV the cathode for the sake of clarification throughout the remainder of this text. The total energy stored in and released by a cell during charge and discharge is controlled by the thermodynamics and kinetics of the active electrode processes.

Herein, this chapter serves as an overview of alkali-ion battery operation with special consideration for Li-ion and Na-ion chemistries. The thermodynamics, kinetics, performance considerations, and material selection of such cells are covered. The structure and properties of vanadium oxide are also detailed.

2.1.1 Li-ion Battery

Among the many types of rechargeable batteries, Li-ion batteries (LIB) are a mature and robust technology that have been extensively used in consumer devices and industrial applications, and are heralded for their high energy and power densities.[10] Li-ion batteries have the highest volumetric (Wh kg^{-1}) and gravimetric (Wh L^{-1}) energy density among all the metal based batteries because of the small ionic radius and low atomic weight of lithium which are 0.76 Å and 6.94 g mol^{-1}, respectively, in addition to its low density of 0.53 g cm^{-3}. More notably, lithium metal has an extremely low redox potential, -3.041 V (vs. standard hydrogen electrode, or SHE), which provides a strong electromotive force to drive the overall reaction. In contrast to disposable or primary batteries, a Li-ion battery is a rechargeable or secondary battery system based off Faradaic reactions with accompanying mass and charge transfer within the electrodes.

The total energy stored in and released by a cell during charge and discharge is controlled by the thermodynamics and kinetics of the active electrode processes, the reaction occurring at the individual electrodes during discharge can be expressed as:

$$\mathrm{Li}_x(\text{anode}) \longrightarrow (\text{anode}) + x\mathrm{Li}^+(\text{electrolyte}) + x\mathrm{e}^-(\text{circuit})$$

and

$$(\text{cathode}) + y\mathrm{Li}^+(\text{electrolyte}) + y\mathrm{e}^-(\text{circuit}) \longrightarrow \mathrm{Li}_y(\text{cathode})$$

The above electrode reactions can be investigated using either half cells or full cells; the only difference being that in a half cell metallic lithium is used as the counter/reference electrode against the working electrode. In a full cell, the electrons produced at the cathode are those

consumed at the anode, and the electrons are conserved provided no side reactions take place at either one of the electrodes.

2.1.2 Na-ion Battery

Current Li-ion batteries are priced at approximately $600 USD per kWh, but several global government agencies have set goals of seeing these costs decrease to $150 USD per kWh with accompanying increases in energy density into the 400-500 Wh kg^{-1} range.[11] One of the most expensive material components of a Li-ion battery, regardless of the configuration, is the cathode, as shown in Fig. 2.3.[12] Reduction of cost has been one of the primary driving forces for the investigation of new cathode materials to replace expensive $LiCoO_2$, particularly for vehicular and grid storage applications. Thus, it is clear that the development of either other battery systems or the refinement of current assemblies using new materials is necessary.

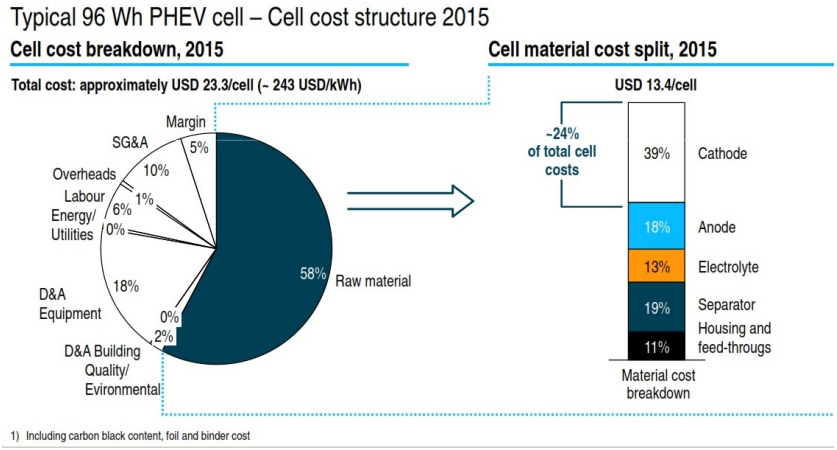

Figure 2.3: Material cost breakdown for a typical 96 Wh PHEV cell.[12]

Compared to the comprehensive body of work on lithium-ion batteries, research on sodium-ion (Na-ion) batteries is still in its nascency. A Na-ion battery functions under the same principles as Li-ion technology, but with different characteristics as dictated by the properties of the transporting ionic species and the consequent effects such has on the electrode materials. Sodium and lithium share similar chemical properties including ionic-

ity, electronegativity, and electrochemical reactivity as they are both alkali metals. They accordingly have comparable synthetic protocols and electrochemical performances, which indicates that the development of sodium-ion batteries can be (ideally) based on previously applied approaches or methods utilized for LIBs. However, the larger size and different bonding characteristics of sodium ions influence the thermodynamic and/or kinetic properties of sodium-ion batteries, and can lead to unexpected behavior in terms of electrochemical performance or reaction mechanism.

Na-ion batteries are attractive because sodium resources are seemingly inexhaustible as well as ubiquitous, and therefore cost considerably less (by a factor of roughly 30-40 times) than lithium; additionally, sodium does not undergo an alloying reaction with aluminum at low voltage, as is the case with lithium, meaning that aluminum can replace copper as the anodic current collector which equates to an overall cell cost savings of 2%.[13, 14, 15] The lower operating voltage of Na-ion cells results in enhanced stability of the non-aqueous electrolyte, but also manifests itself in lower energy density. The majority of the proposed electrode materials for Na-ion battery show similar or slightly lower specic capacity and redox potential than when used in Li-ion cells.[16, 17] However, the accommodation of sodium in traditional host materials is difficult because the ionic radius and reduction potential of sodium are strikingly larger than that of lithium.[18] Therefore, the de/sodiation process induces large distortions in the host lattice that ultimately lead to pulverization of the electrode and the impending failure of the cell.

2.2 Electrode Thermodynamics

Thermodynamics can only be used to construe systems at equilibrium. The concept of equilibrium dictates that a process can move in one of two opposite directions from the equilibrium position, thus reversibility is critical towards treating real processes thermodynamically.

2.2.1 Governing Thermodynamic Considerations

Assuming the cell is in thermodynamic equilibrium, including zero charge exchange, the open-circuit voltage, V ($i = 0$), can be measured. It does not depend on the direction of reaction. According to the first and second laws of thermodynamics, the system has energy:

$$\Delta E = \Delta Q + W = T\Delta S - P\Delta V + W_e \tag{2.1}$$

where *T, S, P, V* are the temperature, entropy, pressure, and volume of the system, respectively. W_e is the electrical work that the cell can provide. Equation 2.1 can be rearranged to yield:

$$W_e = \Delta E - T\Delta S + P\Delta V = \Delta G \tag{2.2}$$

The Gibbs free energy, ΔG, represents the maximum amount of work, and can be extracted from an open-circuit measurement of potential:

$$\Delta G = -W_{max} = QE = -nFE \tag{2.3}$$

where Q is a product of the number of electrons within the cell and the elementary charge, n, is the number of electrons exchanged; F is the Faraday constant of a mole charge ($F = eN_a = 96485$ C or 26.8 Ah), and N is Avogadro's number. E represents the reversible cell voltage and is commonly referred to as the electromotive force (*emf*). The product of nF represents the amount of charge passed, while E represents the reversible potential difference. A negative *emf* value means that electric energy is necessary to drive the electrochemical reaction, while reversing the convention implies a positive *emf* when the reaction is spontaneous. From Equation 2.3, the chemical potential change μ can be obtained from:

$$\mu = \left.\frac{\delta G}{\delta n}\right|_T = -eV \tag{2.4}$$

The equilibrium electrical potential is a function of the chemical potentials μ of the reactants i:

$$\Delta G = \sum_{i=1} v_i \mu i \tag{2.5}$$

where v is $[+1]$ for substances formed (reducing agents) and $[-1]$ for substances consumed (oxidizing agents) in the reaction. Therefore, the thermodynamic component of the cell voltage can be expressed as the sum of the chemical potentials of the substances involved in the reaction:

$$v_\circ = \frac{1}{nF} \sum_{i=1} v_i \mu i \tag{2.6}$$

where $v_\circ$ is known as the standard potential. The full cell potential must also take into account the concentrations of the different reacting species c. The standard thermodynamic relation between chemical potential and concentration is given by:

$$\mu_i = \mu_i^\circ + RT \log c_i \tag{2.7}$$

Equations 2.6 and 2.7 relate the electrical potential to differences in the chemical potential and ionic concentration. Assuming $dP = 0$, and replacing molar fraction by composition, $x = n/N_a$, the change in energy can be described as:

$$dG = -FV dx - SdT \tag{2.8}$$

Other thermodynamic quantities can be derived from electrochemical measurements now that the potential difference across the cell has been linked to the free energy. For example, the entropy change in the cell reaction is given by the temperature dependence of ΔG:

$$\Delta S = -\left(\frac{\delta \Delta G}{\delta T}\right)_P = nF\left(\frac{\delta E_{rxn}}{\delta T}\right)_P \tag{2.9}$$

and

$$\Delta H = \Delta G + T\Delta S = nF\left[T\left(\frac{\delta E_{rxn}}{\delta T}\right)_P - E_{rxn}\right] \tag{2.10}$$

Equations 2.9 and 2.10 relate basic thermodynamic functions to electrochemical parameters. For example, a change of the entropy difference between the two electrodes with alkali-ion concentration is proportional to the change of how the open-circuit voltage depends on temperature at a fixed state of charge.

2.2.2 Gibbs Phase Rule

Crystallographic changes that occur in electrodes during cycling are often reflected in the cell potential. The cell potential alternates between regions of invariance (plateau) and regions of continuous change (redox distributions) as the amount of incorporated alkali metal is varied; the dependence on this alkali metal content can be understood through the Gibbs phase rule. The Gibbs phase rule of thermodynamics can be applied to battery cells provided the system is under thermodynamic equilibrium. The number of degrees of freedom, f, is given by:

$$f = c - p + n \tag{2.11}$$

where c is the number of chemical components, p is the number of coexisting phases, and n is the number of the intensive variables necessary to describe the system. For a closed electrochemical system, the only intensive variables are temperature and pressure, meaning that n is simply 2. Alkali-ion intercalation most often propagates as a two component system composed of the alkali-ions themselves and the host structure. The electrochemical potential varies with composition in the single-phase regions of a binary phase diagram and is composition-independent in two-phase regions if the temperature and total pressure are kept constant. Therefore, there is commonly a single degree of freedom for most electrode materials: the alkali-ion concentration. Thus, the variations of the electrode potential during dis/charge, as well as the phases present and the charge capacity of the electrode, directly

reflet the thermodynamics of the system, meaning that the chemical potential μ (or OCV) is a direct function of the composition, x. Assuming that T and P truly are fixed, all thermodynamic functions such as μ, S, or H would remain constant with composition.

2.3 Electrode Kinetics

Whereas thermodynamics can only be used to describe equilibrium, kinetics describe the evolution of mass flow within and throughout a given system, including both the approach to equilibrium and the dynamic maintenance of that state. Moreover, in the limit of equilibrium, the kinetic equations must collapse to relations of the thermodynamic form.

2.3.1 Arrhenius Relation

The rate of charge transfer can often be the limiting factor in electrochemical cell operation, and it is therefore necessary to consider the kinetics in order to gain a better understanding of the cell itself. Arrhenius was among the first to note that general reaction kinetics have an exponential dependence on $1/T$, and proposed the form:

$$k = k_{\circ}^{'} exp\left(\frac{-Q_a}{k_b T}\right) \tag{2.12}$$

where Q_a is the activation energy or the standard internal energy of activation. It only has a difference of ΔPV compared to the standard enthalpy of activation ΔH (meaning that they become the same when ΔPV is ignored). The attempt frequency factor is designated as $k_{\circ}$. This prefactor can also be included in the product $k_{\circ}^{'}\exp\Delta S/k_B$, which involves the standard entropy of activation, ΔS. Thus the Arrhenius relation (Equation 2.12) can be recast as:

$$k = k_{\circ} exp\left(\frac{-\Delta G}{k_b T}\right) \tag{2.13}$$

where ΔG is the standard Gibbs free energy of activation. Equation 2.13 is an equivalent statement of Equation 2.12, and can be used as an empirical interpretation of reaction kinetics.

2.3.2 Nernst Equation and Tafel Equation on Electrodes

For an electrode reaction, equilibrium is described by the Nernst equation:

$$E = E_{\circ} + \frac{RT}{nF} ln \left(\frac{C_o}{C_r} \right) \tag{2.14}$$

where C_o and C_r are the bulk concentrations of the cathodic and anodic components in the electrode, respectively. The Nernst equation relates the equilibrium reduction potential to the standard electrode potential, temperature, activity, and reaction quotient of the underlying reactions and chemical species. The equation states that if all steps have facile kinetics and are chemically reversible, the electrode potential and the surface concentrations of the initial reactant and final product are in local Nernstian balance at all times, regardless of the current flow.

It has already been established that the reaction rate is governed by the Arrhenius relationship, but the activation energy can be lessened if the battery cell operates under an overpotential, η. The overpotential is the difference between the actual potential and thermodynamically determined reduction potential:

$$\eta = E - E^{\circ} \tag{2.15}$$

where E is the measured potential and E° is the equilibrium potential. In more general terms, the overpotential can be described as the total free energy change per charge transferred. Referring to Equations 2.3 and 2.13, the exchange current experienced by a cathode with an applied overpotential will be decreased by some charge transfer coefficient, α, and the cell activation energy will be decreased by $\alpha n F \eta$. This leads directly to the empirical relation is

known as the Tafel equation:

$$\eta = \left(\frac{k_B T}{\alpha n F}\right) \log i = a + b \log i \tag{2.16}$$

where b is the cathodic Tafel slope, and can be used to relate the rate of an electrochemical reaction to the overpotential.

2.3.3 Marcus Theory of Electron Transfer

Electron transfer occurs quite fast compared to chemical reactions, and takes place without the breaking and forming of chemical bonds. Classically, chemical kinetics are assumed to be independent reactions in dilute solutions whose rates are determined by mean concentrations and follow Butler-Volmer theory. The standard phenomenological model of electrode kinetics is the Butler-Volmer equation, which assumes the dilute solution approximation and operates under thermodynamic equilibrium:

$$\frac{I}{I_\circ} = exp\left(-\frac{\alpha_c n e_\eta}{k_B T}\right) - exp\left(-\frac{\alpha_a n e_\eta}{k_B T}\right) \tag{2.17}$$

where $I_\circ$ is the exchange current and α represents the anodic/cathodic charge transfer coefficients for a single step charge transfer reaction.

Butler-Volmer theory is a convenient assumption to adopt, but may not be applicable to ionically transporting battery systems given that the exchange current can be affected by configurational entropy and enthalpy, electrostatic correlations, and the coherency strain in concentrated solutions. (Coherency strain arises when the molar volume is a function of composition, due to the difference in lattice parameters between the lithiated and non-lithiated phases.) The kinetics associated with the generalized Butler-Volmer equation (Equation 2.17) attempts to apply chemical kinetics in concentrated solutions to Faradaic reactions. However, such generalizations do not apply well to ionic battery systems where the equilibrium electrostatic potential is approximated by the open circuit voltage and the exchange

current to the discharge curve(s) given that these quantities are related by nonequilibrium thermodynamics.[19]

Marcus initially developed his theory to describe electron transfer between small solvated donors and acceptors, and was later able to expand it to include biological electron transfers and electrode reactions.[20] Within these systems, nuclei have no time to shift position during the fast electron transfer processes, thus the electron transfer occurs mainly at or near the intersection of the reactant and product potential energy curves. This intersection also represents the position and energy of the transition state.[21] Marcus theory can be used to explain the dependence of the activation energy (Q_a) on changes in the free energy (ΔG°):

$$Q_a = w + \frac{\lambda}{4}\left(1 + \frac{\Delta G^\circ}{\lambda}\right)^2 = w + \frac{(\lambda + \Delta G^\circ)^2}{4\lambda} \tag{2.18}$$

where w is the work done to bring together either the products or reactants to form an association complex and λ represents the reorganization energy. This energy was defined by Marcus as the energy input necessary to alter the structure (nuclear configuration) of the solvated reactants to match that of the solvated products before electron transfer. Provided Equation 2.3, Equation 2.18 is commonly transcribed as:

$$Q_a = w + \frac{nF(\lambda + \Delta E^\circ)^2}{4\lambda} \tag{2.19}$$

Equation 2.19 reveals that reaction thermodynamics can influence kinetics. In condensed matter, strong interactions alter chemical activities and create variations that can dramatically affect the reaction rate. The extreme case is that of a reaction-driven phase transformation and are common in electrochemistry where charge transfer is accompanied by ion intercalation or deposition in a solid phase.[19]

2.3.4 Fick's Laws

At very high currents, a limiting current may be reached as a result of concentration overpotential. Simplistically, the limiting current is diffusion limited, and can be determined by Fick's laws of diffusion, but more realistically the mass transfer to an electrode is governed by a combination of the Nernst-Planck equation and Fick's first law of diffusion:

$$J_i(x) = -D_i \frac{\delta C_i(x)}{\delta x} - \frac{z_i F}{RT} - D_i C_i \frac{\delta \phi(x)}{\delta x} + C_i v(x) \tag{2.20}$$

where $J_i(x)$ and $C_i(x)$ are flux and concentration of species i at distance x from the surface, D_i is the diffusion coefficient, $\delta C_i(x)/\delta x$ is the concentration gradient at x, and $\delta\phi(x)/\delta x$ is the potential gradient. The three terms represent contributions to the flux from diffusion, migration, and convection, respectively. The Einstein relation is derived from Fick's first law, when only diffusion is considered:

$$D = \frac{uRT}{zF} \tag{2.21}$$

where u is the ionic mobility, z is the number of charges per unit, and F is Faraday's constant. The Einstein relation connects the diffusion coefficient D and ionic mobility u. Since molar conductivity (σ) is equal to the product of zuF we arrive at:

$$\sigma = \frac{Dz^2F^2}{RT} \tag{2.22}$$

as the general expression for conductivity. In the case of a strong electrolyte, the conductivity is the sum of contributions of cations and anions. For time-dependent diffusion processes, Fick's second results in:

$$\frac{\delta C_i(x)}{\delta t} = D_i \frac{\delta^2 C_i(x)}{\delta x^2} \tag{2.23}$$

2.3.5 Electrolyte Conductivity

While the considerations already discussed predominately apply to the electrode materials themselves, it is also worth pointing out that there are limitations regarding the electrolyte as well. Ideally, the electrolyte is ionically conductive while being electronically insulating. The ionic conductivity, κ, of an electrolyte solution derives from the application of a gradient of the electrostatic potential in the electrolyte solution phase, $\nabla\phi$, that causes the anions and cations in the electrolyte solution to move. An electric current is produced because of the flowing ions, and can be expressed in terms of the ionic mobility u, the ion concentration c, and the charge number z:

$$i = -F(z_+c_+u_+ + z_-c_-u_-)\nabla\phi = -\kappa\nabla\phi \tag{2.24}$$

The conductivity of most electrolyte solutions is typically on the order of 10 mS cm^{-2}.

2.3.6 Tortuosity in Porous Electrodes

The overwhelming majority of rechargeable battery systems employ porous electrodes as they provide much larger contact areas per unit volume between electrolyte, reactant, and electronic conductor. At any given time, there will be a large range of reaction rates within the pores because of their varying size and composition (non-active material components). The distribution of these rates will depend on physical structure, conductivity of the matrix and the electrolyte, and on parameters characterizing overpotential phenomena. In galvanic cells this average particle size and accompanying rate distribution directly specifies the power and energy densities that contribute to the polarization losses.[22, 23] The tortuosity of the porous electrode is described by the well-known Bruggeman relation:

$$\tau = \epsilon^{-1/2} \tag{2.25}$$

where τ is the tortuosity and ϵ is the porosity, and their relationship is used as a measure for the decrease in effective electrolyte conductivity and diffusivity due to the microstructure of the electrode. It is worth noting that a portion of the current distribution is related to the current production sites inside the porous electrode itself.

Recent X-ray tomography studies have demonstrated that non-spherical, anisotropically shaped active material particles often align in a manner that increases the tortuosity perpendicular to current collector. This effect can ultimately impact the achievable power density and cycling performance of the overall battery considerably.[24]

2.4 Electrode Material Selection

As is the case in all aspects of material processing, there is a fine balance between the associated material costs and device performance. The main considerations for cost include abundance (or scarcity) of the starting reagents and processing expenses, of which reaction temperature, pressure, and purity are primary aspects. A periodic palette available for the design of electrode materials is presented in Fig. 2.4, where the individual elements are colored by their suitability for battery electrode materials as well as any qualities related to cost, abundance, toxicity, and radioactivity.[25] This is not a steadfast or absolutely resolute guide as there are many batteries specifically tailored to their individual application where it may be possible to make allowances for any unfavorable material aspects. For instance, some transition metals are still actively investigated, such as V and Co, despite their toxicity.

There are many useful trends directly applicable to electrochemical materials that can be quickly gathered from a simple survey of the periodic table. Generally, electronegativity increases as one moves from left to right and upwards across the periodic table; however, there are several exceptions (*i.e.*, copper and zinc). This trend generally holds because there are less screening effects for elements with smaller radius as the positively charged nucleus can more effectively pull and influence the valence electrons, leading to corresponding increases

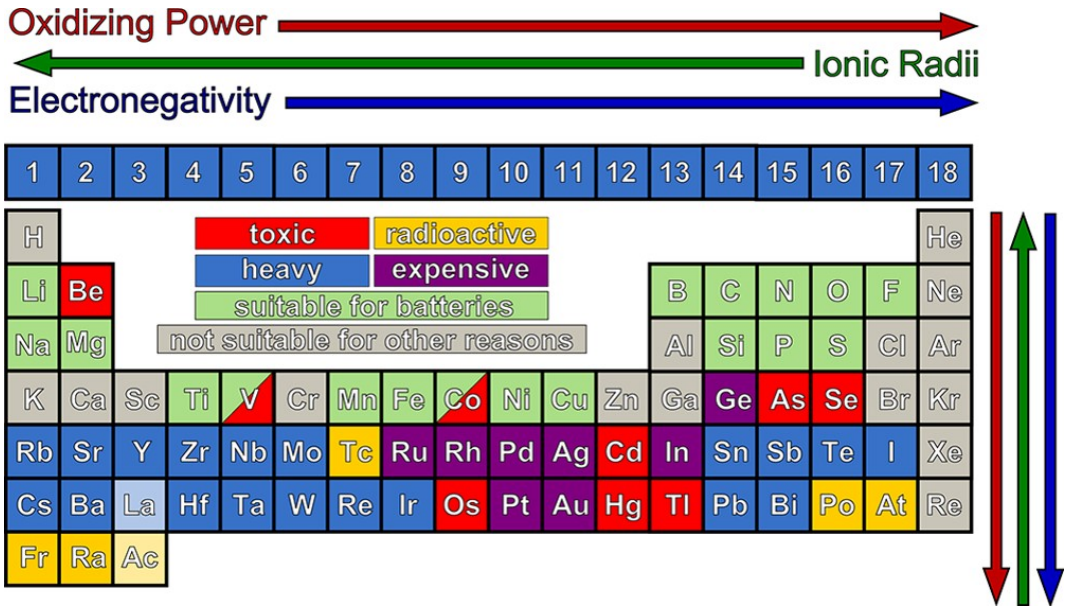

Figure 2.4: Periodic palette available for the design of new electrode materials.[25]

in the electronegativity and ionization energies. Remembering that electronegativity is a measure of the tendency of an atom to attract a bonding pair of electrons, it is clear that such a quality can be used to directly tune the redox potential and ionicity/covalency of insertion electrodes. The redox potential is a measure of the affinity of a substance for electrons taken with respect to hydrogen. Substances more strongly electronegative than (*i.e.*, capable of oxidizing) hydrogen have positive redox potentials, while substances less electronegative than (*i.e.*, capable of reducing) hydrogen have negative redox potentials. Moreover, the ionization energy (the quantity of energy that an isolated, gaseous atom in the ground electronic state must absorb to discharge an electron, resulting in a cation) dictates the oxidizing/reducing power of the atom. For example, monovalent ions are more likely to lose an electron, or be oxidized, than multi-valent ions because it is easier to remove electrons more distanced from the core that have lower ionization energies. It is worth noting that 3d cations of the same charge have more oxidizing power from the left to the right along the periodic table because of atomic size, and thus screening, effects. Clearly, size effects play a role in stabilizing high-valence oxidation states by reducing the coulombic repulsion.

It is well known that the electronegativity values of the constituent elements for a given compound can be used to determine the percent ionic character of that given compound *via*:

$$\% \text{ ionic character} = 100 \times \left[1 - exp\left(-0.25\left(X_a - X_b\right)^2\right)\right] \tag{2.26}$$

where X_a and X_b are the electronegativity values of elements A and B in compound A_yB_z. It is clear intuitively and according to Equation 2.26 that the greater the electronegative difference between two elements or a metal-ligand pair, the greater the percentage of ionic character in the connecting bond. Covalent bonds will have a (somewhat) equal sharing of the electron while ionic bonds will have electron localization around the more electronegative element. This information gathered from the bonding characteristics can be directly used to infer the density of a given compound. Materials with more ionic bonds favor the formation of a dense structure comprised of edge- or face-sharing polyhedra, while covalently bound materials are more often poorly packed structures consisting of corner-shared or isolated polyhedra. The density is of critical importance in layered electrode materials as it is often directly correlated with the magnitude of the diffusion plane through which the intercalating species travels.

A schematic of the relevant energy levels in the electrodes and the electrolyte of a thermodynamically stable LIB relative to one another is shown in Fig. 2.5.[26] The energy separation (E_g) between the lowest unoccupied molecular orbital (LUMO) and the highest occupied molecular orbital (HOMO) of the electrolyte represents the potential window over which the electrolyte can reversibly function. The two electrodes serve as electronic conductors with anode (reductant) and cathode (oxidant) electrochemical potentials of μ_A and μ_C, respectively. If the employed anode has μ_A above the electrolyte LUMO, then the electrolyte will be reduced unless the anode-electrolyte reaction becomes blocked by the formation of a passivating layer (SEI). The same occurs for a cathode with μ_C below the HOMO, but μ_C cannot be lowered below the top of the cathodic anion p-bands which may have an en-

ergy above the electrolyte HOMO; thus, the voltage of many layered oxides is intrinsically self-limited by the top energy of the O2p bands. Therefore, the electrode electrochemical potentials μ_A and μ_C must reside within the electrolyte window to ensure thermodynamic stability, thereby constraining the open-circuit voltage the battery cell.

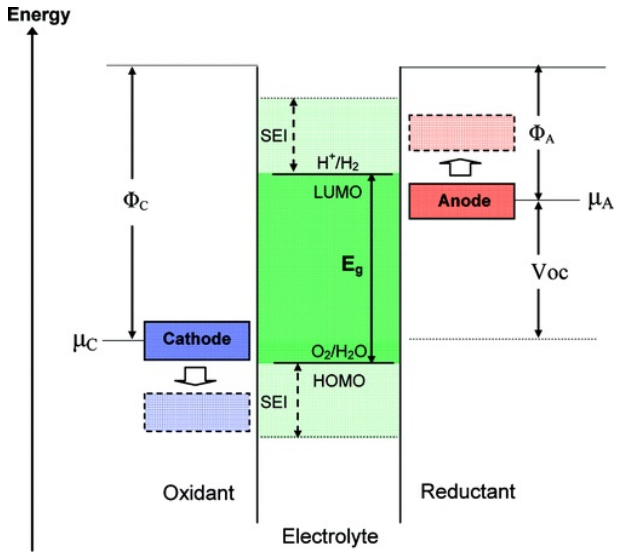

Figure 2.5: Schematic illustration of the open-circuit energy diagram for a typical alkali-ion electrochemical cell (Φ_A and Φ_C are the anode and cathode work functions). The red, blue, and green lines correspond to the Fermi energy of the alkali species in the anode, the lowest energy level of the transition metal antibonding states, and a typical placement for the voltage window for the electrolyte, respectively. The SEI regions are passivation layers that impart kinetic stability.[26]

It is possible to suppress the cathode electron energy level by increasing the ionic nature of the electrode material. The position of the cathodic conduction band states can be directly determined by metal-ligand (MX) bonding characteristics and is reflected in the interatomic distances, where short distances imply stronger (predominately covalent) bonds. Increasing the ionic contribution to the bonding coincides with a decrease in the separation between the bonding (σ) and antibonding (σ^*) orbitals (or any splitting of degenerate orbital states which are often seen in transition metal oxides); this in turn gives rise to a greater difference in energy between the alkali-ion 1s and the lowest unoccupied 3d metal levels (σ^*). This ultimately increases cell potential, and has come to be known as the inductive effect; it has been demonstrated experimentally as an important way to tune redox potentials in a wide

variety of systems. Through this mechanism, it is possible to adjust the open circuit voltage through structural modification which in turn alters the charge density of the MX bonds.[26]

2.4.1 Solid Electrolyte Interphase

It has been well established that the anode of all lithium-ion batteries, regardless of active material or electrolyte selection, is covered by a passivating layer that has been dubbed the solid electrolyte interphase (SEI).[27] The same phenomena has also been observed in many Na-ion cells thus far. Experimental results have also suggested that there is an analogous passivating layer that forms on the cathode as well, but these findings seem to be less ubiquitous and critical to overall cell performance.[28, 29] In general, SEI growth is associated with the irreversible electrochemical decomposition of electrolyte at the electrode surface because of electrolyte instability during charging. Moreover, the film produced from the products of electrolyte reduction is considered to adopt a two-layered structure; a compact inorganic inner layer 1 to 2 nm thick with a porous organic outer layer roughly 10 to 100 nm thick. A vast variety of compounds has been observed in this layer, but the exact structure and composition are dependent on the composition of the electrolyte salt, solvent, and additives, in addition to the electrode itself. There is little understanding of the mechanisms that govern the formation and growth of the SEI.[30] A proposed schematic of the SEI is presented in Fig. 2.6.[27] The formation of a stable and (somewhat) uniform SEI layer is critical towards the successful operation of an full-cell alkali-ion battery because it prevents further electrolyte degradation by blocking electron transport. Lithiation can still be carried out because lithium ions can easily pass through the SEI *via* the exchange of ions between the solvent, SEI compounds, and the lithium intercalated in the active material. The composition, thickness, morphology, conductivity, crystallinity, and density of the SEI are all but a few of its parameters that significantly affect battery performance. The characteristics of the SEI are still poorly understood, and are intensive areas of ongoing investigation. Ideally,

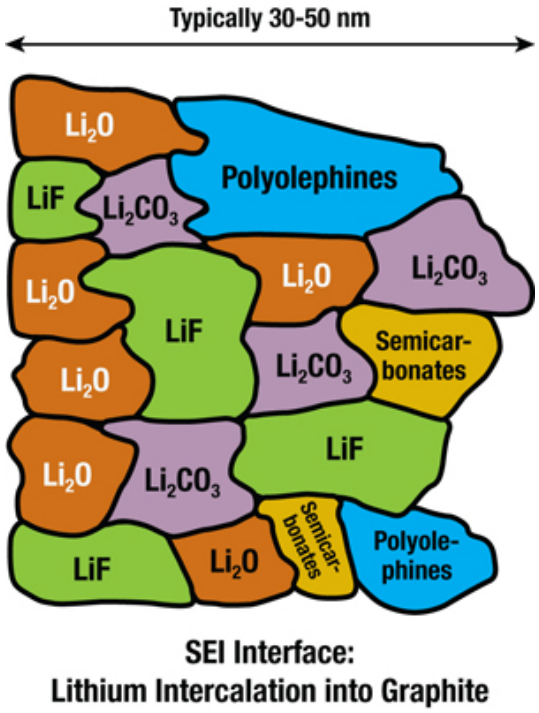

Figure 2.6: Proposed schematic of the SEI layer with the left most edge representing the interface with the electrode surface.[27]

the SEI is ionically conductive, morphologically and chemically homogeneous, mechanically stable, and somewhat flexible as well.[31]

2.5 Electrode Material Performance

There are several ways in which alkali-ions can be repeatedly incorporated and removed from the electro-active material of the electrode. The three main mechanisms through which lithiation or sodiation occur are based on intercalation, alloying, and conversion reactions. A schematic representation of the different reaction mechanisms observed in electrode materials is shown in Fig. 2.7.[32] It is most often the case where there is only a single mechanism operating, but it is possible for there to be a combination of the processes taking place if certain criteria are met.

Alloying reactions are primarily observed in the Group IV (silicon and tin) and V (phosphorus and antimony) elements that serve as anodic materials with high specific capacity.

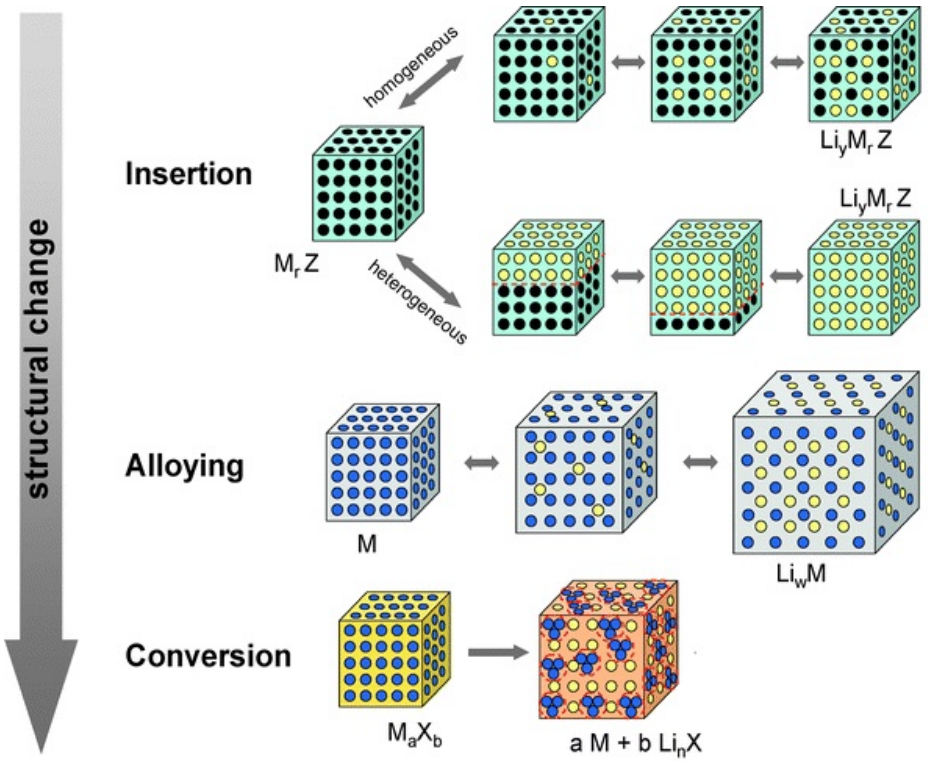

Figure 2.7: A schematic representation of the different reaction mechanisms observed in electrode materials for alkali-ion batteries. Black circles: voids in the crystal structure, blue circles: metal, yellow circles: lithium.[32]

The main challenge for the implementation of alloy anodes is their large volume change (up to 400%) during lithium insertion and extraction, which often leads to pulverization of the active alloy particles and poor cycle stability. In addition, the first-cycle irreversible capacity loss of alloy anodes is too high for practical application (SEI and loss of active material).

A more recently investigated system is the conversion mechanism that involves the formation and decomposition of at least two separate phases through conversion reactions. Reversible conversion reactions can transpire between binary MX compounds, where M is often a transition metal and X a chalcogen or halogen, and metallic lithium, and are based on the reduction and oxidation of metal nanoparticles. Thus it is a reaction that involves heterogeneous lithium storage. It has been determined that the reversibility of the conversion reaction depends on complete reduction of the metal species.

Of the three methods, intercalation is by far the most thoroughly investigated and well understood, and was the system on which initial developments in LIB were based. Intercalation is the reversible insertion of a guest species (ion or molecule) into the lattice of a lamellar host structure. The structure of the host remains unchanged or is only slightly altered in the guest-host complex that is in the intercalation compound (intercalate), however there can be phase changes depending on the degree or extent of intercalation. The rate of intercalation can be controlled by imposing an external potential across the cell, and the reaction will stop when this potential equals the free energy of the system. Deintercalation will occur when the voltage exceeds this free energy. The following considerations will be made based on intercalation systems chemistries alone.

For a given electrode material, the composition, crystal structure, and morphology can dictate the reaction rate and transfer processes for the electrode materials, and can be manipulated to alter the overall electrochemical performance.[26] Provided this synopsis, it is evident that there are several characteristics paramount to good electrode, particularly cathode, performance:

(i) The material contains a readily reducible/oxidizable ion, for example a transition metal.

(ii) The material reacts with lithium in a reversible manner by having tolerance for structural changes during the reversible lithium insertion and extraction process.

(iii) The material reacts with lithium with a high free energy of reaction.

(iv) The material can incorporate large quantities of lithium reversibly with high capacity and at high voltage.

(v) The material should have good electronic conductivity and Li^+ ionic conductivity.

(vi) The material and its synthesis should be inexpensive for commercialization.

(vii) The material is safe and environmentally tolerable.

2.5.1 Performance Metrics

Capacity

The capacity of an electrode material represents the amount of charge that it can store. The gravimetric and volumetric specific capacity can be expressed as:

$$C_g = \frac{1000xF}{3600M_w} \tag{2.27}$$

$$C_v = \rho C_g \tag{2.28}$$

where x is the amount of alkali ions per formula unit of active material that can be reversibly incorporated and ρ is the material density. Equation 2.27 represents the gravimetric capacity and has units of [mA h g^{-1}] while Equation 2.28 expresses the volumetric capacity and has units of [mA h cm^{-3}].

Rate Capability

The term charge/discharge rate or C-rate is often used to describe how fast the cell can be charged or discharged. 1 C denotes either the theoretical charge capacity of a cell or the nominal capacity of the cell, but should be explicitly listed. For example, a C/10 rate means a current allowing full charge or discharge in 10 hours.

Energy Density

Energy density is one of the most important parameters to evaluate the performance of a battery. The energy stored in a battery could be expressed as the integral of voltage upon capacity:

$$E = \int V \, \mathrm{d}C \tag{2.29}$$

The cell energy in terms of total mass and the volume of a battery correspond to the gravimetric and volumetric energy density, respectively. Strictly speaking, it is not correct

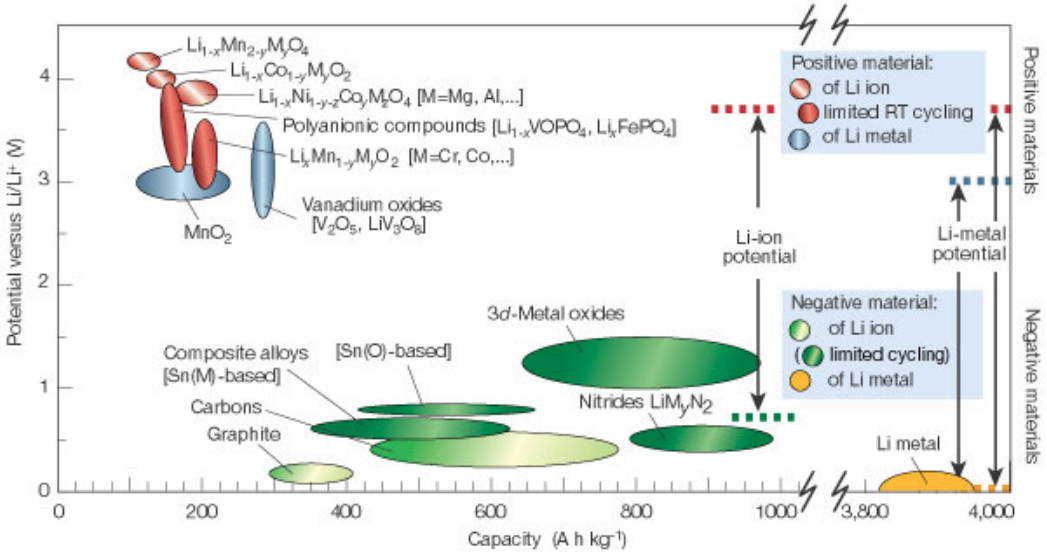

Figure 2.8: Voltage versus capacity for LIB electrode materials.[10]

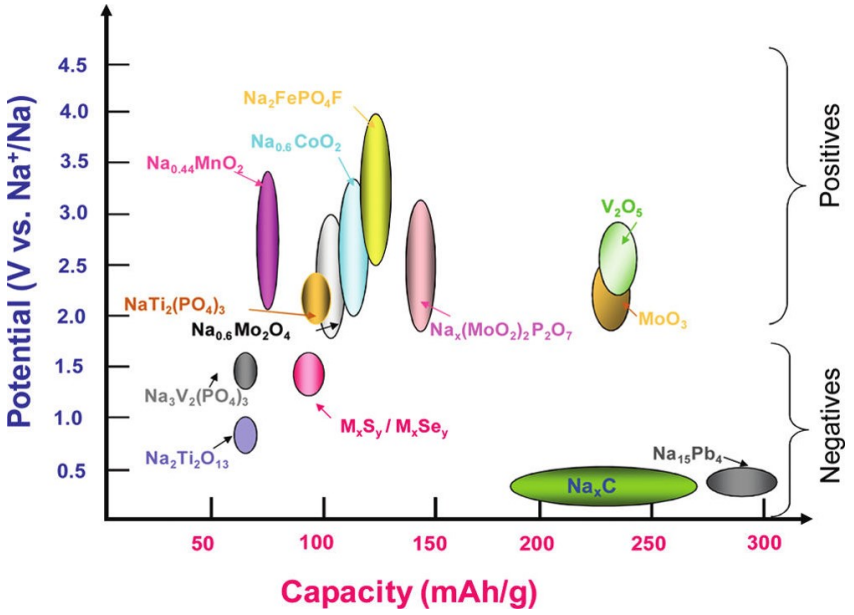

Figure 2.9: Voltage versus capacity for NIB electrode materials.[33]

to report the energy density of a single electrode, as voltage is the difference between two electrodes. However conventionally, the energy density of the cathode is reported based on

the voltage against a lithium anode and only the mass of cathode is included. The specific energy (gravimetric energy density) is typically reported in units of Wh kg^{-1} while the volumetric energy density is exhibited in Wh L^{-1}. Theoretical energy densities of 400 Wh kg^{-1} are obtained when only the active materials of the cathode and anode are considered. The gravimetric energy density of the entire battery must include the weight of the electrolyte, separator, current collectors, and other inactive components which actively serve to lower the value down to one-third to one-half of the theoretical energy density. The input parameters that contribute to energy density for various electrode materials are shown in Fig. 2.8 and 2.9.[10]

Power

The power that a battery can supply is equivalent to the product of the current and voltage, and refers to the energy that can be derived per unit time. A higher current typically leads to a lower voltage, as higher voltage drop exists due to polarization, limits in solid-state diffusion, and phase transformation. Therefore, batteries are typically measured at different currents. To improve power, it is necessary to enhance the diffusion rate of alkali ions and the electrical conductivity.

Cycle Life

Cycle life is another important parameter for evaluating rechargeable battery performance. In industry, the cycle life is defined as the number of cycles it takes for the capacity to degrade to 80% of the initial value. This value is taken as a safety precaution because capacity drops to this level are usually accompanied by lithium plating at the anode which in turn downshifts the entire cell voltage. This will in turn induce stepwise cathode degradation which will lead to additional voltage drops and a self-perpetuating degradation mechanism. The cycle life is dependent on many factors such as the formation of a stable solid electrolyte interphase, the stability of the electrolyte, and the structural stability of the electrodes, *etc.*

2.5.2 Overview of Vanadium Oxide

Despite years of intensive research accompanied with significant progress, the cathode remains a limiting factor towards improved battery performance. Anode materials, even the current commercially available ones, possess stable capacities that are approximately a factor of two better than their cathodic counterparts. Cathode materials on the other hand, are inherently restricted to a considerably lower intercalation capacity and exasperated degradation over long term cycles. Because cathode performance has become a bottleneck for the capacity improvement of alkali-ion batteries, research concerning electrodes is more focused on such. In addition to exploring new cathode materials there has also been strong efforts to improve the intercalation capacity of already well-established cathode materials.

Layered intercalation compounds are one of the more popular battery electrode material candidates, and are for the most part comprised of metal oxides. These layered compounds, for which nearly all of the research and commercialization of cathode materials has been focused, can be further designated into two classes. The first class is comprised of the layered compounds with an anion close-packed or nearly close-packed lattice where the electro-active transition metal ions occupy alternating layers, and lithium is inserted in the unoccupied layers. Both $LiTiS_2$ and $LiCoO_2$, the current commercial cathode of choice, are prime examples of this class of compound. The second class of layered metal oxide compounds can be classified by their more open structures. Primary examples of these structures are tunneled manganese dioxide and the layered vanadium oxides.

Vanadium oxides exhibit intriguing electrochemical, photochemical, catalytical, spectroscopic and optical properties. The electron configuration of vanadium in the ground state is $[Ar]3d^34s^2$. Vanadium exhibits four common oxidation states +5 ([Ar]), +4 ($[Ar]3d^1$), +3 ($[Ar]3d^2$), and +2 ($[Ar]3d^3$) each of which can be distinguished by a respective yellow, blue, green, and violet color as displayed in Fig. 2.10. Vanadium occurs in deposits of phosphate rock, titaniferous magnetite, and uraniferous sandstone and siltstone, in which it constitutes less than 2% of the host rock and is typically collected as a byproduct. The element occurs

naturally in about 65 different minerals and in fossil fuel deposits, and is used by some life forms as an active center of enzymes. Vanadium is used in making specialty steels like rust resistant and high speed tools, and such uses accounted for 93% of the domestic vanadium consumption in 2014.[34] For battery applications, vanadium oxide offers the advantages of being cheap, easy to synthesize, high energy densities, and does not directly complete with the other vanadium applications. Consequently, it has attracted much interest as it also fulfils the electrode material criteria enumerated in the previous section. Some of its basic structural and electrochemical properties are summarized herein.

Figure 2.10: The colorful oxidation states of vanadium, increasing from left to right.

Structure

Vanadium is a transition metal with atomic number 23 and an atomic weight of 50.9415 amu. It is a redox-active element that can be found over a wide range of oxidation states (from -1 to +5) and it can adopt a variety of coordination numbers (CN) and coordination geometries. The ideal coordination polyhedra from CN 4 through 8 are presented in Fig. 2.11, but it should be noted that the real coordination geometries adopted by most vanadium complexes are slightly distorted.[35] The ability of vanadium to take on a host of coordination geometries distinguishes it from other first-row transition metals which are often dominated by a single coordination geometry. Moreover, the acid-base equilibrium plays an important role in the redox behavior of the vanadium center. The Pourbaix diagram (Fig. 2.12) clearly

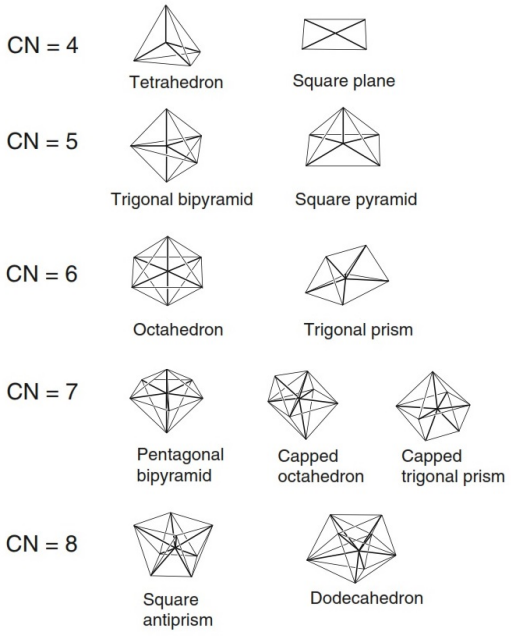

Figure 2.11: Coordination geometries of vanadium species.[35]

demonstrates the redox behavior of vanadium ions in aqueous solution is highly affected by pH. For instance, the V(+3) species exist under acidic conditions, whereas the V(+4) and V(+5) species are dominant under neutral or basic conditions around 0 V.

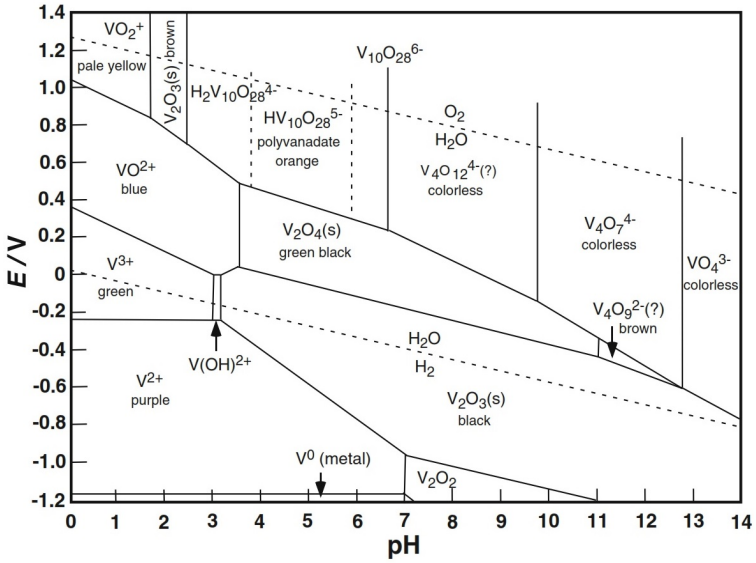

Figure 2.12: Pourbaix diagram of vanadium species.[35]

It has been proposed that there are five stable vanadium-oxygen compounds that can be formed: VO_2, V_2O_3, V_3O_5, V_3O_7, and V_2O_5 with the last being the most common and investigated phase. Numerous other phases that can be formed with the incorporation of lithium. The binary and ternary phase diagrams for the V-O and Li-V-O systems are shown in Fig. 2.13.[36, 37] The pentavalent state of vanadium oxide, V_2O_5, is well known and

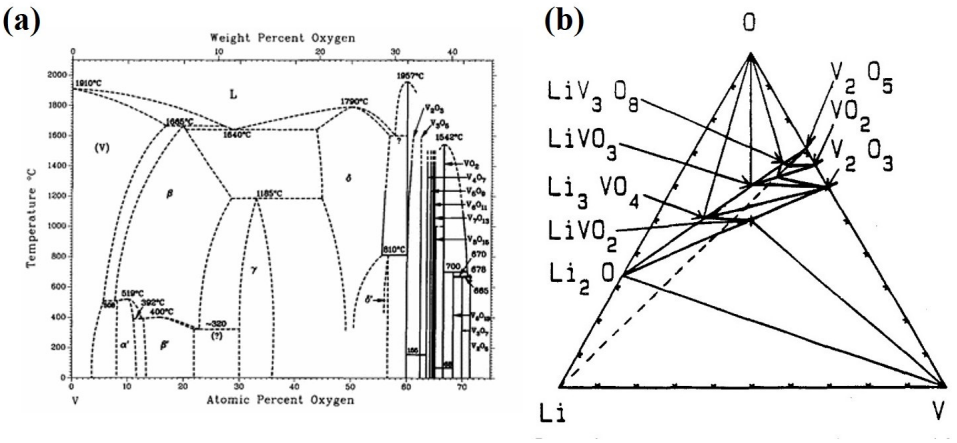

Figure 2.13: (a) Binary V-O and (b) ternary Li-V-O phase diagram.[36, 37]

has a structure that can be described as orthorhombically distorted trigonal bipyramids of VO_5 with shared edges that form zigzag double chains. The structures of the four VO_2 polymorphs, VO_2(R), VO_2(M), VO_2(B), and VO_2(A), are based on an oxygen body-centered-cubic lattice with vanadium in the octahedral sites and somewhat regular oxygen octahedra. VO_2(B) is a layered structure composed of bilayers formed by edge sharing VO_6 octahedra with a three-dimensional framework formed by bridging oxygen atoms between the layers and is one of the few dioxide structure that can reversibly cycle lithium.

As previously mentioned, there are several other vanadium oxide species that can reversibly intercalate lithium or other alkali ions; however, they are not mentioned in this passage for the purpose of remaining succinct.

Vanadium Pentoxide

The pentavalent state of vanadium oxide, V_2O_5, is well known and has a structure that can be described as orthorhombically distorted trigonal bipyramids of VO_5 with shared edges that form zigzag double chains. The V_2O_5 octahedra are irregular with five V-O distances ranging from 0.159 and 0.202 nm and a sixth distance as large as 0.279 nm (Fig. 2.14).[38] Because of the varying V-O distances, and the longest interatomic distance residing opposite the shortest V-O bond directed toward the apex of the square pyramid, it is possible to describe the structure as layered square VO pyramids with five oxygen atoms surrounding the vanadium atom. The apices of the VO_5 pyramids alternate in an up-up-down-down sequence with every third row vacant because of corner sharing of the double chains. The layered assembly is held together *via* van der Waals interactions. It should be noted that the experimentally reported *c*-spacing (4.368 Å) is longer than expected based off of crystallographic arguments (3.830 Å). This is because the vanadium atom establishes a strong covalent bond at the apex of the square pyramid and is thereby slightly pulled out of the basal plane;[39] this in turn lengthens the opposing V-O bond which implies that there is no bonding between the apical oxygen and the out-of-chain vanadium. Similarly, repulsion between layered apical oxygen leads to a weak tilting of the apical V-O bond. V_2O_5 is slightly soluble in water (0.8 g L^{-1}) where it forms an acidic solution that can readily becomes colloidal.

Vanadium pentoxide is an attractive material for application as cathodic material in electrochromic thin film devices and alkali-ion batteries owing to its ability to reversibly accommodate up two alkali ions per oxide formula unit; such intercalation capabilities correspond to high specic capacities of approximately 294 (Li^+, 4 to 2 V) and 236 (Na^+, 4 to 1.5 V) mA h g^{-1}. The electrochemical performance being strongly related to the nature and the amplitude of the structural changes induced by the lithium insertion/deinsertion process, a great number of studies have focused on the structural features of vanadium and

its lithiated $Li_xV_2O_5$ phases. The structural changes accompanied with lithiation are shown in Fig. 2.15.[40]

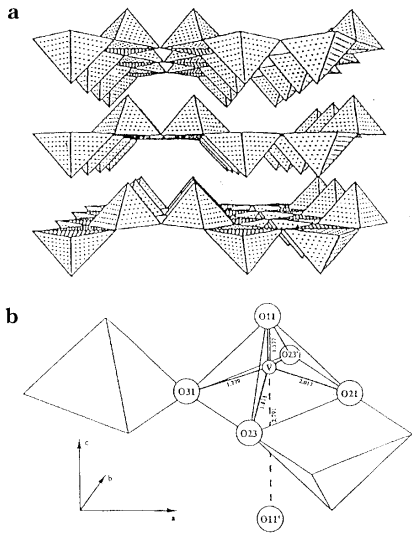

Figure 2.14: V_2O_5 (a) layers and (b) coordination around vanadium.[38]

However, the high specific capacity/energy has not been realized in practical LIB applications because of three primary issues: (1) low electrical conduction, (2) slow lithium-ion diffusion and (3) irreversible phase transitions upon deep discharge. Like most metal oxides, V_2O_5 has very low electronic conductivity due to its low *d*-band mobility and band gap of 2.41 eV.[41] The lithiation/delithiation processes in crystalline V_2O_5 are accompanied by structural phase transitions. Such a phase transition process induces lattice strain due to phase coexistence within the same particle. It is known that the lattice mismatch-induced mechanical strain can cause irreversible structural damage, which not only limits battery life, but also causes irreversible capacity loss. Consequently, V_2O_5 often has very poor rate capability and very limited long-term cyclability.

There are several phases of V_2O_5 formed upon Li^+ intercalation depending on the overall amount of lithium incorporated into the structure. Initially, lithium merely intercalates the structure, first forming the α-phase ($x < 0.1$) and then the ϵ-phase ($0.35 < x < 0.7$) where the layers begin to pucker. In the α-phase, all vanadium crystallographic sites are identical and can readily accommodate the small amount of V^{4+} cations and lithium introduced between

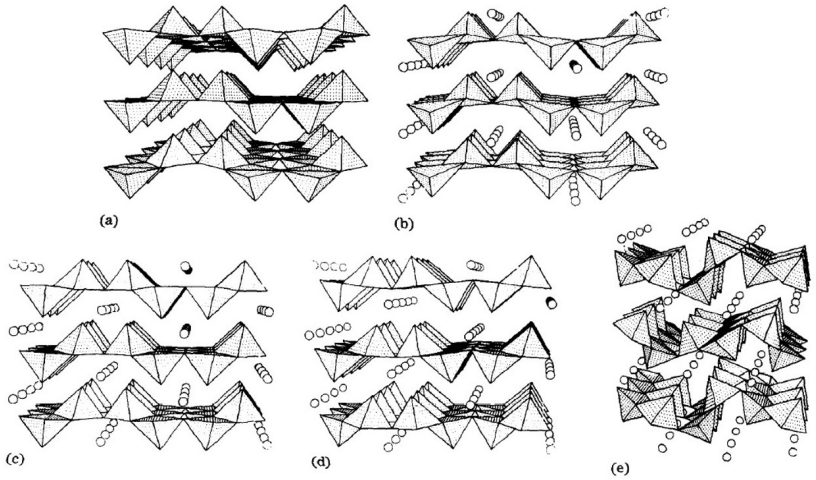

Figure 2.15: Perspective view of the (a) pristine V_2O_5 and lithiated (b) α, (c) ϵ, (d) δ, and (e) γ V_2O_5 structures.[40]

the layers, on sites that can be described as trigonal prisms. Between $0.88 < x < 1$, shifting and puckering of the layers occurs and leads to the formation of the δ-phase. In the δ-phase, one slab over two is shifted by half of a unit cell parameter along the b-axis. No bonds are broken during this process, and thus reversibility is maintained. The VO_5 square pyramids maintain their apical up-up-down-down structure in the α-, ϵ-, and δ-phases, as shown in Fig. 2.15. The intercalation of 1.0 Li^+ per V_2O_5 formula unit corresponds to a specific capacity of 147 mA h g^{-1}.

The intercalation of $1.0 < x < 2.0$ induces transformation to the γ-phase, where the layers are severely puckered and the square pyramid apices now alternate in an up-down-up-down sequence. This structural transformation is reflected in the discharge plateau at approximately 2.3 V (vs. Li/Li^+). Upon further reduction below 1.9 V, corresponding to $2.0 < x < 3.0$, a tetragonal structure is initially formed that later adopts a rock-salt structure, which is known as the ω-$Li_3V_2O_5$ phase. Delmas reviewed these structural modifications and attributes the high OCV at low lithium content to the metastability of the defective rock-salt lattice which can contain up to 60% vacancies on the cation sublattice. The single sloping discharge plateau from almost 4 to less than 2 V makes it uninteresting for practical applications where the change in potential should preferably be under 0.5 V; moreover, this

phase also rapidly loses capacity on cycling and experiences vanadium dissolution into the electrolyte at higher discharge rates.[42]

Approaches to Improve the Electrochemical Properties

The practical application of vanadium oxide has been hampered by its intrinsically low alkali ion diffusion coefcient, relatively low density, moderate electrical conductivity, and poor cycling stability. These intrinsic disadvantages are believed to slow down the kinetics of both ion and electron transports of alkali-ion batteries, and the kinetic problems would be more severe for high-performance alkali-ion batteries that are required to deliver high reversible capacities at high current densities. In the past decades, progressive accomplishments have been achieved that rely on the fabrication of nanostructured materials, cation doping, heterogeneous structures, and the introduction of structural defects - all of which will be highlighted in the succeeding section. Generally, fabrication of nanostructured materials can effectively decrease the ion and electron transport distances while heterogeneous structures and cation doping are able to signicantly increase the electrical conductivity and cycling stability. Implementation of these strategies addresses the problems that are related to the ionic and electronic conductivity as well as structural stability of vanadium oxide. Accordingly, the electrochemical performances of vanadium oxide cathodes are signicantly improved in terms of discharge capacity, rate capability, and cycling stability.

Chapter 3

Nanostructured Electrodes for Rechargeable Battery

The development and characterization of nanostructured electrode materials has been well documented over the past decade; many excellent reviews concerning the benefits of nanostructured materials for electrochemical energy conversion and storage have already been published, to which the reader is referred.[43, 44, 45] However, nanomaterials as a whole suffer from several basic limitations that restrict their performance in energy storage applications. Thus, it is necessary to utilize either one or several exploitive techniques that can easily increase battery performance in order for renewable energy resources to achieve cost parity with traditional energy sources. The remainder of this section will highlight some of the recent developments towards tailoring nanostructures and nanostructure assemblies through the synthesis of faceted (and often high energy) structures, micro/nano-structures, mesocrystals, and the manipulation of surface chemistry for Li-ion battery electrodes with superior performance characteristics.

3.1 Introduction

The development of nanostructured electrode materials has led to great enhancements in Li-ion battery performance, as with many other fields.[43] The nanoscale size reduction leads to enhancements of the Li-ion battery intercalation capability by increasing the specific surface area for interfacial Faradic reactions and the flux of Li-ions across the electrode-electrolyte interface; these effects ultimately enhance the mass and charge diffusion paths and modify the thermodynamics (compared to the bulk), which facilitates phase transitions. However, the most dominant and substantial advantages imparted by nanostructures is drawn from their enhancement of the kinetics and related diffusivities. The Li-ion diffusion time for lithiated or non-lithiated transition metal oxides is proportional to the square of the diffusion path length:

$$t = \frac{L^2}{D} \tag{3.1}$$

where L is the diffusion length and D the diffusion constant. The reduction of the electrode particle size into the nanometer regime tremendously improves the intercalation kinetics and ultimately enhances the overall degree of intercalation. Several studies have also revealed that the implementation of nanostructures as electrode materials has led to an enhancement of the specific capacity beyond the theoretical limits.[46, 47] The increased storage capacity has been attributed to the confined dimensions of nanostructures that make the surface and grain interface effects more prominent. Ultimately, an additional storage mechanism will begin accommodating lithium ions on the surface/interface of the particles or through a conversion reaction when they are below a critical particle size.[46] Therefore, nanostructures of a critical size can undergo an interfacial adsorption mechanism in addition to the traditional bulk intercalation process, and it is possible to modify the nanostructured material phase transition boundary to intercalate more lithium. These studies also revealed that the Li-ion and electron potentials can be modified through the use of exceedingly small particles, producing a change in the electrode potential and overall reaction thermodynamics.[48] All

of these factors make it possible for nanostructured battery electrodes to operate at a higher rate; the use of nanomaterials can also enhance the cycling performance of the material by alleviating some of the lattice strain experienced during cycling due to the de/intercalation of lithium.[48, 49]

The benefits of nanostructured metal oxide electrodes have been well documented throughout the literature. Wagemaker *et al.* compared the lithium ion intercalation performance of anatase TiO_2 micro- and nano-particles.[50] The size of the anatase TiO_2 nanoparticles was incrementally altered in order to investigate the nano-size effects. It was determined that the Li-ion solubility was greater with decreasing particle size, and increased from 0.55 to 0.7 Li^+ per formula unit when the micron-sized TiO_2 particles were replaced with nanoparticles smaller than 40 nm. The discrepancy in the quantity of inserted Li^+ was ascribed to a more homogeneous, and Li-rich, phase in the nanoparticles compared with the micron-sized particles that had coexisting Li-rich/poor phases because they were too large for homogeneous Li^+ penetration.[51] Ganapathy *et al.* also revealed that the Li^+ diffusion rate limiting two-phase boundary between electrode particles has an activation energy of approximately 50 kJ mol^{-1}, but nanomaterials smaller than 40 nm did not have the phase boundary and had an activation energy of 10-25 kJ mol^{-1}.[52] Hu *et al.* also corroborated the enhanced electrochemical effects of nanostructuring TiO_2 as a Li-ion battery electrode material.[53] They revealed that the discrepancy in intercalated Li^+ could be attributed to dissimilar diffusion along the *ab*-plane, and that Li^+ surface storage on the nanoparticles is energetically more favorable than bulk insertion.

While anatase TiO_2 and its derivative structures are well-studied metal oxide electrode materials, it should be noted that layered intercalation compounds are one of the more popular device candidates amongst metal oxide electrodes. These layered compounds, for which nearly all of the research and commercialization of cathode materials has been focused, can be further designated into two classes. The first class is comprised of the layered compounds with an anion close-packed or nearly close-packed lattice where the electro-active transition

metal ions occupy alternating layers, and lithium is inserted in the unoccupied layers. Both $LiTiS_2$ and $LiCoO_2$, the current commercial cathode of choice, are prime examples of this class of compounds. The spinel structured compounds may be classified as a sub-group within this class because the transition metal ions occupy all the layers. Nanostructured $Li_{4+x}Ti_5O_{12}$ spinel has demonstrated superior electrochemical performance when compared to its bulk counterpart due to increased Li-ion occupancy. These results serve as a direct reflection of the enhanced kinetics and transport properties of nanostructured electrodes because $Li_{4+x}Ti_5O_{12}$ spinel is a zero-strain material.

The second class of layered metal oxide compounds can be classified by their more open structures. Primary examples of these structures are the layered vanadium oxides and the tunneled manganese dioxide; the transition-metal phosphates, such as olivine $LiFePO_4$, can also be grouped under this structural classification. The benefits of nanostructuring have been documented for these layered materials as well. Uniform films of V_2O_5 were formed on FTO substrates through a combination of cathodic deposition and catalyzed gelation. The homogenous films were composed of microflakes that ranged from 0.5 to 1.5 μm in diameter, and each flake was composed of nanoparticles measuring 20-30 nm in diameter with 10 nm gaps separating adjacent nanoparticles. Conversely, similar processing routes with the addition of a block copolymer surfactant yielded a porous V_2O_5 structure composed of nanoparticles and pores approximately 100 nm in size. Not surprisingly, the smaller particle and pore size of the surfactant-free specimen led to far greater lithium intercalation capacity (405 vs. 275 mA h g^{-1}), rate performance (70C vs. 60C), and cyclic stability (200 vs. 40 cycles). Thinner films displayed similar benefits when compared to thicker films composed of the same electro-active material.

The development of silicon based anodes for Li-ion batteries has also received a considerable amount of interest over the past several years. The Li-Si binary system indicates that an individual silicon atom can accommodate the insertion of 4.4 lithium ions, yielding one of the highest known theoretical charge capacities (4200 mA h g^{-1}); additionally, the discharge

potential of silicon is quite low, and it is already a highly processed material. Although this theoretical capacity value is eleven times larger than that of the current commercially used graphite anodes, the use of silicon as an anode material is limited because the insertion of 4.4 Li-ions is accompanied by a 400% volume expansion of the lattice. This tremendous expansion results in cracking and disintegration of the electrode, with active material loss *via* reduced electronic contact, giving way to severe capacity fade. Such has been the case for past studies involving Si bulk films and micrometer-sized particles, where capacity fading and short battery lifetimes were attributed to the pulverization and loss of electrical contact between the active material and the current collector. Fortunately, the use of Si nanostructures such as nanowires can alleviate these issues because there is a critical particle size below which fracture will not propagate further. Huggins and Nix calculated the critical size for particle fracture upon lithiation as:[54]

$$h_C = \frac{23}{\pi}\left(\frac{3K_{IC}}{B\epsilon_T}\right)^2 \tag{3.2}$$

where h_C is the critical crack size, K_{IC} is the fracture roughness in MPa$\sqrt{m}$, B is the biaxial Young's modulus of the material, and ϵ_T is the total strain. For silicon, the fracture toughness is 10 MPa$\sqrt{m}$, and the strain associated with the insertion of 4.4 Li^+ per Si ($Li_{22}Si_5$) is approximately 400%. Therefore, the critical particle size below which fracture supposedly does not occur is predicted to be 75 nm.

Experimentally, it has been shown that composite anodes of Si-C nanoparticles ranging from 50 to 100 nm in size have better cycling performance than those in the micrometer range. Alloy particles within the nano-regime can accommodate a larger degree of volume variation because they often display higher plasticity and deformability. The control and tailoring of these considerations resulted in a nano-Si composite anode material with an extremely high and reversible capacity that exhibited none of the capacity fading seen in the micrometer sized material. Chan *et al.* went on to demonstrate that Si nanowires

grown through the vapor-liquid-solid method were better able to accommodate large volume changes without the initiation of fracture due to their small diameter, one dimensional confinement of charge transport, and enhanced contact with the current collector. Additionally, no binders or conductive additives were required to compensate for material shortcomings since each nanowire was attached to the current-carrying electrode; however, the capacity retention at the 2C rate was less than 50% of the initial capacity.[55]

While Li^+ surface storage and increased fracture resistance are performance benefits inherent to many nanostructured electrode materials, an even more complex interaction has been observed in nano-sized $LiFePO_4$ because of its incomplete miscibility gap (region in a phase diagram in which two phases with nearly the same structure have no solubility in one another). Meethong *et al.* showed that the miscibility gap in pristine $LiFePO_4$ diminishes with decreasing nanoparticle size, suggesting that the miscibility gap completely disappears below some critical value.[56] The enhanced solubility of Li in nano-sized $LiFePO_4$ can be ascribed to the presence of multiple phases in the individual particles. The coexistence of two crystallographic phases within one particle leads to a domain-wall-related energy penalty, which is determined by the strain prompted from the difference in the lattice parameters and can destabilize the two-phase coexistence in smaller particles. Nanostructures have been utilized to increase the equilibrium compositions and effectively reduce the lattice mismatch between coexisting phases. Therefore, the energy gain associated with phase separation will drop with decreasing particle size, and the miscibility gap will gradually diminish.[57] The miscibility gap began to decrease while the solubility increased starting with nanoparticles approximately 100 nm in diameter, and showed a strong effect in particles smaller than 35 nm.[58] Changes in the miscibility gap were ascribed to particle size associated modifications in the molar free energy of mixing for either one or both phases. The associated particle size effects were also speculated to emerge from the relative contributions of the particle-matrix surface energy and stress, and/or the coherency or compatibility stresses in the coherently interfaced two-phase particles.[56]

Herein, the remainder of this section will focus on some of the recent developments towards tailoring nanostructures and nanostructure assemblies for fabricating electrodes that will not fall victim to the damaging effects associated with nanomaterials. In addition, the exposure of specific (and often high energy) facets, micro/nano-structures, mesocrystals, surface/defect chemistry manipulation for Li-ion battery electrodes with superior performance characteristics will be discussed.

3.2 Exposure of Specific Surface Facets

It has been demonstrated that the control of particular electrode material crystal facets is beneficial for lithium ion storage. These increased attributes can be ascribed to the unique surface properties of specific facets, including the surface energy and diffusion barrier.[59, 60] Yang *et al.* were amongst the first to synthesize anatase TiO_2 single crystals with a high percentage of reactive (001) facets compared to the more energetically preferred (101) facets, which have surface energies of 0.9 and 0.44 J m^{-2}, respectively.[61] This discrepancy in the energy values was proven experimentally by reversing the relative stability of the facets by terminating the surface with fluorine through the use of hydrofluoric acid. The fluorine terminated surfaces were later cleaned by heat treatment, whereupon the crystal structure and morphology were retained. Many investigations have since been conducted that analyze the novel properties of these faceted structures for environmental, energy storage, biomedical, and catalytic applications.[62]

Of particular interest for such tailored materials is the increased lithium ion storage potential of the exposed high energy facets. Lithium insertion occurs faster on the (001) TiO_2 surface rather than the (101) surface because of a higher charge transfer rate constant (10^{-8} vs. 2×10^{-9} cm s^{-1}) and chemical diffusion coefficient (7×10^{-14} vs. 2×10^{-13} cm^2 s^{-1}) for Li^+ insertion.[60] The charge transfer and chemical diffusion coefficient for TiO_2 is greatest along the (001) facet, and exposing these facets can result in a lower energy barrier

for faster and more efficient Li^+ intercalation. Despite the relatively high percentage of (001) facets, the specific surface area of the TiO_2 crystals was low because they were relatively thick along the [001] direction. With these considerations in mind, Wu *et al.* set out to improve the electrochemical performance by reducing the [001] directional thickness and increasing the two-dimensional lateral size of the (001) plane by synthesizing TiO_2 nanosheets with high-energy facets.[63] While the nanosheet surfaces were dominated by (001) facets, they were initially stabilized by oleylamine which was then removed by calcination; however, this approach led to agglomeration and coarsening of the nanosheets.

Chen *et al.* circumvented this issue by synthesizing hierarchical spheres from large ultrathin anatase TiO_2 nanosheets with nearly 100% exposed (001) facets.[64, 65] Even at a high current rate of 20C (3400 mA g^{-1}), a reversible capacity of 95 mA h g^{-1} could still be delivered, as evidenced in Fig.3.1. Similar results for analogous morphologies have been demonstrated by several other groups as well.[66, 67] The individual nanosheets adopted a

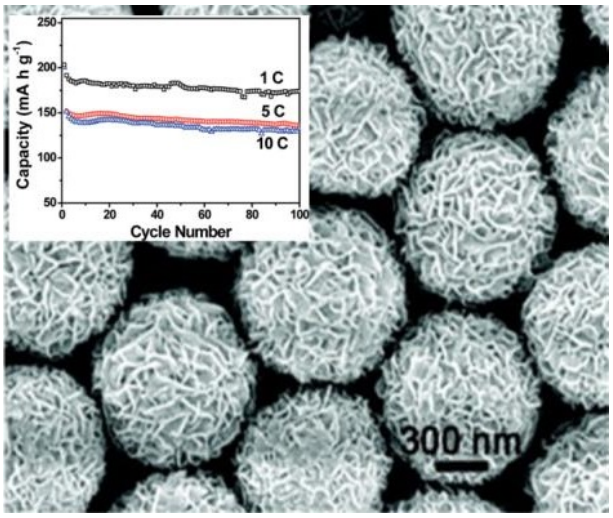

Figure 3.1: FESEM image of as-prepared anatase TiO_2 nanosheet microspheres and (inset) cycle stability at various current rates.[64]

random orientation, which resulted in a three-dimensional highly nanoporous structure with a specific surface area of 170 m^2 g^{-1}. The nanosheet hierarchical structures showed excellent cycle and rate performance when investigated as anode material for Li-ion battery; the specific capacity was 140 and 100 mA h g^{-1} when the electrode was discharged at the high

current rate of 10 and 20C, respectively. The high Coulombic efficiency, excellent capacity retention, and superior rate behavior were ascribed to the inherently short transport path lengths, preferential orientation of the nanosheets, and size confinement of the nanosheets themselves.

Dylla *et al.* went on to demonstrate that the intercalation of Li^+ in TiO_2(B) nanosheets is superior to TiO_2(B) nanoparticles due to the exposure of highly reactive facets that decrease the diffusion barrier during lithium intercalation.[59] Differential capacity plots revealed that the TiO_2(B) nanosheets have a greater influence of surface effects that would change the overall charge-discharge behavior, and the nanoparticles displayed a more discrete redox behavior. Density functional theory with energy penalty (DFT+U) calculations were then performed, and elucidated the varying lithiation mechanisms for the different morphologies. For the TiO_2(B) nanoparticles, the A2 sites near the equatorial TiO_6 octahedra are initially filled, followed by A1 sites near the axial TiO_6 octahedra. Conversely, the TiO_2(B) nanosheets incrementally fill the C sites, followed by the A2 and A1 sites. This variance in the method of lithiation is attributed to the elongated geometry of the nanosheet that effectively reduces lithium interaction between the C and A2 sites. Overall, this study further verifies that the exposure of specific high energy facets can be advantageous towards achieving enhanced lithiation dynamics. Similar calculations have also yielded the same conclusions for spinel $Li_{4+x}Ti_5O_{12}$.[68]

The benefits of faceting have also been observed for other metal oxide electrode materials. $LiMn_2O_4$ nanosheets composed of single-crystalline nanorods with exposed (111) facets demonstrated favorable attributes for energy storage applications because of their two-dimensional nanoporosity and exposed (111) facets.[69] From a Li-insertion performance standpoint, nearly 100% of the initial capacity can be retained after 500 cycles at a 1C discharge rate using the nanoporous nanosheets as cathode; at a discharge rate of 25C, the capacity retention is about 86% of the initial capacity after 500 cycles. These discharge values were approximately 2.5 times better than solid state synthesized LiM_2O_4 particles.

The enhancement in capacity was ascribed to a more uniform, thin, and stable solid electrolyte interphase (SEI) layer forming on the (111) facets that could suppress structural and volumetric changes.

Liang *et al.* successfully synthesized hierarchical LiV_3O_8 nanofibers from nanosheets composed of exposed (100) facets using electrospinning combined with calcination, which showed great potential as anode materials for aqueous Li-ion batteries.[70] An issue that plagues aqueous lithium ion battery systems is the potential of proton intercalation in place of Li^+ intercalation, and is responsible for the capacity fading typically seen in such setups. The (100) facet of the LiV_3O_8 structure has smaller and less numerous channels to accommodate Li^+ insertion, which makes it more difficult for H^+ to intercalate into the anode host. Therefore, the enhancement in electrochemical performance is a result of the high percentage of exposed (100) facets that may effectively alleviate proton co-intercalation into the electrode materials. Correspondingly, the LiV_3O_8 nanofibers from nanosheets composed of exposed (100) and bulk LiV_3O_8 materials exhibited a discharge capacity of 105 and 62 mA h g^{-1}, respectively, when cycled at 60 mA g^{-1}.

Li^+ insertion dependence on exposed crystal facets has also been observed in metal phosphates. $LiFePO_4$ nanoplates with crystal orientation along the (101) facet and (011) facet present similar reversible capacities at low current densities, but the (011) facet shows superior performance at higher rate.[71] The approximate values of the (101) and (011) faceted structures were 160 mA h g^{-1}, but then differentiated at 148 and 28 mA h g^{-1} at 10C, respectively. The results indicate that Fe_{Li} anti-site defect concentration may account for the availability of electrochemically active $LiFePO_4$, while the crystal orientation contributes for rate capability only, further verifying that control of faceted surfaces is a powerful means of enhancing electrode performance. $LiMnPO_4$ microspheres with different crystallographic orientations were assembled from plates, wedges, and prisms. The Li^+ insertion performance of the $LiMnPO_4$ microspheres assembled with plates was far better than the other primary nanoparticle units due to the exposure of (010) facets as well as the confined thickness along

the [010] direction allowing for fast Li^+ diffusion and a short diffusion length.[72] The plate-assembled microspheres ultimately demonstrated discharge capacities of 130.3 mA h g^{-1} at 0.05C, 114.9 mA h g^{-1} at 0.1C, and 96.8 mA h g^{-1} at 0.2C, values which were far superior compared to the microspheres composed of wedge or prism nanoparticles.

Additionally, the effects of surface facet control can be seen for lithium alloying elements as well. For Si insertion materials, Jung *et al.* revealed through DFT calculations, with a slab representation of the surfaces, that once the Li^+ is incorporated into the Si surface, it diffuses faster by at least two orders of magnitude along the [100] direction than along the [111] direction.[73] The notable difference between the Li^+ insertion behaviors in the (100) and (111) surfaces is a distinct rate-determining step; more explicitly, these limitations are the surface incorporation for (100) and subsurface diffusion for (111). These results were then assessed experimentally, where it was determined that a phase boundary separating the crystalline silicon from the amorphous lithiated phase was faster for (110) silicon than along the (100) and (111) orientations.[74] These results imply that subsurface diffusion can play a more important role than surface incorporation in determining the overall intercalation rate, and that the kinetics of Li^+ surface incorporation must be enhanced by metal doping or modification of the SEI to reduce the surface incorporation barrier.

3.3 Micro/nano-structured Electrode Materials

While nanosized electrode materials are advantageous in terms of kinetics and capacity, their practical application suffers from low thermodynamic stability and high propensity to undergo secondary reactions because of their confined size and high surface energy. Therefore, the use of kinetically stabilized nanostructures should be considered. Over the past several years, significant studies have been conducted examining the synthesis and performance of heterogeneous structures. While heterogeneous structures typically refer to the combination of two or more materials, in this case it refers to architectures displaying more

than one size scale (*i.e.*, micro/nano). The design of microstructurally composed nanoparticles, for instance, can circumvent the thermodynamic instability, undesired side reactions, high processing costs, and potential nano-toxicity effects associated with nanoparticle synthesis and processing.[43, 75, 76]

For example, micro/nano-structures of the metastable monoclinic (B) phase of vanadium dioxide were synthesized by Zhang *et al.* using a polymer capping reagent and hydrothermal processing conditions.[77] The final product displayed a flower-like morphology assembled of single-crystalline nanosheets, as shown in Fig. 3.2a.

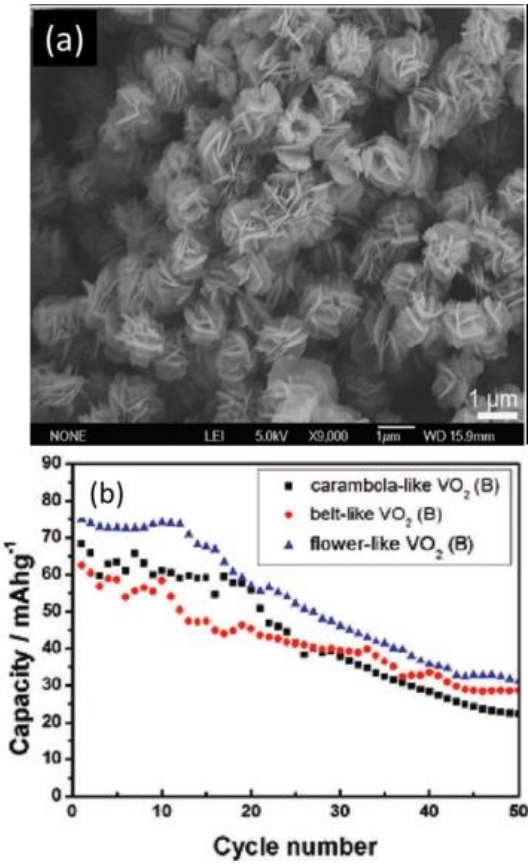

Figure 3.2: FESEM image of the as-prepared flower like VO_2 and (b) corresponding cyclic stability of the $VO_2/LiMn_2O_4$ aqueous cell operating at 60 mA g^{-1} within the voltage range of 1.65-0.5 V.[77]

It was determined that the flower-like morphology was developed through a self-assembly and Ostwald ripening process, where the overall flower-like structure was approximately 1-1.5

μm in diameter composed of nanosheets (the petals of the flower in this case) 20-30 nm thick. The obtained material was employed as the active electrode material for an aqueous Li-ion battery system paired with a $LiMn_2O_4$ counter electrode. The $VO_2/LiMn_2O_4$ cell showed an excellent initial capacity when cycled at 60 mA g^{-1}, but suffered from significant capacity fading upon cycling, as seen in Fig. 3.2b. The high initial Li^+ intercalation performance was attributed to the interconnecting single crystalline nanosheets, which decreased the charge and mass transfer diffusion paths.

Similar flower-like morphologies composed of single crystalline nanosheets were also observed in other electrode material systems, such as $LiMnPO_4$, SnO_2, and $LiFePO_4$.[64, 78, 79] All of these reported studies stated that their respective morphology evolved through the capping of the primary nanoparticles with surfactant followed by the formation of preferential arrangements and subsequent growth. The $LiMnPO_4$ product showed notable capacity retention, but the specific capacity values were not tremendous. The low Li^+ intercalation potentials could be overcome by modifying the nanosheets to grow along the [010] axis that exhibits a preferential Li^+ diffusion pathway. The other flower-like morphology systems showed outstanding electrochemical performance both for prolonged cycling and at high current rates.

3.4 Hollow micro/nano-structures

A great deal of recent research efforts have also focused on the study of hollow nanostructured materials, such as nanotubes and hollow spheres, that demonstrate unique characteristics due to their morphology.[80] Hollow nanostructured materials have been known to exhibit large surface area, low density, and enhanced surface permeability because of their inner cavities; such materials have been used in a wide range of applications such as Li-ion batteries, catalysts, optoelectronic sensors, and drug-delivery systems.[81] The morphology of hollow nanostructured materials is responsible for increasing the electrochemical perfor-

mance of Li-ion batteries in two ways. First, the void within hollow nanostructured materials can serve as a buffer against any localized volume change experienced during the Li^+ intercalation/deintercalation process, thereby improving the cyclic stability; secondly, the large surface area and decreased Li^+ diffusion distance in hollow nanostructured electrodes greatly enhances the specific capacity while decreasing the packing density.[82, 83, 84]

Lieu *et al.* synthesized SnO_2-V_2O_5 nanocapsules approximately 400 nm in diameter through a combination of Ostwald ripening processes. Fig. 3.3 displays the double-shelled structure and hollow interior as confirmed by SEM and TEM characterization, respectively. When tested as an anode material, the nanocapsules exhibited an excellent cycle stability of 673 mA h g^{-1} over the course of 50 cycles at a discharge rate of 250 mA g^{-1}; the rate capability of the nanocapsules also provided encouraging results.[85]

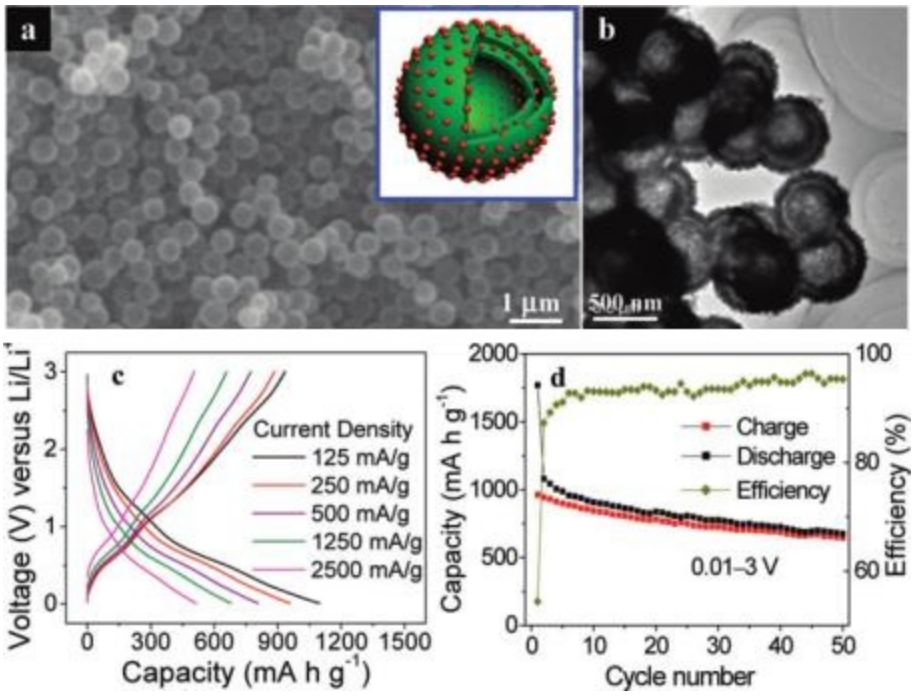

Figure 3.3: (a) SEM and (b) TEM image of V_2O_5-SnO_2 double-shelled nanocapsules. The inset in (a) shows a schematic structure of a double-shelled nanocapsule. The red spheres represent SnO_2 nanocrystals, and the green double shells represent the V_2O_5 matrix. (c) Charge/discharge curves at different current densities. (d) Capacity (left) and efficiency (right) versus cycle number at a current density of 250 mA g^{-1}, showing the capacity retention upon cycling.[85]

Lou and Archer established a templating scheme based on monodisperse nonspherical hematite (α-Fe_2O_3) colloids that yielded nonspherical (ellipsoidal) metal oxide hollow or core-shell particles as exhibited in Fig. 3.4.[86] Additionally, the hematite cores surrounded by the TiO_2 shell could be converted to magnetite (Fe_3O_4) cores to produce tailored magnetic multifunctional particles. It was also revealed that the processing conditions could be altered to adjust the aspect ratio of the as-synthesized product. The as-prepared hematite/TiO_2 core-shell particles were investigated as anode material for Li-ion batteries. Fig. 3.4k shows the commendable cycle life and rate capability of the core-shell TiO_2 particles.

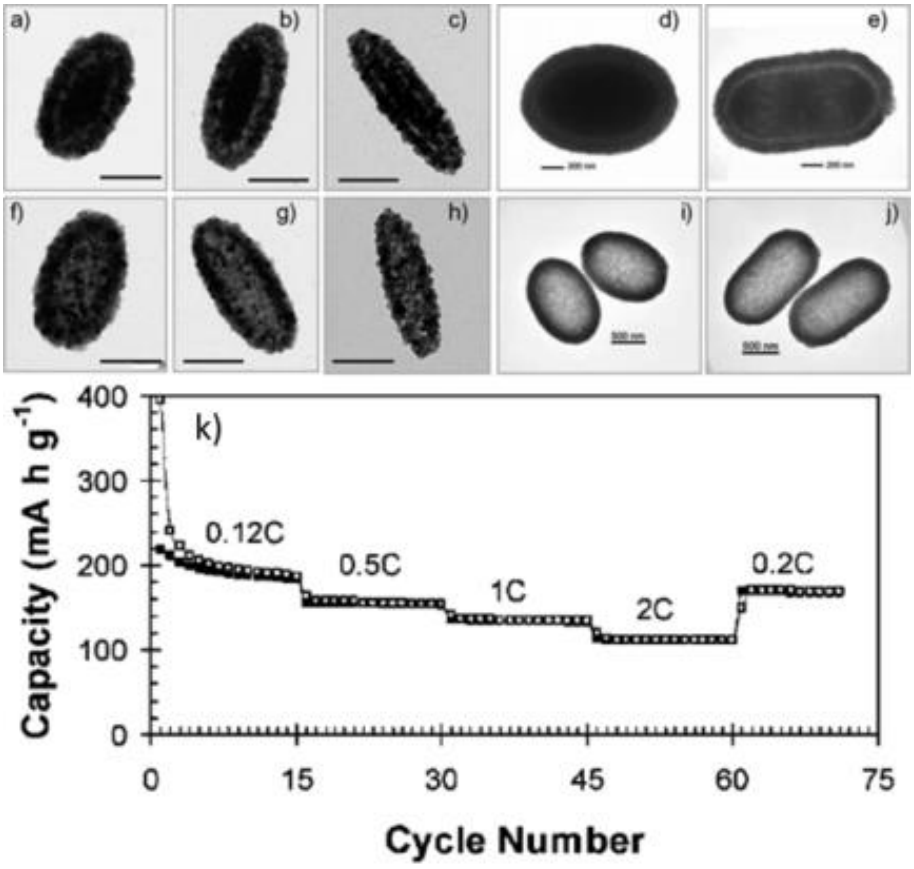

Figure 3.4: TEM images of five other types of hematite/TiO_2 core/shell particles (a-e) and their corresponding TiO_2 hollow particles after removal of hematite cores (f-j), respectively, scale bars in (i) and (j) are 500 nm, all others are 200 nm. (k) Cycling performance at various discharge rates.[86]

More recently, Wu *et al.* synthesized double-walled silicon nanotubes that demonstrated superb intercalation and lifetime performance when tested as anode material.[87] The inner

wall of the double-walled nanotube structure consisted of an active silicon nanotube surrounded by an ion-permeable silicon oxide shell. Due to the novel design, the electrolyte solution is only in contact with the outer surface, and cannot enter the hollow inner space, through which Li^+ permeates to reach the active material. The outer oxide shell also constrained the Si expansion to the inner void, eliminating pulverization and capacity degradation. This unique feature also worked to stabilize the SEI film. The material was cycled over 6,000 times in the half cell configuration while retaining a capacity greater than 600 mA h g^{-1} when cycled at 12C. The excellent electrochemical properties were ascribed to the novel engineered nanostructure that exploits the inherent Li^+ intercalation capability of Si while maintaining battery performance.

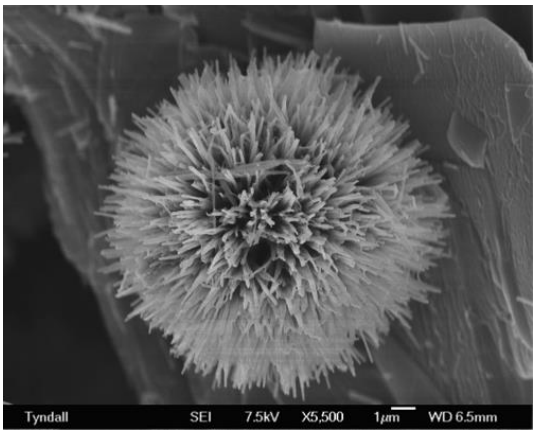

Figure 3.5: SEM of an individual nano-urchin.[88]

While the current literature is full of studies detailing the results of spherical and tubular hollow nanostructures, hollow assemblies are in no way limited to these morphologies. The so-called urchin structure is one such morphology, and is characterized by a microscale spherical core (solid or hollow) from which numerous nanotubes (hollow) or nanofibers (solid) are extruded.[88, 89] A representative image of such a structure is presented in Fig. 3.5. The protruding nanoparticles comprising the urchin-like morphology can potentially enhance the conductivity of the electrode, and ultimately the electrochemical response, by forming a three-dimensional network of interconnected nanoparticles. The void spaces formed between

these interconnects can also enhance the contact between the electrode material and the electrolyte.[90]

An even more novel derivation of hollow nanostructured electrode materials is those where the central cavity is filled with nanoparticles of some secondary material, such as a hollow nanosphere loaded with electroactive nanoparticles. As revealed in Fig. 3.6, Zhang *et al.* successfully encapsulated Sn nanoparticles in hollow elastic carbon spheres approximately 500 nm in diameter and 20 nm thick.[91] Each carbon nanosphere contained approximately 5-10 Sn nanoparticles. The remaining void space within each nanosphere combined with the confining carbon shell meant that the Sn nanoparticles would not experience pulverization (and accompanying cyclic fading) due to volume expansion and contraction experienced during lithiation. Fig. 3.6c displays the moderate cycle stability and good initial discharge capacity. Lee *et al.* also reported the synthesis of single Sn nanoparticles loaded in hollow carbon nanospheres; however, the capacity and cycle stability suffered, most likely due to the low tap density of the electrode material.[92]

Zheng *et al.* also developed templated hollow carbon nanofiber encapsulated sulfur as cathode material.[93] The template structure facilitated sulfur infusion into the hollow fibers and prevented sulfur from coming into contact with the exterior carbon wall. The high aspect ratio of the carbon nanofibers provided an ideal structure for trapping polysulfides while the thin carbon wall permitted rapid Li^+ kinetics. The confined nanoscale dimensions of the nanofibers lead to a large surface area per unit mass for Li_2S deposition during cycling and reduced electrode material pulverization. A high specific capacity of approximately 730 mA h g^{-1} was recorded after 150 cycles at 0.2C rate.

Lieu *et al.* have recently investigated carbon coated single Si nanoparticles with an inherent void space.[94] Single Si nanoparticles with an average size of 100 nm were coated with a 5-10 nm thick amorphous carbon shell, with an 80-100 nm void space surrounding the Si nanoparticle (Si@void@C). The main advantages of this adopted morphology was that the carbon shell acted as a framework that allocated for the growth of a stable SEI layer

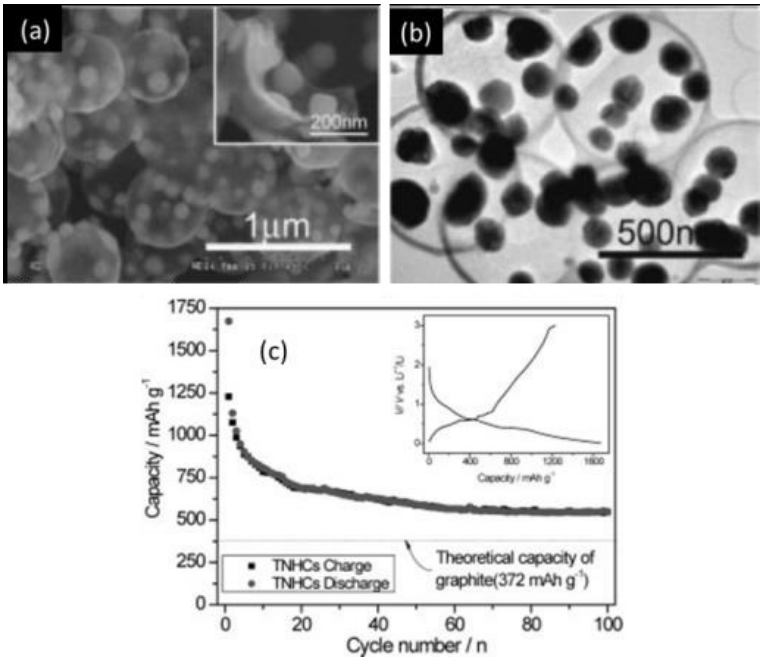

Figure 3.6: (a) SEM and (b) TEM image of Sn encapsulated carbon spheres. The inset in (a) is a close view of a single broken carbon spherical shell studded with Sn particles. (c) The discharge/charge capacity profiles of the Sn encapsulated carbon spheres from a 5 mV to 3 V (vs. Li^+/Li) voltage window and at C/5, the inset shows the initial cycle.[91]

while preventing fracture of the Si nanoparticles due to volume expansion; lithiation of the Si occurred by Li diffusion through the carbon shell into the Si core. Fig. 3.7 shows a sequence of images collected from the in-situ TEM investigation of the Si@void@C particles at various times.

Prior to lithiation, pristine Si nanoparticles were clearly observed and contained within a carbon shell. Subsequently, the Si particles experienced significant volume expansion as Li^+ diffused through the carbon coating and intercalated the Si particles. After 105s of charging, an amorphous Li_xSi shell/crystalline Si core structure was formed as the Si particles were partially lithiated. The diameter of a typical Si particle increased from 185 to 300 nm after lithiation was complete (375s charge time). The thickness of the carbon layer also increased from 5-10 nm to 20 nm, indicating that the carbon coating was also storing Li^+. In situ TEM clearly demonstrated that fracture was not observed during electrochemical cycling of these particles, which resulted in their excellent electrochemical properties as derived from

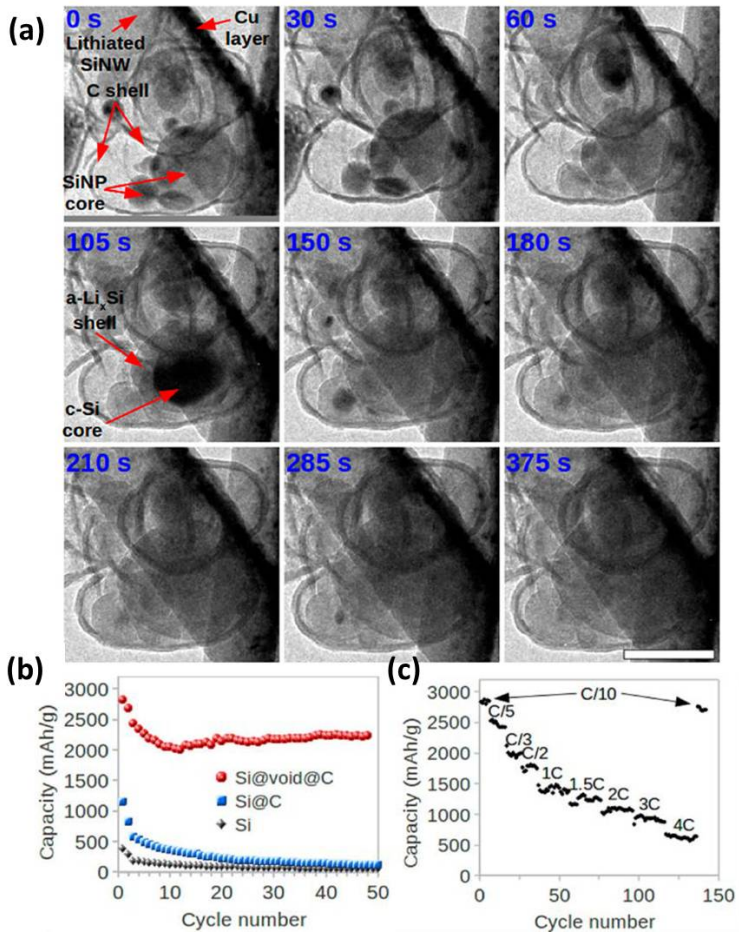

Figure 3.7: (a) In-situ TEM characterization of Si@void@C expansion during electrochemical lithiation, where the silicon particles are observed to expand within the outer carbon shell. Scale bar: 200 nm. (b) Galvanostatic cycling of different silicon nanostructures (PVDF binder). All samples were cycled at 0.2 C for the first cycle, 0.5 C for the second cycle, and 0.1 C for the later cycles. (c) Delithiation capacity of Si@void@C with alginate binder cycled at various rates from 0.1 C to 4 C.[94]

the yolk-shell structure. It is evident from Fig. 3.7b that the yolk-shell morphology was far superior to simply coating Si nanoparticles with carbon; the Si@void@C particles also demonstrated a moderate capacity of 630 mA h g^{-1}, while the initial capacity is relatively maintained even after 150 cycles.

3.4.1 Mesocrystals

Over the past several decades, nanoparticle formation and application integration has been the subject of much academic and industrial research. Nanoparticles are the focus of such intrigue due to their novel properties and tunable functions that can utilized in a wide range of applications.[95] Ensembles and novel arrangements of nanoparticles can collectively exhibit properties vastly different than individual nanoparticles or bulk materials. Mesocrystals are a promising class of hierarchically nanostructured solid materials that coincidentally have many inherent traits that are desired for Li-ion battery electrodes. Such characteristics include: large surface area, high porosity, small primary subunit size, large overall assembly size, and high degree of crystallinity. Recently, there has been much effort in the formation and subsequent understanding of ordered nanoparticle superstructures with a vast range of architectures, particularly mesocrystals. Mesocrystals, short for mesoscopically structured crystals, are crystallographically oriented nanoparticle superstructures and have received much attention since first being introduced by Colfen and Antonietti.[96, 97, 98] Until recently, mesocrystals were only studied in biomineral materials, but current research efforts have shifted to the development of mesocrystalline organic molecules, metal oxides, and other functional materials.[99]

Colloidal crystals and supercrystals, or nanocrystal superlattices, offer novel nanoparticle arrangement; however, such assemblies do not take into account individual nanoparticle orientation. Mesocrystals can be classified by their high degree of crystallinity, high porosity, and subunit alignment along a crystallographic register. These highly desirable properties are due in part to mesocrystal formation mechanisms, which are still poorly understood, and

make mesocrystals the ideal material candidates for catalysis, sensing, and energy storage and conversion applications. Porous materials with large specific surface areas have been shown to enhance the performance of lithium ion battery electrode materials because of more prevalent and uniform pores that ease intercalation by decreasing the Li^+ diffusion distance. Secondary battery cathodes constructed out of mesocrystalline materials could benefit tremendously from the inherent and uniform porosity of the well-defined crystallographic register with which the nanoparticles orient themselves.[95]

Mesocrystal growth often proceeds *via* the aggregation of precursor units, rather than by the classical ion-by-ion growth mechanism. This non-classical growth process can be attributed with the generation of crystals with hierarchical structures and complex morphologies.[97] Organic additives are commonly used to facilitate this process, but are not required by any means.[100] The oriented assembly of nanoparticles leads to the formation of mesocrystals where the constituting crystallites are arranged in a crystallographic register and the product particles demonstrate single crystal behavior. Identification of mesocrystals has proven to be difficult but can be achieved *via* the detection of a number of features including high porosity/large surface area and evidence of mesoscopic subunits as viewed from transmission electron microscopy.[101]

A great deal of the research efforts, to date, concerning mesocrystals have focused on understanding their formation mechanisms, but newer works reviewing their application are starting to emerge. In terms of battery performance, the uniform pore structure inherent to mesocrystals can facilitate contact with the electrolyte thereby leading to fast Li^+ transport mechanics while at the same time accommodating lithiation induced volume expansion and particle strain giving way to improved cycling stability. The oriented arrangement of nanoparticle subunits can eliminate the grain boundaries between adjacent particles thus offering much better charge and mass transport, and ultimately better rate capability. Provided this unique combination of nanoparticle properties and order combined with a microscopic or even macroscopic size, mesocrystals have strong potential as active materials for

lithium-ion battery electrodes. These assemblies possess the structural and chemical stability of microsized electrodes while exploiting the beneficial properties associated with nanosized electrodes and their large reactive surface area.

Mesocrystals have also demonstrated great potential for applications in catalysis, sensors, and electronics. Other applications are yet to be explored where huge surface area and good charge and mass transfer properties are required or the hierarchical structure can offer synergistic advantages; for example, nanostructure-based solar cells, such as dye-sensitized solar cells or quantum dots solar cells, would greatly benefit from the applications of such mesocrystals, as they would offer charge transfer properties similar to single crystals, large surface area as seen for nanoparticles, and desirable light scattering. One of the biggest challenges in the further advancement in mesocrystal research is the lack of fundamental understanding of homoepitaxial aggregation of nanocrystals, so the rationale design and synthesis of desired mesocrystals remains an unattained goal.

3.4.2 Vanadium Oxide

Several studies focusing on the synthesis and performance of mesocrystalline materials as either anode or cathode in lithium ion batteries have already been reported. Cao *et al.* synthesized hollow V_2O_5 microspheres composed of nanorods *via* self-assembly (Fig. 3.8).[102] Hollow microsphere precursors of vanadyl glycolate composed of assembled nanorods were first synthesized utilizing the polyol process, and were then transformed to V_2O_5 with a simple annealing step. No change in the morphology was observed upon annealing. The individual nanorods comprising the structure were approximately 200 nm in diameter and varied in length, while the overall spherical structures were approximately 2 μm in diameter. The structures were successfully able to intercalate up to one Li^+ per V_2O_5 formula unit, and showed moderate capacity retention up to 15 cycles with an initial discharge capacity of 286 mA h g^{-1}.[102] It was determined that interconnecting nanoparticles between the self-assembled nanorods lead to a reduction in the Li^+ diffusion distance, thereby increasing

the kinetics of the material and the overall electrochemical performance. It has since been revealed that hollow structures can result in favorable enhancements in capacity retention with cycling due to the presence of the inner cavity that can accommodate cycling induced strain due to the de/intercalation of Li^+.[81]

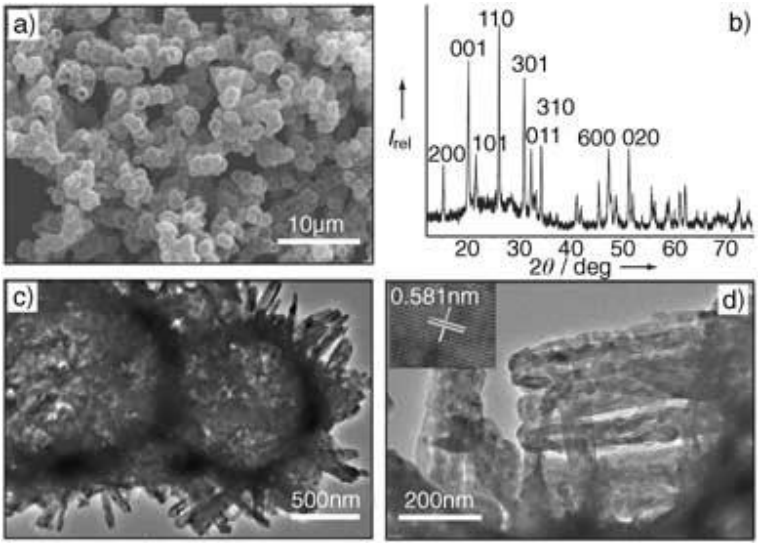

Figure 3.8: SEM, XRD, and TEM of calcined V_2O_5 microspheres.[102]

3.4.3 Titanium Oxide

Ye *et al.* synthesized ellipsoidal anatase TiO_2 mesocrystals approximately 380 nm in length and 280 nm in diameter though the solvothermal reaction of acetic acid and tetrabutyl titanite, the end result of which is shown in Fig. 3.9.[103] The mesocrystalline structures were composed of oriented nanoparticles ranging between 10-20 nm in diameter. Selected area electron diffraction (SAED) measurements confirmed the single crystalline characteristics of the mesocrystal and revealed that the elongated ellipsoid direction corresponded to the [001] direction as observed in the inset of Fig. 3.9c.

The mesocrystalline nature of the particles was most likely achieved through the oriented attachment mechanism and infusion between the TiO_2 nanoparticles, leading to a decrease of the interfacial nucleation sites for the rutile phase. The formation of the TiO_2

mesocrystals through the oriented attachment mechanism also decreased the number of grain boundaries existing between individual TiO_2 nanoparticles, thus resulting in facile electronic conduction and fast Li^+ transport between the electrolyte and the mesocrystal electrode. This speculation was validated when the mesocrystal TiO_2 anode was compared to a TiO_2 anode composed of nanoparticles of approximately the same size as the mesocrystalline subunits (Fig. 3.9e). The mesocrystalline anode demonstrated good rate capability and outperformed its nanoparticle counterpart at higher current rates. The uniformly dispersed nanopores throughout the structure of the mesocrystals can facilitate contact with the electrolyte, hence increasing the electrode/electrolyte interface which favors fast Li^+ transport.

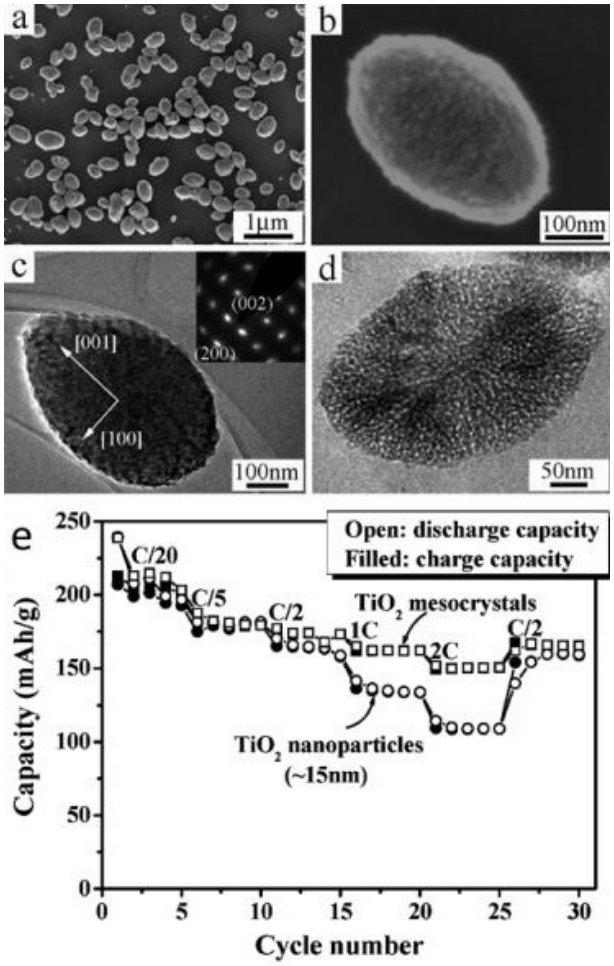

Figure 3.9: SEM (a, b) TEM, (c, d) HRTEM images, and (e) electrochemical performance of nanoporous anatase TiO_2 mesocrystals.[103]

Other, more novel mesocrystal architectures for TiO_2 have also been synthesized. For instance, Hong *et al.* synthesized dumbbell-shaped rutile and quasi-octahedral anatase TiO_2 mesocrystals using a hydrothermal approach.[104] The dumbbell-shaped rutile TiO_2 mesocrystals were constructed from ultrathin nanowires oriented along the [001] crystallographic axis, and quasi-octahedral anatase TiO_2 mesocrystals built from tiny nanoparticles that had a fine microporous structure and large surface area. The galvanostatic charge-discharge performance as a function of current density for both the rutile and anatase mesocrystals were compared to nanoparticles of their corresponding material, and both mesocrystal specimens demonstrated their superiority. At a discharge rate of 5C, the rutile mesocrystals had a discharge capacity of 103 mA h g^{-1}, while the rutile nanoparticles only exhibited 28 mA h g^{-1}. Similarly, the anatase mesocrystals exhibited a discharge capacity of 124 mA h g^{-1}, while the anatase nanoparticles only exhibited 32 mA h g^{-1} at a discharge rate of 5C. The improved Li^+ intercalation rate performance was attributed to the intrinsic characteristics of the mesoscopic TiO_2 superstructures, which had a single crystal-like and porous nature which facilitated fast electron transport and relieved the strain from volumetric change.

3.4.4 Lithium Iron Phosphate

Bilekca *et al.* synthesized $LiFePO_4$ (LFP) mesocrystals *via* an extremely efficient microwave-assisted route.[105] The as obtained product was composed of slightly elongated nanoparticles (100 nm) nearly fused together into discs approximately 1 μm in diameter. The LFP mesocrystals were tested as cathode material for Li-ion battery, and exhibited an initially moderate capacity of 150 mA h g^{-1} that was extremely stable upon cycling. The LFP mesocrystals also show modest rate capability (81%) up to a discharge rate of 8C. However, the study did not clarify the relationship between the unique structural features and the performance of the LFP mesocrystals, and only suggested that the implementation of mesocrystals as electrode material may be the linking factor.[105]

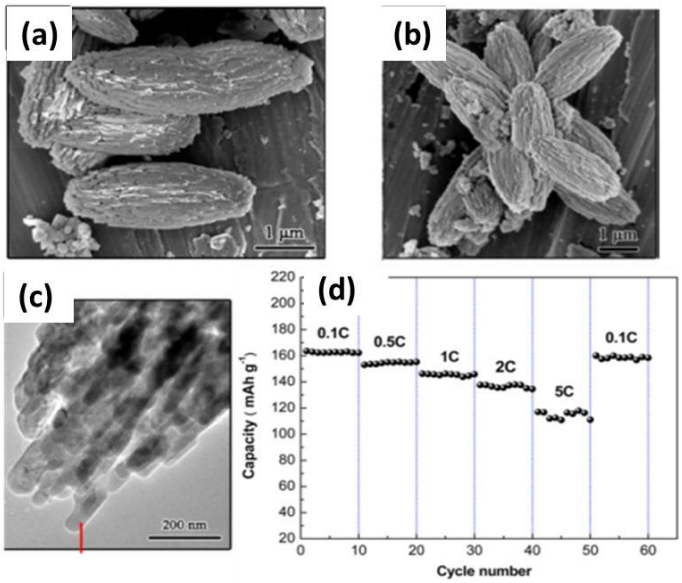

Figure 3.10: Spindle-like LFP structure obtained for a growth period of (a) 20 hr, (b) pH of 10, (d) HRTEM image. (d) The charge/discharge profiles of the spindle-like LFP architecture in the voltage range from 2.5 to 4.2 V at various current rates.[106]

In an attempt to compensate for the low electronic conductivity of LFP, carbon coated LFP mesocrystals were later studied by Xia *et al.*, where they were synthesized using a solvothermal and post-growth annealing route.[106] The annealing route was required in order to convert the L-ascorbic acid into the carbon that coated the surface of the primary nanoparticles. Spindle-like structures approximately 2 μm in length and 1 μm in width, composed of nanoparticles approximately 100 nm in length and 50 nm in width, were observed with SEM and are depicted in Fig. 3.10. TEM analysis revealed the mesocrystalline nature of the obtained product; it was later determined that the product formed through standard non-classical crystallization techniques using a nanoparticle surface modifier as determined from time interval growth studies.

The spindle-like LFP mesocrystals demonstrated good cycling stability of approximately 165 mA h g^{-1} over the course of 50 cycles, and a moderate rate capability that terminated at 120 mA h g^{-1} at a rate of 5C (Fig. 3.10d). The electrochemical performance was attributed to the porous structure that shortened the Li^+ diffusion length, enhanced electrolyte penetration, and increased the electrochemical reaction surface, thus alleviating electrode po-

larization. The incorporation of the uniform carbon coating throughout the structure also aided the electrochemical capability by enhancing the electronic conductivity.

3.5 Surface Chemistry and Defects

As material structure was the main focus of study when the use of intercalation compounds as Li-ion battery electrodes was initially reported, current research efforts have begun to focus on surface modification.[107] Surface chemistry can be controlled through the presence of surface coatings, modifiers, or the introduction of defects. It is possible to manipulate the formation and characteristics of the SEI by altering the surface chemistry of the electrode in contact with the electrolyte, which can directly dictate redox processes and the electrochemical performance of the material. A desirable surface structure leads to a uniform and compact SEI film that may enhance the efficiency and cycling performance of Li-ion batteries.

3.5.1 Surface Modification

Park *et al.* were able to enhance the electrochemical properties of $Li_4Ti_5O_{12}$ by modifying the surface structure and chemistry using a thermal nitridation process.[108] $Li_4Ti_5O_{12}$ was annealed in a NH_3 atmosphere to form a surface coating layer of TiN with metallic conductivity that could increase the overall conductivity of the electrode. The NH_3 surface modified $Li_4Ti_5O_{12}$ specimen demonstrated better capacity retention upon cycling compared to the pristine $Li_4Ti_5O_{12}$ specimen due to surface defects, which serve as a buffer against surface decomposition. Surface modified $Li_4Ti_5O_{12}$ also showed a greater capacity than the pristine sample at higher current rate, an enhancement factor of 6 at 10C. The ammonia gas decomposed the surface of the $Li_4Ti_5O_{12}$ to form the conductive TiN-Li_2CO_3 core-shell morphology on the surface without altering the bulk lattice parameters.

Abel *et al.* recently demonstrated that a small amount of bulk and surface oxygen (20 at.%), introduced during synthesis and post-synthesis low temperature annealing, into nanostructured silicon thin films can increase the cycling stability and rate performance, as demonstrated in Fig. 3.11.[109] Virtually no capacity loss was observed up to 150 cycles when both bulk and surface oxides were present in an annealed film, and only a slight capacity fade was seen between 150-300 cycles. The capacity measured at the 1C rate was 1450 mA h g^{-1}, signifying that the specific capacity was somewhat sacrificed in order to enhance the cycling stability. An investigation on silicon nanowires with hydride, methylated, and siloxane terminated surfaces was also conducted by Xu *et al.*[110] The gathered results revealed that the methyl terminated nanowires were relatively unreactive and tended to passivate the silicon surface, while nanowires terminated with hydride formed SEI layers composed of carbonates, lithium salts, P-F species, and fluorocarbon compounds that enhanced the electrochemical properties. The specific capacity values of the hydrated Si nanowires were approximately 800-1300 mA h g^{-1} greater than the other treated nanowires, even after 15 cycles. These results advocate that surface terminations can be tuned and play a key role in the chemical and mechanical behaviors that dictate the electrochemical properties.

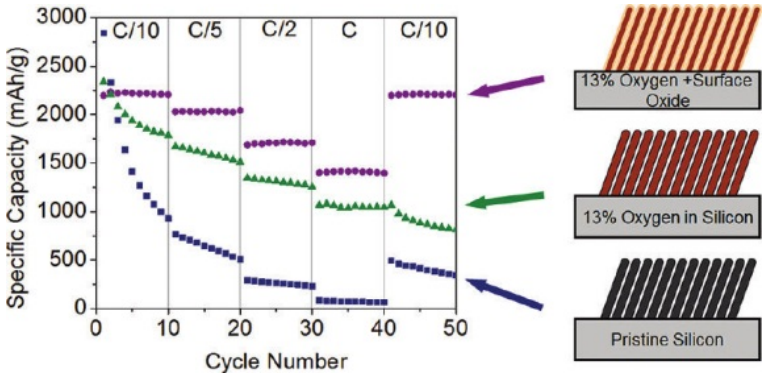

Figure 3.11: The cycling rate performance of pristine Si nanowires compared to nanowires with bulk and surface oxides.[109]

Coating the surface of the electrode material is a common technique used for tailoring the functionality or performance of the electro-active material. Carbon coating is one of the most popular means of easily enhancing the electronic conductivity of electrode materials,

and can also stabilize SEI films.[47] For transition metal cathode materials such as $LiCoO_2$, $LiNiO_2$, and $LiMnO_4$, surface coatings with oxides such as MgO or Al_2O_3 can essentially shield the cathode material from direct exposure with the electrolyte solution, improving the structural integrity of the cathode material and suppressing phase transitions.[111] Another application of oxide coatings is for the removal of hydrogen fluoride (HF) from the electrolyte solution. HF is a by-product resulting from the decomposition of $LiPF_6$ in the presence of moisture. The presence of HF in the electrolyte solution is detrimental to the electrochemical performance of electrode materials because it can dissolve the transition metals and is responsible for surface corrosion of the cathode materials. Oxide coatings such as ZnO or Al_2O_3 can serve as HF scavengers and neutralize or reduce the active concentration of HF in the electrolyte solution by reducing the local acidity of the electrolyte near the material surface.[112]

3.5.2 Role of Defects

Surface defects present at the electrode-electrolyte interface are expected to serve as nucleation sites that promote phase transitions between the redox and charge/mass transfer processes. As nucleation sites, surface defects may lead to the propagation of the transitioning phases into the bulk of the electrode upon cycling or potentially enhance the charge transfer. Surface defects have been documented as having the ability to dominate the electrochemical properties.[113]

Electrode materials displaying surface defects have commonly been synthesized by annealing the pristine materials with reactive gas or through substitutional doping techniques. The difficulty introduced with such techniques is to maintain the desired local chemistry while controlling the physical features at the same time. Suitable manipulation of the surface chemistry and introduced defects may also serve as a buffer zone to protect the electrode material from the electrolyte when submitted to prolonged cycling, or in such cases where the charging process is discontinuous (*i.e.*, frequency regulation); however, the principle aims

of employing surface defects are to enhance the Li^+ storage capacity and improve the overall electrode kinetics.

Lieu *et al.* recently investigated the effects of surface defects on the electrochemical performance by annealing V_2O_5 aerogels in different reactive environments (N_2 and air).[114, 115] The N_2 annealed films adopted a less crystalline structure composed of particles with smaller grain size. The N_2 annealed films also had a narrower bandgap than the air annealed films, and the color indicated that the vanadium valence state was a mix of V^{3+} and V^{4+}. Both of these effects could be attributed to the existence of defects in lower valence states. Electrochemical impedance spectroscopy confirmed an improved electrical conductivity in the N_2 annealed V_2O_5 films with defects such as V^{4+}, V^{3+}, and oxygen vacancies. The N_2 annealed films also showed considerably enhanced capacity and cycle stability when compared to the air annealed films. The discrepancy between the two films was also attributed to the presence of surface defects which can act as nucleation centers in the phase transition during Li^+ de/intercalation. The same general trend was observed for TiO_2 nanotube arrays annealed in CO and N_2; the improved intercalation capacity and rate capability of the CO annealed arrays was attributed to the presence of surface defects and cation groups with oxygen vacancies, which not only improved the charge-transfer conductivity of the arrays but also promoted the phase transition.[116] Another group also confirmed this finding by comparing the Li^+ capacity of pristine and O_2/H_2O treated V_2O_5, and attributed the difference in the electrochemistry of the two materials to the nonstoichiometric and surface point defects, which serve as additional charge storage sites.[117]

Sun *et al.* also explored the role of defects on electrochemical performance by synthesizing highly ordered and defect-rich vanadium oxide nanorolls, further corroborating the importance of defects in improving the electrode material performance.[118] The defected VO nanorolls exhibited superior capacity and cycle stability compared to the pristine VO nanorolls, results that were related to the V^{4+}/V^{5+} ratio, detectable cracks in the wall surfaces, and residual organic surfactant. The electrochemical enhancement was attributed to

the additional redox sites resulting from the atomic-scale disorder and the enhanced accessibility of Li^+ to the nanorolls because of cracks in between the layers and present due to defects. The results suggest that perfectly ordered materials may not be the ideal structure for electrochemical applications due to the limited ion diffusion rate.[118]

In studies less focused on defect formation and characterization, Guo *et al.* synthesized carbon-carbon nanotube composites *via* a soft-templated self-assembly process.[119] The porous and defect-rich structure was initially frozen into the sample by carbonization, but both effects were lost due to solid state amorphization upon cycling. This loss was accompanied by a steep drop in the capacity after the initial cycle and noticeable capacity fading upon cycling. Reddy *et al.* demonstrated that the Li^+ capacity and cycle stability were greater in nitrogen-doped graphene than in un-doped graphene, and ascribed the discrepancy to the introduction of surface defects into the system.[120] Disordered graphene nanosheets have also been shown to enrich Li^+ capacity due to additional reversible storage sites such as edges and other defects.[121]

More recently, it has been demonstrated that anion surface modification of $LiFePO_4$ particles can reduce the electrode-electrolyte charge transfer resistance, thereby preventing irreversible capacity at higher rates.[122] This anion surface modification was accomplished by substituting nitrogen or sulfur for surface oxygen on the (010) surface plane of $LiFePO_4$ nanoplates. DFT calculations show that the barrier for Li-ion transfer is decreased by strong Li^+ binding on surface sites when nitrogen or sulfur is substituted for surface oxygen. Calculations have indicated the activation energy for Li^+ surface diffusion along the surface (010) plane is quite high. Because of the strong covalent nature of the $(PO_4)^{3-}$ anion, it is reasonable to assume that the Li or Fe sites become under-coordinated at the surface and that they can be easily replaced with substitutional anions. Nitrogen and sulfur are of considerable interest towards replacing surface oxygen or $(PO_4)^{3-}$ anions because of their discrepancy in ionic size, formal charge, and electronegativity. Nitrogen can stabilize Li^+ in both the *a*- and *b*-sites because it affects the binding energies both electronically and ionically

(more stable 2p state and more negative charge); whereas sulfur binds directly to a surface Fe atom, providing full coordination of the Fe center. Sulfur substitution increases the binding of Li^+ in the *b*- and *c*- subsurface sites with respect to the surface *a*-site. Ultimately, surface modification can be exploited to engineer the surface energy levels and adjust the charge transfer kinetics. As expected, both N- and S-substitution exhibited considerably enhanced electrode performance than bare $LiFePO_4$ particles of the same size.

3.6 Limitations of Nanostructured Electrode Materials for Li-ion Batteries

Provided all the benefits of nanostructuring, the synthesis and characterization of nanostructured electrode materials of various chemistries have been the extensively investigated. However, the use of nanostructures is not a panacea, and there are several performance issues, either lingering or deriving from nanostructuring, that still need to be addressed. One of the more noticeable effects incurred from nanoscaling is the increased relevancy of the surface chemistry and energy. For nanoscale materials, the surface free energy involves an extra contribution that need be taken into consideration for the chemical potential, and can be approximated by:

$$\mu^{\circ}(r) = \mu^{\circ}_{(r=\infty)} + \frac{\gamma V}{r} \tag{3.3}$$

where γ is the surface tension, r the particle radius, and V the partial molar volume. The capability of nano-insertion materials to surpass the theoretical capacity limits of their bulk counterparts has already been discussed; the larger storage capacity has been attributed to the large and energetically relevant surface area of the nanoparticles that contributes to the high electro-activity toward Li^+ storage. However, the excess free surface energy can also result in several disadvantages. Too high of Li-ion surface insertion leads to passivation of the surface region by surface reconstruction or mechanical failure, and accompanying irreversible

capacity loss is inevitable. Thus, there exists an optimal particle range for nanomaterials where cracks resulting from non-surface related volume expansion will not propagate, and surface reconstruction will not occur.

Morphology also plays a pivotal role in the electrochemical performance; the observation of curved voltage profiles with diminished voltage plateaus has been attributed to the strain and interfacial energy from coexisting lattice terminations within electrode nanoparticles. However, it has been revealed to be the consequence of different structural environments in the near-surface region that result in a distribution of redox potentials. These varying structural environments depend on the distance from the surface and the surface orientation itself, verifying that morphology plays an important role in the particle stability.[123] Hence, the irreversible capacity will be larger for smaller particles with a large surface area greater than some critical value, where the optimal particle size is dictated by the voltage window.[124]

Electronic conductivity and ionic diffusivity have long been limiting factors to the development of electrode materials for Li-ion battery. These barriers stem from several fundamental issues: (1) the metal oxide materials typically employed as cathodes have relatively low electronic conductivity values, (2) an unclear relationship between the electrical and ionic conductivities in electrodes, and (3) phase transformations upon lithiation that can change the conductive properties. Additionally, it has been well established that nanomaterials suffer from resistivity values much greater than their corresponding bulk material; nanowires, for example, typically display resistivity values that are 20% greater than what is seen in the bulk regime, and can extend up to several orders of magnitude.[125] The reason for the drastic increase in the resistivity of nanomaterials is the sheer increase in the relative surface area and the number of grain boundaries that is strongly dependent on the particle size and morphology. These physical parameters negatively impact the conduction mechanisms because of the inelastic scattering of conduction electrons at particle surfaces and the reflection of electrons at grain boundaries. These effects are also more pronounced

in the electrode materials with smaller mean particle size. To compensate for these effects, conductive additives, such as carbon, are typically added to electrodes, but such inclusions decrease the already low packing density of nanostructured electrode materials even further.

The high surface area and corresponding high surface energy of nanoparticles also increases the potential for secondary or side reactions at the particle surface. The main reaction at risk exists between the electrode and electrolyte, and involves electrolyte decomposition which would lead to a considerable degree of irreversibility and capacity fade upon cycling. The SEI layer is a film that typically forms on the anode through the decomposition of the electrolyte into lithium containing organics and inorganics that deposit onto the electrode-electrolyte interface in an attempt to reduce the contact area and thereby prevent further electrolyte decomposition.[126] It should be noted that SEI films formed on graphitic anodes acting as an interfacial stabilizer have also contributed towards improving the capacity retention of the anode over long cycle lifetimes at the expense of a large irreversible capacity drop associated with film formation.[127] In this regard, the formation of a stable SEI layer can be desired, but thicker and unstable SEI films can negatively impact electrode performance.

Regardless, SEI film formation is often unstable, and its ionic and electronic conductivities are relatively low and it effectively intercepts and stores Li^+ that would otherwise be intercalated by the electrode. These mechanisms tremendously decrease the electrochemical performance of the cell by limiting the intercalation capacity and supporting capacity degradation, respectively. Heat generation oftentimes accompanies SEI film formation, thereby causing thermal shifting away from the previously established stable conditions.[128] Thus, the formation of an SEI layer could potentially be the cause of thermal instability, which in turn could result in an irreversible loss in the capacity by hindering the intercalation kinetics.[129, 130] One of the more important factors that dictates SEI layer formation is the morphology and overall size of the electrode material particles.[131] SEI layer formation is therefore more prevalent and evident on nanostructured electrodes, compared to

the bulk, because of their inherently large surface area and corresponding energy at the electrode-electrolyte interface. This oftentimes results in thicker and denser SEI layers that produce more heat during formation, factors all of which negatively impact electrochemical performance.[132]

Past studies have clearly demonstrated the deleterious effects of SEI layer formation on nanostructured electrodes. It was confirmed that a thicker SEI layer would form on $LiCoO_2$ as the particle size decreased.[133] The thicker layers negated the positive effects of nanostructuring the electrode material by severely impeding Li-ion diffusion, and diminishing the electrode performance at higher current densities. Similar results were seen for $LiMn_2O_4$ where the SEI layer thickness on a cycled electrode increased in a near linear fashion with the number of cycles, and the cycle stability was the performance parameter most impacted.[134] However, thick SEI films formed on nanostructured transition metal oxides during Li^+ intercalation have been shown to disappear completely during deintercalation due to a catalysis reaction involving the transition metal, leading to a continuously reiterative capacity fade upon repetitive cycling.[43]

Processing conditions are also heavily impacted by the high reactivity of nanoparticles. Many nanomaterials exhibit poor stability when exposed to ambient atmosphere; such is the case for olivine $LiFePO_4$ due to the reactivity of Fe^{2+} in the presence of atmospheric oxygen and water. This undesired reaction under ambient exposure is known to be more pronounced for smaller particles because of their increased surface/exposure area, and can result in spontaneous lithium extraction and surface oxidation.[135] It has also been revealed that nanostructured electrode materials with poor adherence to the current collector will agglomerate during cycling; nano-SnSb undergoes successive agglomeration during Li^+ insertion and extraction, and experiences quick capacity fade as a result.[136] Thus, the application of some electro-active materials may be limited due to the high processing costs associated with avoiding these secondary reactions and stability issues.

Another size-stability issue with transition metal oxide nanoparticles is their propensity of the electro-active metal ion to dissolve in the electrolyte, further resulting in capacity degradation. Electro-active metal ion dissolution has been well documented for $LiMn_2O_4$, where Mn-ions in the electrode easily dissolved into the electrolyte as induced by acids generated *via* oxidation of the solvent molecules.[137, 138] To date, this issue has been resolved by coating the nanoparticles with oxides and non-oxide systems to decrease the surface area and terminate the side reactions.[139] Despite the implementation of such strides to eliminate these performance issues, the cyclic stability remains a serious problem for nanostructured $LiMn_2O_4$, and related manganese oxide electrodes. The stabilized electrochemical operating voltage range for nanostructured electrode materials also becomes narrower, compared with bulk materials, for similar reasons.

3.7 Remarks

This contribution highlights a wide range of recent advances in the synthesis and implementation of functional nanomaterials used as electrodes for Li-ion battery application. Several general strategies towards the synthesis of advanced energy storage materials have been emphasized, such as the use of nanomaterials, micro/nano-structured architectures, hollow architectures, mesocrystals, and the manipulation of surface chemistry. The nanostructuring of electrode materials for Li-ion battery results in enhanced Li^+ kinetics and the alleviation of localized strain, which leads to an improved rate capability and cycling performance. However, the Coulombic efficiency of nanostructured electrodes is decreased due to the large surface area of the nanomaterials. The design of micro/nano- heterostructures overcomes these issues by exploiting the nanostructure traits in a microstructured assembly. Such architectures exhibit enhanced thermodynamic stability and the elimination of undesired side reactions and nano-toxicity effects while being inexpensive to produce. Hollow nanostructured electrodes also demonstrate enhanced rate capability and cycling stability,

but suffer from reduced volumetric energy density because of the presence of the inner cavity. It may be possible to compensate for this trade-off by optimizing the shell thickness and void size. Mesocrystals, on the other hand, exhibit near single crystalline behavior and can be classified by their high degree of crystallinity, high porosity, and subunit alignment along a crystallographic register all of which have been proven to increase electrochemical performance. Recent advances have also demonstrated that thermodynamic non-equilibrium effects can be exploited towards optimizing electrode performance. The presence of surface defects has also demonstrated the ability to modify the surface thermodynamics and facilitate the phase transition boundaries. Surface chemistry modifications and surface defects may enhance the storage capacity by shifting the phase transition boundary and introducing a fast mass and charge transport path. Further development and optimization of these materials can still be achieved through the synergy of these techniques. These energy storage materials with high capacity, long cycling life, and a high degree of safety will certainly improve the performance of energy storage devices and facilitate their widespread application.

Chapter 4

Polyol-mediated Solvothermal Synthesis and Electrochemical Performance of Nanostructured V_2O_5 Hollow Microspheres

Hollow vanadyl glycolate nanostructured microspheres were synthesized *via* a highly scalable and template free polyol induced solvothermal process. Subsequent calcination transformed the precursor material into vanadium pentoxide, a well-studied transition metal oxide. The vanadyl glycolate nanoparticles were synthesized through a self-seeding process, and then aggregated around N_2 microbubbles formed during the reaction that acted as quasi-micelles due to the large polarization discrepancy between nitrogen and water. The proposed formation mechanism provides a firm understanding of the processes leading to the observed hollow microsphere morphology. The thermally treated material was tested as cathode for lithium-ion battery, and showed excellent cycle stability and high rate performance. The exceptional electrochemical performance was attributed to the relatively thin walled structure that ensured fast phase penetration between the electrolyte and active material, and

shortened lithium-ion migration distance. The prolonged cycling stability is ascribed to the inherent morphological void that can readily accommodate volume expansion and contraction upon cycling.

4.1 Introduction

Self-assembled nanostructures with particular morphology and novel properties have been the subject of intense research over the past several decades due to their specific properties and tunable functions that can be utilized in a wide range of applications.[96, 140, 141] The use of organic surfactants and polymers in nanoparticle synthesis has been a popular method of achieving morphological control, where the polymer or foreign ions typically work to regulate and stabilize the surface of the nanoparticles.[142] One of the most common and facile approaches that utilize this technique is the polyol method. Initial studies concerning the polyol method focused on the preparation of elemental metals and alloys by exploiting the reducing properties of a high-boiling alcohol (*i.e.*, glycerol or glycol) towards a suitable metal precursor. The alcohol often acts as a stabilizing agent that effectively limits particle growth and hinders aggregation.

The polyol process is heralded for its self-seeding mechanism and lack of required hard or soft templating materials, making it an ideal process for potential industrial scale-up due to the low-cost and ease of processing.[143, 144] Over the past several years, the number of oxide material systems synthesized *via* the polyol method has steadily increased; several reports have summarized the polyol method of oxide materials as a sol-gel process carried out at elevated temperature that is suitable for the preparation of a host of binary and ternary oxides.[145] The polyol process has since been utilized for the synthesis of a wide range of metal oxide materials, including VO_x,[146] TiO_2,[147] PbO, and SnO_2.[148] Several investigations have considered the role of the inorganic species in controlling the shape of metal and metal oxide nanoparticles, as they may provide as powerful a means as organic

surfactants and polymers for controlling the shape of the synthesized nanoparticles.[149, 150, 151, 152, 153, 154]

Ethylene glycol (EG) is among one of the most widely used solvents for the polyol synthesis of metal and metal oxide nanoparticles due to its strong reducing capability, relatively high boiling point (197°C), and high dielectric constant which increases the solubility of inorganic salts.[155, 156] EG is commonly used as a cross-linking reagent because of its propensity to coordinate to the central metal ion and form a metal glycolate, leading to subsequent oligomerization.[157] Herricks *et al.* revealed that for the formation of platinum (Pt) nanowires, the critical factor dictating the morphological control was the nitrate anion, whose function was to substantially slow the reduction of Pt(II) and Pt(IV) species in EG.[154] Jiang *et al.* demonstrated that EG is an effective reagent in the formation of various metal oxide nanowires that formed a chain-like precursor after refluxing a suitable metal salt in EG.[148] It was also determined that the as-synthesized glycolate precursors could later be converted to their more common metal oxide derivatives when calcined in air, all while maintaining the original precursor morphology. Such was the formation mechanism for the fabrication of titanium oxide, tin dioxide, zirconium oxide, and niobium oxide mesostructures.[148]

In this study, a simple and convenient method has been developed for the large-scale synthesis of nanostructured V_2O_5 hollow microspheres with diameters of approximately 3.0 μm. A great deal of recent research efforts have been focused on the study of hollow nanostructured materials, such as nanotubes and hollow spheres, that demonstrate unique characteristics due to their distinct morphology.[80] Hollow nanostructured materials have been known to exhibit large surface area, low density, and enhanced surface permeability because of their inner voids; such materials have been used in a wide range of applications, including lithium-ion (Li-ion) batteries, catalysts, optoelectronic sensors, and drug-delivery systems.[81, 158] Nanostructured vanadyl glycolate microspheres were first formed *via* the polyol process, and then converted to orthorhombic crystalline V_2O_5 by calcining in air at

elevated temperature. The glycolate precursor was transformed into the corresponding metal oxide without experiencing any change in morphology. Electron microscopy and diffraction studies were used to characterize the morphology, crystallinity, and structure of the hollow nanostructured microspheres. The highly mono-disperse product was ultimately tested as a Li-ion battery cathode material, and showed excellent stability and high-rate reversible capacity upon cycling.

4.2 Experimental Procedure

4.2.1 Materials and Synthesis

Nanostructured V_2O_5 hollow microspheres were synthesized *via* a solvothermal route followed by thermal treatment. In brief, 0.1754 g of ammonium metavanadate (NH_4VO_3, Sigma Aldrich) was stirred in 20 mL of ethylene glycol ($H_2C_6O_2$, VWR) for 8 hours. The solution was loaded into a 50 mL polytetrafluoroethylene (PTFE) lined stainless steel autoclave and then solvothermally treated for 24 hours at 180°C, after which it was cooled naturally. Following precipitate isolation and drying, the samples were annealed at 500°C for 2 hours in air.

4.2.2 Characterization

The phase and crystallite size of the V_2O_5 microspheres were studied using X-ray diffraction (XRD, D8 Bruker X-ray diffractometer); the sample was scanned with Cu-K_α radiation within the range of 10° to 70° (2θ), with a step size of 0.02° and an exposure time of 10 s. The accelerating voltage and current were 40 kV and 40 mA, respectively. Infrared absorption spectra were recorded using a Perkin Elmer 1640 Fourier Transform Infrared (FTIR, Perkin Elmer) Spectrophotometer with KBr pellets. The surface morphology of the microspheres was examined using scanning electron microscopy (SEM, JEOL JSM-7000F). Transmission electron microscopy (TEM) was carried out using a FEI Tecnai G2 F20 operating at 200 kV

after the samples had been embedded in Araldite 502 (SPI-Chem) epoxy resin and then cut to 100 nm thick segments using a Leica EM UC6 ultramicrotome. The nitrogen sorption was performed using a Quantachrome NOVA 4200e. The specific surface area, micropore, and mesopore volumes were determined using multipoint Brunauer-Emmett-Teller (BET), t-method, and Barrett-Joyner-Halenda (BJH) desorption analyses, respectively.

4.2.3 Electrochemical Measurements

The electrode slurry was prepared by mixing the annealed V_2O_5 microsphere powder, Super P conductive carbon (TIMCAL Graphite & Carbon), and polyvinylidene fluoride (PVDF) binder dispersed in a N-Methyl-2-pyrrolidone (NMP, Alfa Aesar) solution at a respective weight ratio of 80:12:08. The slurry was spread onto aluminum foil and dried in a vacuum oven at 80°C overnight prior to coin-cell assembly. The 2032 type half-cells were assembled in a glove box (MTI Corp.) filled with ultra-high purity argon. Lithium metal foil, 1 M $LiPF_6$ in ethylene carbonate (EC)/dimethyl carbonate (DMC) (1:1 v/v), and Celgard 2400 membrane were used as the counter/reference electrode, electrolyte, and separator, respectively. Cyclic voltammetry (CV) was completed using an electrochemical analyzer (CH Instruments, Model 605B) in the voltage range of 2.0-4.0 V (vs. Li/Li^+) at a scan rate of 0.2 mV s^{-1}. The current density and cycle stability performance of the V_2O_5 microspheres was evaluated using an Arbin Battery Tester (BT-2000, Arbin Instruments) operating at room temperature. The half-cells were tested within the voltage range of 2.0-3.8 V vs. Li/Li^+ at various charging rates based on the weight of the active material alone, and assuming a 1 C current density of 294 mA g^{-1}.

4.3 Results and Discussion

The XRD and FTIR spectra of the pre- and post-calcined samples are shown in Fig. 4.1. Prior to calcination the phase was indexed as vanadyl glycolate, $VO(CH_2O)_2$, with some

potential hydrogen or carbon additions.[146] Following the calcination step, the microsphere morphology of the sample was preserved and could be indexed to the orthorhombic form of vanadium oxide, V_2O_5 (space group: Pmmn (59), a=11.516, b=3.566, c=3.777 $\AA$; JCPDS card no. 411426). The transition from the vanadyl glycolate precursor to crystalline V_2O_5 was also noted by the sample changing color from black (pre-calcined) to orange (post-calcined).

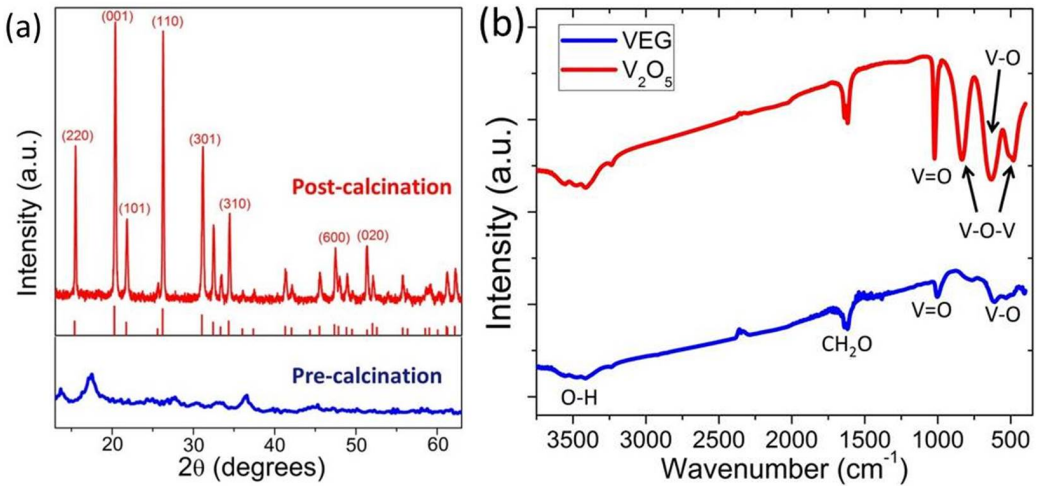

Figure 4.1: Respective (a) XRD and (b) FTIR spectra of the pre- and post-calcined vanadyl glycolate (VEG) and V_2O_5 microspheres.

The transformation from the vanadyl glycolate precursor to V_2O_5 was also confirmed by means of FTIR, as shown in Fig. 4.1b. In the vanadyl glycolate curve, the peak centered at 3412 cm^{-1} corresponds to the O-H stretching band, and the peak at 1628 cm^{-1} corresponds to the [CH_2O] group of the vanadyl glycolate compound. Similarly, the peak centered at 1005 cm^{-1} can be assigned to the V=O stretching bond, and the peaks centered at 761 and 611 cm^{-1} potentially originate from the V-O bond. For V_2O_5, the V=O stretching bond appears at 1022 cm^{-1}, whereas the peaks at 509 and 834 cm^{-1} are attributed to the symmetric and asymmetric stretching of the V-O-V bond, respectively. The peak at 631 cm^{-1} corresponds to the stretching of V-O bond, while the 836 cm^{-1} peak can be attributed to the coupled vibration between the V=O and V-O-V bonds.[146, 159] Comparison with the V_2O_5 spectra demonstrates that many of the absorption peaks corresponding to the vanadyl

glycolate complex disappear following calcination. The V=O vibrational bonds tend to shift to higher wavenumbers with increasing valence of the vanadium species, from 1005 cm^{-1} for vanadyl glycolate to 1022 cm^{-1} for V_2O_5. This vibration shift is most likely caused by the increase in the number of electron withdraw group (O) surrounding the V=O group since the transformation from vanadyl glycolate to V_2O_5 is an oxidation process ($V^{4+} \Rightarrow V^{5+}$), where the increase in the vanadium species valence state shifts the V=O bond vibrations to higher wavenumbers.

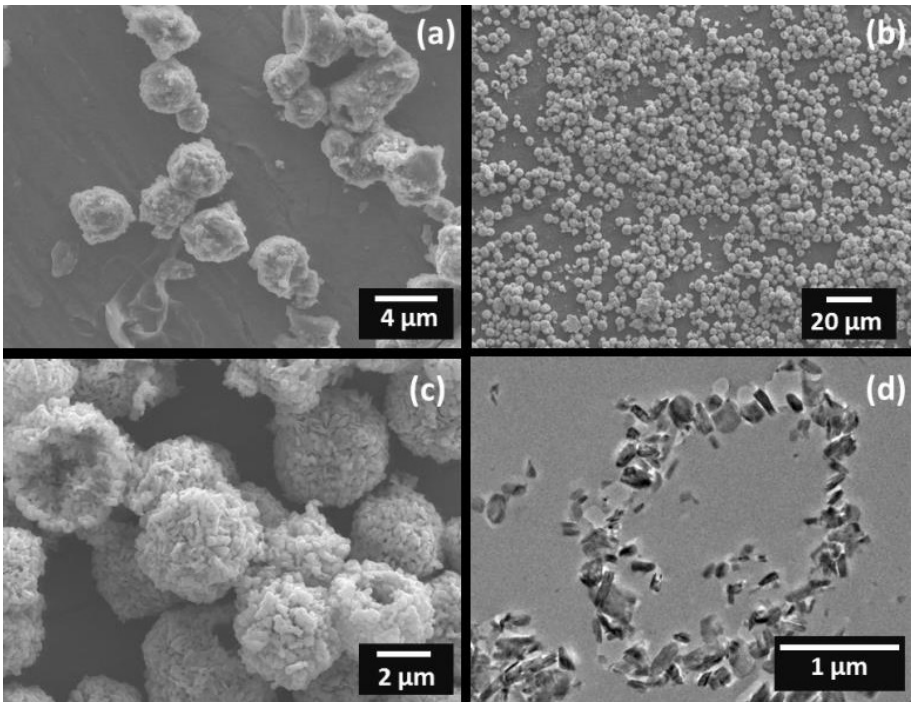

Figure 4.2: SEM images of the (a) pre-calcined vanadyl glycolate microspheres; (b, c) SEM and (d) cross-sectional TEM images of the post-calcined hollow V_2O_5 nanostructured microspheres.

SEM results demonstrated that a mono-disperse, non-agglomerated, high yield product can be achieved employing the described solvothermal, template-free synthesis technique. The collected SEM micrographs also show that the hollow microspheres, with an average outer diameter of approximately 3.0 μm and an inner diameter of approximately 750 nm, were composed of aggregated nanoparticles both before and after calcination. The size of the individual nanoparticles that formed the hierarchical aggregate nanostructure ranged from

60-110 nm, and was confirmed with a calculated average size of 77 nm as determined by applying the Scherrer equation to the full width at half-maximum of the (001) peak from the XRD spectrum. Cross-sectional TEM characterization further confirms the size of the individual nanoparticles and that the aggregated microspheres are hollow (Fig. 4.2).

The BJH pore size distribution (Fig. 4.3) obtained from the adsorption-desorption isotherm suggests that the V_2O_5 sample contains broadly distributed pores with sizes below 10 nm, the majority of which are in the 5-8 nm size range. The BET specific surface area was approximated to be 21.9 m^2 g^{-1}, which is a reasonable value for materials containing pores on the aforementioned scale. The relatively large surface area of the prepared porous V_2O_5 nanostructures ensures short Li-ion diffusion distances, and therefore holds the potential for enhanced electrochemical performance.[160]

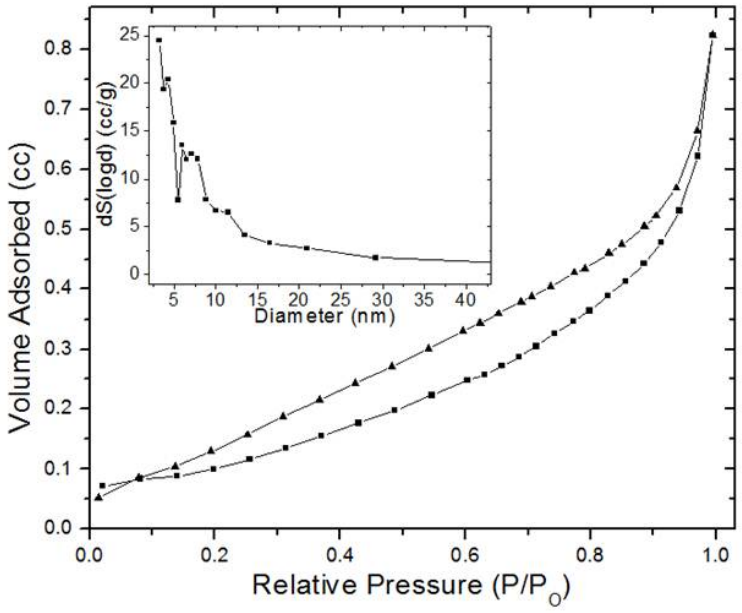

Figure 4.3: N_2 adsorption-desorption isotherm and corresponding BET pore size distribution curves (inset) for the hollow V_2O_5 microspheres.

The polyol process, or use of polyol or diol as the reducing reagent, has been widely applied to reduce metal salts to metal nanoparticles, and is typically used in combination with a surfactant in order to control particle morphology.[150] However, it has also been established that inorganic species may provide a means as powerful as organic surfactants

and polymers for controlling the shape of metallic and metal oxide nanoparticles.[153, 149, 150, 151, 152] The reaction between NH_4VO_3 and EG has been previously documented by Ragupathy *et al.*,[146] who used the precursor materials to synthesize vanadyl glycolate *via* the polyol reaction method that was transformed to V_2O_5 nanostrips with subsequent calcination, according to:

$$NH_4VO_3 + C_2H_6O_2 \Rightarrow N_2 + VO(CH_2O)_2 + H_2O$$

Where the vanadyl glycolate structure is comprised of one dimensional chains that contain edge sharing VO_5 square pyramids. The oxygen atoms within the chain derive from a vanadyl group, a chelating (-OCH_2CH_2O-) ligand, and one end of two other (-OCH_2CH_2O-) ligands present, as shown in Fig. 4.4.[161]

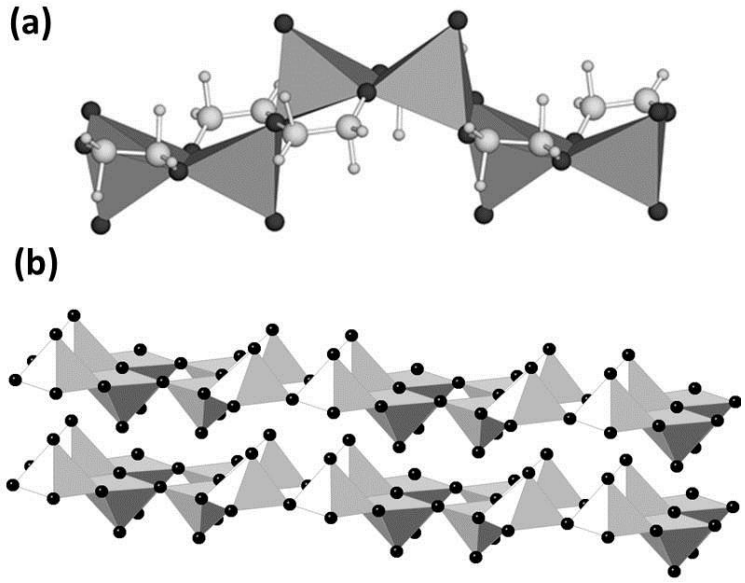

Figure 4.4: The structures of (a) vanadyl glycolate and (b) V_2O_5.

In this study, ethylene glycol served as both the solvent and the reducing agent for the reaction.[142] Ethylene glycol has been established as a cross-linking reagent, and has been used for the controlled synthesis of metal nanoparticles;[149, 154, 157, 84] Xia and co-workers proposed that the synthesis of metal nanoparticles in the presence of EG occurs in two steps: (1) coordination of EG to the central metal ion to form a metal glycolate, and (2) subsequent oligomerization.[154] In the presence of the reducing agent, a bimodal distribution of

vanadyl glycolate nanoparticles will form through a self-seeding process, followed by subsequent homogeneous and heterogeneous nucleation. Formation of the nanoparticles proceeds through two separate steps - a very short nucleation step followed by a particle growth step controlled either by the kinetics of the chemical reaction or the interfacial diffusion of the reacting species. Over the course of the solvothermal growth process, Ostwald ripening will manage the size of the nanoparticles with larger particles growing at the expense of their smaller counterparts.[157] In essence, the nanoparticles initially nucleate and then grow with the oligomerization of vanadyl glycolate *via* the LaMer scheme.[162]

It is proposed that the hollow microsphere morphology of the aggregated vanadyl glycolate nanoparticles can be attributed to the formation of N_2 microbubbles, formed in accordance with the previously mentioned formation reaction equation. The vanadyl glycolate nanoparticles aggregate around the N_2 microbubbles produced during the reaction in an attempt to minimize their interfacial energy (Fig. 4.5).[163] The aggregation reaction can be likened to the case where a templating surfactant, such as polyvinylpyrrolidone (PVP), is used. The templating nature of PVP can be ascribed to the hydrophobic vinyl group and hydrophilic carbonyl group that lead to the formation of polarized micelles. Hollow microspheres of vanadium oxide were previously formed through a polyol reaction involving vanadium (III) acetylacetonate (acac), where PVP assisted in the formation of spherical micelles in EG.[102] The carbonyl groups of the PVP chains face outwards and the bidentate $[C_5H_8O_2]$ ligand of $[V(acac)_3]$ is gradually replaced by EG to form vanadyl glycolate, which can be easily adsorbed onto the micelle surface through the abundant hydroxy groups.

While no templating agents were used in this study, the N_2 microbubbles act as quasi-micelles because of the difference in the polarizability of the phases during solvothermal synthesis. As opposed to directly measuring the polarization value, it is possible to compare the dielectric constant of the two phases since the dielectric constant scales with polarization, according to:

$$D = \epsilon_O E + P \tag{4.1}$$

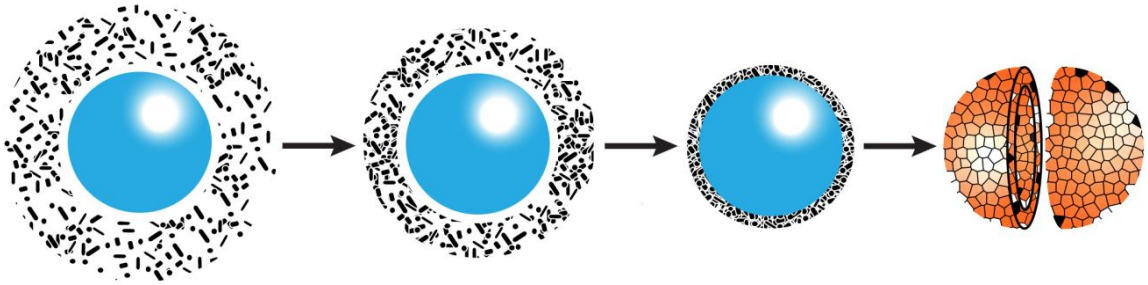

Figure 4.5: Schematic depicting the formation of vanadyl glycolate nanoparticle aggregated hollow microspheres (cross-sectional view) and the resulting V_2O_5 nanoparticle aggregated hollow microspheres following calcination.

The dielectric constant for H_2O and N_2 at room temperature is 80.4 (34.5 at 200°C) and 1.0 (1.4 at 170°C), respectively. Aggregation of the vanadyl glycolate nanoparticles around the N_2 microbubbles is driven by this large difference in polarization between H_2O and N_2, and the incentive for the nanoparticles to decrease their interfacial energy at the solid-liquid interface. Once enough particles coat the microbubble, the structure can become self-supporting and incredibly stable as proven by the microscopy and electrochemical results. This aggregation process has been previously reported for the formation of various monodispersed oxide particles,[164] where the driving force for the colloid particle reorganization corresponds to a reduction in the surface free energy. Such a mechanism may be equipped to explain the formation and morphology of the vanadyl glycolate precursors, and eventual V_2O_5 metal oxide, synthesized in this study.

It should be noted that the morphology of the individual nanoparticles was altered from nanorods to nanoparticles upon transitioning from vanadyl glycolate to V_2O_5. This small change in the morphology can be attributed to the nanorods disassembling during the annealing process because of lattice mismatch and accompanying strain experienced during the transformation process. Ostwald ripening and, a slight degree of, sintering then took place, producing the V_2O_5 nanoparticles; however the morphology and size of the aggre-

gated microspheres remained the same. Fig. 4.6 displays the growth process as examined by harvesting the synthesized products at different reaction time intervals. Complete vanadyl glycolate microspheres were nearly formed even after 1 hr of solvothermal growth; subsequently collected specimens show that the individual particles coarsened with time, but the overall sphere morphology and size became more mono-disperse.

The V_2O_5 structure can be viewed as corner- and edge-sharing VO_6 octahedra, Fig. 4.4, where the octahedra are irregular with five V-O distances ranging from 0.159 and 0.202 nm with a sixth distance as large as 0.279 nm,[165] leading to a large V-O separation along the crystallographic *c*-direction. Because of the varying V-O distances, it is possible to describe the structure as layered square VO pyramids, with five oxygen atoms surrounding the vanadium atom, and the separation distance between each layer depending on the water content of the compound. Ultimately, these factors all make the layered structure of V_2O_5 ideal for functioning as an intercalation host,[107, 165] which is why the compound has been extensively studied since being reported by Whittingham.[107] A wide assortment of V_2O_5 nanostructures have already been synthesized by a variety of methods, including reverse-micelle transition, sol-gel processing, hydrothermal treatment, and electrochemical deposition.[95]

The intercalation of V_2O_5 occurs with compensating electrons leading to the formation of vanadium bronzes, and can be expressed as $V_2O_5 + xLi^+ + xe^- \Longleftrightarrow Li_xV_2O_5$ when lithium is the intercalating species. V_2O_5 has a reversible capacity of 294 mA h g^{-1} that corresponds to the intercalation of two Li^+ per formula unit before the transition to the $Li_3V_2O_5$ irreversible phase occurs; however, V_2O_5 is notoriously known for its poor cycle stability. One method of overcoming the poor cyclic stability is by employing hollow nanostructured materials, such as hollow microspheres, as the electro-active material of the electrode. Hollow nanostructured materials have been known to exhibit large surface area, low density, and enhanced surface permeability because of their inner cavities. The morphological void of hollow nanostructured materials is the feature responsible for enhancing the electrochemical performance in two

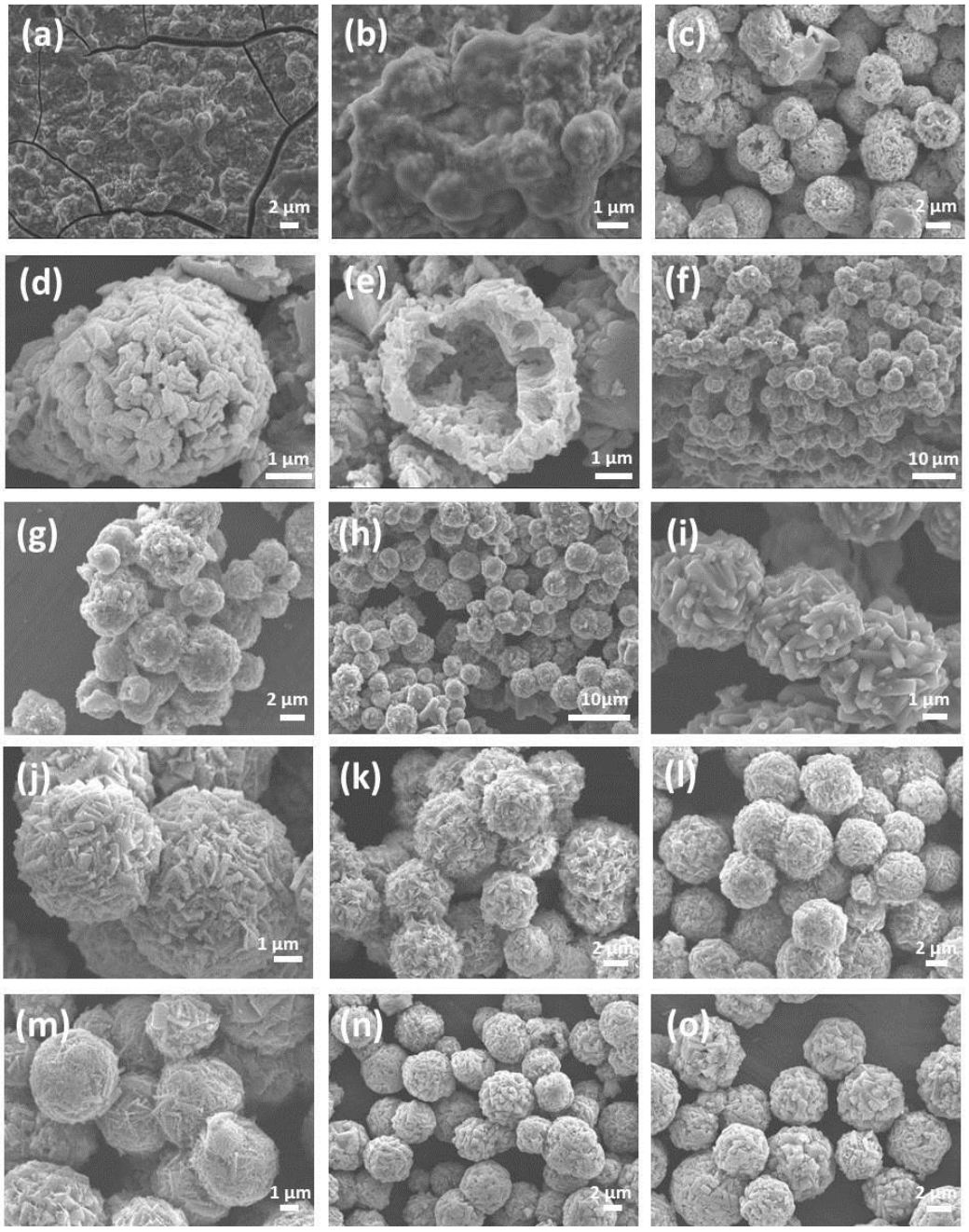

Figure 4.6: SEM micrographs of the pre-calcined vanadyl glycolate microspheres after solvothermal treatment times of (a, b) 1 hr, (c-e) 2 hr, (f, g) 4 hr, (h, i) 8 hr, (j, k) 12 hr, (l, m) 16 hr, and (n, o) 20 hr.

ways. First, the void within hollow nanostructured materials may alleviate any localized volume change experienced during the Li^+ intercalation/deintercalation process, thereby improving the cyclic stability by alleviating any strain the electrode incurs; secondly, the large surface area and decreased Li^+ diffusion distance in hollow nanostructured electrodes greatly enhances the specific capacity while decreasing the packing density.[82, 83, 84] To date, there have only been a few reports of hollow V_2O_5 microspheres, but the precursor materials or experimental conditions used in these studies are either expensive or time consuming. Additionally, the 1C current density in these studies is often defined as the insertion of one Li-ion per V_2O_5 formula over the course of one hour, or 150 mA g^{-1}.[82, 83, 102] Therefore, a study concerning inexpensive, easy processable hollow V_2O_5 microspheres that demonstrate excellent electrochemical performance has yet to be reported.

The cycling performance of the prepared electrodes was tested within the voltage range of 2.0 to 3.8 V. The selected voltage window was chosen to avoid the formation of the irreversible ω-phase of $Li_xV_2O_5$ ($2 < x < 3$) that occurs at lower depth of discharge, thereby improving the cycle stability.[166] It should be noted that only the V_2O_5 mass was included in the calculation of the specific capacity of the electrode. As shown in Fig. 4.7a, several well-defined redox peaks are observed between 3.4 and 2.3 V (vs. Li/Li^+) in the initial cyclic voltammogram collected at a rate of 0.2 mV s^{-1}. These peaks were attributed to the insertion/extraction of lithium-ions into the host structure, and the corresponding phase transitions have been labeled. Fig. 4.7b shows the discharge capacities of the V_2O_5 microspheres at current densities of 300 (1 C), 900 (3 C), 1800 (6 C), 3600 (12 C), and 6000 (20 C) mA g^{-1}, which were 241, 165, 127, 96, and 78 mA h g^{-1}, respectively. As previously mentioned, these values are considerably higher than others reported in literature.

There was a small degree of irreversible capacity loss from 241 to 206 mA h g^{-1} occurring between the first and second discharge at 1 C (Fig. 4.8), which can be attributed to remnant localized strain effects from solid-state amorphization or pulverization experienced during cycling.[167, 168] The cycle stability of the cell was then analyzed following rate performance

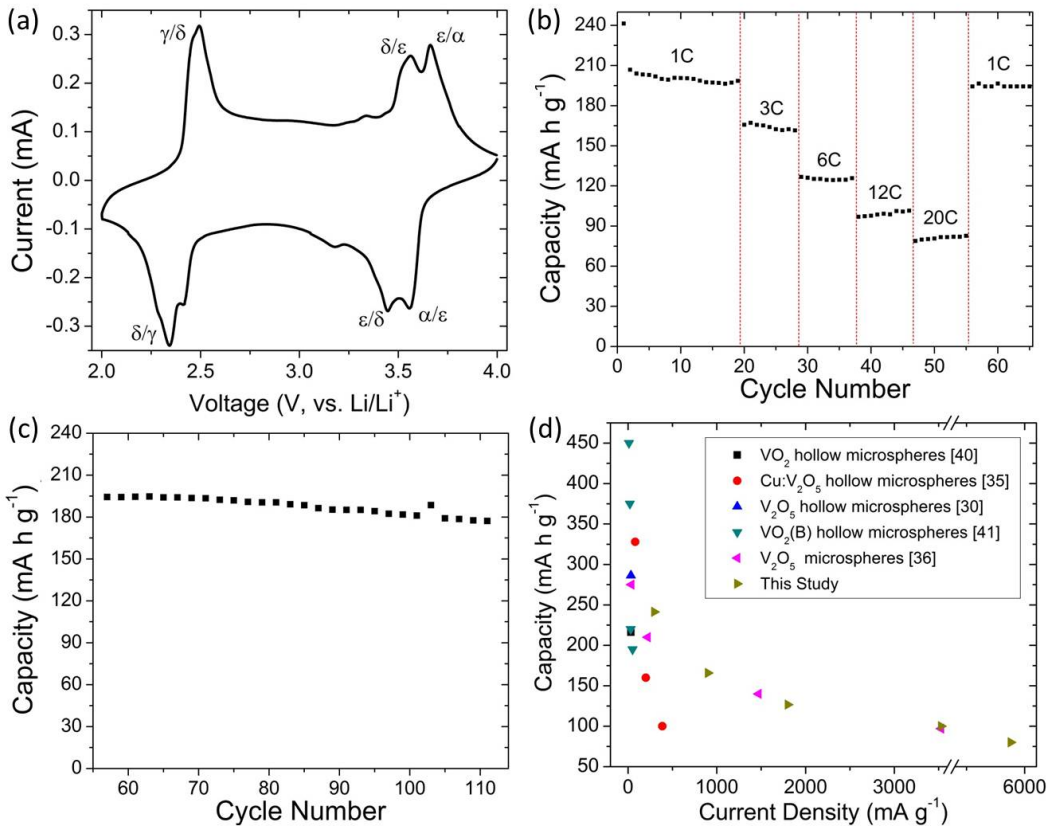

Figure 4.7: (a) Cyclic voltammogram obtained at a scan rate of 0.2 mV s^{-1}; (b) rate performance of the V_2O_5 microsphere electrode at 1, 3, 6, 12, and 20 C; (c) cycle stability of the V_2O_5 microsphere electrode when tested at 1 C after rate performance testing; (d) rate performance comparison with other VO_X microspheres as gathered from the literature.

cycling, the results of which are shown in Fig. 4.7c. The V_2O_5 microspheres were reasonably stable at a discharge rate of 1 C with capacity values of approximately 190 mA h g^{-1}, even after being cycled at a high discharge rate of 20 C. The Li-ion capacity values of the V_2O_5 microspheres synthesized in this study were compared to similar structures listed in the literature. Fig. 4.7d shows the findings of this comparison; it is evident that the V_2O_5 microspheres reported here are far superior to any other microspherical VO_x materials to date, especially at higher current densities.[169, 170] It should be noted that the conductive additive loadings in these studies were all equal to or greater than the amount of conductive additive used in this study (12%).

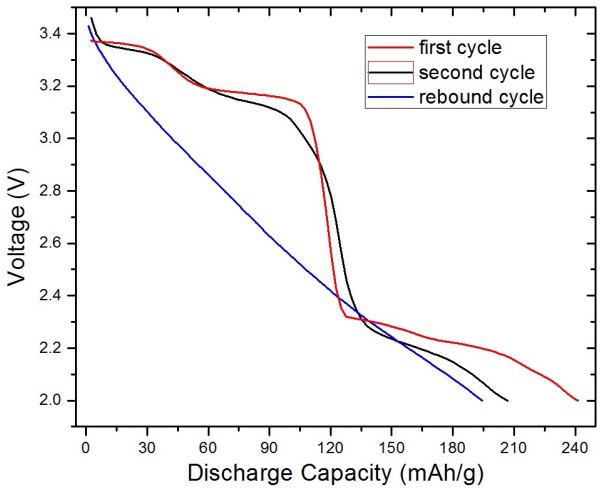

Figure 4.8: The first, second, and rebound (after varying the discharge current at higher rates) discharge profiles of the V_2O_5 microsphere electrode at 1 C. There are no plateaus detectable in the rebound discharge profile, indicating that the sample has become amorphous.

The enhanced electrochemical high-rate and cycling performance of the hollow microspheres can be attributed to the improved kinetic properties as a result of their morphology. The hollow microsphere morphology composed of nanoparticles eases the transportation of lithium-ions by increasing the ratio of active material surface area to electrolyte, and ensures rapid ionic and electronic conduction throughout the electrode. Also, the void within hollow nanostructured materials can alleviate any localized volume change experienced during the Li^+ intercalation/deintercalation process, thereby decreasing the degree of pulverization the active material experiences upon cycling, further improving the cycle stability.

4.4 Conclusions

In conclusion, the development of a highly scalable and reproducible template free process was developed for the synthesis of hollow V_2O_5 microspheres composed of aggregated nanoparticles. It was proposed that N_2 microbubbles formed during the reaction acted as aggregation centers for the synthesized vanadyl glycolate nanoparticles, resulting in the observed hollow microsphere morphology. The synthesized material showed excellent cy-

cle stability and high discharge rate performance, which can be ascribed to the thin shell that ensures fast phase penetration between the electrolyte and active material and a short lithium-ion migration distance during intercalation/deintercalation, and the morphological void which accommodates cycling induced localized strain. The current results clearly demonstrate that hollow V_2O_5 microspheres are well suited for application as cathode materials for Li-ion batteries.

Chapter 5

Enhanced Intercalation Dynamics and Stability of Engineered Micro/nano-structured Electrode Materials: Vanadium Oxide Mesocrystals

An additive and template free process is developed for the facile synthesis of VO_2(B) mesocrystals *via* the solvothermal reaction of oxalic acid and vanadium pentoxide. The six-armed star architectures are composed of stacked nanosheets homoepitaxially oriented along the [100] crystallographic register with respect to one another, as confirmed by means of selected area electron diffraction and electron microscopy. It is proposed that the mesocrystal formation mechanism proceeds through classical as well as non-classical crystallization processes and is possibly facilitated or promoted by the presence of a reducing/chelating agent. The synthesized VO_2(B) mesocrystals are tested as a cathodic electrode material for lithium-ion batteries, and show good capacity at discharge rates ranging from 150-1500 mA g^{-1} and

a cyclic stability of 195 mA h g^{-1} over fifty cycles. The superb electrochemical performance of the VO_2(B) mesocrystals is attributed to the porous and oriented superstructure that ensures large surface area for redox reaction and short diffusion distances. The mesocrystalline structure ensures that all the surfaces are in good contact with the electrolyte, and that lithium-ion intercalation occurs uniformly throughout the entire electrode. The exposed (100) facets also lead to fast lithium intercalation, and the homoepitaxial stacking of nanosheets offers a strong inner-sheet binding force that leads to better accommodation of the strain induced during cycling, thus circumventing the capacity fading issues typically associated with VO_2(B) electrodes.

5.1 Introduction

The development and implementation of nanostructured electrode materials has led to great enhancements in Li-ion battery performance, as with many other fields.[43] The nanoscale size reduction leads to enhancements of the Li-ion battery intercalation capability by increasing the specific surface area for interfacial Faradaic reactions and the flux of Li^+ across the electrode-electrolyte interface; these effects ultimately enhance the mass and charge diffusion paths and modify the thermodynamics (compared to the bulk), which facilitates phase transitions.[158, 171] Provided all the benefits of nanostructuring, the synthesis and characterization of nanostructured electrode materials of various chemistries have been extensively investigated. However, the use of nanostructures is not a panacea, and there are several performance issues, either lingering or deriving from nanostructuring, that still need to be addressed.[172] Most notably, nanostructured electrodes exhibit diminished conductivity, reactivity, stability, and packing density.[123, 125, 126, 133, 137, 173]

The design of structurally aligned nanoparticles can circumvent the thermodynamic instability, undesired side reactions, high processing costs, and potential nano-toxicity effects associated with nanoparticle synthesis and processing.[43, 75, 76] There has been a great deal

of recent efforts in the formation and understanding of ordered nanoparticle superstructures with a vast range of architectures; in particular, crystallographically oriented nanoparticle superstructures, or mesocrystals, have been the central focus of such intrigue since described by Colfen and Antonietti.[96, 98, 100, 140] Until recently, mesocrystals were only studied in biomineral materials, but current research efforts have shifted towards the development of mesocrystalline organic molecules,[99, 100] metal oxides,[103, 174, 175, 176] and other functional materials.[177, 178]

Novel nanoparticle arrangement has historically been achieved through the synthesis of nanocrystalline superlattices, or supercrystals, and colloidal crystals. However, individual nanoparticle orientation is not taken into account by such assemblies. Mesocrystals can be classified by their high degree of crystallinity, porosity, and subunit alignment along a crystallographic register.[98] These highly desirable properties are due in part to the mesocrystal formation mechanisms, which are still poorly understood, and make mesocrystals ideal material candidates for catalysis, sensing, and energy storage/conversion applications.[140] Mesocrystal growth often proceeds *via* the aggregation of precursor units, rather than the classical ion-by-ion growth mechanism, which can be attributed with the generation of crystals with hierarchical structures and complex morphologies. Several investigations of mesocrystalline $LiFePO_4$ and TiO_2 used as the electro-active material for lithium-ion battery electrodes have already been produced, but a report of mesocrystalline vanadium oxide for such an application is lacking.[103, 176] Herein, we report on the solvothermal synthesis, potential formation mechanism, and electrochemical performance of VO_2(B) mesocrystals synthesized using an additive free solvothermal approach. Moreover, remarkable phase stability and excellent lithium-ion intercalation properties have been demonstrated for the obtained VO_2(B) mesocrystals.

5.2 Experimental Procedure

5.2.1 Materials and Synthesis

VO_2(B) mesocrystals were synthesized by adopting the methods of Li *et al.*[179] In a typical reaction, 25 mmol of V_2O_5 (Alfa Aesar) was combined with 15 mL of 0.1 M oxalic acid (Sigma-Aldrich) and stirred for 18 hours. The oxalic acid served as the reducing and chelating agent. Completion of the reaction was noted by the color of the solution transitioning from yellow to blue, signifying a reduction of the vanadium species. The solution was then transferred into a polytetrafluoroethylene (PTFE) lined, 25 mL capacity stainless steel autoclave. The solvothermal reaction was carried out at 180°C for 12 hours, after which the final product was isolated and dried at 80°C overnight.

5.2.2 Characterization

The phase and crystallite size of the VO_2(B) mesocrystal material was studied using X-ray diffraction (XRD, Bruker X-ray diffractometer); the sample was scanned with Cu-K_α radiation within the range of 10° to 70° (2θ) using a step size of 0.02° and an exposure time of 10 s. The accelerating voltage and current were 40 kV and 40 mA, respectively. The surface morphology of the VO_2(B) mesocrystals was examined using scanning electron microscopy (SEM, JEOL JSM-7000F). The specific surface area and pore size distribution was determined by nitrogen sorption isotherms at 77 K using the Brunauer-Emmett-Teller (BET) and Barrett-Joyner-Halenda (BJH) desorption analyses, respectively (Quantachrome NOVA 4200e). Transmission electron microscopy (TEM) and selected-area electron diffraction (SAED) studies were carried out using an aberration-corrected Titan 80-300 scanning/transmission electron microscope (S/TEM) at 80 kV after the sample had been embedded in Araldite 502 (SPI-Chem) epoxy resin and then cut to 100 nm thick segments with using a Leica EM UC6 ultramicrotome.

5.2.3 Electrochemical Measurements

The electrode slurry was prepared by mixing the as-synthesized VO_2(B), Super P conductive carbon (TIMCAL Graphite & Carbon), and poly(vinylidene fluoride) (PVDF, Sigma-Aldrich) binder dispersed in a N-Methyl-2-pyrrolidone (NMP, Alfa Aesar) solution at a weight ratio of 80:12:08, respectively. The slurry was spread onto aluminum foil and dried in an oven at 80°C overnight prior to coin-cell assembly. The 2032-type half-cells were assembled in an argon filled glove box (MTI, Corp.). A polypropylene membrane (Celgard 2400) was used as the separator, Li-metal as the counter and reference electrodes, and 1 M $LiPF_6$ in ethylene carbonate/dimethyl carbonate (1:1, v/v ratio) as electrolyte. Cyclic voltammograms (CVs) were collected using an electrochemical analyzer (CH Instruments, Model 605B) in the voltage range of 2.0-3.8 V (vs. Li/Li^+). The Li-ion cycle stability and rate performance of the VO_2(B) mesocrystals was evaluated using an Arbin Battery Tester BT-2000 (Arbin Instruments, College Station, TX) operating at room temperature. The half-cells were tested within a voltage cut-off range of 2.0-3.8 V vs. Li/Li^+ at various current rates; the capacity values were based on the weight of the electro-active material alone.

5.3 Results and Discussion

VO_2(B) mesocrystals were synthesized by adopting the methods of Li *et al.*[179] The size and morphology of the as-prepared material was examined using scanning electron microscopy (SEM), the results of which are displayed in Fig. 5.1. Fig. 5.1(a-c) display several representative individual mesocrystal assemblies, while the later SEM images show overall micrographs of a typical specimen which is largely composed of uniformly micro-sized ellipsoidal star structures with an average height and width of approximately 2.8 μm and 1.5 μm, respectively. As the higher magnification micrographs reveal, each star-structure is composed of six arms that are self-assembled from stacked nanosheets 20-60 nm thick that are radially aligned with respect to the center of the structure. Each nanosheet is intimately connected

to its neighbors, resulting in a highly porous structure that should facilitate the penetration of the electrolyte into the material, alleviate cycling induced strain, and decrease the lithium-ion diffusion distance. The overall thickness of each hierarchically nanostructured arm is approximately 200-300 nm.

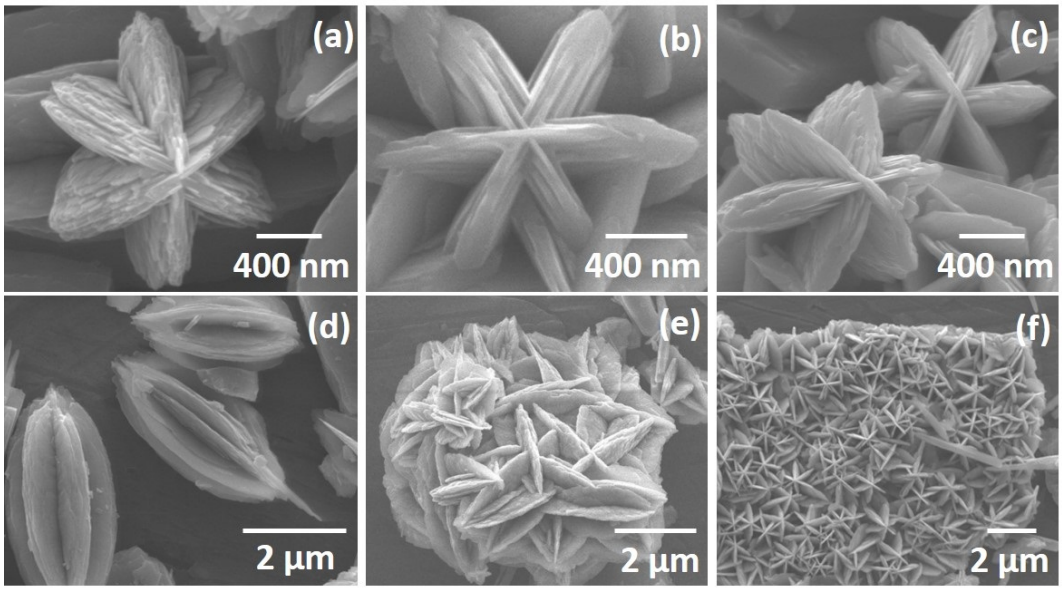

Figure 5.1: SEM images of the synthesized vanadium oxide mesocrystals; (a-c) representative view of individual assemblies showing the stacked nanosheets composing each arm, (d) longitudinal view of star-structure, and (e, f) overall view of as-synthesized specimen displaying the packing density.

Fig. 5.1(e, f) illustrate that the star-assemblies appear to have a relatively mono-disperse size distribution, and are tightly packed which should result in a porous and layered microstructure assembly with enhanced volumetric density and conductivity. A slight degree of variation with the morphology is apparent (Fig. 5.1e); however, such effects are considered negligible because the arms of the structures are composed of stacked nanosheets.

Fig. 5.2a displays the X-ray diffraction (XRD) pattern of the as synthesized material which can be indexed to the monoclinic crystalline phase of VO_2(B) (space group C2/m and JCPDS card no. 081-2392) with lattice parameters a, b, c, and β equal to 12.092, 3.702, 6.433 Å, and 106.6°, respectively (Fig. 5.3); this is consistent with literature reports.[180, 181] The interlayer spacing of the phase is determined to be 6.15 Å from the (001) reflection. The sharp

and high intensity diffraction peaks are indicative that the product is highly crystalline. No secondary or parasitic phases are detected, and the formation of crystalline VO_2(B) indicates that the V^{5+} ions from the original V_2O_5 precursor have been reduced to V^{4+} during the solvothermal synthesis by oxalic acid.[179, 182, 183]

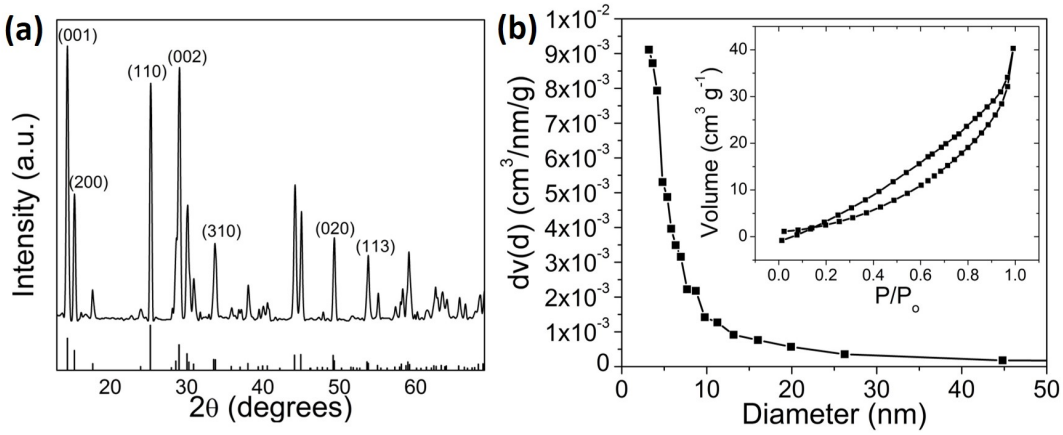

Figure 5.2: (a) XRD spectrum and the (b) BJH desorption pore size distribution for the as synthesized VO_2(B) mesocrystals (inset: N_2 adsorptiondesorption isotherm).

Peak broadening analysis of the (001) XRD reflection using the Scherrer equation indicated that the average crystallite size was approximately 17 nm, substantiating the microscopy results that the VO_2(B) mesocrystals were composed of nanocrystalline subunits. The presence of the nanoparticle subunits and the porous nature of the sample were confirmed by the corresponding nitrogen sorption isotherms and the BJH desorption analyses, which indicated that the majority of pores within the sample are below 15 nm (Fig. 5.2b). The BET derived surface area was determined to be 28.4 $m^2\ g^{-1}$, which is a reasonable value given the overall microscale of the synthesized assemblies. The amply sized pores can provide excellent channels and cavities for complete and homogeneous Li^+ diffusion and intercalation throughout the material. Some residual chelating agent synthesized during the reaction may remain on or between the surfaces of the VO_2(B) nanosheets, and similar incorporations have been known to decrease the overall porosity of mesocrystals.[184]

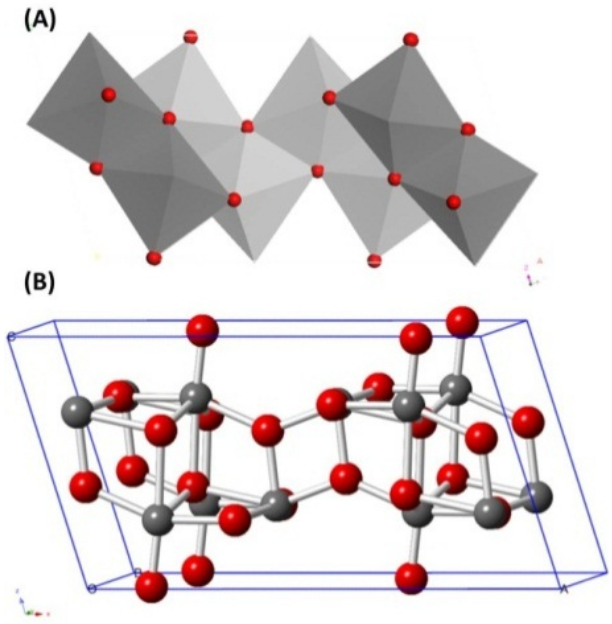

Figure 5.3: Polyhedral and atomic crystal structures of VO_2(B). Red indicates oxygen, while grey indicates vanadium.

TEM was performed on a single star-assembly cross section that was prepared using an ultramicrotome, as displayed in Fig. 5.4a. The cross sectioned image reveals that each arm of the star-assembly is separate from the others, indicating that the structure is not truly single crystalline. Fig. 5.4b presents the vertex of two arms as identified by the highlighted region in Fig. 5.4a, and confirms the superstructure arms are composed of stacked nanosheets. A thinner ultramicrotomed specimen would have made the nanosheet stacking more pronounced; however, specimens cut to thicknesses of 60 and 80 nm continually shifted when exposed to the electron gun, most likely due to heating effects with the epoxy resin (or residual organic matter existing between the nanosheets) when cut so thin. The nanosheets measure several tens of nanometers as observed with TEM, supporting the SEM and XRD findings of the mesocrystalline primary nanoparticle size.

SAED can be used to demonstrate the single crystalline behavior of mesocrystals due to the subunit nanoparticle alignment along a crystallographic register; the SAED pattern for a mesocrystal is nearly identical to that of a single crystalline sample of the same material, making SAED a popular method for characterizing mesocrystals. Fig. 5.4c displays the

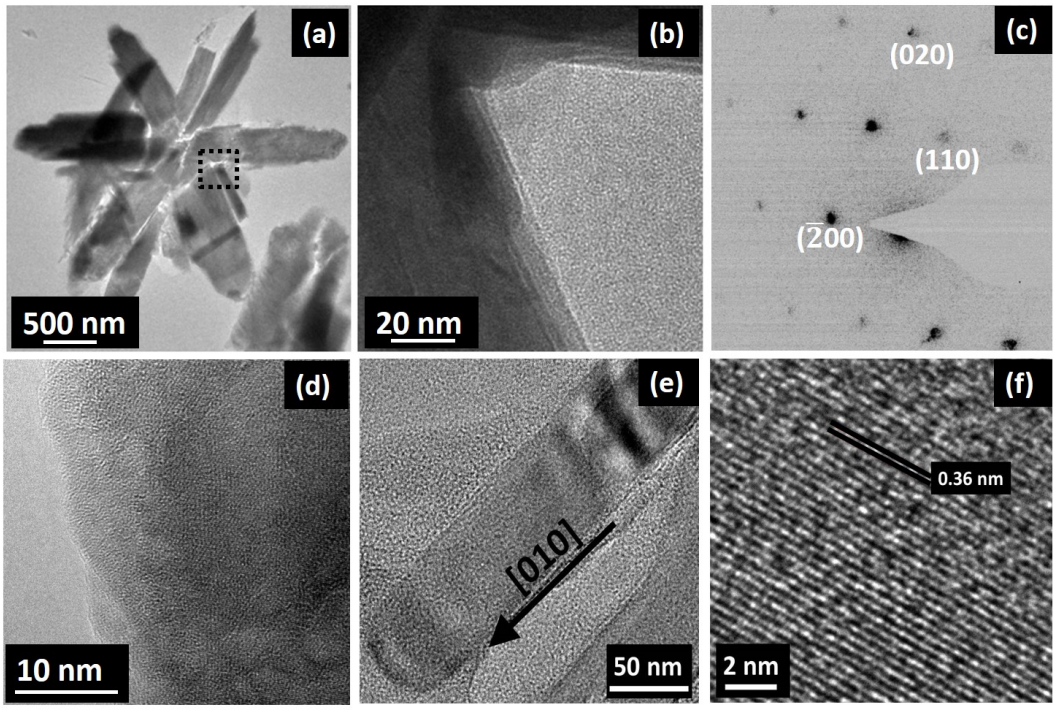

Figure 5.4: (a) TEM image of a cross-sectioned VO_2(B) star-assembly; (b) magnified image of arm intersection; (c) corresponding indexed SAED pattern (on the (002) zone axis); (d) magnified arm edge; (e) overall and (f) magnified view showing the [010] growth direction of the VO_2(B) nanobelts collected 4 hrs into the solvothermal growth process.

corresponding SAED pattern of the region from Fig. 5.4b. The single crystal-like diffraction pattern is consistent with literature reports that index similar patterns as single crystalline VO_2(B).[185, 186, 187] Some distortion of the SAED pattern should be expected as the TEM image clearly shows that there are secondary particles present in addition to the arms of the cross sectioned star-structure being examined.

Fig. 5.4d displays an enhanced TEM image of a VO_2(B) star-assembly edge. The single crystalline nature of the VO_2(B) nanosheet is clearly visible as noted by the lattice fringes, and the dispersion of pores throughout the structure is also apparent. The preferred growth direction of the VO_2(B) structure is realized by considering the relative stacking rate of the octahedra at various crystal faces (Fig. 5.3). The shortest average bond in the VO_2(B) structure is along the [010] direction, which, based on the proposed formation mechanism, can account for the shape of the synthesized nanosheets and the overall architecture. Fig. 5.4e

and 5.4f depict the growth direction of the VO_2(B) nanobelts collected before the solvothermal growth process was complete, where the lattice interspacing of 3.67 Å corresponds to the d_{010} spacing and the distance between two (010) crystal planes of the monoclinic structure; these findings corroborate that growth occurred along the [010] direction.[188]

The establishment of the individual nanobelt and nanosheet growth directions, as viewed along the (002) zone axis, also reveal that the stacked nanosheets are oriented with one another along the [100] direction, and that the exposed surfaces of the nanosheets correspond to the (100) facet. Overall and lattice-resolution TEM imaging revels that the individual VO_2(B) nanobelts and nanosheets exhibit preferential growth and stacking along the [010] and [100] directions, respectively, which is in agreement with previous literature results.[187]

The VO_2(B) nanostructures reported here were developed from the reduction of commercially available V_2O_5 utilizing additive-free solution-based processing methods as governed by the following reaction: $V_2O_5 + H_2C_2O_4 \longrightarrow VO_2(B) + H_2O + CO_2$, where oxalic acid served as both the reducing and chelating agents because of its disposition to serve as a bidentate ligand. The precursor vanadium oxalate is synthesized as an intermediate during the reaction as the conjugate base of oxalic acid, oxalate, is an excellent ligand for metal ions and usually binds forming a five-membered MO_2C_2 ring. The presence of the chelating agent should modify the surfaces of the growing nanocrystals, particularly the surfaces that possess the lowest electronic density, thus leading to the growth of specific surfaces and aiding in the synthesis of the observed micro-architectured nanosheet morphology.[189, 190] The effects of solvothermal treatment time and oxalic acid concentration on the final superstructure are shown in Fig. 5.5.

Although the exact formation mechanism is not entirely clear, a schematic of the mesocrystal formation mechanism is proposed and illustrated in Fig. 5.6. Fig. 5.6a starts off with the VO_2(B) nanobelts that were directly observed 4 hours into the solvothermal treatment. The nanobelts in solution will coarsen and grow into ellipsoidal VO_2(B)

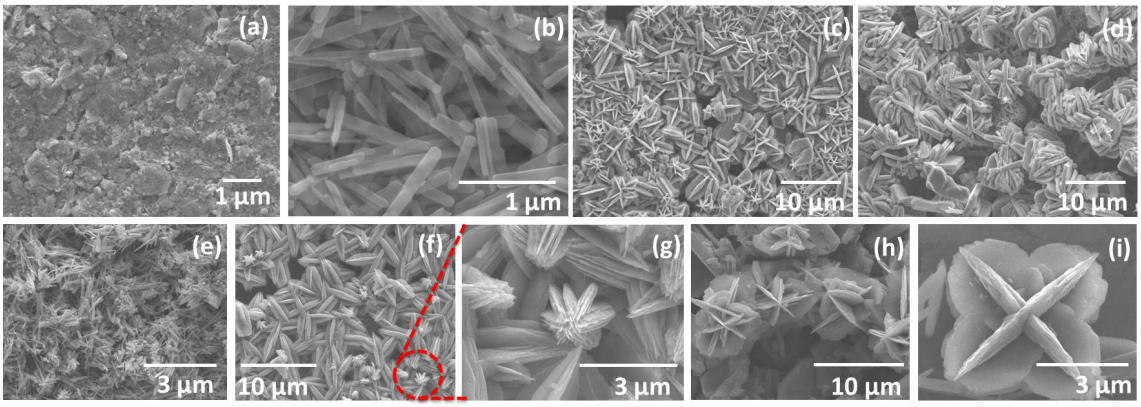

Figure 5.5: Time resolved solvothermal growth of the VO_2(B) structures after (a) 2 hr, (b) 4 hr, (c) 13 hr, and (d) 14 hr; VO_2(B) structures solvothermally grown for 12 hrs with oxalic acid concentrations of (e) 0.08 M, (f, g) 0.12 M, and (h, i) 0.14 M.

nanosheets through Ostwald ripening. The [010] growth direction of the VO_2(B) nanobelts is maintained during this step, as determined from SAED.[179, 183, 187]

Several nanosheets then stack homoepitaxially over one another in order to minimize the energy of the system. Residual chelating agent remaining on the (100) surface of each nanosheet effectively decreases the Debye length of the electric double layer and stabilizes the van der Waals forces of the constituting components, leading to superstructure formation while preventing fusion between individual nanosheets (Fig. 5.6b).[175] Following this step, several series of stacked VO_2(B) nanosheets will coalesce together to form the star-like architecture through the oriented attachment mechanism, as depicted in Fig. 5.6c.[191] There may be some degree of subsequent coarsening after the process is complete, but fusion of the individual VO_2(B) nanosheets should be circumvented due to the presence of the oxalic acid derived chelating agent. This proposed formation mechanism is supported with time resolved SEM growth images, as shown in Fig. 5.7.

Fig. 5.10 presents the cyclic voltammetry (CV), variable rate discharge, cyclic stability curves, and literature comparison of the VO_2(B) mesocrystal electrodes. Fig. 5.10a depicts the first, second, and fifth CV curves collected at a scan rate of 0.5 mV s^{-1}. The cathodic and anodic peaks are located at 2.45 and 2.72 V vs. Li/Li^+, and correspond, respectively, to

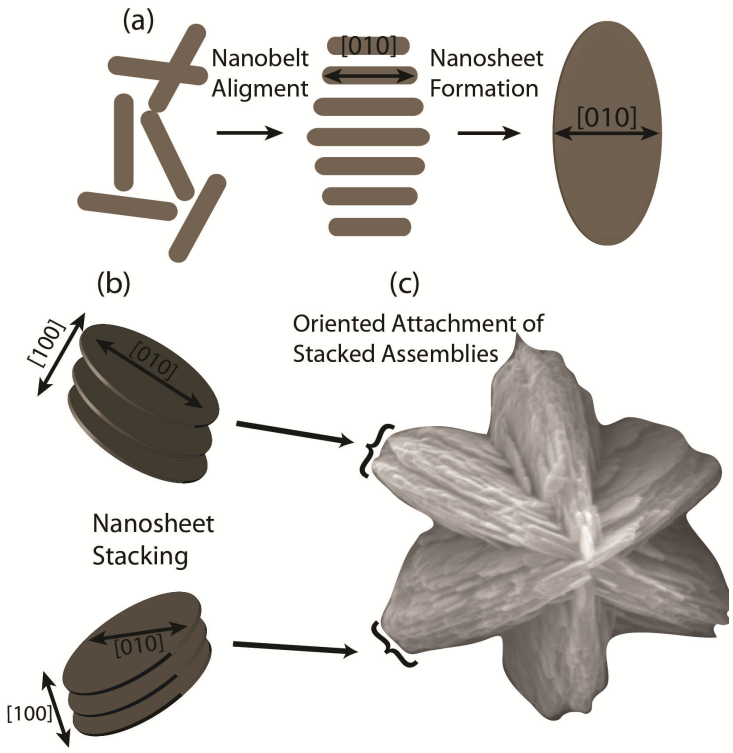

Figure 5.6: Proposed formation mechanism of the VO_2(B) mesocrystals: (a) VO_2(B) nanobelts transform in to VO_2(B) ellipsoidal nanosheets through Ostwald ripening where the semi-major axis of the nanosheet runs along the [010] crystallographic direction; (b) several nanosheets stack on top of one another along the [100] direction (normal to the nanosheet surface) while residual chelating agent on surface prevents fusion; (c) series of stacked VO_2(B) nanosheets then form the star-like architecture through the oriented attachment mechanism.

the insertion and extraction of Li^+ into and out of the VO_2(B) structure. The diminishing peaks of the CV curve with cycling suggest that the star-assemblies are experiencing some degree of pulverization due to the incorporation of lithium upon cycling, but also reaffirm that the as-obtained VO_2(B) mesocrystals can reversibly intercalate lithium.

It has been demonstrated, at least for the case of TiO_2, that the exposure of specific high-energy facets can increase the Li-ion intercalation capability due to their unique surface properties. The charge transfer and chemical diffusion coefficient for TiO_2 is greatest along the (001) facet, and exposure of these facets can result in a lower energy barrier for faster and more efficient Li-ion intercalation.[160, 192] Additionally, the TiO_2(B) (100) facet, taking into account surface relaxation effects, has the greatest surface energy amongst the low-index

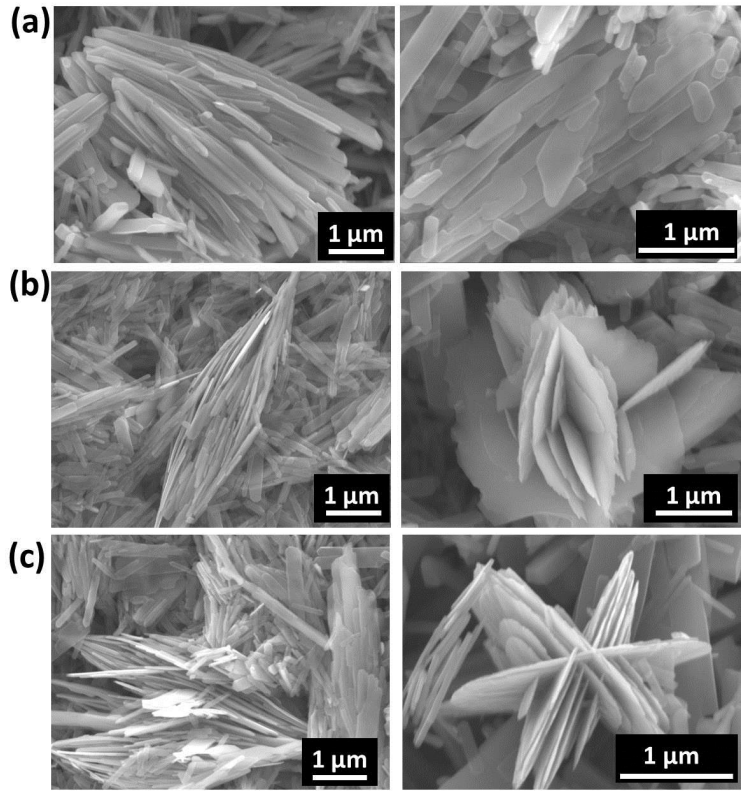

Figure 5.7: SEM images collected at various time intervals corresponding to the intermediate products in the proposed formation mechanism: (a) product collected between 2 and 4 hrs solvothermal treatment times, the VO_2(B) nanobelts collected 2 hrs into synthesis begin to stack with respect to one another forming nanosheets; (b) product collected between 6 and 8 hrs solvothermal treatment times, the VO_2(B) nanosheets begin to stack with respect to one another orientationally; (c) product collected between 10 and 12 hrs solvothermal treatment times, the stacked nanosheet products coalesce to form the overall star-shaped architecture.

surfaces,[193] and is of great significance given that the crystal structures of TiO_2(B) and VO_2(B) are analogous.

Therefore, a similar mechanism may be at play for the case of VO_2(B) mesocrystals, where the exposed (100) facets at the surfaces of the nanosheets effectively enhances the Li-ion intercalation performance. This mechanism was investigated both qualitatively (Fig. 5.8 and Table 5.1) by comparing the surface energies of specific facets by calculating the dangling (or broken) bonds per surface area upon cleaving particular lattice planes, and quantitatively (Fig. 5.9 and Table 5.2) using *ab*-initio calculations; relaxation effects after cleaving were not considered for the qualitative case.

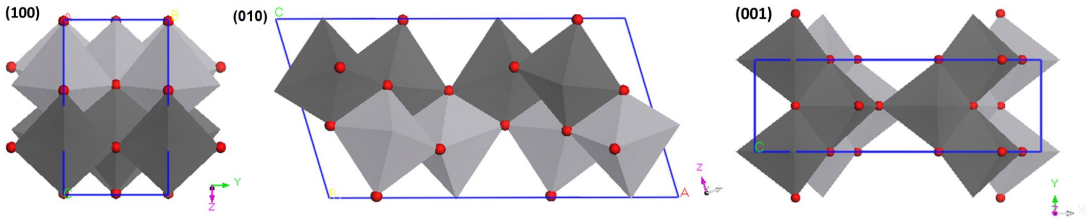

Figure 5.8: Primary facet surfaces and corresponding dangling bonds upon cleaving.

Table 5.1: Primary facet surfaces and corresponding dangling bond energy upon cleaving (surface relaxation effects not considered).

Lattice plane	Dangling bonds	Area (Å^2)	Bonds per area
(010)	6	74.53	0.08
(110)	8	81.34	0.10
(011)	10	89.73	0.11
(001)	6	44.76	0.13
(100)	4	23.81	0.17
(101)	8	38.19	0.21

Qualitatively, it was determined that the (100) facet has a relatively high surface energy compared to the other facets, *i.e.* (010), (110), (011), and (001), which corroborates the findings of Vittadini *et al.* for their analysis of TiO_2(B).[193] Of the considered facets, only the (101) facet had a larger qualitative surface energy. Thus, the exposure of the (100) facets should enhance the Li-ion intercalation performance of the VO_2(B) mesocrystalline

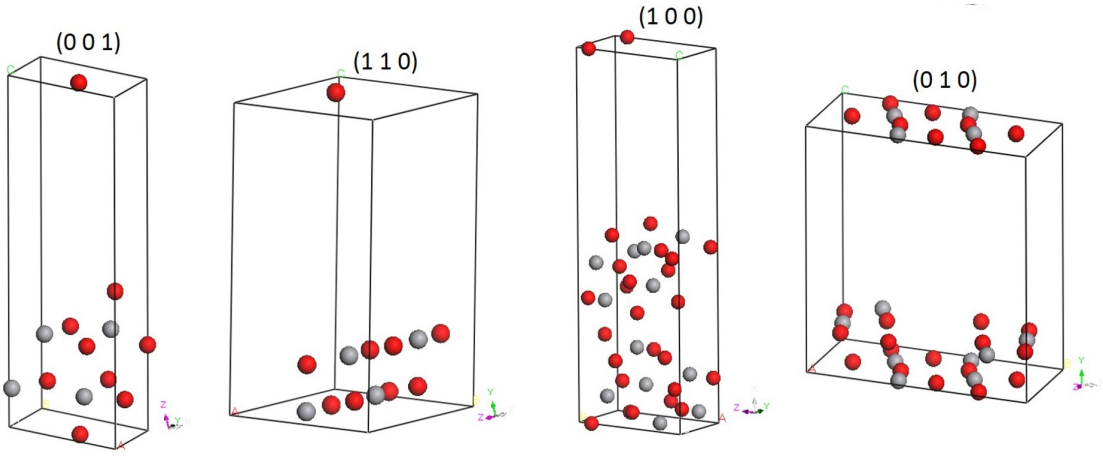

Figure 5.9: Schematics of the low-index VO_2(B) surfaces analyzed *via* DFT

Table 5.2: Computed surface energies (γ) for the un/relaxed low-index surfaces of VO_2(B) and their fractional abundance.

Facet	Energy (J m^{-2})		Composition
	Unrelaxed	Relaxed	
(001)	0.49	0.38	0.41
(100)	1.67	0.74	0.22
(010)	1.42	0.63	0.00
(110)	1.20	0.57	0.37

star-assemblies. Our computational analysis expands upon this by considering relaxation effects upon cleaving a surface when considering the facet surface energy. The VO_2(B) surfaces were represented with periodically repeated slab models, using a 10 Å vacuum space imposed to decouple the surfaces. All the atoms were allowed to relax, and atoms not in the near surface region were constrained. Because each slab exposes two equivalent surfaces, the surface energy, γ, was evaluated using Equation 5.1:

$$\gamma = \frac{[E_{slab} - nE_{bulk}]}{2A} \tag{5.1}$$

where A is the area of the surface, n is the number of VO_2(B) stoichiometric units contained in the slab, E_{slab} is the total energy of the slab model, and E_{bulk} is the total energy of a single VO_2(B) stoichiometric unit as obtained from the calculations on bulk VO_2(B).

The rate capability of the VO_2(B) mesocrystals when tested at incremental discharge rates for 15 cycles starting at 150 mA g^{-1} and terminating at 1500 mA g^{-1} is demonstrated in Fig. 5.10b. The initial capacity was 258 mA h g^{-1}, but steadily dropped to 225 mA h g^{-1} after 15 cycles. The subsequent discharge tests showed reasonably stable capacity profiles of approximately 196, 177, 166, and 158 mA h g^{-1} over the course of 15 cycles at discharge rates of 450, 900, 1200, and 1500 mA g^{-1}, respectively. The exceptional discharge capacities can be attributed to the mesocrystalline structure that promotes electrolyte penetration, thereby increasing the contact area between the electrolyte and the electrode itself. Such traits,

along with the oriented nanosheet structure, lead to great enhancement in the lithium-ion diffusivity, and the overall capacity.

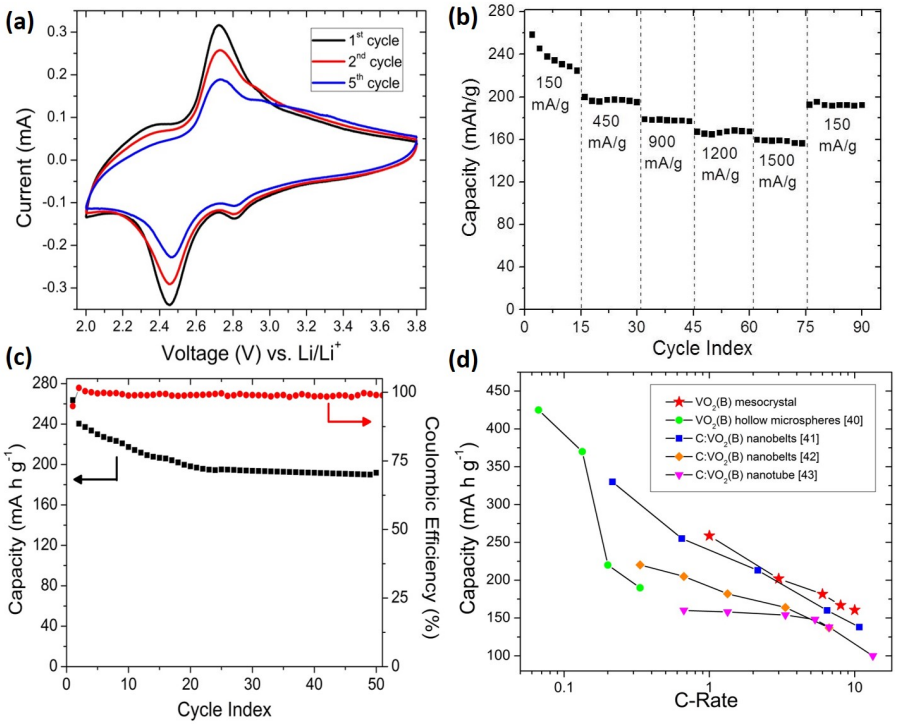

Figure 5.10: (a) CV curves obtained at a scan rate of 0.5 mV s^{-1} for the 1st, 2nd, and 5th cycles; (b) discharge-rate capability at various current densities; (c) cycle stability and Coulombic efficiency over 50 cycles at 150 mA g^{-1}; and (d) comparison with various VO_2(B) structures from literature (assuming a 1 C current density of 150 mA g^{-1}).

The discharge rate was returned to 150 mA g^{-1} after the tests at higher discharge were completed, and was accompanied by a moderate drop from the initial capacity to approximately 195 mA h g^{-1}. The drop in capacity following cycling at higher discharge rates can be realized by examining the cycle stability test performed at 150 mA g^{-1} (Fig. 5.10c). The initial capacity is equivalent to what was seen in the rate capability data, approximately 258 mA h g^{-1}. The capacity then drops with each cycle number until reaching the 20th cycle, at which point the capacity appears to level off at approximately 195 mA h g^{-1}. These results indicate that there may be a slight degree of pulverization or solid state amorphization occurring in the VO_2(B) mesocrystals during the preliminary cycles due to the incorporation of lithium into the system, but an equilibrium is quickly established and then maintained.

Fig. 5.10d compares the mesocrystal intercalation performance with that of other VO_2(B) structures taken from the literature.[170, 194, 195, 196] It should be noted that the conductive additive loadings in these studies were all equal to or greater than the amount of conductive additive used in this study. Despite their overall micro-scale size, the mesocrystals exhibit one of the highest intercalation performance and capacity retention, especially upon cycling at higher discharge rates. The excellent cycle stability can be attributed to the crystallographically oriented nanosheets that provide sufficient accommodation of the volume expansion and contraction upon cycling, assuring that good electrochemical stability and mechanical integrity can be guaranteed for many cycles.

5.4 Conclusions

An additive and template-free solvothermal process was developed for the facile synthesis of mesocrystalline VO_2(B). The VO_2(B) mesocrystals were proposed to form through the combination of classical as well as non-classical crystallization mechanisms. The synthesized VO_2(B) mesocrystals showed excellent cycle stability and high rate discharge when tested as positive electrode material for lithium-ion battery. The stacking of the nanosheets and pores throughout the material can also better accommodate cycling induced strain, thus improving the cycle stability. Moreover, these results reveal that mesocrystals of functional materials with high crystallinity, high porosity, and nanoparticle alignment are promising for potential energy storage applications.

Chapter 6

Amorphous Vanadium Oxide Electrode for Sodium-Ion Battery

In this study, amorphous and nanocrystalline vanadium pentoxide (V_2O_5) films were prepared through a combination of sol-gel processing paired with electrochemical deposition, and characterized as cathode for sodium-ion battery. The degree of crystallinity of the individual electrodes was controlled by managing the annealing profile and environment employed. Amorphous V_2O_5 demonstrated superior sodium-ion intercalation properties as compared to its crystalline counterpart when examined as positive electrode material for Na-ion battery application. More specifically, the amorphous vanadium pentoxide film showed a sodium ion storage capacity of 241 mA h g^{-1}, twice the capacity of its crystalline counterpart, 120 mA h g^{-1}. In addition, the amorphous vanadium pentoxide film possessed much higher discharge potential and energy density. The significant difference between the crystalline and amorphous phases arises from the fast Faradaic reactions which potentially give way to an additional pseudo-capacitive storage contribution. Moreover, because the diffusion-controlled sodium-ion intercalation process is supplemented by surface storage reactions, the overall dis/charge rates are much faster. The percolation of certain diffusion channels in amorphous materials can be activated because of the disordered structure. Such

effects synergistically work to improve charge and ionic transfer at the electrode/electrolyte interface during the sodiation process, yielding a positive electrode material for sodium-ion battery application with superior energy density and strong cycling performance. The possible relationship between the disparity in intercalation properties and structure is discussed.

6.1 Introduction

The progress of energy storage materials and devices appreciably lags the rapid progression of other electronic components in spite of steady advancements in these technologies and has increasingly become a bottleneck impeding device development.[197, 198] Among the commercially available energy storage technologies, lithium-ion (Li-ion) batteries are a mature and robust technology that has been extensively used in consumer devices and applications because of their high energy density and portability.[43, 45, 158, 173] Despite great commercial success, lithium-based batteries have several drawbacks associated with safety issues, high cost, and resource scarcity. Conversely, sodium-ion (Na-ion) batteries have been gaining considerable traction as a realistic alternative to Li-ion battery, for large-scale energy storage applications, in the past several years.[199, 200, 201]

A quick comparison of the differences between metallic lithium and sodium can be gathered from Table 6.1. Na-ion batteries are attractive because sodium resources are seemingly inexhaustible as well as ubiquitous, and therefore cost considerably less (by a factor of roughly 30-40 times) than lithium.[13] Additionally, sodium does not undergo an alloying reaction with aluminum at low voltage, as is the case with lithium, meaning that aluminum can replace copper as the anodic current collector which equates to an overall cell cost savings of 2%; this is significant for large scale grid storage, which is the target market for sodium-ion batteries.[14, 15] The lower operating voltage of Na-ion cells results in enhanced stability of the non-aqueous electrolyte, but also manifests itself in lower energy density. The majority of the proposed electrode materials for Na-ion battery show similar or slightly lower

specic capacity and redox potential than when used in Li-ion cells.[16, 17] Moreover, the accommodation of sodium in traditional host materials is difficult because the ionic radius and reduction potential of sodium are strikingly larger than that of lithium.[18] Therefore, the de/sodiation process induces large distortions in the host lattice that ultimately lead to pulverization of the electrode and the impending failure of the cell.

Table 6.1: Comparison of metallic lithium and sodium.

Parameter	Lithium	Sodium
Cationic radius (Å)	0.76	1.06
Atomic weight (g mol^{-1})	6.9	23.0
E° (V vs. SHE)	-3.04	-2.71
Carbonate cost ($/ton)	5000	150
Metallic capacity (mA h g^{-1})	3829	1165
Coordination preference	octahedral and tetrahedral	octahedral and prismatic

Crystalline materials have been the primary electro-active species choice in the battery field for some time now, but their synthesis can be time-consuming, energy intensive, and costly. It has recently been demonstrated that disordered materials may form percolation pathways *via* the opening of active diffusion channels that could potentially facilitate ionic diffusion;[18, 202] several studies have revealed that Li-ion diffusion in amorphous materials proceeds more rapidly than in crystalline materials with similar particle size and morphology.[203] Based on these considerations, it is worth investigating amorphous or structurally disordered transition metal oxides because of their isotropic characteristics that may enhance Na-ion diffusion by offering diffusion paths that are not highly anisotropic, as is the case for crystalline materials.[204] Short-range ordered materials may also have a lower entropic energy associated with the ordering of incorporated ions and a more open framework to facilitate ionic transport. In this sense, it is possible to describe amorphous materials as homogeneously disordered, in terms of anisotropy and potential defects, and crystalline materials as heterogeneously disordered. Contributions from a pseudocapacitive energy storage mechanism may also be at play, where electron transfer reactions of ions from Faradaic

processes occur at the surface of the electrode as these effects are increasingly important at the nanoscale.[46, 205]

Vanadium oxide is an attractive multifunctional material used for widespread application in various fields such as catalysis,[206] energy storage,[207] and biomedical devices;[208] a wide assortment of V_2O_5 nanostructures have already been synthesized by a variety of methods.[95, 160] The intercalation of Li^+ into V_2O_5 has been well documented and occurs with compensating electrons leading to the formation of vanadium bronzes; however, reports concerning the use of vanadium oxide for sodium based energy storage systems are limited. Tepavcevic *et al.* demonstrated that the deintercalation of bilayered V_2O_5 electrodes was accompanied with the loss of long-range order, whereas short-range order was preserved. The bilayered V_2O_5 cathodes were able to maintain 85% of their initial capacity after 350 cycles with current density varying from 20-630 mA g^{-1}.[209] Bilayered V_2O_5 nanobelts with comparable performance have also been reported more recently.[210] NaV_6O_{15} nanorods showed moderate capacity values but poor capacity retention,[211] and V_2O_5 based Na-ion pseudo-capacitors delivered a maximum specific energy of 40 Wh kg^{-1} and retained 80% of the original capacity after 900 cycles at a 60 C discharge rate.[212] Yet, a study concerning amorphous vanadium oxide has yet to be reported. Herein, we detail the electrochemical deposition of V_2O_5 using vanadium based gels and their application in Na-ion battery.[166] The amorphous V_2O_5 electrode displayed superior electrochemical performance compared to its crystalline counterpart, readily demonstrating that the use of amorphous materials may be of considerable value for future electrode design pending further optimization.

6.2 Experimental Procedure

6.2.1 Gel Synthesis

The films synthesized and examined in this work were prepared *via* electrochemical deposition using a diluted vanadium pentoxide solution, the synthesis of which was adopted

from a previously reported procedure. In brief, V_2O_5 powder (99.8%, Alfa Aesar) was added to deionized water and H_2O_2 (30wt%, Sigma Aldrich) to yield a solution with a V_2O_5 concentration of 0.3 M and with a H_2O_2 to V ratio of 8.05:1. The resulting solution was stirred for 15 minutes, and then ultrasonicated for 10 minutes. Deionized water was added until the concentration was 0.06 M, after which the solution was ultrasonicated for an additional 80 minutes.

6.2.2 Deposition

The synthesized gel was further diluted to a concentration of 7.5 mM in deionized water and stirred until the transparent solution was free of flocculates. Cathodic deposition was carried out using Ni foil (0.125 mm thick, Sigma Aldrich) as the deposition substrate and a piece of Pt foil as the counter electrode. The distance between the two electrodes was kept constant at 1.5 cm and the deposition voltage was (-2.4) V. The deposition process was carried out for 30 minutes unless otherwise noted. After being dried in a 70°C oven overnight the films were either annealed at 180°C under vacuum or 450°C under air for 3 hours.

6.2.3 Characterization

The phase and crystallite size of the annealed V_2O_5 films were studied using X-ray diffraction (XRD, D8 Bruker X-ray diffractometer); the sample was scanned with Cu-Kα radiation within the range of 10° to 70° (2θ), with a step size of 0.02° and an exposure time of 10 s. The accelerating voltage and current were 40 kV and 40 mA, respectively. Infrared absorption spectra were recorded using a Perkin Elmer 1640 Fourier Transform Infrared (FTIR) Spectrophotometer with KBr pellets. X-ray photoelectron spectroscopy (XPS) was completed using a Surface Science Instruments S-probe spectrometer. The X-ray spot size was 800 × 800 μm and the take-off angle was 55°, corresponding to a sampling depth of approximately 50-70 Å. XPS data analysis was carried out using the Service Physics ESCA 2000-A analysis program (Service Physics, Bend, OR). X-ray absorption spectroscopy

(XAS) was conducted at the Advanced Photon Source, 13ID-E in transmission mode. Several layers of V_2O_5 were dispersed on Kapton tape for the measurement to minimize the effect of thickness inhomogeneity, and the data sets were processed using the IFFEFIT software package. Microscopy investigations were carried out using a JEOL JSM-7000F scanning electron microscopy (SEM) and FEI Tecnai G2 F20 transmission electron microscopy (TEM) operating at 200 kV. The nitrogen sorption was performed using a Quantachrome NOVA 4200e. The specific surface area, micropore, and mesopore volumes were determined using multipoint Brunauer-Emmett-Teller (BET), t-method, and Barrett-Joyner-Halenda (BJH) desorption analyses, respectively. Thermogravimetric (TGA) analysis of the V_2O_5 films were investigated from room temperature to 450°C (TGA 7, PerkinElmer) under nitrogen flow at a heating rate of 5°C min^{-1}.

6.2.4 Electrochemical Analysis

For electrochemical analysis, 2016 type half-cells were assembled in a glove box (Mbraun) filled with high purity argon. Sodium metal foil (Sigma Aldrich), 1 M $NaPF_6$ in ethylene carbonate (EC)/dimethyl carbonate (DMC) (1:1 v/v), and Celgard 2400 membrane were used as the counter/reference electrode, electrolyte, and separator, respectively. Lithium metal foil and a 1 M $LiPF_6$ ethylene carbonate (EC)/dimethyl carbonate (DMC) (1:1 v/v) solution were used as the counter/reference electrode and electrolyte, respectively, for the Li-ion half-cells. Cyclic voltammetry (CV) was completed using an electrochemical analyzer (CH Instruments, Model 605C) in the voltage range of 3.8-1.5 V (vs. Na/Na^+) at scan rates ranging from 0.1 to 5.0 mV s^{-1}. Electrochemical impedance spectroscopy (EIS) was carried out on crystalline and amorphous V_2O_5, with frequency ranging from 100 kHz to 10 mHz and the AC amplitude set at 5.0 mV. The current density and cycle stability performance of the V_2O_5 materials were evaluated using an Arbin Battery Tester (BT-2000, Arbin Instruments) operating at room temperature. The half-cells were tested within the voltage range of 3.8-1.5

V vs. Na/Na^+ at various charging rates based on the weight of the active material alone, and assuming a 1 C current density of 236 mA g^{-1}.

6.3 Results and Discussion

The method of gel preparation was adopted from previous work,[213] and involved several parallel or sequential chemical reactions in association with the decomposition of excess hydrogen peroxide:

$$V_2O_5 + 4H_2O_2 \longrightarrow 2[VO(O_2)_2(OH_2)]^- + 2H^+ + H_2O \tag{6.1}$$

$$V_2O_5 + 2H_+ + 2H_2O_2 + 3H_2O \longrightarrow 2[VO(O_2)_2(OH_2)_3]^+ + O_2 \tag{6.2}$$

$$2[VO(O_2)_2(OH_2)]^+ + 4H^+ + 2H_2O \longrightarrow 2[VO(O_2)(OH_2)_3]^+ + O_2 \tag{6.3}$$

$$2[VO(O_2)(OH_2)_3]^+ \longrightarrow 2[VO_2] + O_2 + 6H_2O \tag{6.4}$$

$$[VO_2] \longrightarrow gelation \tag{6.5}$$

The initially aqueous V_2O_5 solution changed color from yellow to orange following the addition of H_2O_2, which is ascribed to the formation of the diperoxovanadate anion $[VO(O_2)_2(OH_2)]^-$ (Equation 6.1). The solution then took on a red color following sonication for several minutes, which suggests that the monperoxovanadate cation $[VO(O_2)(OH_2)_3]^+$ is the main ionic species in the solution (Equations 6.2 and 6.3). The release of oxygen gas was noted by vigorous bubbling that occurred during the mixing of V_2O_5 and H_2O_2. The solution was then further diluted to 0.06 M and sonicated for 80 minutes, during which the color gradually turned to a brownish red while the solution was notably more viscous. These changes could be attributed to the transformation of the dioxovanadium cation $[VO_2]^+$ (Equation 6.4). The increased viscosity and brownish red hue of the gel suggests that $V_2O_5 \cdot nH_2O$ gelation has occurred (Equation 6.5). After sonication, the brownish red

mixture of $V_2O_5 \cdot nH_2O$ gel and solution was diluted to 7.5 mM for deposition. During cathodic deposition, electrons were directed towards the negatively charged Pt counter electrode, and the V^{5+} species from the V_2O_5 colloidal particles and $[VO_2]^+$ dioxovanadate cations were reduced on the surface of the Ni-foil (Equation 6.6 and 6.7):

$$V_2O_5 + 4H^+ \longrightarrow 2[VO_2]^+ + 2H_2O \tag{6.6}$$

$$[VO_2]^+ + e^- \longrightarrow VO_2 \tag{6.7}$$

VO_2 serves as the nucleation center that initiates and catalyzes the formation of $V_2O_5 \cdot nH_2O$ through low pH conditions upon deposition.

$$2[VO_2]^+ + nH_2O \longrightarrow V_2O_5 \cdot nH_2O + 2H^+ \tag{6.8}$$

Ultimately, hydrous vanadium oxide was deposited through the cathodic deposition of VO_2 and the catalyzed gelation of V^{4+} which serves as a nucleation center that initiates and catalyzes the formation of $V_2O_5 \cdot nH_2O$. Following deposition, the coated Ni-foil substrates were processed under different thermal treatment conditions: drying under ambient (as-processed), 180°C anneal under vacuum (180°C/vac) for 3 hours, and 450°C anneal in air (450°C/air) for 3 hours. These temperatures and atmospheres were chosen based off previous results showing that V_2O_5 initiates crystallization at approximately 216°C. The main reason for annealing under vacuum at 180°C is to remove a considerable amount of the crystalline water while preserving the amorphous homogeneity and suppress crystallization. The morphology of the films was observed by SEM, a representative image of which is shown in Fig. 6.1. SEM reveals that the V_2O_5 was homogenously deposited and composed of layers stacked parallel to the substrate that are composed of irregularly shaped nanoparticles with an average size of 500 nm.

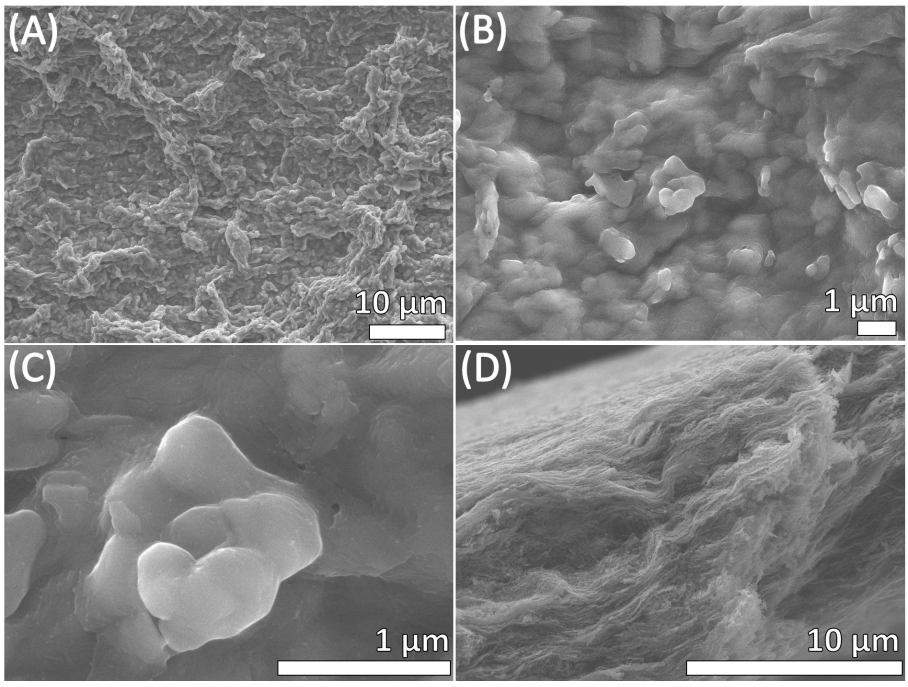

Figure 6.1: Representative SEM images of V_2O_5 films deposited on Ni-foil for one hour: (a, b) low-resolution, (c) high-resolution, and (d) cross-sectional images.

The layered structure is a product of the deposition process that took place through a combination of cathodic deposition and catalyzed gelation, and imparts a significant degree of structural stabilization unto the sample.[95, 115, 166] The overall morphology of the various samples did not differ significantly with thermal treatment, but the observed roughness did increase with temperature. The slight increase in roughness is most likely caused by minor coarsening effects brought on by exposure to higher temperature.

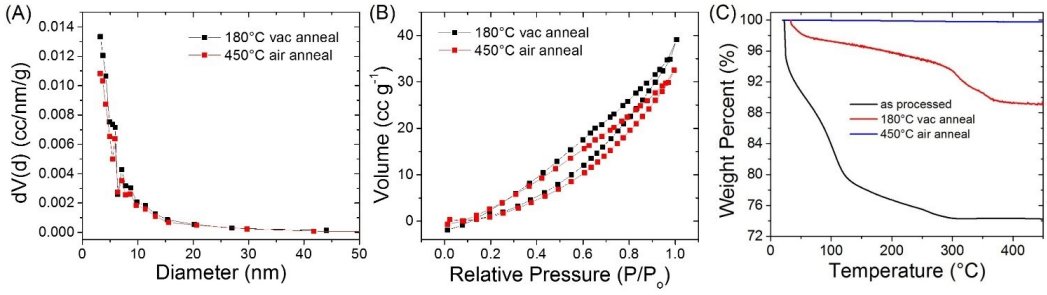

Figure 6.2: (a) BJH desorption pore size distributions, (b) the nitrogen adsorption-desorption isotherms, and (c) TGA analysis for the V_2O_5 samples.

Nitrogen sorption-desorption isotherms were collected in order to determine and compare surface and pore information. The BJH pore size distribution obtained from the nitrogen adsorption-desorption isotherm suggests that the annealed samples contain broadly distributed pores mostly smaller than 15 nm. The 180°C/vac and 450°C/air annealed samples and with a respective average pore size and overall pore volume 3.22 nm and 0.060 cm^3 g^{-1} compared to 3.19 nm and 0.054 cm^3 g^{-1}, respectively. Moreover, the BET derived specific surface areas were 38.7 and 32.6 m^2 g^{-1}, respectively, which confirms that the varying thermal treatments had little change on morphology outside of slight coarsening and surface roughening effects. The amount of water in the samples was examined using TGA, and was quantified at approximately 12% and 0.4% for the vacuum and air annealed materials, respectively (Fig. 6.2c). These results were substantiated by bulk density measurements using the specific gravity method that calculated the density of the 180°C/vac and 450°C/air annealed materials at 2.1 cm^3 g^{-1} and 2.7 cm^3 g^{-1}, respectively. XAS results elucidated the location of the water, and will be covered later.

The crystallinity of the samples was initially compared using X-ray diffraction (XRD, Fig. 6.3a). The 450°C/air annealed specimen could be indexed to the orthorhombic form of vanadium pentoxide, (V_2O_5, space group: Pmmn (59), $a = 11.516$, $b = 3.566$, $c = 3.777$ $\mathring{A}$; JCPDS card no. 41-1426), with no detectable impurities or secondary phases. There were no detected peaks in the as-processed and 180°C/vac annealed samples; the lack of any diffraction peak is a strong indication and confirmation of their amorphous quality, this was further confirmed by TEM, Fig. 6.6. However, the XRD spectra offer little information in terms of bonding, coordination, and chemical identification. Fourier transform infrared (FTIR, Fig. 6.3b), X-ray photoelectron (XPS, Fig. 6.3c), and X-ray absorption (XAS, Fig. 6.3d) spectroscopy were therefore conducted in order to reliably characterize the chemical nature of the amorphous specimen for comparison with its crystalline counterpart.

FTIR was utilized to chemically identify the seemingly amorphous, as determined by XRD, compounds. As shown in Fig. 6.3b, the absorption peak stemming from the sym-

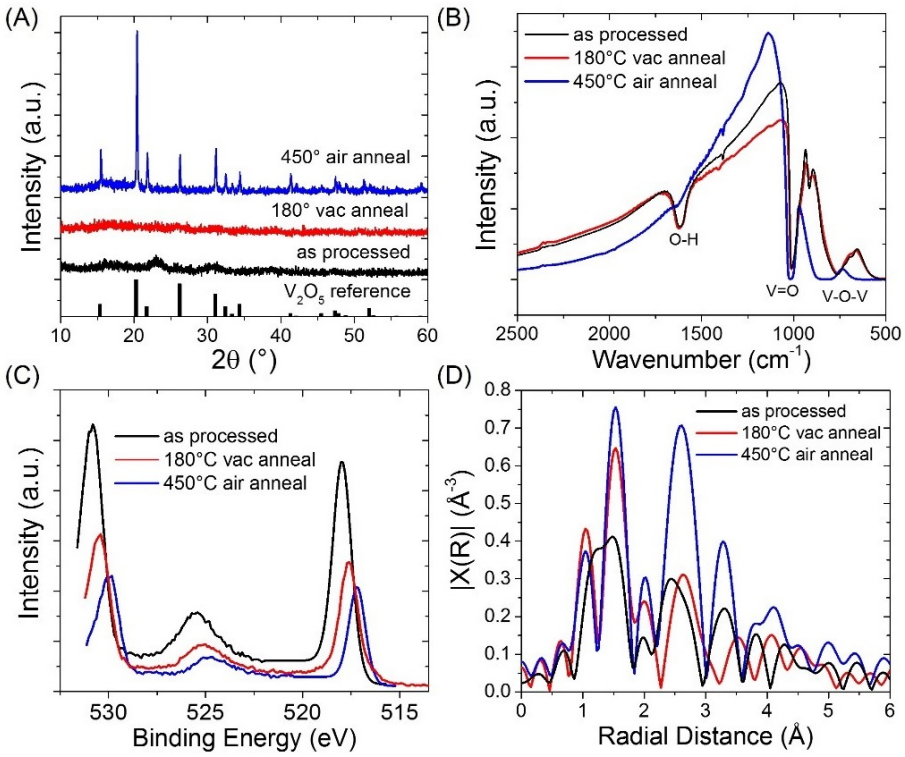

Figure 6.3: (a) XRD patterns, (b) FTIR spectra, (c) high-resolution XPS spectra, and (d) k^3-weighted Fourier transform of the V k-edge EXAFS of the V_2O_5 samples.

metric stretching mode of the terminal oxygen V=O bond is clearly observed at approximately 1012 cm^{-1} for all of the compounds. However, the same stretching vibration was shifted to a slightly higher value (1019 cm^{-1}) for the 450°C/air sample. For the as-processed and 180°C/vac samples, the peaks localized at 767 and 532 cm^{-1} are assigned to the 3-fold-coordinated oxygen asymmetric and symmetric stretching vibrations modes of V-O-V, respectively. The FTIR peak positions for all samples are reported in Table 6.2. The lack of long range crystallographic order in the samples thermally treated at lower temperatures leads to homogeneously disordered material, and is ultimately accountable for the wide distribution and shifting of peaks at lower wavenumber. The changes in the vibration modes can potentially be ascribed to the differences in the long range order of the V_2O_5 crystal structure. The absorption peak at 1615 cm^{-1} is assigned to the hydroxyl group (O-H) stemming from absorbed water,[214] and is also not detected in the fully crystallized material.

The incorporation of absorbed water may also account for some of the disparity amongst the vibration modes;[215, 216] water molecules incorporating themselves into the short-range order of the amorphous materials can effectively alter the ionic transport pathways.[217, 218] It has been demonstrated for $V_2O_5 \cdot nH_2O$ xerogel that the presence of water molecules can expand the interlayer distance which correspondingly enhances the intercalation capacity as a result.[219] This modification is usually detected by XRD where the (100) peak will shift from its standard value ($2\theta = 20.258°$) to a lower value ($2\theta = 8°$), but cannot be used in this investigation given the amorphous nature of the 180°C/vac sample. Consequently, such effects will lengthen the bond distance decrease the strength of the V=O bond while correspondingly strengthening the 3-fold-coordinated V-O-V bond, leading to the shift in the detected bond vibrations. These spectra match well with those for amorphous V_2O_5 previously reported in the literature.[214, 216, 220]

Table 6.2: FTIR peak position data for the as-processed, 180°C/vac annealed, and 450°C/air annealed V_2O_5 samples.

Peak assignment	Peak position(cm^{-1}) for:		
	as-processed	180°C/vac	450°C/air
O-H	1614.6	1620.9	1634.1
V=O	1012.8	1012.8	1015.9
	916.0	914.2	–
V-O-V	763.4	759.7	827.2

XPS was carried out on the samples prior to sodiation in order to gain more information on the chemical state of the vanadium species present and for additional phase identification. High-resolution scans, emphasizing the V2p and O1s peaks, and broad survey scans were collected for all samples, and are shown in Fig. 6.3c and Fig. 6.4, respectively. All materials were characterized as V_2O_5 with the only vanadium species present being V^{5+}. Shouldering on the higher binding energy side of all the O1s peaks indicates the presence of chemisorbed hydroxyl (-OH) groups or adsorbed carbon dioxide molecules in the electrochemically synthesized V_2O_5. The trends between peak position, peak spacing, and their

literature comparisons are shown graphically in Fig. 6.4 and in Table 6.3. The location of the

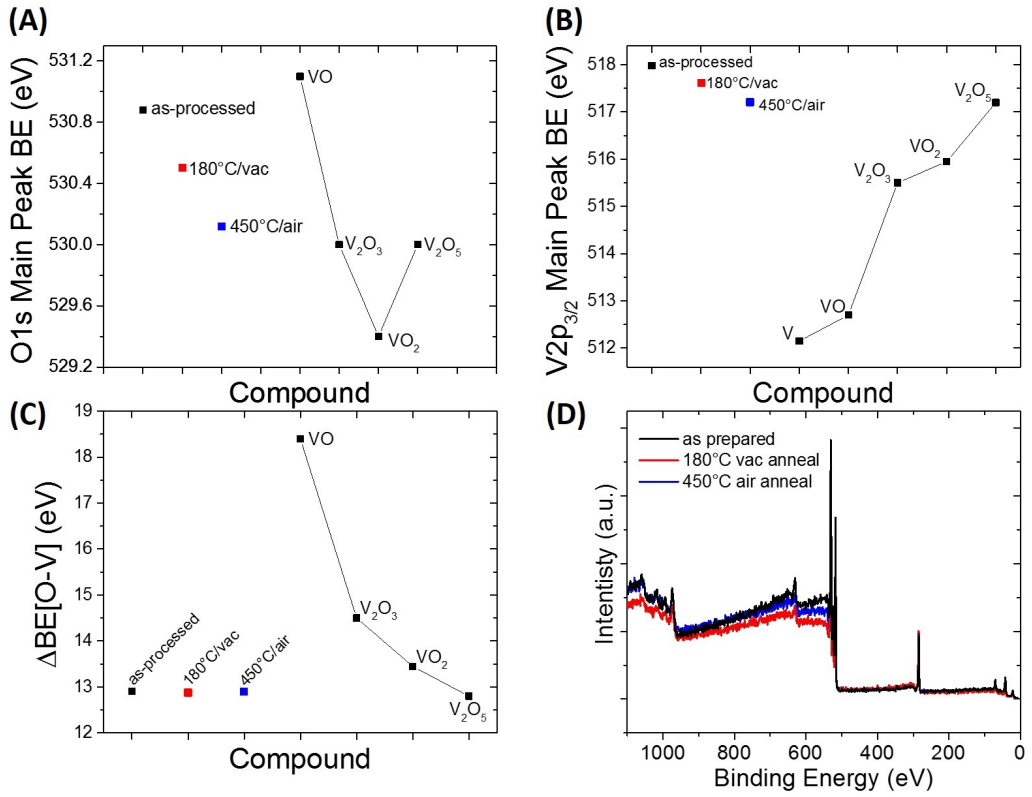

Figure 6.4: (a-c) High-resolution XPS O1s and V2p peak values and ΔBE[O-V] for the as-processed, 180°C/vac annealed, and 450°C/air annealed V_2O_5 samples compared to the, respectively, equivalent literature values for various vanadium oxide compounds. Literature values taken from [1].(d) Broad survey and XPS spectra of the as-processed, 180°C/vac annealed, and 450°C/air annealed V_2O_5 samples.

main O1s peak, attributed to lattice oxygen (O-V), is indicative that the material is V_2O_5, but the measured peak position diminishes with annealing temperature. The as-processed, 180°C/vac, and 450°C/air annealed specimens recorded O1s peak positions of 530.9, 530.5, and 530.1 eV, respectively, while the equivalent literature standard is typically taken to be 530.0 eV.[1] The adjusted $V2p_{3/2}$ peak binding energy was 518.0, 517.6, and 517.2 eV for the as-prepared, 180°C/vac, and 450°C/air specimens, respectively, which is consistent with literature reports for V_2O_5. As a whole, the $V2p_{3/2}$ and O1s peaks for the non-crystalline materials were slightly shifted to higher binding energies than expected, but overall peak-to-peak spacing was conserved. Slight shifts in the peak positions were attributed to the lack

of long-range order and the non-homogeneous chemical makeup of the structure. The V_2O_5 phase was confirmed by the spin-orbit splitting of approximately 7.5 eV between the $V2p_{3/2}$ and $V2p_{1/2}$ orbitals and the energy difference of 12.9 eV between the binding energy of the $V2p_{3/2}$ and O1s orbitals for all of the fabricated films, which is consistent with literature reports.[221, 222, 223]

Table 6.3: XPS peak fit values for the as-processed, 180°C/vac annealed, and 450°C/air annealed V_2O_5 samples.

Sample	Peak	Peak Location (eV)	ΔBE(O-V) (eV)
as-processed	O1s	530.9	12.9
	V2p	518.0	
180°C/vac	O1s	530.5	12.9
	V2p	517.6	
450°C/air	O1s	530.1	12.9
	V2p	517.2	

XAS was carried out in transmission mode at the Advanced Photon Source, sector 13ID-E and the data sets were processed using the IFFEFIT software package.[224] The normalized extended X-ray absorption fine structure (EXAFS) and V k-edge X-ray absorption near edge structure (XANES) plots are shown in Fig. 6.3d and Fig. 6.5, respectively. The pre-edge peak in the XANES spectra corresponds to the 1s to 3d electronic transition, for which the position and intensity are very responsive towards the crystal field symmetry surrounding the vanadium and the distortion of the local structure as it influences the degree of hybridization between the O2p and the V3d orbitals.[220] A decrease in the pre-edge peak intensity suggests an increase in the vanadyl V=O distance, which decreases the degree of distortion of the local structure and effectively increases the local symmetry within the VO_5 square pyramid.[225, 226] The absorption edge itself is associated with the 1s to 4p dipole transition. Comparison of the crystalline and amorphous absorption spectra further verifies that both thermally treated specimens are in fact V_2O_5.

The k^3-weighted Fourier transform of EXAFS can provide information on the coordination shell distance between atomic neighbors. The direct comparison of the crys-

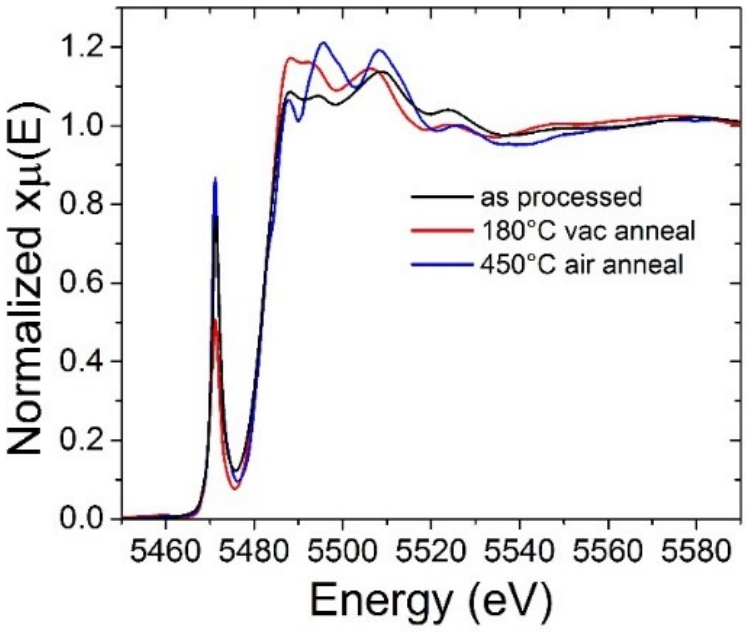

Figure 6.5: XANES of the V k-edge for the as-processed, 180°C/vac annealed, and 450°C/air annealed V_2O_5 samples.

talline and amorphous Fourier transforms, Fig. 6.3d, displays the radial structure functions for the central absorbing vanadium atom and highlights the variation in the local structures. The amplitude of the peaks for the 180°C/vac material is lower than that of the 450°C/air material, indicating a higher degree of structural disorder and diminished extending coordination.[227, 228] The experimental data for the crystalline material shows three well defined peaks at 1.50, 2.70, and 3.25 Å that derive from the V-O single scatter contribution (1st coordination sphere), V-V (2nd sphere), and V-V (3rd sphere). As expected, the intensity of these peaks drops with increasing coordination because of increased scattering events. The amorphous material shows similar first and second degree coordination, but drastic differences in the third. This is also expected provided that the amorphous structure lacks long range order and the third shell contains contributions from a large number of overlapping single as well as multiple-scattering contributions. Moreover, the 180°C/vac spectrum is extremely similar to others gathered for amorphous V_2O_5 presented

in the literature.[225] The manifestation of this diminished coordination would be a more open structure that would be conducive towards improved sodiation. Based on these results, it is probable that the majority of the water detected by TGA corresponds to surface adsorbed water. If anything, the water will add to the disorder between neighboring domains which could potentially expand pathways for Na-ion transport.

Transmission electron microscopy (TEM) was carried out in order to qualitatively compare the extent of crystallinity inherent to each sample. Fig. 6.6 displays the TEM images collected for the as-processed, 180°C/vac, and 450°C/air samples. The inset in each figure is the corresponding FFT pattern which can also be used to, more objectively, interpret the degree of crystallinity. The amorphous nature of the as-processed and 180°C/vac samples is noted, as revealed in Fig. 6.6(a & b). Moreover, the as-processed and 180°C/vac annealed samples have near similar trace amounts of crystallographic order as seen in the micrographs and diffuse diffraction spots. These findings, when paired with TGA, indicate that the low-temperature vacuum annealing process effectively maintains the non-crystalline, amorphous quality of the V_2O_5 material while removing surface absorbed water. The single crystallinity of the 450°C/air sample is evident, as noted by the atomic columns of the crystallographic lattice; the FFT pattern (Fig. 6.6c inset) shows clean V_2O_5 diffraction, attesting to the highly crystalline nature of the material. This characterization is also supported by the measured fringe interspacing of 3.34 Å that corresponds to the $d_{(001)}$ spacing and the distance between two (001) crystallographic planes of the orthorhombic V_2O_5 structure.

The energy-storage performance of the electrochemically deposited V_2O_5 was investigated as a Na-ion battery positive electrode material candidate using a half-cell configuration with sodium foil as the counter and reference electrode. However, prior to this the 450°C/air annealed V_2O_5 was tested as a Li-ion battery cathode in order to establish a baseline merit of performance. Lithium and sodium ion batteries function in an identical manner to one another, with the main differences being their reduction potential and electronegativity of the alkali element and ionic size. The 450°C/air annealed sample was cycled against Li/Li^+

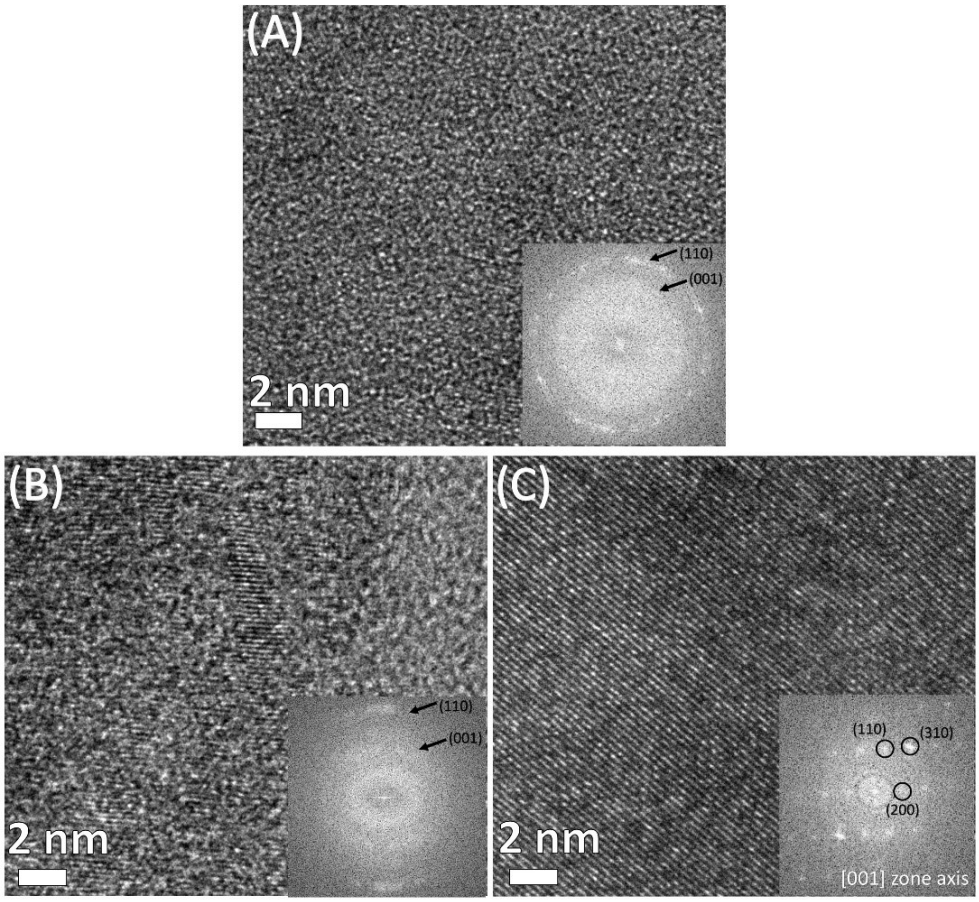

Figure 6.6: High-resolution TEM images of the (a) as-processed, (b) 180°C/vac annealed, and (c) 450°C/air annealed V_2O_5 samples. The inset in each figure is the corresponding FFT pattern for the displayed image. The deposited V_2O_5 films were exfoliated from their Ni-foil substrate following thermal treatment.

at a discharge rate of 44.7 mA g^{-1} (0.1 C) and within the voltage window of 3.8-1.5 V leading to the formation of $Li_3V_2O_5$, and the discharge profile is shown in Fig. 6.7. As expected, several discharge plateaus are clearly seen. The de/intercalation mechanism in crystalline materials is characteristically distinguished by plateaus in the discharge potential profile that indicate phase separation and transformation, and ultimately define the limiting values for the stability of each of the phases that evolve during the ionic de/intercalation process. The plateaus at 3.5, 2.9, and 2.4 V correspond to the ϵ/δ, δ/γ, and γ/ω phase transitions, respectively. While this material exhibits a high initial capacity of approximately 390 mA

h g^{-1}, the irreversible phase transition associated with the intercalation of a third Li^+ per V_2O_5 formula unit results in severe capacity degradation upon cycling.

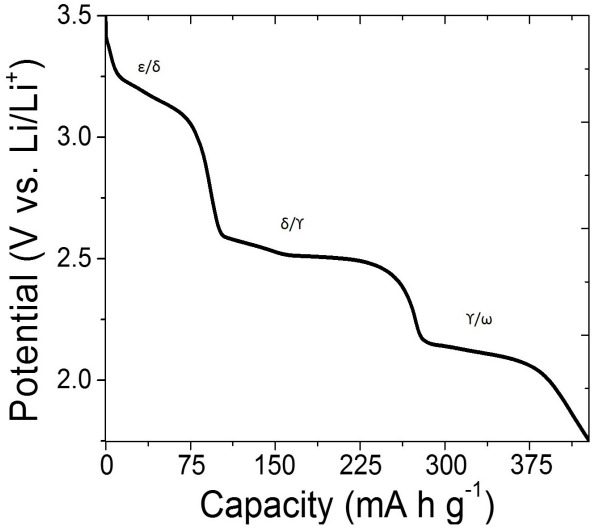

Figure 6.7: Initial discharge voltage profile curves for the crystalline (450°C/air) V_2O_5 cycled against Li/Li^+ at 45 mA g^{-1} current density (0.1 C)

Following this baseline test, the 180°C/vac and 450°C/air annealed were cycled against Na/Na^+ at 23.6 mA g^{-1} corresponding to fully cycled $Na_2V_2O_5$ products, the results of which are shown in Fig. 6.8. When cycled against Na/Na^+, the crystalline 450°C/air annealed V_2O_5 electrode demonstrated a moderately flat discharge plateau at approximately 2.5 V and a discharge capacity of approximately 120 mA h g^{-1} which in turn demonstrates that one Na^+ ion was successfully intercalated for each vanadium. Use of the same solvent and ion containing salt for the electrolyte of the different systems (Na- and Li-ion) holds the transporting ionic species solely accountable for the apparent differences in the discharge profile and capacity. Contrary to its crystalline form, the 180°C vacuum annealed material featured a smooth discharge profile concurrent with the evolution of sodium-ion incorporation culminating in a discharge capacity of approximately 241 mA h g^{-1}. The energy density, or area under the discharge curve, of the amorphous material (625.3 Wh kg^{-1}) was also markedly greater than that of the crystalline material (282.6 Wh kg^{-1}).

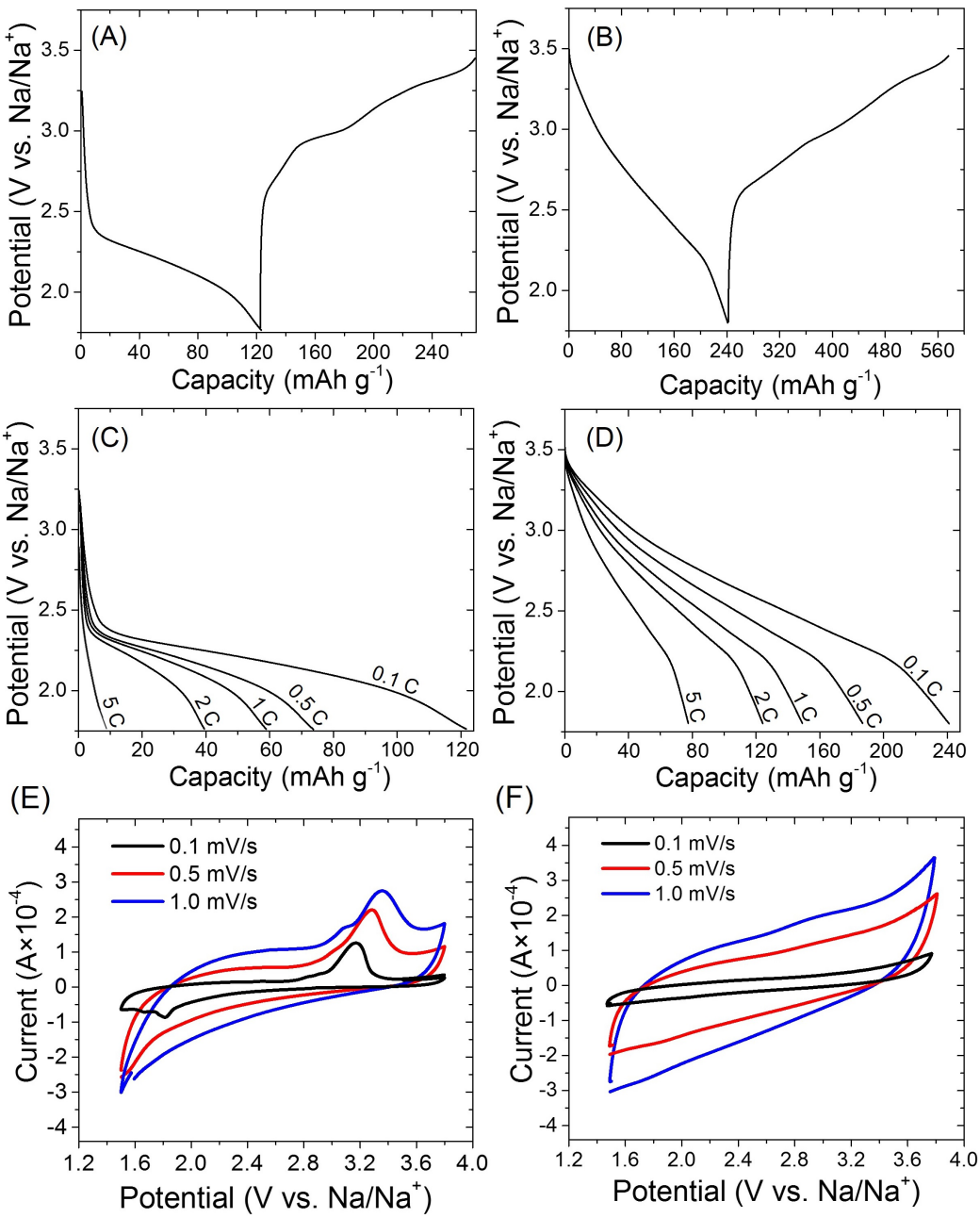

Figure 6.8: Initial charge-discharge curves for the (a) crystalline (450°C/air) and (b) amorphous (180°C/vac) V_2O_5 against Na/Na^+ at a current density of 23.6 mA g^{-1} (0.1 C); the rate capability of the (c) crystalline and (d) amorphous V_2O_5 when discharged at current densities ranging from 23.6 (0.1 C) to 1170 mA g^{-1} (5 C). Cyclic voltammograms at various scan rates for the (e) crystalline and (f) amorphous V_2O_5.

Since their introduction, crystalline transition metal oxides have been regarded as very attractive candidates for intercalation based storage applications because of their open, yet ordered structures that offer ample sites for accommodating guest species intercalation.[107, 229] Moreover, there are multiple Faradic charge storage mechanisms that can simultaneously contribute to the overall charge storage. For layered oxides, these mechanisms either occur at the particle surface or within the interlayer spacing of the material. Surface storage is pseudo-capacitive in nature, and can manifest itself *via* the monolayer adsorption of ions at the electrode surface or through surface redox reactions. Intercalation based storage mechanisms, on the other hand, ensue in one of two ways - with or without an accompanying material phase change. Ion intercalation that does not result in a phase change is a characteristic typically associated with capacitors, while battery materials often experience phase change(s). Redox based surface reaction and non-phase change intercalation are analogous to one another in that there are pseudo-capacitive effects where ion adsorption is associated with the reduction of metal ions located at either the surface or along the interlayer lattice planes, respectively.[230]

Previous studies have shown that the character of the discharge profile shows a strong dependence on the particle size and degree of order of the electro-active species.[231, 232, 233] More specifically, these factors can be independently correlated to the sloped discharge profile seen here (Fig. 6.8).[231, 232, 233] For nanoparticles below a critical size, pseudo-capacitive behavior stemming from the fast and reversible Faradaic reactions occurring at or near the particle surface culminates in a sloped discharge profile occurring over a wide potential window.[234, 235] Contrastingly, disordering has been shown to lead to sloped potential profiles given that there is a wider distribution of intercalation site energies in a disordered material; these discrepancies in the intercalation site energy may be negated by diminished interaction between the intercalation species and a distribution of the activation barrier varying with the local atomic environment, meaning that the Na-ion diffusivity is more independent of the Na-ion concentration.[202]

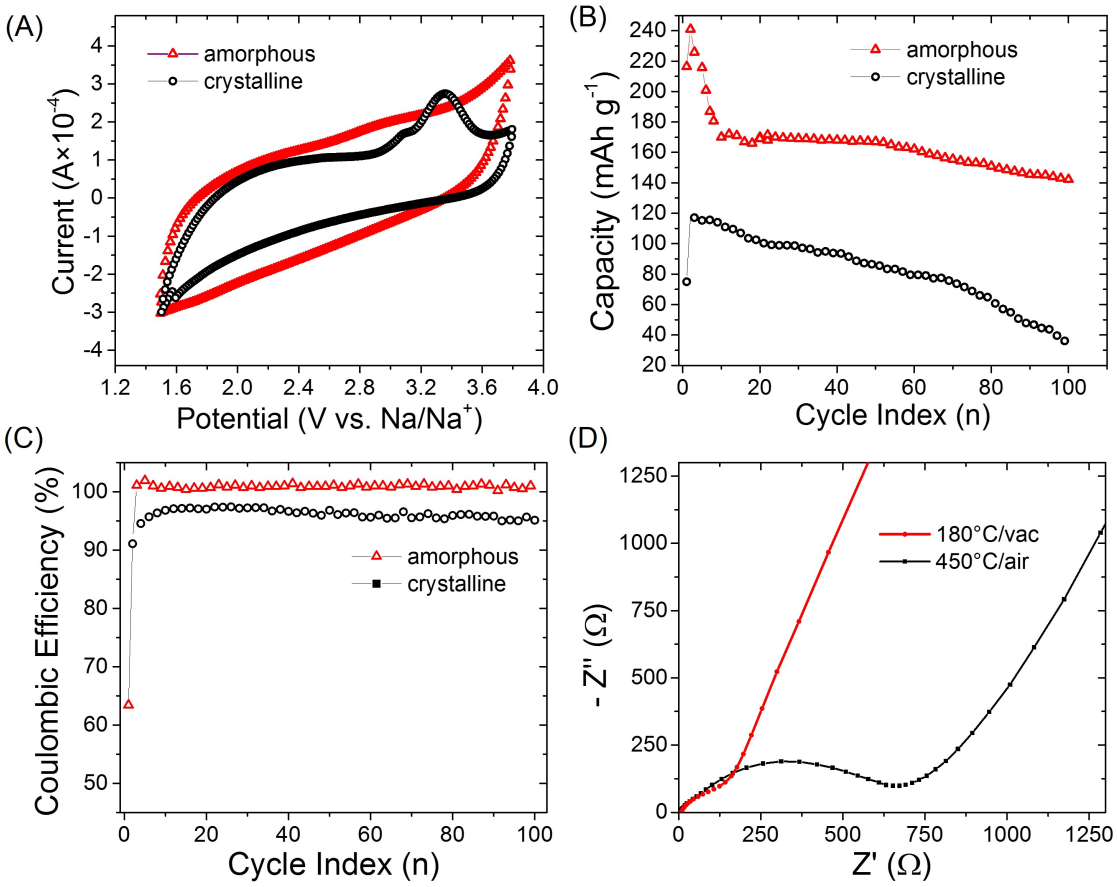

Figure 6.9: (a) Cyclic voltammograms for the amorphous (180°C/vac) and crystalline (450°C/air) V_2O_5 at 1.0 mV s^{-1}; (b) the cycle stability (c) and Coulombic efficiency gathered at a current density of 23.6 mA g^{-1}. (d) Nyquist plots of the amorphous (180°C/vac annealed) and crystalline (450°C/air annealed) V_2O_5 samples from 100 kHz to 10 mHz with an AC amplitude of 5.0 mV.

Based off of previous studies focusing on amorphous materials for Li-ion cells, it is proposed that there was a combination of sodium-ion intercalation and surface adherence to the amorphous V_2O_5 particles, which eventually led to superior discharge capacity, energy density, and cycle-life performance when compared to its corresponding crystalline material cycled under analogous conditions.[236, 237] For amorphous nanomaterials, it is possible that both the nano-based pseudo-capacitive and amorphous based homogeneous disorder effects can contribute towards the sloped discharge profile. It may be possible to distinguish between these two effects in amorphous materials by synthesizing crystalline nanoparticles of equivalent morphology over a decrementing size range and monitoring CV for the attenuation of any redox peaks and the adoption of a rectangular CV profile, which is a characteristic trait of pseudo-capacitive storage. Regardless, the obtained results indicate that Na-ion insertion/extraction in amorphous V_2O_5 is not accompanied by an abrupt phase change or an alteration of the structure as seen in its crystalline equivalent; this attribute ultimately supports improved cycling stability and makes it possible for the potential to serve as a direct read of the depth of discharge.

CV was accordingly performed to investigate the redox processes at play for V_2O_5 in the amorphous and crystalline states, the results of which are shown in Fig. 6.8d and 6.8f, and directly compared in Fig. 6.9a. The test cells were successively cycled at 0.1, 0.5, and 1.0 mV s^{-1} and within a voltage window of 3.8-1.5 V vs. Na/Na^+. The amorphous material does not exhibit any peaks over the potential range, but the voltammetric response marginally scales with the potential and the current is greater than that of the crystalline material; such CV performance is typical of amorphous materials because of the broad energy distribution associated with the sodiation sites, occupied through a percolation mechanism, that gives way to a wide distribution of the redox events.[46] Conversely, the CV scans for the crystalline V_2O_5 show broad anodic peaks ranging between 3.2 and 3.3 V. There is also an initial cathodic peak at approximately 1.8 V that becomes attenuated upon scanning at higher rates. When paired with the discharge profiles, these results clearly highlight how the

structural differences between the amorphous and crystalline phases can directly impact the Faradaic processes at play.

The cycle stability of the half-cells was examined using a voltage window of 3.8-1.5 V vs. Na/Na^+ and a current density of 23.6 mA g^{-1} (0.1 C rate), the results of which are shown in Fig. 6.9b. The amorphous V_2O_5 material exhibited an initial discharge capacity of 216 mA h g^{-1}, but that increased to 241 mA h g^{-1} with the second cycle. However, there was a drop in capacity following this peak which eventually stabilized at approximately 160 mA h g^{-1}. Similarly, the crystalline V_2O_5 material showed an increase in capacity following the initial cycle. The overall capacity of this material peaked in the second cycle at 120 mA h g^{-1} and then experienced moderate but steady capacity degradation throughout the cycling process, with an increase in the degradation rate towards the end of cycling. One would expect these results to be attributed to differences in pore characteristics as induced by the different annealing profiles; however, the differences in average pore size and overall pore volume were considered to be negligible. These findings were based on the BET results which indicated that the 180°C/vac annealed material had only slightly larger pores and overall pore volume than the 450°C/air annealed material with values of 3.22 nm and 0.060 cm^3 g^{-1} compared to 3.19 nm and 0.054 cm^3 g^{-1}, respectively. Thus, given this information along with the similarity in morphology, it can be surmised that the disparity in electrochemical performance is directly correlated to the differences in crystallinity, or the apparent lack thereof, and the associated ionic insertion/reaction processes. The presence of surface-adsorbed or short-range crystalline water in the amorphous V_2O_5 could also be the driving difference in performance. It is worth mentioning that when reproduced the capacity values can vary slightly given the non-monotonous cycle stability behavior, but the overall trends hold true.

EIS was carried out on crystalline and amorphous V_2O_5 with frequency ranging from 100 kHz to 10 mHz and the AC amplitude set at 5.0 mV, and are shown in Fig. 6.9d. The semicircle at the high frequency region relates to the combined process of the surface

film (R_{sf}) and the charge transfer resistance (R_{ct}). The calculated R_{sf+ct} values for the amorphous and crystalline materials were 26.4 and 38.1 kΩ, respectively. Based on these findings, it is clear that the amorphous material has improved electrical conductivity. In addition to these results, the discharge rate capability of the amorphous 180°C/vac annealed material was examined. When discharged at current densities of 23.6, 118, 236, 472, and 1180 mA g^{-1} the amorphous V_2O_5 demonstrated capacity values of 241, 186, 149, 124, and 78 mA h g^{-1}, respectively (Fig. 6.9d). The high capacity of the amorphous V_2O_5 compares well with the theoretical capacity (236 mA h g^{-1}) leading to the formation of $Na_2V_2O_5$, in which each unit cell can accommodate approximately two sodium ions. The merger of the cycling stability and rate capability results indicate that the amorphous V_2O_5 structure can successfully sustain the intercalation of Na^+ ions over a wide concentration range.

Provided these findings, the use of amorphous nanoscale V_2O_5 with short-range order has proven to be beneficial to the performance of Na-ion battery, at least when compared to its crystalline counterpart, because of the low entropic energy associated with the ordering of intercalated atoms and a more open framework. The less structured and more open channels reduce the diffusion barrier for sodium ions to transition between the intercalation or surface-reaction sites leading to high rate capability and power density. The amorphous surface may also make it possible for the Na^+ ion to more easily penetrate the crystal, thereby diffusing deeper into the material. These effects can lead to a larger capacity at higher current densities since more of the electro-active material can be infiltrated more rapidly because of the larger charge diffusion depth. Moreover, the absence of a phase transformation upon Na^+ incorporation can potentially be ascribed to an intercalation pseudo-capacitive behavior over a wide range of compositions that leads to a highly improved and reversible cycling performance. The pseudo-capacitive behavior may also play a role in maximizing the electrostatic attraction of Na^+ ions into the V_2O_5 matrix. Recent studies have also shown that ion diffusion in disordered materials can be facile because the percolation of certain diffusion channels become active in disordered structures, effectively opening a new avenue for

the design of disordered electrode materials with high capacity and energy density.[202] These effects work to improve charge and ionic transfer, respectively, at the electrode/electrolyte interface during the sodiation process, yielding a positive electrode material for sodium-ion battery application. This in turn can lead to a larger capacity at higher current densities since more of the electro-active material can be infiltrated more rapidly, and ultimately support the development and optimization of amorphous electrode materials for future sodium-ion battery application.

6.4 Conclusions

In summary, amorphous V_2O_5 electrodes have unambiguously demonstrated that their sodiation capacity, storage energy density, and cyclic stability are far better than their crystalline counterpart. The amorphous V_2O_5 electrodes with short range order and a more open framework demonstrated a discharge capacity of 241 mA h g^{-1} when examined as positive electrode material for Na-ion battery application while its crystalline counterpart only had a capacity of 120 mA h g^{-1}. The significant difference between the crystalline and amorphous phases arises from the fast Faradaic reactions which occur in amorphous V_2O_5 stemming from a percolated diffusion network, and potentially inducing an additional pseudo-capacitive storage contribution. Moreover, because diffusion now occurs through isotropic percolation and is not confined along a preferential pathway, the overall charging/discharging rates are much faster as evidenced by the 78 mA h g^{-1} capacity at a current density of 1180 mA g^{-1}. Provided these results, the investigation of amorphous electrode materials is expected to be a promising development worthy of further research towards yielding high energy density and cycle-life rechargeable sodium batteries.

Chapter 7

Elucidating the Role of Defects in Sodium Vanadium Oxide for use as Sodium Ion Battery Electrode

$Na_xV_3O_8$ was synthesized *via* a wet chemical decomposition route involving the reduction of V_2O_5 in oxalic acid and $NaNO_3$ followed by calcination. It was possible to control the sodium composition in the final product by adjusting the amount of sodium precursor added during synthesis. It was determined that deficient and surplus sodium contents, with respect to the ideal stoichiometry, are accommodated by the generation of oxygen vacancies and partial transition metal reduction, or cation disordering, respectively. When examined as NIB electrode material, the superior performance of the cation disordered material was clear, especially at higher current discharge densities. The formation of oxygen vacancies initially seemed promising, but was coupled with stability issues and capacity fading with further cycling. The disparity in electrochemical performance was attributed to variations in the electronic distribution as promoted through Na-ion interactions and the direct influence of such on the oxygen framework (sub-lattice); these factors were determined to have significant impact on the migration energy and diffusion barriers.

7.1 Introduction

The proliferation of electrical energy demand has driven the rapid progression of improved technologies related to energy distribution and storage. However, energy storage materials and devices have come to be viewed as a crux impeding advanced device development. Lithium-ion (Li-ion) batteries are a mature and robust technology because of their high energy density and portability. Despite their success in such application, Li-ion batteries (LIBs) are a poorly suited choice for large-scale energy storage applications because of their high cost, associated with resource scarcity, as well as safety concerns. Conversely, sodium-ion (Na-ion) batteries have been gaining considerable traction as a realistic candidate for large-scale energy storage applications over the past several years.

Na-ion batteries (NIB) are attractive because sodium resources are seemingly inexhaustible as well as ubiquitous, and therefore cost considerably less (by a factor of roughly 30-40 times) than lithium; additionally, sodium does not undergo an alloying reaction with aluminum at low voltage, as is the case with lithium, meaning that aluminum can replace copper as the anodic current collector which equates to an overall cell cost savings of 2%.[14, 238] The lower operating voltage of Na-ion cells results in enhanced stability of the non-aqueous electrolyte, but also manifests itself in lower energy density. The majority of the proposed electrode materials for Na-ion battery show similar or slightly lower specic capacity and redox potential than when used in Li-ion cells. Moreover, the accommodation of sodium in traditional host materials is difficult because the ionic radius and reduction potential of sodium are strikingly larger than that of lithium. Therefore, the de/sodiation process induces large distortions in the host lattice that ultimately lead to pulverization of the electrode and the impending failure of the cell.[13]

The majority of investigations, to date, examining Na-ion battery cathodes have focused on intercalation based materials, particularly layered transition metal oxides. The overall process of electrochemical intercalation can be broken down into three simultaneous and sequential processes: (i) redox reactions at the electrode-electrolyte interface, (ii) nucleation

and growth of the new interfacial phase, and (*iii*) charge and mass transfer. Within the layered transition metal oxide paradigm, vanadium oxide is an attractive multifunctional material used for widespread application in various fields such as catalysis and energy storage. Of the many stoichiometries and polymorphs, sodium trivanadate, $Na_xV_3O_8$, is a propitious positive electrode material for alkali-ion insertion because of its low cost, easy synthesis, and good electrochemical performance. This oxide has a layered structure, with the anionic V_3O_8 layers held together by alkali-ions, typically Li^+ or Na^+ which have respective theoretical capacities of 372 and 352 mA h g^{-1} when cycled against their constituent metal.

Simple defect modification is a powerful means towards improving material intercalation capabilities that has been receiving considerable interest lately as it can directly alter both chemical and structural characteristics; techniques of note include cationic disordering, amorphization, doping, partial cation reduction, and manipulation of intrinsic defects (*i.e.* oxygen vacancies, denoted $V_O^{\circ\circ}$ in the Kroger-Vink notation).[115, 202, 239, 240, 241, 242, 243, 244, 245] Surface defects can directly impact alkali-ion intercalation by shifting the thermodynamics and improving kinetics.[19] The presence of surface defects increases the surface energy and can potentially serve as nucleation sites that facilitate the electrochemical phase transition. Surface-reaction-limited (SRL) dynamics predict the phase boundary extends from surface to surface along planes of fast ionic diffusion where defects or facet edges can act as nucleation sites.[246] Such results have been verified experimentally, where defects have been reported to promote the phase transition of TiO_2 by providing low energy mass transport routes during the phase transition process.[247, 248] Defects may also reduce the stress and the electrostatic repulsion between adjacent oxygen layers, which can directly alter the migration energy and diffusion barriers the alkali-ion must overcome during intercalation.[249]

Disordering has been shown to increase the solid solution behavior, reduce the two-phase transformation domains, lower the alkali-ion extraction energy, and modify the diffusion/transport properties during the de/intercalation processes;[202, 250, 251, 252, 253, 254]

the use of amorphous structures is proposed to work in a similar manner while providing a more open framework for ion migration.[16, 18, 203, 204, 239] Cation disorder involves the intermixing between the alkali-ion and the transition metal sub-lattice, and is more likely to exist in systems where there are different redox sites, be it in the form of several transition metal elements or a single multivalent element. Doping is often used as a means to achieve partial cation reduction, although the later can be successfully done without such means, to introduce mixed valence states in the transition metal and, thus, tune the electronic transport properties of the material.[255] Mixed conductivity is necessary, both electronic and ionic, at the atomic scale for charge neutrality preservation during alkali-ion transport, where the chemical diffusion coefficient is ultimately rate-limited by the slower of the two processes. The introduction of oxygen vacancies is well known for increasing conductivity in oxide materials.[256, 257] Supervalent metal doping in $LiFePO_4$ was shown to increase the electronic conductivity of by a factor of 10^8, effectively overcoming the low intrinsic limitations of the material.[258]

Several studies have been devoted to examining the effects of lithium nonstoichiometry in LIB electrodes, particularly for $LiCoO_2$ where such effects are accommodated by oxygen vacancies that can also be accompanied with either cation mixing and/or a perturbation of the oxygen stacking layers. Accordingly, the local environment of some cobalt ions can be modified by the presence of the oxygen vacancies. The structure of these lithium over-stoichiometric compounds makes them more stable against the (de)lithiation process and is a beneficial approach towards preventing structural distortion, and thus show potential for LIB electrode development.[259, 260] Notwithstanding, the recent rejuvenation in NIB research activity has revealed, if nothing else, that analogous materials can behave substantially different than expected based off their prior LIB performance.[261] There have been minimal reports concerning the role of defects on NIB electrode materials and the potential impact they may have on the overall electrochemical performance.[262, 263] Towards these ends, we propose synthesizing $Na_xV_3O_8$ with oxygen vacancies and partial cation reduction

by adjusting the sodium stoichiometry to induce the formation of such defects. Structural as well as chemical analyses were conducted to verify the presence of these defects, and the electrochemical performance of the corresponding materials was evaluated as positive electrode material for NIB application.

7.2 Experimental Procedure

7.2.1 Material Synthesis

All chemicals were of analytical grade and were used as received without further purification. Approximately 0.90 g V_2O_5 (99.8%, Alfa Aesar) and 1.33 g oxalic acid (Sigma Aldrich) were incorporated into 40 mL of deionized (DI) water and magnetically stirred at room temperature until the formation of a clear blue solution was noted, indicating the formation of vanadium oxalate. The reaction can be expressed as follows:

$$V_2O_5 + 3H_2C_2O_4 \longrightarrow 2VOC_2O_4 + 2CO_2 + 3H_2O$$

Subsequently, various amounts of $NaNO_3$ (99.995%, Aldrich) were added into the VOC_2O_4 solutions under stirring for 1 h in order to control the sodium content. Three stoichiometric quantities of $NaNO_3$ corresponding to sodium ratios of 0.75, 1.0, and 1.25, where 1.0 is the ideal stoichiometry ($Na_{1.25}V_3O_8$), were then added. The solution was dried at 80°C before calcination at 400°C under ambient for 3 h. The obtained materials were designated as deficient ($Na_{1.25x}V_3O_8$, $x < 0$), ideal ($Na_{1.25x}V_3O_8$, $x = 1$), and excessive ($Na_{1.25x}V_3O_8$, $x > 1$) as based on their stoichiometric sodium concentration, respectively.

7.2.2 Characterization

Microscopy investigations were carried out using a FEI Sirion scanning electron microscope (SEM). The nitrogen sorption was performed using a Quantachrome NOVA 4200e. The specific surface area, micropore, and mesopore volumes were determined using multipoint Brunauer-Emmett-Teller (BET), t-method, and Barrett-Joyner-Halenda (BJH) desorption

analyses, respectively. Thermogravimetric analysis (TGA) was conducted from room temperature to 550°C (PerkinElmer TGA 7) under nitrogen flow at a heating rate of 5°C min^{-1}. The phase and crystallite size of the calcined sodium vanadium oxides were studied using X-ray diffraction (XRD, D8 Bruker X-ray diffractometer) with Cu-Kα radiation over the range of 10° to 70° (2θ), a step size of 0.02°, and an exposure time of 10 s. The accelerating voltage and current were 40 kV and 40 mA, respectively. The corresponding Rietveld refinement for each pattern was carried out using the GSAS package.[264] The intensities of all the spectra are normalized to the highest intensity peak. Infrared absorption spectra were recorded using a Perkin Elmer 1640 Fourier Transform Infrared (FTIR) Spectrophotometer with ATR. X-ray photoelectron spectroscopy (XPS) was completed using a Surface Science Instruments S-probe spectrometer. The X-ray spot size was 800 × 800 μm and the take-off angle was 55°, corresponding to a sampling depth of approximately 50-70 Å. XPS data analysis was carried out using the Service Physics ESCA 2000-A analysis program (Service Physics, Bend, OR).

7.2.3 Electrochemical Analysis

An electrode slurry was prepared by mixing the synthesized $Na_xV_3O_8$ powders, carbon black (Cabot Vulcan XC72R), and polyvinylidene fluoride (PVDF, MTI) binder dispersed in a N-Methyl-2-pyrrolidone (NMP, Alfa Aesar) solution at a respective weight ratio of 80:12:08. The slurry was spread onto aluminum foil (99.3%, MTI) and dried in a vacuum oven at 80°C overnight prior to coin-cell assembly. For electrochemical analysis, 2032 half-cells (Hoshen) were assembled in a glove box (Mbraun) filled with high purity argon. Metallic sodium (Sigma Aldrich), 1 M $NaClO_4$ (98%, Sigma Aldrich) in ethylene carbonate (BASF)/propylene carbonate (anhydrous 99.7%, Sigma Aldrich) (1:1 vol.), and Whatman GF/A glass microfiber filter were used as the counter/reference electrode, electrolyte, and separator, respectively. Cyclic voltammetry (CV) was completed using an electrochemical analyzer (CH Instruments, Model 605C) in the voltage range of 4.0-1.5 V (vs. Na/Na^+) at scan rates ranging from 0.01

to 10.0 mV s^{-1}. The current density and cycle stability performance of the electrodes were evaluated using a BT-2000 Arbin Battery Tester operating at room temperature. The half-cells were tested within the voltage range of 4.0-1.5 V vs. Na/Na^+ at various charging rates based on the weight of the active material alone, and assuming a 1C current density of 350 mA g^{-1} corresponding to the total accommodation of four sodium ions per $[V_3O_8]$ formula unit.

7.3 Results and Discussion

Sodium trivanadate, $Na_xV_3O_8$, is a propitious positive electrode material for alkali-ion insertion because of its low cost, easy synthesis, and good electrochemical performance. This oxide has a layered structure, with the anionic V_3O_8 layers held together by alkali-ions, typically Li^+ or Na^+, distributed over two crystallographically independent sites - the inter-layer octahedral as well as tetrahedral (but with lessened occupancy).[265, 266] The V_3O_8 framework is comprised of two structural units, namely double chains of edge-sharing VO_6 octahedra and double chains of edge-sharing trigonal bi-pyramids. These chains are linked by corner-shared oxygen that effectively form a continuously puckered sheet of VO_6 octahedra that comprise the stacked V_3O_8 strands. Sodium ions are situated between these quasi layers and form layers along the crystallographic [100] direction and double layers along the [001] direction. In this manner, the positively charged sodium ions electrostatically hold together the $[V_3O_8]^-$ strands. Additionally, there are several distorted octahedra that share faces with tetrahedra that form a two-dimensional interlinked tetrahedral-octahedral network that supports Na-ion transport between layers. The sodium ions have the inclination to serve as pillar cations by stabilizing the structure against volumetric changes during the (de)insertion processes of guest-ions at the vacant tetrahedral sites. There are six tetrahedral sites available per unit cell, in which excess sodium may be accommodated. Larger cations typically induce larger interlayer spacing values which can increase the diffusion rate

and improve the (dis)charge kinetics of the material, and is evidenced by the higher Li-ion insertion ability of $Na_xV_3O_8$ than that in isostructural $Li_xV_3O_8$.[266, 267] The structure can be likened to an analogue of the barnesite or metahewettite groups.[268, 269, 270, 271, 272] The chemical decomposition synthesis procedure utilized in this investigation allowed for the

Table 7.1: Physical properties of $Na_xV_3O_8$ products with deficient, ideal, and excess sodium stoichiometry.

Sample	Water (wt%)	BET Surface Area (m^2 g^{-1})	BJH Pore Size (nm)	Na content (at%) Calculated	EDX	XPS Na:V ratio Ideal	Average
Na-deficient	0.70	8.93	3.18	6.96	6.87	0.32	0.31
Na-ideal	0.48	11.41	3.18	9.28	9.06	0.42	0.38
Na-excess	0.26	13.42	3.20	11.60	10.30	0.52	0.49

direct control, within certain means, of the sodium content. Thus, by adjusting the amount of $NaNO_3$ precursor added to the VOC_2O_4 solution it was possible to attain $Na_xV_3O_8$ products with deficient, ideal, and excess sodium stoichiometry. A moderately low calcination temperature (400°C) was employed in order to preserve the purity and structural integrity of the material. When calcined at too high of temperature (> 525°C) a NaV_6O_{15} secondary phase forms, as determined through Rietveld refinement, that exhibits markedly lower kinetics towards sodium ions.[211] As previously mentioned, sodium plays a signicant role in stabilizing the interlayer structure, and the implementation of a high temperature calcination profile to affect hydration level can result in collapse of the interlayer structure.[273]

TGA was performed to verify that sodium content deficiency was not compensated by hydration or hydrogenation, as was the case for $Na_xV_2O_5{\cdot}nH_2O$ where the water content was found to be inversely proportional to the sodium level.[273] The deficient, ideal, and excess Na samples were revealed to have considerably low water contents of 0.70, 0.48, and 0.26%, substantiating that sodium level manipulation was not compensated through a secondary mechanism (shown numerically in Table 7.1 and graphically in Fig. 7.1). Nitrogen adsorption-desorption isotherms were collected in order to evaluate the surface area and pore

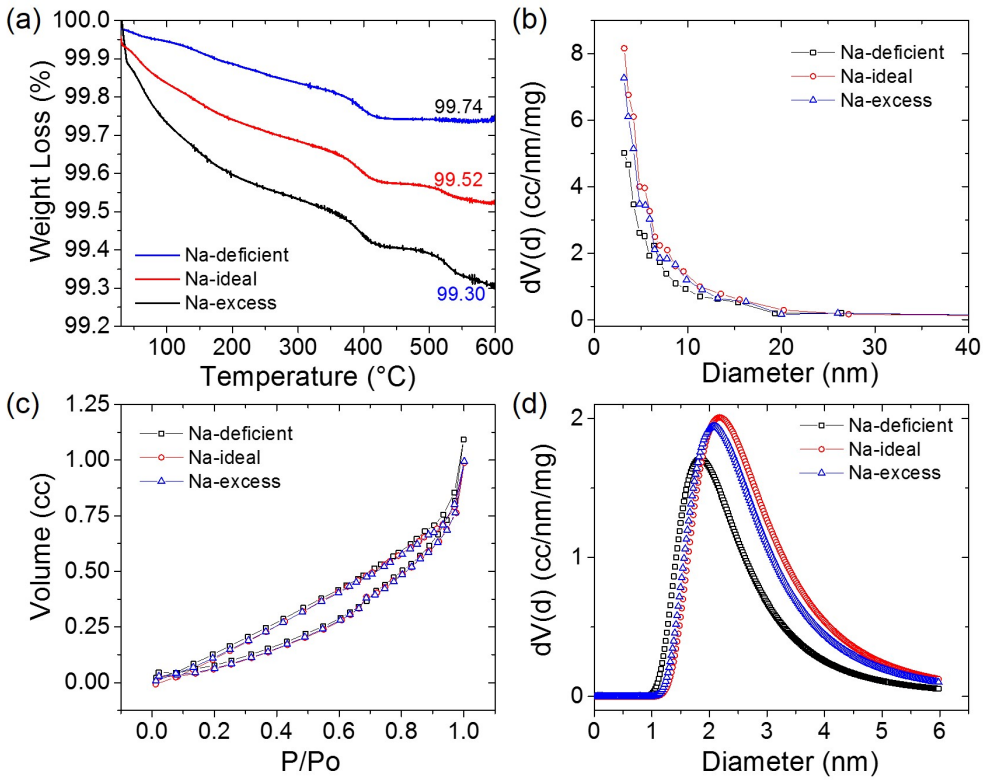

Figure 7.1: TGA and BET results for the $Na_xV_3O_8$ products with various Na-content.

characteristics. The BJH pore size distribution obtained from the adsorption-desorption isotherms suggests that the $Na_xV_3O_8$ samples contain broadly distributed pores with sizes below 15 nm, as listed in Table 7.1 and displayed in Fig. 7.1, and the majority of which are in the 2-5 nm size range. The BET specific surface area was approximated to be 8.9, 11.4, and 13.4 $m^2\ g^{-1}$ for the deficient, ideal, and excess Na samples which are reasonable values for materials containing pores on the aforementioned scale. The moderate surface area of the prepared $Na_xV_3O_8$ materials ensures short alkali-ion diffusion distances, and therefore holds the potential for enhanced electrochemical performance.

The morphology of the $Na_xV_3O_8$ compounds following calcination was observed by SEM, the micrographs of which are shown in Fig. 7.2(a-c). Comparison of the different samples demonstrates the profound effects that Na-content can have on morphology, homogeneity, and particle size distribution. The resulting particle morphology seems to shift from elon-

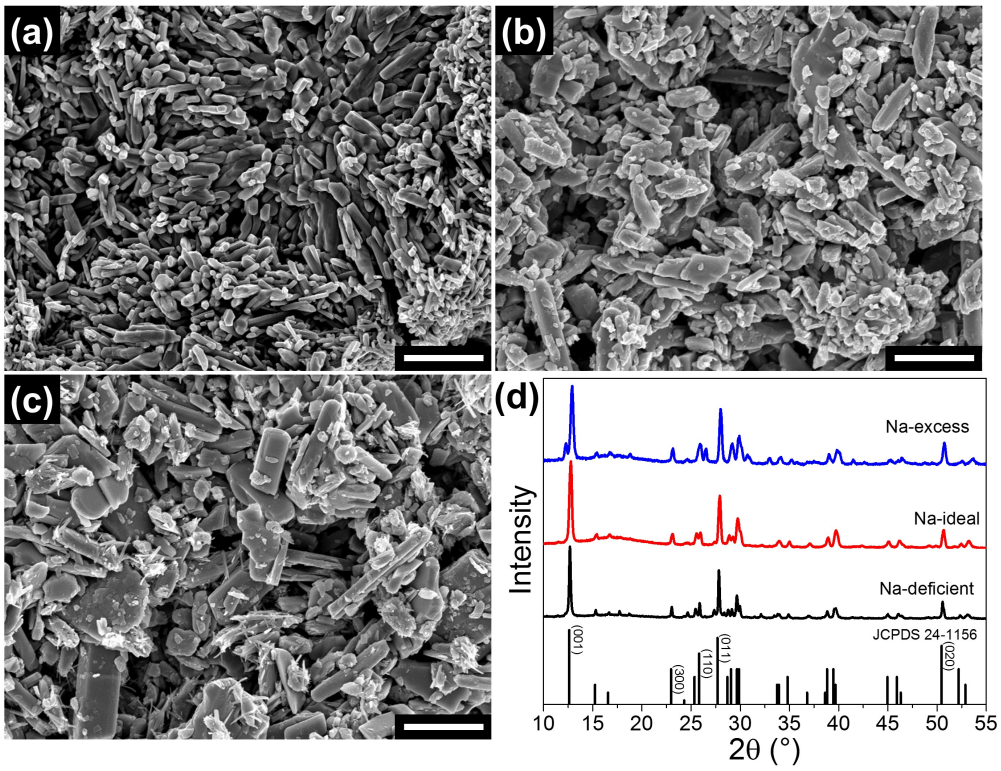

Figure 7.2: SEM micrographs of the $Na_xV_3O_8$ products with (a) deficient, (b) ideal, and (c) excess sodium stoichiometry where the scale bar in each image is equivalent to 2 μm; (d) normalized XRD patterns.

gated nanoparticles with approximate width and thickness of 800 and 300 nm, respectively, to 900 nm long and 60 nm wide nanowires with increasing Na-content; correspondingly, the average particle size also decreases. It should be noted that the ideal and excess sodium samples have a wider dispersion of particle morphology, where the elongated nanoparticle morphology is primarily maintained. The Na-deficient material (Fig. 7.2a) has noticeable striations running along the edges that are apparent in the higher magnification images and are somewhat present in the images corresponding to the materials with higher Na-content, perhaps providing insight into the nanowire formation mechanism.

Quantitative elemental analysis was carried out using energy-dispersive X-ray spectroscopy (EDS), the results of which are tabulated and compared with their ideal values in Table 7.1. The experimentally determined sodium contents match incredibly well the

expected values based off of precursor quantities used during synthesis. These sodium compositions are accommodated by the formation of oxygen vacancies and partial transition metal reduction for the deficient and surplus sodium compositions, respectively; the vanadium valency will be verified by XPS. These suppositions are substantiated by previous studies involving overstoichiometric Li_xCoO_2 samples, where it was deduced that the charge imbalance resulting from excess lithium is compensated by oxygen vacancies;[274] however, structural and electrostatic considerations should not be as overly influential in this system considering the *d*-electron configurations, affecting the formal valence state and covalent bonding interactions with the nearest-neighbor anions, of the cobalt and vanadium redox couples are disparate. Furthermore, Rietveld refinement was successively completed to ensure that the detected elemental sodium originates from $Na_xV_3O_8$ and not some vanadia derivative or sodium oxide impurity.

Table 7.2: Rietveld refinement of $Na_xV_3O_8$ products with deficient, ideal, and excess sodium stoichiometry.

Sample	$Na_{1.25}V_3O_8$	Lattice Parameters				Fit Parameters		
	(%)	a (Å)	b (Å)	c (Å)	β(°)	χ^2	wR_p	R_p
JCPDS 24-1156	100	7.32	3.61	12.14	106.73	-	-	-
deficient	98.3	7.37	3.63	12.21	107.28	1.85	0.07	0.03
ideal	98.6	7.36	3.63	12.20	107.26	1.93	0.04	0.03
excess	94.4	7.28	3.62	12.18	106.99	2.02	0.09	0.06

Following the calcination step, the crystal structure of the samples was analyzed and could be indexed to $Na_{1.25}V_3O_8$ phase (space group: P21/m (11), JCPDS card 24-1156) *via* XRD, Fig. 7.2d. Quantitative phase analysis was performed using Rietveld refinement (Table 7.2 and Fig. 7.3) as to affirm the phase homogeneity of the various samples and detect any potential differences in the crystal lattices, primarily along the interlayer *c*-direction. The monoclinic $Na_{1.25}V_3O_8$ phase was the predominant phase detected, with near complete phase composition for the deficient and ideal Na-content samples based off the fitting results, and slightly reduced phase homogeneity for the surplus Na-content specimen which is to be

expected on account of partial cation reduction; differences in the calculated interlayer c-direction spacing were negligible. Analogous interlayer spacing values are reassuring as any variations in electrochemical performance can then be directly tied to defect states and is not dependent on structural disparities. Thus, SEM and Rietveld refinement have proven crucial in validating the purity and commensurable qualities of the differing samples, and reinforce that any further distinctions amongst the various samples are rooted in chemical disparity prompted by means of the defect nature.

FTIR was conducted to distinguish the chemical nature and comparatively analyze the structural characteristics of the specimens with different Na-content, as shown in Fig. 7.4a; the absorption band values have been compiled in Table 7.3. The absorption bands stemming from the symmetric stretching mode of the vanadyl V=O bond is observed at approximately 991 and 944 for all of the samples; the small inflections in the ideal and excess Na-content correspond to this mode as well. The 3-fold-coordinated oxygen asymmetric and symmetric stretching vibrations modes of V-O-V are represented by the bands localized at 745 and 527 cm^{-1}, respectively. The lack of sodium, or presence of oxygen vacancies, in the Na-deficient specimen appears to have its largest impact on this mode (Table 7.3). The 840 cm^{-1} band for the Na-deficient sample can be attributed to the coupled vibration between the V=O and V-O-V bonds, but may be an artifact resulting from oxygen vacancies.[146, 159]

Table 7.3: FTIR peak locations of $Na_xV_3O_8$ products with deficient, ideal, and excess sodium stoichiometry.

Sample	V=O stretching		V=O + V-O-V couple	V-O-V stretching	
				asymmetric	symmetric
deficient	991.8	936.2	842.2	738.7	529.7
ideal	991.3	944.6	-	746.5	526.1
excess	992.4	946.6	-	747.7	526.6

XPS was carried out on the samples prior to electrochemical testing in order to obtain more information on the chemical state of the vanadium species present. High-resolution scans, emphasizing the V2p and O1s peaks, were collected and are shown in Fig. 7.4b,

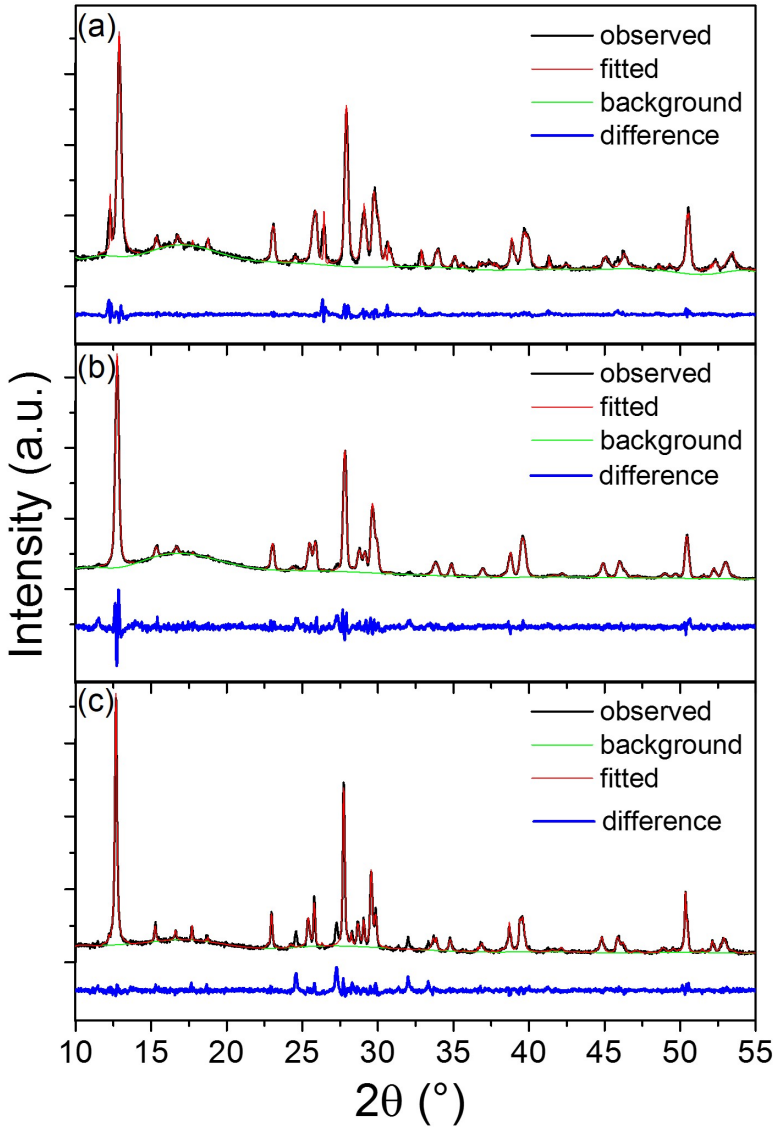

Figure 7.3: Rietveld refinement fits of $Na_xV_3O_8$ with (a) excess, (b) ideal, and (c) deficient sodium stoichiometry.

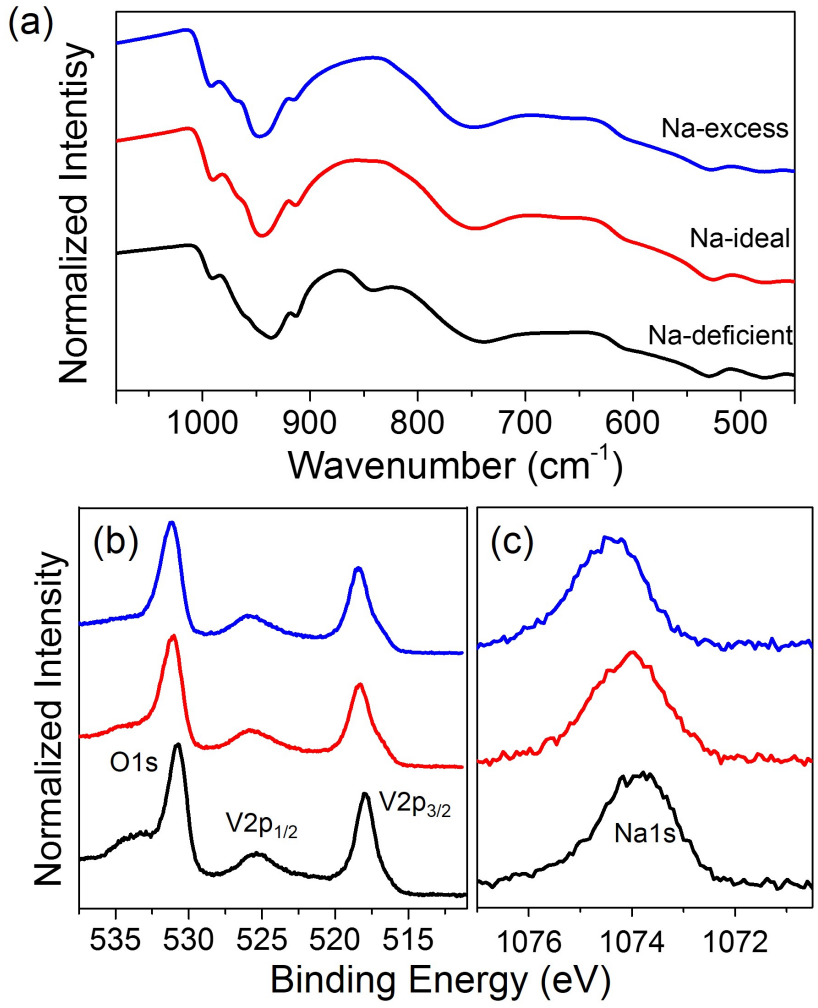

Figure 7.4: (a) FTIR, (b) V2p/O1s XPS, and (c) Na1s XPS spectra of the $Na_xV_3O_8$ products with deficient (black), ideal (red), and excess (blue) sodium stoichiometry.

while Fig. 7.4c showcases the Na1s results. The raw fitted scans are displayed in Fig. 7.5. The trends between peak position, peak spacing, and their literature comparisons reveal that both the V2$p_{3/2}$ and O1s orbital peak positions incrementally rose with sodium content. The V2$p_{3/2}$/O1s peak positions for the deficient, ideal, and excess Na samples were 530.8/517.9, 531.1/518.3, and 531.2/518.4 eV, respectively. The valence of the vanadium phase was confirmed to be predominately pentavalent as determined by the difference in binding energy between the V2$p_{3/2}$ and O1s orbitals, which was approximately 12.8 eV for all of the analyzed specimens. The difference in binding energy (ΔBE) between the O1s and V2$p_{3/2}$ level is commonly used to determine the oxidation state of vanadium oxides.[275, 276, 277] This was further corroborated by the V2$p_{3/2}$ and V2$p_{1/2}$ spin-orbit splitting of approximately 7.5 eV for all samples. These findings are consistent with literature reports.[278, 279]

A noticeable shoulder on the low binding energy side of the V2$p_{3/2}$ peak for the ideal and excess Na-content samples is indicative of a secondary vanadium species, namely V^{4+}. Previous studies have indicated that even in stoichiometric specimens, there is a slight preferential occupation of V^{4+} at preferential vanadium sites.[280] This is also expected as the ideal stoichiometry, $Na_{1.25}V_3O_8$, can only be achieved with the presence of some tetravalent vanadium species, but the comparison between the two is still valid because of their concentration differences. An additional feature of interest is the broad peak extending beyond the main O1s peak, in the 532.5 to 535 eV range, for the Na-deficient a sample that may be attributed to C-O(H).[228] The Na1s peak for all samples is approximately 1074 eV, which is somewhat higher than typical literature values, and there is a clear shift towards higher BE concurrent with the sodium content.[278, 281] The combination of EDX and XPS results tabulates the sodium contents (x in $Na_xV_3O_8$) for the deficient, ideal, and excess specimens at 0.92 $\pm$ 0.01 ($Na_{0.92}V_3O_8$), 1.18 $\pm$ 0.05 ($Na_{1.18}V_3O_8$), and 1.42 $\pm$ 0.04 ($Na_{1.42}V_3O_8$), respectively.

Cyclic voltammograms of the $Na_xV_3O_8$ specimens with varying Na-content collected at potential sweep rates ranging from 0.1 to 5 mV s^{-1} are shown in Fig. 7.6. Scans were

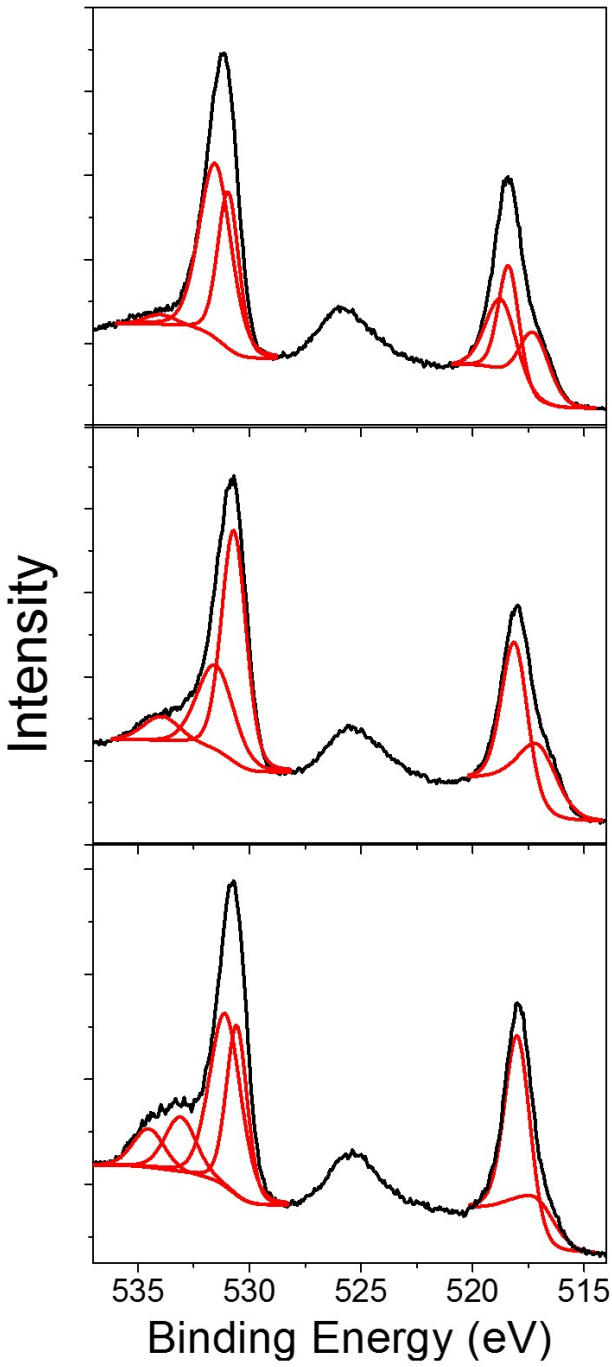

Figure 7.5: Fitted V2p and O1s XPS peaks of $Na_xV_3O_8$ with (a) excess, (b) ideal, and (c) deficient sodium stoichiometry.

performed up to 10 mV s^{-1} but only voltammograms collected at lower rate are shown so that features can be properly observed. The peak magnitude and area of the redox peaks noticeably increase with the potential sweep rate, while the oxidation peaks and corresponding reduction peaks shifted to higher and lower potentials, respectively, due to polarization at the higher sweep rates. These features confirm the favorable charge transfer kinetics even at high potential sweep rates. The raw peaks and their locations show similarities that have previously been correlated with annealing temperature; specifically, the sodium content would appear to be inversely related to crystallinity.[282] However, this is known to not be the case as determined on the basis of Rietveld refinement. A linear dependency between the anodic and cathodic peak currents and the square root of the potential sweep rate indicates that the sodiation process is limited by solid state diffusion in the host material. If the rate-limiting step is sodium diffusion in the electrode and the charge transfer at the interface is fast enough, the relationship between the peak current and the CV scan rate can be expressed by the Randles-Sevcik equation:[283]

$$I_p = \left(2.69 \times 10^5\right) n^{3/2} A C_{Na}^{*} D_{Na}^{1/2} \nu^{1/2} \tag{7.1}$$

where I_p, n, A, and ν are the peak current, number of exchanged electrons, surface area of the electrode, and potential sweep rate; D_{Na} is the sodium ion chemical diffusion coefficient and C_{Na}^{*} is the bulk concentration of sodium (0.011 mol cm^{-3} for $Na_xV_3O_8$ derived from the theoretical density of 3.55 g cm^{-3}).[284] The average value of D_{Na} into the $Na_xV_3O_8$ samples of deficient, ideal, and excess sodium stoichiometry is calculated to be 3.05, 1.53, and 1.89 $\times 10^{-14}$ cm^2 s^{-1}, respectively. The improved diffusion coefficients of the deficient and excess sodium content materials in comparison to the ideal stoichiometry show that Na diffusion is highly dependent on the local environment and configurations of Na ions, and Na-Na interactions through association.[285]

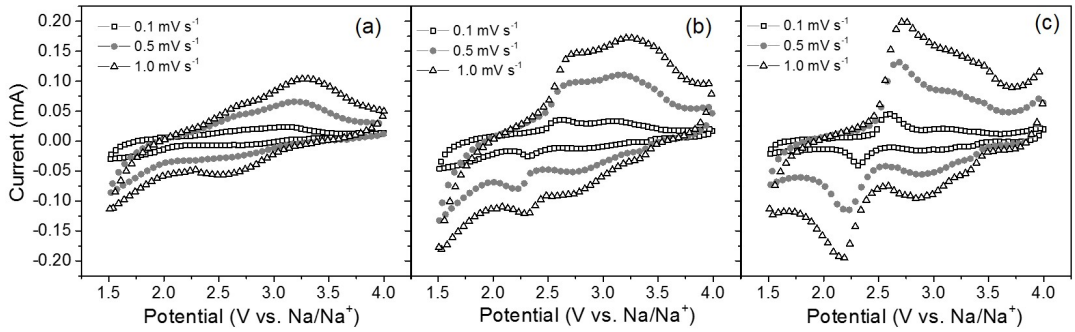

Figure 7.6: Cyclic voltammograms of $Na_xV_3O_8$ with (a) deficient, (b) ideal, and (c) excess sodium content at different potential sweep rates from the inner to the outer of 0.1, 0.5, and 1.0 mV s^{-1}.

All electrodes were electrochemically tested in the Na-ion half-cell configuration, and assuming a theoretical capacity of 350 mA h g^{-1} corresponding to the total incorporation of 4 Na^+ per $[V_3O_8]$ formula unit. The initial current density was 17.5 mA g^{-1} (0.05C) so as to produce a stable cathode-electrolyte interface, or cathode solid electrolyte interphase (SEI) analogue. Following this, the cells were cycled at 35 (0.1C), 175 (0.5C), and 350 (1.0C) mA g^{-1} for 50, 100, and 100 cycles, respectively. The potential discharge profiles from the first complete cycle collected at 35 mA g^{-1} are shown collectively in Fig. 7.7b, with the schematic inset illustrating the change in crystal structure upon sodiation up to $Na_4V_3O_8$. The overall discharge profiles are very similar with the only real differences being the onset and duration of the potential plateau. The $Na_xV_3O_8$ cells with deficient, ideal, and excess Na-content delivered initial discharge capacities of 189, 169, and 235 mA h g^{-1}, respectively.

The cycle stability, rate performance, and Coulombic efficiency (CE) of the deficient, ideal, and excess Na-content $Na_xV_3O_8$ cells are also displayed in Fig. 7.7(c-d), and depict a fairly different story than originally expected based off the discharge profiles. Subsequent cycles at 0.1C saw somewhat erratic capacity values and stability issues as discerned through the CE. This was most apparent for the oxygen vacancy containing $Na_xV_3O_8$ electrode as the CE dropped from 91 to 66% (Fig. 7.7c); there were similar preliminary issues for the

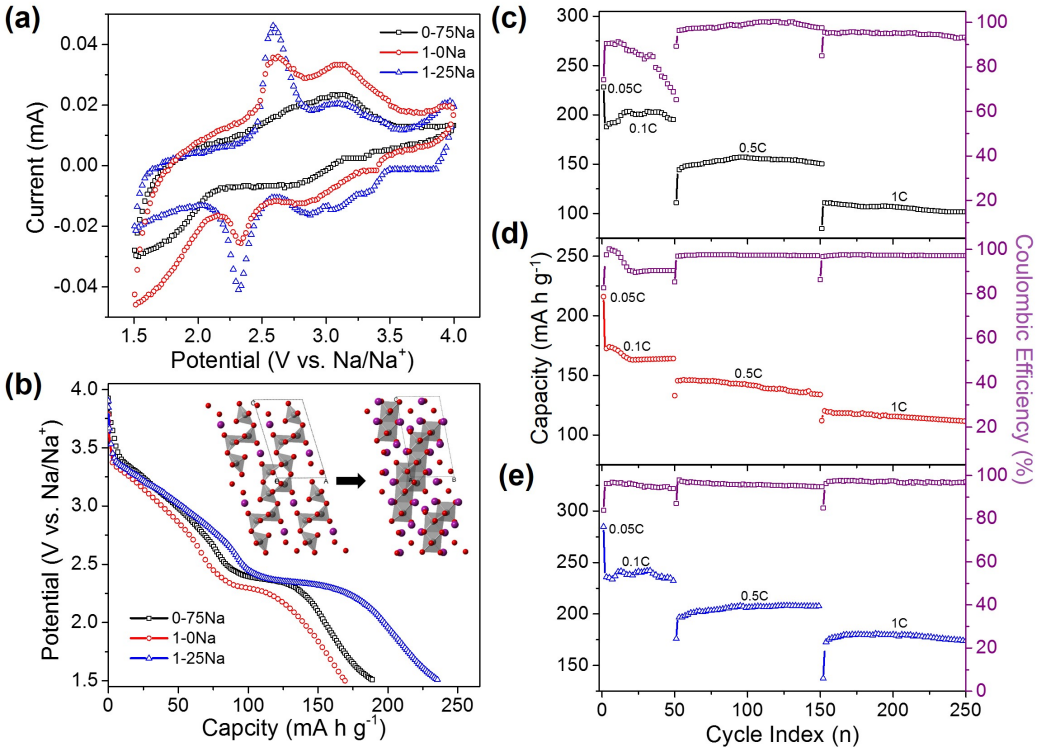

Figure 7.7: (a) Cyclic voltammograms collected at 0.1 mV s^{-1} potential sweep rate and (b) initial full cycle discharge potential profiles of $Na_xV_3O_8$ products with different sodium stoichiometry; inset shows schematic depiction of crystallographic changes undergone during sodiation. Cycle stability, rate performance, and Coulombic efficiency of $Na_xV_3O_8$ with (c) deficient, (d) ideal, and (e) excess sodium stoichiometry.

pristine $Na_xV_3O_8$ electrode which seemed to stabilize and reach an equilibria with successive cycling (Fig. 7.7d), whereas the mixed cation (Na-excess) electrode showed comparatively stable capacities and the highest CE of 96%. The deficient, ideal, and excess Na-content $Na_xV_3O_8$ cell capacities respectively dropped to 150, 145, and 201 mA h g^{-1} and then again to 112, 121, and 180 mA h g^{-1} when the discharge current was increased to 175 and 350 mA g^{-1}.

The CE values were markedly more stable at these increased current densities as well. The Na-deficient electrode still exhibited some stability issues as observed through the CE and the strikingly larger drops in capacity, as compared to the other electrodes, accompanying increases in current density. The pristine electrode material actually overtook the

Na-deficient electrode in terms of capacity and CE at the 1.0C rate. The initially enhanced capacity of the crystalline matrix populated with vacancies can be attributed to weaker Na-O bond strength that accelerates Na hopping between occupied and vacant oxygen sites. However, the ordering of oxygen framework is eventually induced as a result of either transition metal or sodium diffusion in an attempt to reduce the structural free energy.[242] The vacancies order into channels that are easily accessible for sodium ion intercalation, but this eventually leads to capacity retention and stability issues as revealed through prolonged cycling.[286, 287] Fell *et al.* recently showed that, for the $\mathrm{Li}(\mathrm{Ni}_x\mathrm{Li}_{\frac{1}{3}-\frac{2x}{3}}\mathrm{Mn}_{\frac{2}{3}-\frac{x}{3}})\mathrm{O}_2$ ($x = \frac{1}{5}$) structure, microstrain can originate from a lithium deficient structure (point defects and vacancies), and that there are multiple phenomena occurring in the bulk such as transition metal migration as well as oxygen loss.[242] This has further been corroborated by experimental studies showing that the presence of oxygen vacancies can lead to the loss of domain order and capacity fading due to structural collapse, and a similar mechanism may play a role in the performance seen here.[288]

Electronic localization has been directly observed in other layered transition metal oxides directly affirming that the exhibited electronic properties are strongly correlated to the Na-ion distribution in the interlayer space.[289] Thus, the cationic distribution of the individual samples could differ significantly since the sodium content levels are unequal. On a more global level, the cationic distribution is comprised of: electrostatic repulsions between the individual Na-ions along the interlayer c-axis, Na^{+}-V^{5+} repulsion occurring through the common face of the VO_6 polyhedra, as well as the intra-electron interactions within the vanadium layers. For any given system, the cationic distribution will seek to reach a minimum. Thus, the cationic distribution is highly sensitive to the sodium content as it can have serious impact on the constituent influences. A slight change in sodium composition may be enough to induce the formation of an entirely new cationic distribution.[290]

Electron transport has been demonstrated to be affected strongly by solid-solution formation and, correspondingly, other means of introduced atomic-level disorder.[291] Conse-

quently, the structure of excess sodium-containing $Na_xV_3O_8$ lends itself to both favorable mass and electronic charge transport. The excess sodium bolsters the mechanical integrity of the layered structure itself while the Na^+ in the original lattice gives way to additional metal-oxygen bonds other than V-O. This ultimately reduces the number of sp^3 orbitals of oxygen available for bonding with the incoming sodium-ions, and the interaction between tetrahedrally coordinated Na^+ and O^{2-} is weak enough to grant fast movement of sodium from site to site.[292, 293] Based off purely electrostatic considerations, it would be expected that $Na_xV_3O_8$ with excess sodium would suffer from low-migration energy given that the sodium sites generate strong electrostatic repulsion on one another. The activation of such forces would induce high migration energy barriers. Moreover, Na-ion ordering or structuring would also be anticipated to negatively impact sodium diffusion in a substantial manner provided the considerable effect of Na-Na interactions on the local Na migration energy. However, cationic mixing poses a route of overcoming these deficiencies by potentially perturbing the ordering of the transition metal sub-lattice, which would consequently result in a weaker Na ordering and thereby improve sodium diffusion. The defected (disordered) materials consistently delivered higher capacities than the more ordered (pristine) counterpart, clearly demonstrating the critical role of structural ordering on kinetics.

7.4 Conclusions

In the present work, we successfully synthesized defective $Na_xV_3O_8$ where it was possible to control the dominant defect type through sodium stoichiometry manipulation. Thus, Na-deficiency lead to the formation of oxygen vacancies and Na-excess lead to partial cation reduction, or the formation of a cation disordered structure. When examined as NIB electrode material, the superior performance of the Na-excess, cation disordered, materials was clearly revealed, especially at higher current discharge densities. The formation of oxygen vacancies initially seemed promising, but was coupled with stability issues and capacity fading

with further cycling. The disparity in electrochemical performance was attributed to variations in the electronic distribution as promoted through Na-ion interactions and the direct influence of such on the oxygen framework (sub-lattice); these factors were determined to have significant impact on the migration energy and diffusion barriers. This study provides insight on defect and stoichiometry considerations for cathode materials, and provides a potential mechanism towards significantly improving the performance of rechargeable alkali-ion batteries.

Chapter 8

Conclusions

This dissertation includes the experimental work and analysis of the results towards understanding and developing new methods and materials that allow for the exploitation of efficient alkali-ion intercalation electrodes based on vanadium oxide. The experimental work was mainly based on solution based methods such as electrochemical deposition, solvothermal precipitation, sol-gel processing, and chemical decomposition. The fabrication of structurally and defect modified nanomaterials were the two primary topics of focus. The findings garnered from these studies should, at the least, be taken into consideration for a range of electrode materials during production. The results gained are by no means limited to the originally investigated systems, but rather strive to serve as a model system showcasing how small structural or chemical alterations can have significant impact on device performance.

The polyol induced solvothermal synthesis of hollow vanadyl glycolate nanostructured microspheres, their conversion to hollow nanostructured V_2O_5 microspheres, and their subsequent electrochemical properties. The work proposes a novel formation mechanism involving N_2 microbubbles that act as quasi-micelles due to the large polarization discrepancy between nitrogen and water, and provides a firm understanding of the processes leading to the observed hollow microsphere morphology. The encouraging electrochemical performance of the thermally treated material was attributed to the relatively thin walled structure that

ensured fast phase penetration between the electrolyte and active material, and the inherent morphological void that can readily accommodate volume expansion and contraction upon cycling.

The solvothermal synthesis of VO_2(B) mesocrystals via an additive and template free process is discussed. The homoepitaxially oriented nanostructures were produced through classical as well as non-classical crystallization processes. Despite their overall micro-scale size, the mesocrystals exhibit one of the highest Li-ion intercalation performance and capacity retention values for VO_2(B) when compared to the results from other VO_2(B) structures taken from the literature, especially upon cycling at higher discharge rates. The excellent cycle stability can be attributed to the crystallographically oriented nanoparticle structure that ensures good electrochemical stability and mechanical integrity can be guaranteed for many cycles.

The positive role of the amorphous structure for V_2O_5 electrode materials used as sodium-ion cathode battery is described. The crystallinity of the electrode was controlled by managing the annealing profile and environment employed. Amorphous V_2O_5 demonstrated superior sodium-ion intercalation properties as compared to its crystalline counterpart when examined as positive electrode material for Na-ion battery application. The percolation of certain diffusion channels in amorphous materials can be activated because of the disordered structure. Such effects improve charge and ionic transfer at the electrode/electrolyte interface during the sodiation process, yielding a positive electrode material for sodium-ion battery application with superior energy density and strong cycling performance. The possible relationship between the disparity in intercalation properties and structure is discussed.

A continuation of the analysis of the positive role of defects to sodium ion intercalation capability for $Na_xV_3O_8$ was then covered. It was possible to control the sodium composition in the final product by adjusting the amount of sodium precursor added during synthesis. It was determined that deficient and surplus sodium contents, with respect to the ideal stoichiometry, are accommodated by the generation of oxygen vacancies and partial transition

metal reduction, or cation disordering, respectively. The disparity in electrochemical performance was attributed to variations in the electronic distribution as promoted through Na-ion interactions and the direct influence of such on the oxygen framework (sub-lattice); these factors were determined to have significant impact on the migration energy and diffusion barriers.

Bibliography

[1] E. Hryha, E. Rutqvist, and L. Nyborg. Stoichiometric Vanadium Oxides Studied by XPS. *Surface and Interface Analysis*, 44(8):1022–1025, 2012.

[2] U.S. Energy Information Administration. Annual Energy Outlook 2014. pages DOE/EIA–0383ER, 2014.

[3] J. I. San Martn, I. Zamora, J. J. San Martn, V. Aperribay, and P. Egua. Energy Storage Technologies for Electric Applications. *European Association for the Development of Renewable Energies, Environment and Power Quality*, 2011.

[4] C.H. Hamann, A. Hamnett, and W. Vielstich. *Electrochemistry*. Wiley, 1998.

[5] Woodbank Communications Ltd. Battery and Energy Technologies - Cell Chemistries. page http://www.mpoweruk.com/chemistries.html, January 2014.

[6] K. Kordesch and W. Taucher-Mautner. Histoy of Primary Batteries. In *Encyclopedia of Electrochemical Power Sources*, pages 555–564. Elsevier, Amsterdam, 2009.

[7] Elsa Olivetti, Jeremy Gregory, and Randolph Kirchain. Life Cycle Impacts of Alkaline Batteries with a Focus on End-Of-Life. *National Electrical Manufacturers Association*, 2010.

[8] G.B. Haxel, J.B. Hedrick, and G.J. Orris. Rare Earth Elements-Critical Resources for High Technology. *US Geological Survey Fact Sheet 087-02*, 2002.

[9] Brian W. Jaskula. Lithium. *US Geological Mineral Commodity Summaries*, pages 94–95, 2014.

[10] J. M. Tarascon and M. Armand. Issues and Challenges Facing Rechargeable Lithium Batteries. *Nature*, 414(6861):359–367, 2001.

[11] Chen-Xi Zu and Hong Li. Thermodynamic Analysis on Energy Densities of Batteries. *Energy Environ. Sci.*, 4:2614–2624, 2011.

[12] Roland Berger Stratgey Consultants. Technology & Market Drivers for Stationary and Automotive Battery Systems. *Batteries 2012*.

[13] Michael D. Slater, Donghan Kim, Eungje Lee, and Christopher S. Johnson. Sodium-Ion Batteries. *Advanced Functional Materials*, 23(8):947–958, 2013.

[14] Nicholas Hudak and Dale Huber. Nanostructured Lithium-Aluminum Alloy Electrodes for Lithium-Ion Batteries. *ECS Transactions*, 33(24):1–13, 2011.

[15] Linda Gaines and Roy Cuenca. Costs of Lithium-Ion Batteries for Vehicles. *Center for Transportation Research, Energy Systems Division, Argonne National Lab*, pages ANL/ESD–42, 2000.

[16] Y. Kim, Y. Park, A. Choi, N. S. Choi, J. Kim, J. Lee, J. H. Ryu, S. M. Oh, and K. T. Lee. An Amorphous Red Phosphorus/Carbon Composite as a Promising Anode Material for Sodium Ion Batteries. *Adv Mater*, 25(22):3045–9, 2013.

[17] Shyue Ping Ong, Vincent L. Chevrier, Geoffroy Hautier, Anubhav Jain, Charles Moore, Sangtae Kim, Xiaohua Ma, and Gerbrand Ceder. Voltage, Stability and Diffusion Barrier Differences Between Sodium-Ion and Lithium-Ion Intercalation Materials. *Energy and Environmental Science*, 4(9):3680–3688, 2011.

[18] Hui Xiong, Michael D. Slater, Mahalingam Balasubramanian, Christopher S. Johnson, and Tijana Rajh. Amorphous TiO_2 Nanotube Anode for Rechargeable Sodium Ion Batteries. *The Journal of Physical Chemistry Letters*, 2(20):2560–2565, 2011.

[19] Martin Z. Bazant. Theory of Chemical Kinetics and Charge Transfer based on Nonequilibrium Thermodynamics. *Accounts of Chemical Research*, 46(5):1144–1160, 2013.

[20] R.A. Marcus and Norman Sutin. Electron Transfers in Chemistry and Biology. *Biochimica et Biophysica Acta (BBA) - Reviews on Bioenergetics*, 811(3):265 – 322, 1985.

[21] Todd P. Silverstein. Marcus Theory: Thermodynamics can Control the Kinetics of Electron Transfer Reactions. *Journal of Chemical Education*, 89(9):1159–1167, 2012.

[22] John S. Newman and Charles W. Tobias. Theoretical Analysis of Current Distribution in Porous Electrodes. *Journal of The Electrochemical Society*, 109(12):1183–1191, 1962.

[23] John Newman and William Tiedemann. Porous-electrode Theory With Battery Applications. *AIChE Journal*, 21(1):25–41, 1975.

[24] Martin Ebner, Ding-Wen Chung, R. Edwin Garca, and Vanessa Wood. Tortuosity Anisotropy in Lithium-Ion Battery Electrodes. *Advanced Energy Materials*, 2013.

[25] Brent C. Melot and J.-M. Tarascon. Design and Preparation of Materials for Advanced Electrochemical Storage. *Accounts of Chemical Research*, 46(5):1226–1238, 2013.

[26] John B. Goodenough and Youngsik Kim. Challenges for Rechargeable Li Batteries. *Chemistry of Materials*, 22(3):587–603, 2010.

[27] E. Peled, D. Golodnitsky, and G. Ardel. Advanced Model for Solid Electrolyte Interphase Electrodes in Liquid and Polymer Electrolytes. *Journal of The Electrochemical Society*, 144(8):L208–L210, 1997.

[28] K. Edstrm, T. Gustafsson, and J.O. Thomas. The Cathode-Electrolyte Interface in the Li-Ion Battery. *Electrochimica Acta*, 50(23):397–403, 2004.

[29] M. Balasubramanian, H. S. Lee, X. Sun, X. Q. Yang, A. R. Moodenbaugh, J. McBreen, D. A. Fischer, and Z. Fu. Formation of SEI on Cycled Lithium-Ion Battery Cathodes: Soft X-Ray Absorption Study. *Electrochemical and Solid-State Letters*, 5(1):A22–A25, 2002.

[30] Maureen Tang and John Newman. Electrochemical Characterization of SEI-Type Passivating Films Using Redox Shuttles. *Journal of The Electrochemical Society*, 158(5):A530–A536, 2011.

[31] Pallavi Verma, Pascal Maire, and Petr Novk. A Review of the Features snd Analyses of the Solid Electrolyte Interphase in Li-Ion Batteries. *Electrochimica Acta*, 55(22):6332–6341, 2010.

[32] M. Rosa Palacin. Recent Advances in Rechargeable Battery Materials: a Chemist's Perspective. *Chem. Soc. Rev.*, 38:2565–2575, 2009.

[33] Premkumar Senguttuvan, Gwenalle Rousse, Vincent Seznec, Jean-Marie Tarascon, and M.Rosa Palacn. $Na_2Ti_3O_7$: Lowest Voltage Ever Reported Oxide Insertion Electrode for Sodium Ion Batteries. *Chemistry of Materials*, 23(18):4109–4111, 2011.

[34] Desiree E. Polyak. Vanadium. *US Geological Mineral Commodity Summaries*, pages 176–177, 2015.

[35] Kan Kanamori and Kiyoshi Tsuge. Inorganic Chemistry of Vanadium. In Hitoshi Michibata, editor, *Vanadium*, pages 3–31. Springer Netherlands, 2012.

[36] Gerhard Deublein and Robert A. Huggins. Hydrogen Transparent Metal Surfaces Produced by Use of Molten Salts with Very Low Oxygen and Water Activities. *Journal of The Electrochemical Society*, 136(8):2234–2238, 1989.

[37] H.A. Wriedt. The O-V (Oxygen-Vanadium) System. *Bulletin of Alloy Phase Diagrams*, 10(3):271–277, 1989.

[38] J. S. Braithwaite, C. R. A. Catlow, J. D. Gale, and J. H. Harding. Lithium Intercalation into Vanadium Pentoxide: a Theoretical Study. *Chemistry of Materials*, 11(8):1990–1998, 1999.

[39] Jean Galy. Vanadium Pentoxide and Vanadium Oxide Bronzes-Structural Chemistry of Single (S) and Double (D) Layer $M_xV_2O_5$ Phases. *Journal of Solid State Chemistry*, 100(2):229–245, 1992.

[40] J.M. Cocciantelli, J.P. Doumerc, M. Pouchard, M. Broussely, and J. Labat. Crystal Chemistry of Electrochemically Inserted $Li_xV_2O_5$. *Journal of Power Sources*, 34(2):103–111, 1991.

[41] P.A. Cox. *Transition Metal Oxides: An Introduction to Their Electronic Structure and Properties*. International Series of Monographs on Chemistry. Clarendon Press, 1992.

[42] C. Delmas, S. Brthes, and M. Mntrier. ω-$Li_xV_2O_5$ a New Electrode Material for Rechargeable Lithium Batteries. *Journal of Power Sources*, 34(2):113–118, 1991.

[43] Yu-Guo Guo, Jin-Song Hu, and Li-Jun Wan. Nanostructured Materials for Electrochemical Energy Conversion and Storage Devices. *Advanced Materials*, 20(15):2878–2887, 2008.

[44] Dawei Liu and Guozhong Cao. Engineering Nanostructured Electrodes and Fabrication of Film Electrodes for Efficient Lithium Ion Intercalation. *Energy Environ. Sci.*, 3:1218–1237, 2010.

[45] Bruno Scrosati and Jrgen Garche. Lithium Batteries: Status, Prospects and Future. *Journal of Power Sources*, 195(9):2419–2430, 2010.

[46] P. Balaya, A.J. Bhattacharyya, J. Jamnik, Yu.F. Zhukovskii, E.A. Kotomin, and J. Maier. Nano-Ionics in the Context of Lithium Batteries. *Journal of Power Sources*, 159(1):171–178, 2006.

[47] Yanyi Liu, Dawei Liu, Qifeng Zhang, Danmei Yu, Jun Liu, and Guozhong Cao. Lithium Iron Phosphate/Carbon Nanocomposite Film Cathodes for High Energy Lithium Ion Batteries. *Electrochimica Acta*, 56(5):2559–2565, 2011.

[48] Peter G. Bruce, Bruno Scrosati, and Jean-Marie Tarascon. Nanomaterials for Rechargeable Lithium Batteries. *Angewandte Chemie International Edition*, 47(16):2930–2946, 2008.

[49] C. Delmas, H. Cognac-Auradou, J.M. Cocciantelli, M. Mntrier, and J.P. Doumerc. The $Li_xV_2O_5$ System: an Overview of the Structure Modifications Induced by the Lithium Intercalation. *Solid State Ionics*, 69(34):257–264, 1994.

[50] Marnix Wagemaker, Wouter J. H. Borghols, and Fokko M. Mulder. Large Impact of Particle Size on Insertion Reactions. A Case for Anatase Li_xTiO_2. *Journal of the American Chemical Society*, 129(14):4323–4327, 2007.

[51] M. Wagemaker, A. P. M. Kentgens, and F. M. Mulder. Equilibrium Lithium Transport Between Nanocrystalline Phases in Intercalated TiO_2 Anatase. *Nature*, 418(6896):397–399, 2002.

[52] S. Ganapathy, E. R. van Eck, A. P. Kentgens, F. M. Mulder, and M. Wagemaker. Equilibrium Lithium-Ion Transport Between Nanocrystalline Lithium-Inserted Anatase TiO_2 and the Electrolyte. *Chemistry*, 17(52):14811–6, 2011.

[53] Y.-S. Hu, L. Kienle, Y.-G. Guo, and J. Maier. High Lithium Electroactivity of Nanometer-Sized Rutile TiO_2. *Advanced Materials*, 18(11):1421–1426, 2006.

[54] R.A. Huggins and W.D. Nix. Decrepitation Model for Capacity Loss During Cycling of Alloys in Rechargeable Electrochemical Systems. *Ionics*, 6(1-2):57–63, 2000.

[55] C. K. Chan, H. Peng, G. Liu, K. McIlwrath, X. F. Zhang, R. A. Huggins, and Y. Cui. High-performance Lithium Battery Anodes Using Silicon Nanowires. *Nat Nanotechnol*, 3(1):31–5.

[56] Nonglak Meethong, Hsiao-Ying Shadow Huang, W. Craig Carter, and Yet-Ming Chiang. Size-Dependent Lithium Miscibility Gap in Nanoscale $Li_{1-x}FePO_4$. *Electrochemical and Solid-State Letters*, 10(5):A134, 2007.

[57] Genki Kobayashi, Shin-ichi Nishimura, Min-Sik Park, Ryoji Kanno, Masatomo Yashima, Takashi Ida, and Atsuo Yamada. Isolation of Solid Solution Phases in Size-Controlled Li_xFePO_4 at Room Temperature. *Advanced Functional Materials*, 19(3):395–403, 2009.

[58] Marnix Wagemaker, Deepak P. Singh, Wouter J.H. Borghols, Ugo Lafont, Lucas Haverkate, Vanessa K. Peterson, and Fokko M. Mulder. Dynamic Solubility Limits in Nanosized Olivine $LiFePO_4$. *Journal of the American Chemical Society*, 133(26):10222–10228, 2011.

[59] Anthony G. Dylla, Penghao Xiao, Graeme Henkelman, and Keith J. Stevenson. Morphological Dependence of Lithium Insertion in Nanocrystalline TiO_2(B) Nanoparticles and Nanosheets. *The Journal of Physical Chemistry Letters*, 3(15):2015–2019, 2012.

[60] Wen Qi Fang, Xue-Qing Gong, and Hua Gui Yang. On the Unusual Properties of Anatase TiO_2 Exposed by Highly Reactive Facets. *The Journal of Physical Chemistry Letters*, 2(7):725–734, 2011.

[61] Hua Gui Yang, Cheng Hua Sun, Shi Zhang Qiao, Jin Zou, Gang Liu, Sean Campbell Smith, Hui Ming Cheng, and Gao Qing Lu. Anatase TiO_2 Single Crystals with a Large Percentage of Reactive Facets. *Nature*, 453:638–641, 2008.

[62] Jiehua Liu and Xue-Wei Liu. Two-Dimensional Nanoarchitectures for Lithium Storage. *Advanced Materials*, 24(30):4097–4111, 2012.

[63] Binghui Wu, Changyou Guo, Nanfeng Zheng, Zhaoxiong Xie, and Galen D. Stucky. Nonaqueous Production of Nanostructured Anatase with High-Energy Facets. *Journal of the American Chemical Society*, 130(51):17563–17567, 2008.

[64] Jun Song Chen, Yi Ling Tan, Chang Ming Li, Yan Ling Cheah, Deyan Luan, Srinivasan Madhavi, Freddy Yin Chiang Boey, Lynden A. Archer, and Xiong Wen Lou. Constructing Hierarchical Spheres from Large Ultrathin Anatase TiO_2 Nanosheets with Nearly 100% Exposed (001) Facets for Fast Reversible Lithium Storage. *Journal of the American Chemical Society*, 132(17):6124–6130, 2010.

[65] Shujiang Ding, Jun Song Chen, Zhiyu Wang, Yan Ling Cheah, Srinvivasan Madhavi, Xiao Hu, and Xiong Wen Lou. TiO_2 Hollow Spheres aith Large Amount of Exposed

(001) Facets for Fast Reversible Lithium Storage. *J. Mater. Chem.*, 21:1677–1680, 2011.

[66] Yanlong Yu, Xiaoliang Wang, Hongyu Sun, and Mashkoor Ahmad. 3D Anatase TiO_2 Hollow Microspheres Assembled With High-Energy 001 Facets for Lithium-Ion Batteries. *RSC Adv.*, 2:7901–7905, 2012.

[67] Lichen Liu, Qi Fan, Chuanzhi Sun, Xianrui Gu, Hao Li, Fei Gao, Yanfeng Chen, and Lin Dong. Synthesis of Sandwich-like TiO_2@C Composite Hollow Spheres with High Rate Capability and Stability for Lithium-Ion Batteries. *Journal of Power Sources*, 221(0):141–148, 2013.

[68] Swapna Ganapathy and Marnix Wagemaker. Nanosize Storage Properties in Spinel $Li_4Ti_5O_{12}$ Explained by Anisotropic Surface Lithium Insertion. *ACS Nano*, 6(10):8702–8712, 2012.

[69] Weiwei Sun, Feng Cao, Yumin Liu, Xingzhong Zhao, Xiaogang Liu, and Jikang Yuan. Nanoporous $LiMn_2O_4$ Nanosheets with Exposed 111 Facets as Cathodes for Highly Reversible Lithium-Ion Batteries. *J. Mater. Chem.*, 22:20952–20957, 2012.

[70] Lin Liang, Min Zhou, and Yi Xie. Electrospun Hierarchical LiV_3O_8 Nanofibers Assembled from Nanosheets with Exposed 100 Facets and their Enhanced Performance in Aqueous Lithium-Ion Batteries. *Chemistry An Asian Journal*, 7(3):565–571, 2012.

[71] Li Wang, Xiangming He, Wenting Sun, Jianlong Wang, Yadong Li, and Shoushan Fan. Crystal Orientation Tuning of $LiFePO_4$ Nanoplates for High Rate Lithium Battery Cathode Materials. *Nano Letters*, 12(11):5632–5636, 2012.

[72] Xiao-Liang Pan, Cheng-Yan Xu, and Liang Zhen. Synthesis of $LiMnPO_4$ Microspheres Assembled by Plates, Wedges and Prisms with Different Crystallographic Orientations and Their Electrochemical Performance. *CrystEngComm*, 14:6412–6418, 2012.

[73] Sung Chul Jung and Young-Kyu Han. Facet-Dependent Lithium Intercalation into Si Crystals: Si(100) vs. Si(111). *Phys. Chem. Chem. Phys.*, 13:21282–21287, 2011.

[74] Matt Pharr, Kejie Zhao, Xinwei Wang, Zhigang Suo, and Joost J. Vlassak. Kinetics of Initial Lithiation of Crystalline Silicon Electrodes of Lithium-Ion Batteries. *Nano Letters*, 12(9):5039–5047, 2012.

[75] Andre Nel, Tian Xia, Lutz Mdler, and Ning Li. Toxic Potential of Materials at the Nanolevel. *Science*, 311(5761):622–627, 2006.

[76] Vicki L Colvin. The Potential Environmental Impact of Engineered Nanomaterials. *Nature Publishing Group*, 21:1166–1170, 2003.

[77] Shudong Zhang, Yingmei Li, Changzheng Wu, Fei Zheng, and Yi Xie. Novel Flowerlike Metastable Vanadium Dioxide (B) Micronanostructures: Facile Synthesis and Application in Aqueous Lithium Ion Batteries. *The Journal of Physical Chemistry C*, 113(33):15058–15067, 2009.

[78] Ping Nie, Laifa Shen, Fang Zhang, Lin Chen, Haifu Deng, and Xiaogang Zhang. Flower-like $LiMnPO_4$ Hierarchical Microstructures Assembled from Single-Crystalline Nanosheets for Lithium-Ion Batteries. *CrystEngComm*, 14:4284–4288, 2012.

[79] Qiang Wang, Weixin Zhang, Zeheng Yang, Shaoying Weng, and Zhuojie Jin. Solvothermal Synthesis of Hierarchical $LiFePO_4$ Microflowers as Cathode Materials for Lithium Ion Batteries. *Journal of Power Sources*, 196(23):10176–10182, 2011.

[80] Frank Caruso, Rachel A. Caruso, and Helmuth Mhwald. Nanoengineering of Inorganic and Hybrid Hollow Spheres by Colloidal Templating. *Science*, 282(5391):1111–1114, 1998.

[81] Jun Liu and Dongfeng Xue. Hollow Nanostructured Anode Materials for Li-Ion Batteries. *Nanoscale Research Letters*, 5:1525–1534, 2010.

[82] D. Zhu, H. Liu, L. Lv, Y.D. Yao, and W.Z. Yang. Hollow Microspheres of V_2O_5 and Cu-doped V_2O_5 as Cathode Materials for Lithium-Ion Batteries. *Scripta Materialia*, 59(6):642–645, 2008.

[83] Suqing Wang, Zhenda Lu, Da Wang, Chunguang Li, Chunhua Chen, and Yadong Yin. Porous Monodisperse V_2O_5 Microspheres as Cathode Materials for Lithium-Ion Batteries. *J. Mater. Chem.*, 21:6365–6369, 2011.

[84] Jiayan Luo, Liang Cheng, and Yongyao Xia. $LiMn_2O_4$ Hollow Nanosphere Electrode Material with Excellent Cycling Reversibility and Rate Capability. *Electrochemistry Communications*, 9(6):1404–1409, 2007.

[85] Jun Liu, Hui Xia, Dongfeng Xue, and Li Lu. Double-Shelled Nanocapsules of V_2O_5-Based Composites as High-Performance Anode and Cathode Materials for Li Ion Batteries. *Journal of the American Chemical Society*, 131(34):12086–12087, 2009.

[86] Xiong Wen Lou and Lynden A. Archer. A General Route to Nonspherical Anatase TiO_2 Hollow Colloids and Magnetic Multifunctional Particles. *Advanced Materials*, 20(10):1853–1858, 2008.

[87] Hui Wu, Gerentt Chan, Jang Wook Choi, Ill Ryu, Yan Yao, Matthew T. McDowell, Seok Woo Lee, Ariel Jackson, Yuan Yang, Liangbing Hu, and Yi Cui. Stable Cycling of Double-Walled Silicon Nanotube Battery Anodes through Solid-Electrolyte Interphase Control. *Nature Nanotechnology*, 7:310–315, 2012.

[88] C. O'Dwyer, D. Navas, V. Lavayen, E. Benavente, M. A. Santa Ana, G. Gonzlez, S. B. Newcomb, and C. M. Sotomayor Torres. Nano-Urchin: The Formation and Structure of High-Density Spherical Clusters of Vanadium Oxide Nanotubes. *Chemistry of Materials*, 18(13):3016–3022, 2006.

[89] Guicun Li, Kun Chao, Chuanqin Zhang, Qingshan Zhang, Hongrui Peng, and Kezheng Chen. Synthesis of Urchin-like VO_2 Nanostructures Composed of Radially Aligned Nanobelts and Their Disassembly. *Inorganic Chemistry*, 48(3):1168–1172, 2009.

[90] Chang Liu, Feng Li, Lai-Peng Ma, and Hui-Ming Cheng. Advanced Materials for Energy Storage. *Advanced Materials*, 22(8):E28–E62, 2010.

[91] Wei-Ming Zhang, Jin-Song Hu, Yu-Guo Guo, Shu-Fa Zheng, Liang-Shu Zhong, Wei-Guo Song, and Li-Jun Wan. Tin-Nanoparticles Encapsulated in Elastic Hollow Carbon Spheres for High-Performance Anode Material in Lithium-Ion Batteries. *Advanced Materials*, 20(6):1160–1165, 2008.

[92] Kyu T. Lee, Yoon S. Jung, and Seung M. Oh. Synthesis of Tin-Encapsulated Spherical Hollow Carbon for Anode Material in Lithium Secondary Batteries. *Journal of the American Chemical Society*, 125(19):5652–5653, 2003.

[93] Guangyuan Zheng, Yuan Yang, Judy J. Cha, Seung Sae Hong, and Yi Cui. Hollow Carbon Nanofiber-Encapsulated Sulfur Cathodes for High Specific Capacity Rechargeable Lithium Batteries. *Nano Letters*, 11(10):4462–4467, 2011.

[94] Nian Liu, Hui Wu, Matthew T. McDowell, Yan Yao, Chongmin Wang, and Yi Cui. A Yolk-Shell Design for Stabilized and Scalable Li-Ion Battery Alloy Anodes. *Nano Letters*, 12(6):3315–3321, 2012.

[95] Ying Wang and Guozhong Cao. Synthesis and Enhanced Intercalation Properties of Nanostructured Vanadium Oxides. *Chemistry of Materials*, 18(12):2787–2804, 2006.

[96] Helmut Colfen and Markus Antonietti. Mesocrystals: Inorganic Superstructures Made by Highly Parallel Crystallization and Controlled Alignment. *Angewandte Chemie International Edition*, 44(35):5576–5591, 2005.

[97] Markus Niederberger and Helmut Colfen. Oriented Attachment and Mesocrystals: Non-Classical Crystallization Mechanisms Based on Nanoparticle Assembly. *Phys. Chem. Chem. Phys.*, 8:3271–3287, 2006.

[98] Rui-Qi Song and Helmut Colfen. MesocrystalsOrdered Nanoparticle Superstructures. *Advanced Materials*, 22(12):1301–1330, 2010.

[99] Fiona Meldrum and Helmut Colfen. Crystallization and Formation Mechanisms of Nanostructures. *Nanoscale*, 2:2326–2327, 2010.

[100] Rui-Qi Song and Helmut Colfen. Additive Controlled Crystallization. *CrystEngComm*, 13:1249–1276, 2011.

[101] Virany M. Yuwono, Nathan D. Burrows, Jennifer A. Soltis, and R. Lee Penn. Oriented Aggregation: Formation and Transformation of Mesocrystal Intermediates Revealed. *Journal of the American Chemical Society*, 132(7):2163–2165, 2010.

[102] An-Min Cao, Jin-Song Hu, Han-Pu Liang, and Li-Jun Wan. Self-Assembled Vanadium Pentoxide (V_2O_5) Hollow Microspheres from Nanorods and Their Application in Lithium-Ion Batteries. *Angewandte Chemie International Edition*, 44(28):4391–4395, 2005.

[103] Jianfeng Ye, Wen Liu, Jinguang Cai, Shuai Chen, Xiaowei Zhao, Henghui Zhou, and Limin Qi. Nanoporous Anatase TiO_2 Mesocrystals: Additive-Free Synthesis, Remarkable Crystalline-Phase Stability, and Improved Lithium Insertion Behavior. *Journal of the American Chemical Society*, 133(4):933–940, 2011.

[104] Zhensheng Hong, Yuxia Xu, Yubin Liu, and Mingdeng Wei. Unique Ordered TiO_2 Superstructures with Tunable Morphology and Crystalline Phase for Improved Lithium Storage Properties. *Chemistry A European Journal*, 18(34):10753–10760, 2012.

[105] Idalia Bilecka, Andreas Hintennach, Igor Djerdj, Petr Novak, and Markus Niederberger. Efficient Microwave-Assisted Synthesis of $LiFePO_4$ Mesocrystals with High Cycling Stability. *J. Mater. Chem.*, 19:5125–5128, 2009.

[106] Yang Xia, Wenkui Zhang, Hui Huang, Yongping Gan, Jian Tian, and Xinyong Tao. Self-assembled Mesoporous $LiFePO_4$ with Hierarchical Spindle-Like Architectures for High-Performance Lithium-Ion Batteries. *Journal of Power Sources*, 196(13):5651–5658, 2011.

[107] M. S. Whittingham. Electrical Energy Storage and Intercalation Chemistry. *Science*, 192(4244):1126–1127, 1976.

[108] Kyu-Sung Park, Anass Benayad, Dae-Joon Kang, and Seok-Gwang Doo. Nitridation-Driven Conductive $Li_4Ti_5O_{12}$ for Lithium Ion Batteries. *Journal of the American Chemical Society*, 130(45):14930–14931, 2008.

[109] Paul R. Abel, Yong-Mao Lin, Hugo Celio, Adam Heller, and C. Buddie Mullins. Improving the Stability of Nanostructured Silicon Thin Film Lithium-Ion Battery Anodes through Their Controlled Oxidation. *ACS Nano*, 6(3):2506–2516, 2012.

[110] Wanli Xu, Sri Sai S. Vegunta, and John C. Flake. Surface-Modified Silicon Nanowire Anodes for Lithium-Ion Batteries. *Journal of Power Sources*, 196(20):8583–8589, 2011.

[111] L.J. Fu, H. Liu, C. Li, Y.P. Wu, E. Rahm, R. Holze, and H.Q. Wu. Surface Modifications of Electrode Materials for Lithium Ion Batteries. *Solid State Sciences*, 8(2):113 – 128, 2006.

[112] Zonghai Chen, Yan Qin, Khalil Amine, and Y.-K. Sun. Role of Surface Coating on Cathode Materials for Lithium-Ion Batteries. *J. Mater. Chem.*, 20:7606–7612, 2010.

[113] Debra R. Rolison and Bruce Dunn. Electrically Conductive Oxide Aerogels: New Materials in Electrochemistry. *J. Mater. Chem.*, 11:963–980, 2001.

[114] Adam F Gross, Channing C Ahn, Sky L Van Atta, Ping Liu, and John J Vajo. Fabrication and Hydrogen Sorption Behaviour of Nanoparticulate MgH_2 Incorporated in a Porous Carbon Host. *Nanotechnology*, 20(20):204005, 2009.

[115] Dawei Liu, Yanyi Liu, Anqiang Pan, Kenneth P. Nagle, Gerald T. Seidler, Yoon-Ha Jeong, and Guozhong Cao. Enhanced Lithium-Ion Intercalation Properties of V_2O_5 Xerogel Electrodes with Surface Defects. *The Journal of Physical Chemistry C*, 115(11):4959–4965, 2011.

[116] Dawei Liu, Yunhuai Zhang, Peng Xiao, Betzaida Batalla Garcia, Qifeng Zhang, Xiaoyuan Zhou, Yoon-Ha Jeong, and Guozhong Cao. TiO_2 Nanotube Arrays Annealed in CO Exhibiting High Performance For Lithium Ion Intercalation. *Electrochimica Acta*, 54(27):6816–6820, 2009.

[117] Karen E. Swider-Lyons, Corey T. Love, and Debra R. Rolison. Improved Lithium Capacity of Defective V_2O_5 Materials. *Solid State Ionics*, 152153(0):99–104, 2002.

[118] D. Sun, C.W. Kwon, G. Baure, E. Richman, J. MacLean, B. Dunn, and S.H. Tolbert. The Relationship Between Nanoscale Structure and Electrochemical Properties of Vanadium Oxide Nanorolls. *Advanced Functional Materials*, 14(12):1197–1204, 2004.

[119] Bingkun Guo, Xiqing Wang, Pasquale F. Fulvio, Miaofang Chi, Shannon M. Mahurin, Xiao-Guang Sun, and Sheng Dai. Soft-Templated Mesoporous Carbon-Carbon Nanotube Composites for High Performance Lithium-ion Batteries. *Advanced Materials*, 23(40):4661–4666, 2011.

[120] Arava Leela Mohana Reddy, Anchal Srivastava, Sanketh R. Gowda, Hemtej Gullapalli, Madan Dubey, and Pulickel M. Ajayan. Synthesis Of Nitrogen-Doped Graphene Films For Lithium Battery Application. *ACS Nano*, 4(11):6337–6342, 2010.

[121] Dengyu Pan, Song Wang, Bing Zhao, Minghong Wu, Haijiao Zhang, Yong Wang, and Zheng Jiao. Li Storage Properties of Disordered Graphene Nanosheets. *Chemistry of Materials*, 21(14):3136–3142, 2009.

[122] Kyu-Sung Park, Penghao Xiao, So-Yeon Kim, Anthony Dylla, Young-Min Choi, Graeme Henkelman, Keith J. Stevenson, and John B. Goodenough. Enhanced Charge-Transfer Kinetics by Anion Surface Modification of $LiFePO_4$. *Chemistry of Materials*, 24(16):3212–3218, 2012.

[123] Marnix Wagemaker, Fokko M. Mulder, and Anton Van der Ven. The Role of Surface and Interface Energy on Phase Stability of Nanosized Insertion Compounds. *Advanced Materials*, 21(25-26):2703–2709, 2009.

[124] U. Lafont E. M. Kelder W. J. H. Borghols, M. Wagemaker and F. M. Mulder. Size Effects in the $Li_{4+x}Ti_5O_{12}$ Spinel. *Journal of the American Chemical Society*, 131(39):17786–17792, 2009.

[125] M. N. Ou, S. R. Harutyunyan, S. J. Lai, C. D. Chen, T. J. Yang, and Y. Y. Chen. Thermal and Electrical Transport Properties of a Single Nickel Nanowire. *Physica Status Solidi (B)*, 244(12):4512–4517, 2007.

[126] B.V. Ratnakumar, M.C. Smart, and S. Surampudi. Effects of SEI on the Kinetics of Lithium Intercalation. *Journal of Power Sources*, 9798(0):137–139, 2001.

[127] F. Bguin, F. Chevallier, C. Vix-Guterl, S. Saadallah, V. Bertagna, J.N. Rouzaud, and E. Frackowiak. Correlation of the Irreversible Lithium Capacity with the Active Surface Area of Modified Carbons. *Carbon*, 43(10):2160–2167, 2005.

[128] Jun ichi Yamaki, Hideyasu Takatsuji, Tetsuya Kawamura, and Minato Egashira. Thermal Stability of Graphite Anode with Electrolyte in Lithium-Ion Cells. *Solid State Ionics*, 148(34):241–245, 2002.

[129] Andrzej Lewandowski and Agnieszka widerska Mocek. Ionic Liquids as Electrolytes for Li-Ion Batteries an Overview of Electrochemical Studies. *Journal of Power Sources*, 194(2):601–609, 2009.

[130] Sheng Shui Zhang. A Review on Electrolyte Additives For Lithium-Ion Batteries. *Journal of Power Sources*, 162(2):1379–1394, 2006.

[131] K. Edstrm, A.M. Andersson, A. Bishop, L. Fransson, J. Lindgren, and A. Hussnius. Carbon Electrode Morphology and Thermal Stability of the Passivation Layer. *Journal of Power Sources*, 9798(0):87–91, 2001.

[132] Yoon-Soo Park and Sung-Man Lee. Effects of Particle Size on the Thermal Stability of Lithiated Graphite Anode. *Electrochimica Acta*, 54(12):3339–3343, 2009.

[133] Minki Jo, Young-Sik Hong, Jaebum Choo, and Jaephil Cho. Effect of $LiCoO_2$ Cathode Nanoparticle Size on High Rate Performance for Li-Ion Batteries. *Journal of The Electrochemical Society*, 156(6):A430–A434, 2009.

[134] Jinglei Lei, Lingjie Li, Robert Kostecki, Rolf Muller, and Frank McLarnon. Characterization of SEI Layers on $LiMn_2O_4$ Cathodes with In Situ Spectroscopic Ellipsometry. *Journal of The Electrochemical Society*, 152(4):A774–A777, 2005.

[135] Jean Frdric Martin, Atsuo Yamada, Genki Kobayashi, Shin-ichi Nishimura, Ryoji Kanno, Dominique Guyomard, and Nicolas Dupr. Air Exposure Effect on $LiFePO_4$. *Electrochemical and Solid-State Letters*, 11(1):A12–A16, 2008.

[136] Hong Li, Lihong Shi, Qing Wang, Liquan Chen, and Xuejie Huang. Nano-Alloy Anode for Lithium Ion Batteries. *Solid State Ionics*, 148(34):247–258, 2002.

[137] Dong H. Jang, Young J. Shin, and Seung M. Oh. Dissolution of Spinel Oxides and Capacity Losses in 4V $Li/Li_xMn_2O_4$ Cells. *Journal of The Electrochemical Society*, 143(7):2204–2211, 1996.

[138] Dong H. Jang and Seung M. Oh. Electrolyte Effects on Spinel Dissolution and Cathodic Capacity Losses in 4V $Li/Li_xMn_2O_4$ Rechargeable Cells. *Journal of The Electrochemical Society*, 144(10):3342–3348, 1997.

[139] Ting-Feng Yi, Yan-Rong Zhu, Xiao-Dong Zhu, J. Shu, Cai-Bo Yue, and An-Na Zhou. A Review of Recent Developments in the Surface Modification of $LiMn_2O_4$ as Cathode Material of Power Lithium-Ion Battery. *Ionics*, 15(6):779–784, 2009.

[140] Markus Antonietti and Geoffrey A. Ozin. Promises and Problems of Mesoscale Materials Chemistry or Why Meso? *Chemistry A European Journal*, 10(1):28–41, 2004.

[141] Jun Liu, Guozhong Cao, Zhenguo Yang, Donghai Wang, Dan Dubois, Xiaodong Zhou, Gordon L. Graff, Larry R. Pederson, and Ji-Guang Zhang. Oriented Nanostructures for Energy Conversion and Storage. *ChemSusChem*, 1(8-9):676–697, 2008.

[142] Franklin Kim, Stephen Connor, Hyunjoon Song, Tevye Kuykendall, and Peidong Yang. Platonic Gold Nanocrystals. *Angewandte Chemie*, 116(28):3759–3763, 2004.

[143] Laifa Shen, Evan Uchaker, Changzhou Yuan, Ping Nie, Ming Zhang, Xiaogang Zhang, and Guozhong Cao. Three-Dimensional Coherent TitaniaMesoporous Carbon Nanocomposite and its Lithium-Ion Storage Properties. *ACS Applied Materials and Interfaces*, 4(6):2985–2992, 2012.

[144] Laifa Shen, Xiaogang Zhang, Evan Uchaker, Changzhou Yuan, and Guozhong Cao. $Li_4Ti_5O_{12}$ Nanoparticles Embedded in a Mesoporous Carbon Matrix as a Superior Anode Material for High Rate Lithium Ion Batteries. *Advanced Energy Materials*, 2(6):691–698, 2012.

[145] Claus Feldmann and Hans-Otto Jungk. Polyol-Mediated Preparation of Nanoscale Oxide Particles. *Angewandte Chemie International Edition*, 40(2):359–362, 2001.

[146] P. Ragupathy, S. Shivakumara, H. N. Vasan, and N. Munichandraiah. Preparation of Nanostrip V_2O_5 by the Polyol Method and its Electrochemical Characterization as Cathode Material for Rechargeable Lithium Batteries. *The Journal of Physical Chemistry C*, 112(42):16700–16707, 2008.

[147] X. Jiang, T. Herricks, and Y. Xia. Monodispersed Spherical Colloids of Titania: Synthesis, Characterization, and Crystallization. *Advanced Materials*, 15(14):1205–1209, 2003.

[148] Xuchuan Jiang, Yuliang Wang, Thurston Herricks, and Younan Xia. Ethylene Glycol-Mediated Synthesis of Metal Oxide Nanowires. *J. Mater. Chem.*, 14:695–703, 2004.

[149] Benjamin Wiley, Thurston Herricks, Yugang Sun, and Younan Xia. Polyol Synthesis of Silver Nanoparticles: Use of Chloride and Oxygen to Promote the Formation of Single-Crystal, Truncated Cubes and Tetrahedrons. *Nano Letters*, 4(9):1733–1739, 2004.

[150] Chao Liu, Xiaowei Wu, Timothy Klemmer, Nisha Shukla, Xiaomin Yang, Dieter Weller, Anup G. Roy, Mihaela Tanase, and David Laughlin. Polyol Process Synthesis of Monodispersed FePt Nanoparticles. *The Journal of Physical Chemistry B*, 108(20):6121–6123, 2004.

[151] Jingyi Chen, Thurston Herricks, Matthias Geissler, and Younan Xia. Single-Crystal Nanowires of Platinum Can Be Synthesized by Controlling the Reaction Rate of a Polyol Process. *Journal of the American Chemical Society*, 126(35):10854–10855, 2004.

[152] M. P. Pileni. The Role of Soft Colloidal Templates in Controlling the Size snd Shape of Inorganic Nanocrystals. *Nature Materials*, 2(3):145–150, 2003.

[153] K. K. Caswell, Christopher M. Bender, and Catherine J. Murphy. Seedless, Surfactantless Wet Chemical Synthesis of Silver Nanowires. *Nano Letters*, 3(5):667–669, 2003.

[154] Thurston Herricks, Jingyi Chen, and Younan Xia. Polyol Synthesis of Platinum Nanoparticles: Control of Morphology with Sodium Nitrate. *Nano Letters*, 4(12):2367–2371, 2004.

[155] Chunman Ho, Jimmy C. Yu, Tszyan Kwong, Angelo C. Mak, and Sukyin Lai. Morphology-Controllable Synthesis of Mesoporous CeO_2 Nano- and Microstructures. *Chemistry of Materials*, 17(17):4514–4522, 2005.

[156] Nan Zhou, Yanyi Liu, Jiangang Li, Evan Uchaker, Suqin Liu, Kelong Huang, and Guozhong Cao. Synthesis and Characterization of High Power $LiFePO_4$/C Nano-Plate Thin Films. *Journal of Power Sources*, 213(0):100–105, 2012.

[157] Yugang Sun, Yadong Yin, Brian T. Mayers, Thurston Herricks, and Younan Xia. Uniform Silver Nanowires Synthesis by Reducing $AgNO_3$ with Ethylene Glycol in the Presence of Seeds and Poly(Vinyl Pyrrolidone). *Chemistry of Materials*, 14(11):4736–4745, 2002.

[158] Laifa Shen, Hongsen Li, Evan Uchaker, Xiaogang Zhang, and Guozhong Cao. General Strategy for Designing CoreShell Nanostructured Materials for High-Power Lithium Ion Batteries. *Nano Letters*, 12(11):5673–5678, 2012.

[159] Haitao Fu, Xuchuan Jiang, Xiaohong Yang, Aibing Yu, Dawei Su, and Guoxiu Wang. Glycothermal Synthesis of Assembled Vanadium Oxide Nanostructures for Gas Sensing. *Journal of Nanoparticle Research*, 14(6):1–14, 2012.

[160] Yanyi Liu, Evan Uchaker, Nan Zhou, Jiangang Li, Qifeng Zhang, and Guozhong Cao. Facile Synthesis of Nanostructured Vanadium Oxide As Cathode Materials for Efficient Li-Ion Batteries. *J. Mater. Chem.*, 22:24439–24445, 2012.

[161] Curtis Weeks, Yanning Song, Masatsugu Suzuki, Natasha A. Chernova, Peter Y. Zavalij, and M. Stanley Whittingham. The One Dimensional Chain Structures of Vanadyl Glycolate and Vanadyl Acetate. *J. Mater. Chem.*, 13:1420–1423, 2003.

[162] Victor K. LaMer and Robert H. Dinegar. Theory, Production and Mechanism of Formation of Monodispersed Hydrosols. *Journal of the American Chemical Society*, 72(11):4847–4854, 1950.

[163] Qing Peng, Yajie Dong, and Yadong Li. ZnSe Semiconductor Hollow Microspheres. *Angewandte Chemie International Edition*, 42(26):3027–3030, 2003.

[164] Manuel Ocaa, Rafael Rodriguez-Clemente, and Carlos J. Serna. Uniform colloidal particles in solution: Formation mechanisms. *Advanced Materials*, 7(2):212–216, 1995.

[165] A. Talledo and C. G. Granqvist. Electrochromic VanadiumPentoxideBased Films: Structural, Electrochemical, and Optical Properties. *Journal of Applied Physics*, 77(9), 1995.

[166] Yanyi Liu, Jiangang Li, Qifeng Zhang, Nan Zhou, Evan Uchaker, and Guozhong Cao. Porous Nanostructured V_2O_5 Film Electrode with Excellent Li-Ion Intercalation Properties. *Electrochemistry Communications*, 13(11):1276–1279, 2011.

[167] Pimpa Limthongkul, Young-Il Jang, Nancy J. Dudney, and Yet-Ming Chiang. Electrochemically-Driven Solid-State Amorphization in Lithium-Silicon Alloys and Implications for Lithium Storage. *Acta Materialia*, 51(4):1103–1113, 2003.

[168] Yang Liu, Nicholas S. Hudak, Dale L. Huber, Steven J. Limmer, John P. Sullivan, and Jian Yu Huang. In Situ Transmission Electron Microscopy Observation of Pulverization of Aluminum Nanowires and Evolution of the Thin Surface Al_2O_3 Layers during LithiationDelithiation Cycles. *Nano Letters*, 11(10):4188–4194, 2011.

[169] F. Y. Kong, M. Li, X. Y. Yao, J. M. Xu, A. D. Wang, Z. P. Liu, and G. H. Li. Template-Free Hydrothermal Synthesis of VO_2 Hollow Microspheres. *CrystEngComm*, 14:3858–3861, 2012.

[170] Haimei Liu, Yonggang Wang, Kaixue Wang, Eiji Hosono, and Haoshen Zhou. Design and Synthesis of a Novel Nanothorn VO_2(B) Hollow Microsphere and Their Application in lithium-ion batteries. *J. Mater. Chem.*, 19:2835–2840, 2009.

[171] Laifa Shen, Evan Uchaker, Xiaogang Zhang, and Guozhong Cao. Hydrogenated $Li_4Ti_5O_{12}$ Nanowire Arrays for High Rate Lithium Ion Batteries. *Advanced Materials*, 24(48):6502–6506, 2012.

[172] Evan Uchaker, Nan Zhou, Yanwei Li, and Guozhong Cao. Polyol-Mediated Solvothermal Synthesis and Electrochemical Performance of Nanostructured V_2O_5 Hollow Microspheres. *The Journal of Physical Chemistry C*, 117(4):1621–1626, 2013.

[173] Qifeng Zhang, Evan Uchaker, Stephanie L. Candelaria, and Guozhong Cao. Nanomaterials for Energy Conversion and Storage. *Chem. Soc. Rev.*, 42:3127–3171, 2013.

[174] Rafael O. Da Silva, Ricardo H. Goncalves, Daniel G. Stroppa, Antonio J. Ramirez, and Edson R. Leite. Synthesis of Recrystallized Anatase TiO_2 Mesocrystals with Wulff Shape Assisted By Oriented Attachment. *Nanoscale*, 3:1910–1916, 2011.

[175] Christine Lausser, Helmut Colfen, and Markus Antonietti. Mesocrystals of Vanadium Pentoxide: A Comparative Evaluation of Three Different Pathways of Mesocrystal Synthesis from Tactosol Precursors. *ACS Nano*, 5(1):107–114, 2011.

[176] Jelena Popovic, Rezan Demir-Cakan, Julian Tornow, Mathieu Morcrette, Dang Sheng Su, Robert Schlgl, Markus Antonietti, and Maria-Magdalena Titirici. $LiFePO_4$ Mesocrystals for Lithium-Ion Batteries. *Small*, 7(8):1127–1135, 2011.

[177] Andrew Baynton, Tomoko Radomirovic, Mark I. Ogden, Colin L. Raston, William R. Richmond, and Franca Jones. Small Molecules Induce Mesocrystal Formation: Nanoparticle Aggregation Directed by Self-Assembling Calixarenes. *CrystEngComm*, 13:109–112, 2011.

[178] Stephen Mann. Self-assembly and Transformation of Hybrid Nano-Objects and Nanostructures Under Equilibrium and Non-Equilibrium Conditions. *Nature Materials*, 8(10):781–792, 2009.

[179] Guicun Li, Kun Chao, Hongrui Peng, Kezheng Chen, and Zhikun Zhang. Low-Valent Vanadium Oxide Nanostructures with Controlled Crystal Structures and Morphologies. *Inorganic Chemistry*, 46(14):5787–5790, 2007.

[180] Graham Armstrong, Jess Canales, A. Robert Armstrong, and Peter G. Bruce. The synthesis and lithium intercalation electrochemistry of VO_2(B) ultra-thin nanowires. *Journal of Power Sources*, 178(2):723–728, 2008.

[181] A.M. Kannan and A. Manthiram. Synthesis and Electrochemical Evaluation of High Capacity Nanostructured VO_2 Cathodes. *Solid State Ionics*, 159(34):265–271, 2003.

[182] Haihong Yin, Ke Yu, Zhengli Zhang, and Ziqiang Zhu. Morphology-Control of VO_2(B) Nanostructures in Hydrothermal Synthesis snd their Field Emission Properties. *Applied Surface Science*, 257(21):8840–8845, 2011.

[183] Guicun Li, Kun Chao, Chuanqin Zhang, Qingshan Zhang, Hongrui Peng, and Kezheng Chen. Synthesis of Urchin-like VO_2 Nanostructures Composed of Radially Aligned Nanobelts and Their Disassembly. *Inorganic Chemistry*, 48(3):1168–1172, 2009.

[184] Lei Zhou and Paul OBrien. Mesocrystals - Properties and Applications. *The Journal of Physical Chemistry Letters*, 3(5):620–628, 2012.

[185] Wentao Jiang, Juan Ni, Ke Yu, and Ziqiang Zhu. Hydrothermal Synthesis and Electrochemical Characterization of VO_2(B) with Controlled Crystal Structures. *Applied Surface Science*, 257(8):3253–3258, 2011.

[186] Ch. Leroux, G. Nihoul, and G. Van Tendeloo. From VO_2(B) to VO_2(R): Theoretical Structures of VO_2 Polymorphs and In Situ Electron Microscopy. *Phys. Rev. B*, 57:5111–5121, Mar 1998.

[187] Junfeng Liu, Qiuhong Li, Taihong Wang, Dapeng Yu, and Yadong Li. Metastable Vanadium Dioxide Nanobelts: Hydrothermal Synthesis, Electrical Transport, and Magnetic Properties. *Angewandte Chemie International Edition*, 43(38):5048–5052, 2004.

[188] C. M. Julien, A. Mauger, and K. Zaghib. Surface Effects on Electrochemical Properties Of Nano-Sized $LiFePO_4$. *J. Mater. Chem.*, 21:9955–9968, 2011.

[189] Anqiang Pan, Hao Bin Wu, Le Yu, and Xiong Wen (David) Lou. Template-Free Synthesis of VO_2 Hollow Microspheres with Various Interiors and Their Conversion into V_2O_5 for Lithium-Ion Batteries. *Angewandte Chemie International Edition*, 52(8):2226–2230, 2013.

[190] Anqiang Pan, Ting Zhu, Hao Bin Wu, and Xiong Wen (David) Lou. Template-Free Synthesis of Hierarchical Vanadium-Glycolate Hollow Microspheres and Their Conversion to V_2O_5 with Improved Lithium Storage Capability. *Chemistry A European Journal*, 19(2):494–500, 2013.

[191] Virany M. Yuwono, Nathan D. Burrows, Jennifer A. Soltis, and R. Lee Penn. Oriented Aggregation: Formation and Transformation of Mesocrystal Intermediates Revealed. *Journal of the American Chemical Society*, 132(7):2163–2165, 2010.

[192] Cheng Hua Sun, Xiao Hua Yang, Jun Song Chen, Zhen Li, Xiong Wen Lou, Chunzhong Li, Sean C. Smith, Gao Qing (Max) Lu, and Hua Gui Yang. Higher Charge/Discharge Rates of Lithium-Ions Across Engineered TiO2 Surfaces Leads To Enhanced Battery Performance. *Chem. Commun.*, 46:6129–6131, 2010.

[193] Andrea Vittadini, Maurizio Casarin, and Annabella Selloni. Structure and Stability of TiO_2-B Surfaces: A Density Functional Study. *The Journal of Physical Chemistry C*, 113(44):18973–18977, 2009.

[194] M.M. Rahman, Jia-Zhao Wang, Nurul Hayati Idris, Zhixin Chen, and Huakun Liu. Enhanced Lithium Storage in a VO_2(B)-Multiwall Carbon Nanotube Microsheet Composite Prepared via an In Situ Hydrothermal Process. *Electrochimica Acta*, 56(2):693–699, 2010.

[195] Qianqian Zhao, Lifang Jiao, Wenxiu Peng, Haiyan Gao, Jiaqin Yang, Qinghong Wang, Hongmei Du, Li Li, Zhan Qi, Yuchang Si, Yijing Wang, and Huatang Yuan. Facile Synthesis of VO_2(B)/Carbon Nanobelts with High Capacity and Good Cyclability. *Journal of Power Sources*, 199(0):350–354, 2012.

[196] Xianhong Rui, Daohao Sim, Chen Xu, Weiling Liu, Huiteng Tan, Kangming Wong, Huey Hoon Hng, Tuti Mariana Lim, and Qingyu Yan. One-pot Synthesis of Carbon-Coated VO_2(B) Nanobelts for High-Rate Lithium Storage. *RSC Adv.*, 2:1174–1180, 2012.

[197] John B. Goodenough and Kyu-Sung Park. The Li-Ion Rechargeable Battery: A Perspective. *Journal of the American Chemical Society*, 135(4):1167–1176, 2013.

[198] Vinodkumar Etacheri, Rotem Marom, Ran Elazari, Gregory Salitra, and Doron Aurbach. Challenges in the Development of Advanced Li-Ion Batteries: a Review. *Energy and Environmental Science*, 4(9):3243–3262, 2011.

[199] Veronica Palomares, Paula Serras, Irune Villaluenga, Karina B. Hueso, Javier Carretero-Gonzalez, and Teofilo Rojo. Na-ion Batteries, Recent Advances and Present Challenges to Become Low Cost Energy Storage Systems. *Energy and Environmental Science*, 5(3):5884–5901, 2012.

[200] Sung-Wook Kim, Dong-Hwa Seo, Xiaohua Ma, Gerbrand Ceder, and Kisuk Kang. Electrode Materials for Rechargeable Sodium-Ion Batteries: Potential Alternatives to Current Lithium-Ion Batteries. *Advanced Energy Materials*, 2(7):710–721, 2012.

[201] Brian L. Ellis and Linda F. Nazar. Sodium and Sodium-Ion Energy Storage Batteries. *Current Opinion in Solid State and Materials Science*, 16(4):168–177, 2012.

[202] Xin Li Dong Su Geoffroy Hautier Gerbrand Ceder Jinhyuk Lee, Alexander Urban. Unlocking the Potential of Cation-Disordered Oxides for Rechargeable Lithium Batteries. *Science*, 343(6170):519–522, 2014.

[203] Hai-Tao Fang, Min Liu, Da-Wei Wang, Tao Sun, Dong-Sheng Guan, Feng Li, Jigang Zhou, Tsun-Kong Sham, and Hui-Ming Cheng. Comparison of the Rate Capability of Nanostructured Amorphous and Anatase TiO_2 for Lithium Insertion Using Anodic TiO_2 Nanotube Arrays. *Nanotechnology*, 20(22), 2009.

[204] G. Venkatesh, V. Pralong, O. I. Lebedev, V. Caignaert, P. Bazin, Raveau, and B. Amorphous Sodium Vanadate $Na_{1.5+y}VO_3$, a Promising Matrix for Reversible Sodium Intercalation. *Electrochem. Commun.*, 40:100–102, 2014.

[205] Wouter J. H. Borghols, Dirk Luetzenkirchen-Hecht, Ullrich Haake, Wingkee Chan, Ugo Lafont, Erik M. Kelder, Ernst R. H. van Eck, Arno P. M. Kentgens, Fokko M. Mulder, and Marnix Wagemaker. Lithium Storage in Amorphous TiO_2 Nanoparticles. *Journal of the Electrochemical Society*, 157(5):A582–A588, 2010.

[206] Jerzy Haber. Fifty Years of My Romance with Vanadium Oxide Catalysts. *Catalysis Today*, 142(3-4):100–113, 2009.

[207] Z. J. Lao, K. Konstantinov, Y. Tournaire, S. H. Ng, G. X. Wang, and H. K. Liu. Synthesis of Vanadium Pentoxide Powders with Enhanced Surface-Area for Electrochemical Capacitors. *Journal of Power Sources*, 162(2):1451–1454, 2006.

[208] John D. Jarrell, Brandon Dolly, and Jeffrey R. Morgan. Controlled Release of Vanadium From Titanium Oxide Coatings for Improved Integration of Soft Tissue Implants. *Journal of Biomedical Materials Research Part A*, 90A(1):272–281, 2009.

[209] Sanja Tepavcevic, Hui Xiong, Vojislav R. Stamenkovic, Xiaobing Zuo, Mahalingam Balasubramanian, Vitali B. Prakapenka, Christopher S. Johnson, and Tijana Rajh. Nanostructured Bilayered Vanadium Oxide Electrodes for Rechargeable Sodium-Ion Batteries. *Acs Nano*, 6(1):530–538, 2012.

[210] Dawei Su and Guoxiu Wang. Single-Crystalline Bilayered V_2O_5 Nanobelts for High-Capacity Sodium-Ion Batteries. *ACS Nano*, 2013.

[211] Haimei Liu, Haoshen Zhou, Lipeng Chen, Zhanfeng Tang, and Wensheng Yang. Electrochemical Insertion/Deinsertion of Sodium on NaV_6O_{15} Nanorods as Cathode Material of Rechargeable Sodium-Based Batteries. *Journal of Power Sources*, 196(2):814–819, 2011.

[212] Zheng Chen, Veronica Augustyn, Xilai Jia, Qiangfeng Xiao, Bruce Dunn, and Yunfeng Lu. High-Performance Sodium-Ion Pseudocapacitors Based on Hierarchically Porous Nanowire Composites. *Acs Nano*, 6(5):4319–4327, 2012.

[213] C. J. Fontenot, J. W. Wiench, M. Pruski, and G. L. Schrader. Vanadia Gel Synthesis via Peroxovanadate Precursors. 1. In Situ Laser Raman and V-51 NMR Characterization of the Gelation Process. *Journal of Physical Chemistry B*, 104(49):11622–11631, 2000.

[214] Jian-Mei Song Lian-Mei Chen Xiao-Yang Ji Jian-Hua Huang, Quiong-Yu Lai. Capacitive Performance of Amorphous V_2O_5 for Supercapacitor. *Chinese Journal of Inorganic Chemistry*, 23(2):237–242, 2007.

[215] A. Ignatiev A. Z. Moshfegh. Formation and Characterization of Thin Film Vanadium Oxides: Auger Electron Spectroscopy, X-Ray Photoelectron Spectroscopy, X-Ray Diffraction, Scanning Electron Microscopy, and Optical Reflectance Studies. *Thin Solid Films*, 198:251–268, 1991.

[216] G. Lucazeau C. Sanchez, J. Livage. Infrared and Raman Study of Amorphous V_2O_5. *Journal of Raman Spectroscopy*, 12(1):68–72, 1982.

[217] Ying Wang, Katsunori Takahashi, Kyoungho Lee, and Guozhong Cao. Nanostructured Vanadium Oxide Electrodes for Enhanced Lithium-Ion Intercalation. *Advanced Functional Materials*, 16(9):1133–1144, 2006.

[218] P. Aldebert, N. Baffier, N. Gharbi, and J. Livage. Layered Structure Of Vanadium Pentoxide Gels. *Materials Research Bulletin*, 16(6):669–676, 1981.

[219] Y. Wang, H. Shang, Chou T., and G. Cao. Effects of Thermal Annealing on the Li^+ Intercalation Properties of V_2O_5 nH_2O Xerogel Films. *The Journal of Physical Chemistry B*, 109:11361–11366, 2005.

[220] J. Livage M. Nabavi, C. Sanchez. Structure and Properties of Amorphous V_2O_5. *Philosophical Magazine B*, 63(4):941–953, 1991.

[221] Nilgun Ozer. Electrochemical Properties of Sol-Gel Deposited Vanadium Pentoxide Films. *Thin Solid Films*, 305:80–87, 1997.

[222] A. Bennouna E.L. Ameziane M. Benmoussa, E. Ibnouelghazi. Structural, Electrical and Optical Properties of Sputtered Vanadium Pentoxide Thin Films. *Thin Solid Films*, 265:22–28, 1995.

[223] C. W. Zou, X. D. Yan, J. Han, R. Q. Chen, and W. Gao. Microstructures and Optical Properties of β-V_2O_5 Nanorods Prepared by Magnetron Sputtering. *Journal of Physics D: Applied Physics*, 42(14):145402, 2009.

[224] B. Ravel and M. Newville. *ATHENA*, *ARTEMIS*, *HEPHAESTUS*: Data Analysis For X-Ray Absorption Spectroscopy Using *IFEFFIT*. *Journal of Synchrotron Radiation*, 12(4):537–541, Jul 2005.

[225] A. N. Mansour, S. Dallek, P. H. Smith, and W. M. Baker. Thermogravimetry and X-Ray Absorption Spectroscopy Study of Heated V_2O_5 nH_2O Aerogels and Ambigels. *Journal of The Electrochemical Society*, 149(12):A1589–A1597, 2002.

[226] A. N. Mansour, P. H. Smith, W. M. Baker, M. Balasubramanian, and J. McBreen. A Comparative In Situ X-Ray Absorption Spectroscopy Study of Nanophase V_2O_5 Aerogel and Ambigel Cathodes. *Journal of The Electrochemical Society*, 150(4):A403–A413, 2003.

[227] W. Avansi, L.J.Q. Maia, C. Ribeiro, E.R. Leite, and V.R. Mastelaro. Local Structure Study of Vanadium Pentoxide 1D-Nanostructures. *Journal of Nanoparticle Research*, 13(10):4937–4946, 2011.

[228] Geert Silversmit, Jeroen A. van Bokhoven, Hilde Poelman, Ad M.J. van der Eerden, Guy B. Marin, Marie-Franoise Reyniers, and Roger De Gryse. The Structure of Supported and Unsupported Vanadium Oxide Under Calcination, Reduction and Oxidation Determined with {XAS}. *Applied Catalysis A: General*, 285(12):151 – 162, 2005.

[229] M. S. Whittingham. Lithium Batteries and Cathode Materials. *Chemical Reviews*, 104(10):4271–4301, 2004.

[230] Veronica Augustyn, Jeremy Come, Michael A. Lowe, Jong Woung Kim, Pierre-Louis Taberna, Sarah H. Tolbert, Hector D. Abruna, Patrice Simon, and Bruce Dunn. High-Rate Electrochemical Energy Storage Through Li+ Intercalation Pseudocapacitance. *Nature Materials*, 12(6):518–522, 2013.

[231] Marnix Wagemaker, Wouter J. H. Borghols, Ernst R. H. van Eck, Arno P. M. Kentgens, Gordon L. Kearley, and Fokko M. Mulder. The Influence of Size on Phase Morphology and Li-Ion Mobility in Nanosized Lithiated Anatase TiO_2. *Chemistry-a European Journal*, 13(7):2023–2028, 2007.

[232] T. Brezesinski S. Tolbert J. Wang, J. Polleux and B. Dunn. The Pseudocapacitive Behavior of TiO_2 (Anatase) Nanoparticles. *ECS Transactions*, 11(31):101–111, 2008.

[233] Jong Woung Kim, Veronica Augustyn, and Bruce Dunn. The Effect of Crystallinity on the Rapid Pseudocapacitive Response of Nb_2O_5. *Advanced Energy Materials*, 2(1):141–148, 2012.

[234] Patrice Simon and Yury Gogotsi. Materials for Electrochemical Capacitors. *Nature Materials*, 7(11):845–854, 2008.

[235] B. E. Conway. Transition From Supercapacitor To Battery Behavior In Electrochemical Energy-Storage. *Journal of the Electrochemical Society*, 138(6):1539–1548, 1991.

[236] K. Le Van, H. Groult, A. Mantoux, L. Perrigaud, F. Lantelme, R. Lindstrom, R. Badour-Hadjean, S. Zanna, and D. Lincot. Amorphous Vanadium Oxide Films Synthesised by Al CVD for Lithium Rechargeable Batteries. *Journal of Power Sources*, 160(1):592–601, 2006.

[237] S. Okada, T. Yamamoto, Y. Okazaki, J. Yamaki, M. Tokunaga, and T. Nishida. Cathode Properties of Amorphous and Crystalline $FePO_4$. *Journal of Power Sources*, 146(1-2):570–574, 2005.

[238] M. Mikkor. Graphite Aluminum and Silicon Carbide Coated Current Collectors for Sodium Sulfur Cells. *Journal of The Electrochemical Society*, 132(5):991–998, 1985.

[239] E. Uchaker, Y. Z. Zheng, S. Li, S. L. Candelaria, S. Hu, and G. Z. Cao. Better than Crystalline: Amorphous Vanadium Oxide for Sodium-Ion Batteries. *Journal of Materials Chemistry A*, 2(43):18208–18214, 2014.

[240] Yanwei Li, Jinhuan Yao, Evan Uchaker, Ming Zhang, Jianjun Tian, Xiaoyan Liu, and Guozhong Cao. Sn-Doped V_2O_5 Film with Enhanced Lithium-Ion Storage Performance. *Journal of Physical Chemistry C*, 117(45):23507–23514, 2013.

[241] Kyler J. Carroll, Danna Qian, Chris Fell, Scott Calvin, Gabriel M. Veith, Miaofang Chi, Loic Baggetto, and Ying Shirley Meng. Probing the Electrode/Electrolyte Interface in the Lithium Excess Layered Oxide $Li_{1.2}Ni_{0.2}Mn_{0.6}O_2$. *Physical Chemistry Chemical Physics*, 15(26):11128–11138, 2013.

[242] Christopher R. Fell, Danna Qian, Kyler J. Carroll, Miaofang Chi, Jacob L. Jones, and Ying Shirley Meng. Correlation Between Oxygen Vacancy, Microstrain, and Cation Distribution in Lithium-Excess Layered Oxides During the First Electrochemical Cycle. *Chemistry of Materials*, 25(9):1621–1629, 2013.

[243] Danna Qian, Bo Xu, Miaofang Chi, and Ying Shirley Meng. Uncovering the Roles of Oxygen Vacancies in Cation Migration in Lithium Excess Layered Oxides. *Physical Chemistry Chemical Physics*, 16(28):14665–14668, 2014.

[244] Jie Song, Dong Wook Shin, Yuhao Lu, Charles D. Amos, Arumugam Manthiram, and John B. Goodenough. Role of Oxygen Vacancies on the Performance of $Li[Ni_{0.5x}Mn_{1.5+x}]O_4$ (x = 0, 0.05, and 0.08) Spinel Cathodes for Lithium-Ion Batteries. *Chemistry of Materials*, 24(15):3101–3109, 2012.

[245] Peter V. Sushko, Kevin M. Rosso, Ji-Guang Zhang, Jun Liu, and Maria L. Sushko. Oxygen Vacancies and Ordering of d-levels Control Voltage Suppression in Oxide Cathodes: the Case of Spinel $LiNi_{0.5}Mn_{1.5}O_{4-\delta}$. *Advanced Functional Materials*, 23(44):5530–5535, 2013.

[246] Gogi K. Singh, Gerbrand Ceder, and Martin Z. Bazant. Intercalation Dynamics in Rechargeable Battery Materials: General Theory and Phase-Transformation Waves in $LiFePO_4$. *Electrochimica Acta*, 53(26):7599–7613, 2008.

[247] H. Y. Zhu, Y. Lan, X. P. Gao, S. P. Ringer, Z. F. Zheng, D. Y. Song, and J. C. Zhao. Phase Transition between Nanostructures of Titanate and Titanium Dioxides via Simple Wet-Chemical Reactions. *Journal of the American Chemical Society*, 127(18):6730–6736, 2005.

[248] X. H. Wang, J. G. Li, H. Kamiyama, M. Katada, N. Ohashi, Y. Moriyoshi, and T. Ishigaki. Pyrogenic Iron(III)-Doped TiO_2 Nanopowders Synthesized in RF Thermal Plasma: Phase Formation, Defect Structure, Band Gap, and Magnetic Properties. *Journal of the American Chemical Society*, 127(31):10982–10990, 2005.

[249] K. Mizushima, P. C. Jones, P. J. Wiseman, and J. B. Goodenough. $LixCoO_2$: a New Cathode Material for Batteries of High Energy Density. *Materials Research Bulletin*, 15(6):783–789, 1980.

[250] Hugues Duncan, Bin Hai, Michal Leskes, Clare P. Grey, and Guoying Chen. Relationships between Mn^{3+} Content, Structural Ordering, Phase Transformation, and Kinetic Properties in $LiNi_xMn_{2x}O_4$ Cathode Materials. *Chemistry of Materials*, 26(18):5374–5382, 2014.

[251] Mi Ru Jo, Yong-Il Kim, Yunok Kim, Ji Su Chae, Kwang Chul Roh, Won-Sub Yoon, and Yong-Mook Kang. Lithium-Ion Transport through a Tailored Disordered Phase on the $LiNi_{0.5}Mn_{1.5}O_4$ Surface for High-Power Cathode Materials. *ChemSusChem*, 7(8):2248–2254, 2014.

[252] Dong Wook Shin, Craig A. Bridges, Ashfia Huq, M. Parans Paranthaman, and Arumugam Manthiram. Role of Cation Ordering and Surface Segregation in High-Voltage Spinel $LiMn_{1.5}Ni_{0.5x}M_xO_4$ (M = Cr, Fe, and Ga) Cathodes for Lithium-Ion Batteries. *Chemistry of Materials*, 24(19):3720–3731, 2012.

[253] Jie Xiao, Xilin Chen, Peter V. Sushko, Maria L. Sushko, Libor Kovarik, Jijun Feng, Zhiqun Deng, Jianming Zheng, Gordon L. Graff, Zimin Nie, Daiwon Choi, Jun Liu, Ji-Guang Zhang, and M. Stanley Whittingham. High-Performance $LiNi_{0.5}Mn_{1.5}O_4$ Spinel Controlled by Mn3+ Concentration and Site Disorder. *Advanced Materials*, 24(16):2109–2116, 2012.

[254] Eunseok Lee and Kristin A. Persson. Revealing the Coupled Cation Interactions Behind the Electrochemical Profile of LixNi0.5Mn1.5O4. *Energy & Environmental Science*, 5(3):6047–6051, 2012.

[255] Tula R. Paudel, Andriy Zakutayev, Stephan Lany, Mayeul d'Avezac, and Alex Zunger. Doping Rules and Doping Prototypes in A_2BO_4 Spinel Oxides. *Advanced Functional Materials*, 21(23):4493–4501, 2011.

[256] J. A. Kilner and R. J. Brook. A study of Oxygen Ion Conductivity in Doped Non-Stoichiometric Oxides. *Solid State Ionics*, 6(3):237–252, 1982.

[257] Jia-Yan Luo, Li-Juan Chen, Yu-Jun Zhao, Ping He, and Yong-Yao Xia. The effect of Oxygen Vacancies on the Structure and Electrochemistry of $LiTi_2(PO_4)_3$ for Lithium-ion Batteries: a Combined Experimental and Theoretical Study. *Journal of Power Sources*, 194(2):1075–1080, 2009.

[258] Sung-Yoon Chung, Jason T. Bloking, and Yet-Ming Chiang. Electronically Conductive Phospho-Olivines as Lithium Storage Electrodes. *Nat Mater*, 1(2):123–128, 2002.

[259] L. Dahron, H. Martinez, R. Dedryvre, I. Baraille, M. Mntrier, C. Denage, C. Delmas, and D. Gonbeau. Surface Properties of $LiCoO_2$ Investigated by XPS Analyses and Theoretical Calculations. *The Journal of Physical Chemistry C*, 113(14):5843–5852, 2009.

[260] Miwa Murakami, Yasuto Noda, Yukinori Koyama, K. Takegoshi, Hajime Arai, Yoshiharu Uchimoto, and Zempachi Ogumi. Local Structure and Spin State of Cobalt Ion at Defect in Lithium Overstoichiometric $LiCoO_2$ As Studied by 6/7Li Solid-State NMR Spectroscopy. *The Journal of Physical Chemistry C*, 118(28):15375–15385, 2014.

[261] Sung You Hong, Youngjin Kim, Yuwon Park, Aram Choi, Nam-Soon Choi, and Kyu Tae Lee. Charge Carriers in Rechargeable Batteries: Na Ions vs. Li Ions. *Energy & Environmental Science*, 6(7):2067–2081, 2013.

[262] Dibakar Datta, Junwen Li, and Vivek B. Shenoy. Defective Graphene as a High-Capacity Anode Material for Na- and Ca-Ion Batteries. *ACS Appl Mater Interfaces*, 6(3):1788–1795, 2014.

[263] John M. Clark, Prabeer Barpanda, Atsuo Yamada, and M. Saiful Islam. Sodium-ion Battery Cathodes $Na_2FeP_2O_7$ and $Na_2MnP_2O_7$: Diffusion Behaviour for High Rate Performance. *Journal of Materials Chemistry A*, 2(30):11807–11812, 2014.

[264] Brian H Toby. EXPGUI, a Graphical User Interface for GSAS. *Journal of Applied Crystallography*, 34(2):210–213, 2001.

[265] L. A. de Picciotto, K. T. Adendorff, D. C. Liles, and M. M. Thackeray. Structural Characterization of $Li_{1+x}V_3O_8$ Insertion Electrodes by Single-Crystal X-Ray Diffraction. *Solid State Ionics*, 62(34):297–307, 1993.

[266] A. D. Wadsley. Crystal Chemistry of Non-stoichiometric Pentavalent Vanadium Oxides: Crystal Structure of $Li_{1+x}V_3O_8$. *Acta Crystallographica*, 10:261–267, 1957.

[267] Diem Nguyen, Jihyeon Gim, Vinod Mathew, Jinju Song, Sungjin Kim, Docheon Ahn, and Jaekook Kim. Plate-Type NaV_3O_8 Cathode by Solid State Reaction for Sodium-Ion Batteries. *ECS Electrochemistry Letters*, 3(7):A69–A71, 2014.

[268] H. T. Evans and J. M. Hughes. Crystal Chemistry of the Natural Vanadium Bronzes. *American Mineralogist*, 75(5-6):508–521, 1990.

[269] H. T. Evans. The Crystal-Structure of Hewettite. *Canadian Mineralogist*, 27:181–188, 1989.

[270] W. H. Barnes. Hewettite and Metahewettite. *American Mineralogist*, 40(7-8):689–691, 1955.

[271] R. L. Frost, K. L. Erickson, and M. L. Weier. Hydrogen Bonding in Selected Vanadates: a Raman and Infrared Spectroscopy Study. *Spectrochimica Acta Part a-Molecular and Biomolecular Spectroscopy*, 60(10):2419–2423, 2004.

[272] R. L. Frost, K. L. Erickson, M. L. Weier, and O. Carmody. Raman and Infrared Spectroscopy of Selected Vanadates. *Spectrochimica Acta Part a-Molecular and Biomolecular Spectroscopy*, 61(5):829–834, 2005.

[273] C. Y. Lee, A. C. Marschilok, A. Subramanian, K. J. Takeuchi, and E. S. Takeuchi. Synthesis and Characterization of Sodium Vanadium Oxide Gels: the Effects of Water (n) and Sodium (x) Content on the Electrochemistry of $Na(x)V_2O_5nH_2O$. *Phys Chem Chem Phys*, 13(40):18047–54, 2011.

[274] Stphane Levasseur, Michel Mntrier, Yang Shao-Horn, Laurent Gautier, Albane Audemer, Grard Demazeau, Alain Largeteau, and Claude Delmas. Oxygen Vacancies and Intermediate Spin Trivalent Cobalt Ions in Lithium-Overstoichiometric $LiCoO_2$. *Chemistry of Materials*, 15(1):348–354, 2002.

[275] Geert Silversmit, Diederik Depla, Hilde Poelman, Guy B. Marin, and Roger De Gryse. Determination of the V2p XPS Binding Energies for Different Vanadium Oxidation States (V^{5+} to V^{0+}). *Journal of Electron Spectroscopy and Related Phenomena*, 135(23):167–175, 2004.

[276] J. Mendialdua, R. Casanova, and Y. Barbaux. XPS studies of V_2O_5, V_6O_{13}, VO_2 and V_2O_3. *Journal of Electron Spectroscopy and Related Phenomena*, 71(3):249–261, 1995.

[277] M. Demeter, M. Neumann, and W. Reichelt. Mixed-Valence Vanadium Oxides Studied by XPS. *Surface Science*, 454456(0):41–44, 2000.

[278] Yougen Tang, Dan Sun, Haiyan Wang, Xiaobing Huang, Hui Zhang, Suqin Liu, and Younian Liu. Synthesis and electrochemical properties of NaV_3O_8 nanoflakes as high-performance cathode for Li-ion battery. *RSC Advances*, 4(16):8328–8334, 2014.

[279] Jiaguo Yu, Jimmy C. Yu, Wingkei Ho, Ling Wu, and Xinchen Wang. A Simple and General Method for the Synthesis of Multicomponent $Na_2V_6O_{16}$ $3H_2O$ Single-Crystal Nanobelts. *Journal of the American Chemical Society*, 126(11):3422–3423, 2004.

[280] Michael Schindler, Frank C. Hawthorne, Malcolm A. Alexander, Rory A. Kutluoglu, Petre Mandaliev, Norman M. Halden, and Roger H. Mitchell. $NaLi[V_3O_8]$ Insertion Electrodes: Structures and Diffusion Pathways. *Journal of Solid State Chemistry*, 179(8):2616–2628, 2006.

[281] Hanna He, Guanhua Jin, Haiyan Wang, Xiaobing Huang, Zehua Chen, Dan Sun, and Yougen Tang. Annealed NaV_3O_8 Nanowires with Good Cycling Stability as a Novel Cathode for Na-Ion Batteries. *Journal of Materials Chemistry A*, 2(10):3563, 2014.

[282] S. Liang, T. Chen, A. Pan, D. Liu, Q. Zhu, and G. Cao. Synthesis of $Na_{1.25}V_3O_8$ Nanobelts with Excellent Long-Term Stability for Rechargeable Lithium-Ion Batteries. *ACS Appl Mater Interfaces*, 5(22):11913–7, 2013.

[283] A.J. Bard and L.R. Faulkner. *Electrochemical Methods: Fundamentals and Applications*. Wiley, 2000.

[284] H. Heli, H. Yadegari, and A. Jabbari. Investigation of the Lithium Intercalation Behavior of Nanosheets of LiV_3O_8 in an Aqueous Solution. *The Journal of Physical Chemistry C*, 115(21):10889–10897, 2011.

[285] Yifei Mo, Shyue Ping Ong, and Gerbrand Ceder. Insights into Diffusion Mechanisms in P2 Layered Oxide Materials by First-Principles Calculations. *Chemistry of Materials*, 26(18):5208–5214, 2014.

[286] Hui Xiong, Handan Yildirim, Elena V. Shevchenko, Vitali B. Prakapenka, Bonil Koo, Michael D. Slater, Mahalingam Balasubramanian, Subramanian K. R. S. Sankaranarayanan, Jeffrey P. Greeley, Sanja Tepavcevic, Nada M. Dimitrijevic, Paul Podsiadlo, Christopher S. Johnson, and Tijana Rajh. Self-Improving Anode for Lithium-Ion Batteries Based on Amorphous to Cubic Phase Transition in TiO_2 Nanotubes. *The Journal of Physical Chemistry C*, 116(4):3181–3187, 2011.

[287] Rong Huang, Yumi H. Ikuhara, Teruyasu Mizoguchi, Scott D. Findlay, Akihide Kuwabara, Craig A. J. Fisher, Hiroki Moriwake, Hideki Oki, Tsukasa Hirayama, and Yuichi Ikuhara. Oxygen-Vacancy Ordering at Surfaces of Lithium Manganese(III,IV) Oxide Spinel Nanoparticles. *Angewandte Chemie International Edition*, 50(13):3053–3057, 2011.

[288] Xiaoguang Hao, Xianke Lin, Wei Lu, and Bart M. Bartlett. Oxygen Vacancies Lead to Loss of Domain Order, Particle Fracture, and Rapid Capacity Fade in Lithium Manganospinel ($LiMn_2O_4$) Batteries. *ACS Appl Mater Interfaces*, 6(14):10849–10857, 2014.

[289] Q Huang, M L Foo, J W Lynn, H W Zandbergen, G Lawes, Yayu Wang, B H Toby, A P Ramirez, N P Ong, and R J Cava. Low Temperature Phase Transitions and Crystal Structure of $Na_{0.5}CoO_2$. *Journal of Physics: Condensed Matter*, 16(32):5803, 2004.

[290] R. Berthelot, D. Carlier, and C. Delmas. Electrochemical investigation of the P2Na_xCoO_2 phase diagram. *Nat Mater*, 10(1):74–80, 2011.

[291] Ming Tang, W. Craig Carter, and Yet-Ming Chiang. Electrochemically Driven Phase Transitions in Insertion Electrodes for Lithium-Ion Batteries: Examples in Lithium Metal Phosphate Olivines. *Annual Review of Materials Research*, 40(1):501–529, 2010.

[292] G. Pistoia, S. Panero, M. Tocci, R. V. Moshtev, and V. Manev. Solid Solutions $Li_{1+x}V_3O_8$ as Cathodes for High Rate Secondary Li Batteries. *Solid State Ionics*, 13(4):311–318, 1984.

[293] H. Y. P. Hong. Solid Electrolytes Containing both Mobile and Immobile Alkali Ions. *Journal of Power Sources*, 5(1):137–142, 1980.